NATIONAL AERONAUTICS AND SPACE ADMINISTRATION

Technical Report 32-1262

Surveyor VI Mission Report
Part II: Science Results

Prepared by:

The Surveyor Investigator Teams, Scientific Evaluation Advisory Team, and Working Groups

JET PROPULSION LABORATORY
CALIFORNIA INSTITUTE OF TECHNOLOGY
PASADENA, CALIFORNIA

January 10, 1968

NATIONAL AERONAUTICS AND SPACE ADMINISTRATION

Technical Report 32-1262

Surveyor VI Mission Report
Part II: Science Results

Prepared by:

The Surveyor Investigator Teams, Scientific Evaluation Advisory Team, and Working Groups

JET PROPULSION LABORATORY
CALIFORNIA INSTITUTE OF TECHNOLOGY
PASADENA, CALIFORNIA

January 10, 1968

TECHNICAL REPORT 32-1262

Prepared Under Contract No. NAS 7-100
National Aeronautics & Space Administration

Preface

This three-part document constitutes the Project Mission Report on *Surveyor VI*, the sixth in a series of unmanned lunar soft-landing missions.

Part I of this Technical Report consists of a technical description and an evaluation of engineering results of the systems used in the *Surveyor VI* mission. Part II presents the scientific data derived from the mission, and the scientific analyses conducted by the *Surveyor* Scientific Evaluation Advisory Team, the *Surveyor* Investigator Teams, and the Associated Working Groups. Part III consists of selected pictures from *Surveyor VI* and appropriate explanatory material.

Results given in this report are based on data evaluation prior to December 21, 1967. It is expected that future evaluation and analysis of the *Surveyor VI* data will provide additional science results.

Contents

Contents (contd)

Contents (contd)

Contents (contd)

I. Introduction

L. D. Jaffe

Surveyor VI was launched from Cape Kennedy, Florida, at 07:39:01 GMT on November 7, 1967. An *Atlas/Centaur* launch vehicle placed the *Surveyor* into a parking orbit and, at 08:03:30 GMT, injected it into a trajectory intersecting the moon. A midcourse maneuver was performed at 02:20:02 GMT on November 8. At 01:01:05.5 GMT on November 10, the spacecraft landed in Sinus Medii.

Inflight radio tracking data gave a position of 1.37 $\pm$0.05°W longitude, 0.4 $\pm$0.2°N latitude. Tracking after landing gave 1.37 $\pm$0.02°W longitude, 0.458 $\pm$0.007°N latitude.[1] Views of nearby terrain features obtained after landing by the *Surveyor VI* television camera were correlated with earlier *Lunar Orbiter* photographs; this correlation allowed the identification of *Surveyor's* position to within a meter. The landing site is a nearly flat, heavily cratered mare area, about 200 m northwest of the foot of a mare ridge about 30 m high. The corresponding selenographic coordinates, as read from the Orthographic Atlas (Ref. I-1), are 1.40°W longitude, 0.49°N latitude.[2] The discrepancy between the positions obtained from *Lunar Orbiter* photographs and from post-landing tracking data is due, in part, to inaccuracies in the selenographic grid.

[1]F. B. Winn, see Section X of this report.

[2]E. A. Whitaker; see Section III of this report.

Surveyor VI (Fig. I-1) was essentially a duplicate of *Surveyor V* (Ref. I-2), carrying an alpha-particle backscattering instrument to analyze the chemical composition of the lunar soil, and a television camera. However, instead of the color filters used on the *Surveyor V* camera, three polarizing filters were carried by *Surveyor VI;* some modifications were also made in its scanning mirror assembly to improve the positioning accuracy of the mirror and to extend the limits of view of the camera. To improve the view of the surface below one of the vernier engines, a third auxiliary mirror was added to the two mirrors flown on *Surveyor V*. The spacecraft mass at launch was 1007.9 kg; at touchdown, 299.6 kg.

The vertical velocity at landing was 3.4 $\pm$0.1 m/sec; the horizontal velocity was 0.3 $\pm$0.06 m/sec. After the landing, the longitudinal (roll) axis of the spacecraft was within 0.8 deg of the local vertical. At 10:32 GMT on November 17, the vernier rocket engines were fired for 2.5 sec. The spacecraft rose 3.5 m above the lunar surface and moved horizontally 2.4 m, landing 6.1 sec after liftoff at 3.8 $\pm$0.3 m/sec vertical velocity and 0.55 $\pm$0.06 m/sec horizontal velocity. *Surveyor* stopped with its roll axis 4 deg from the local vertical. The roll about this axis was 4 deg counterclockwise, as viewed from above, relative to the orientation before the firing. This hop permitted stereoscopic viewing and mapping of the

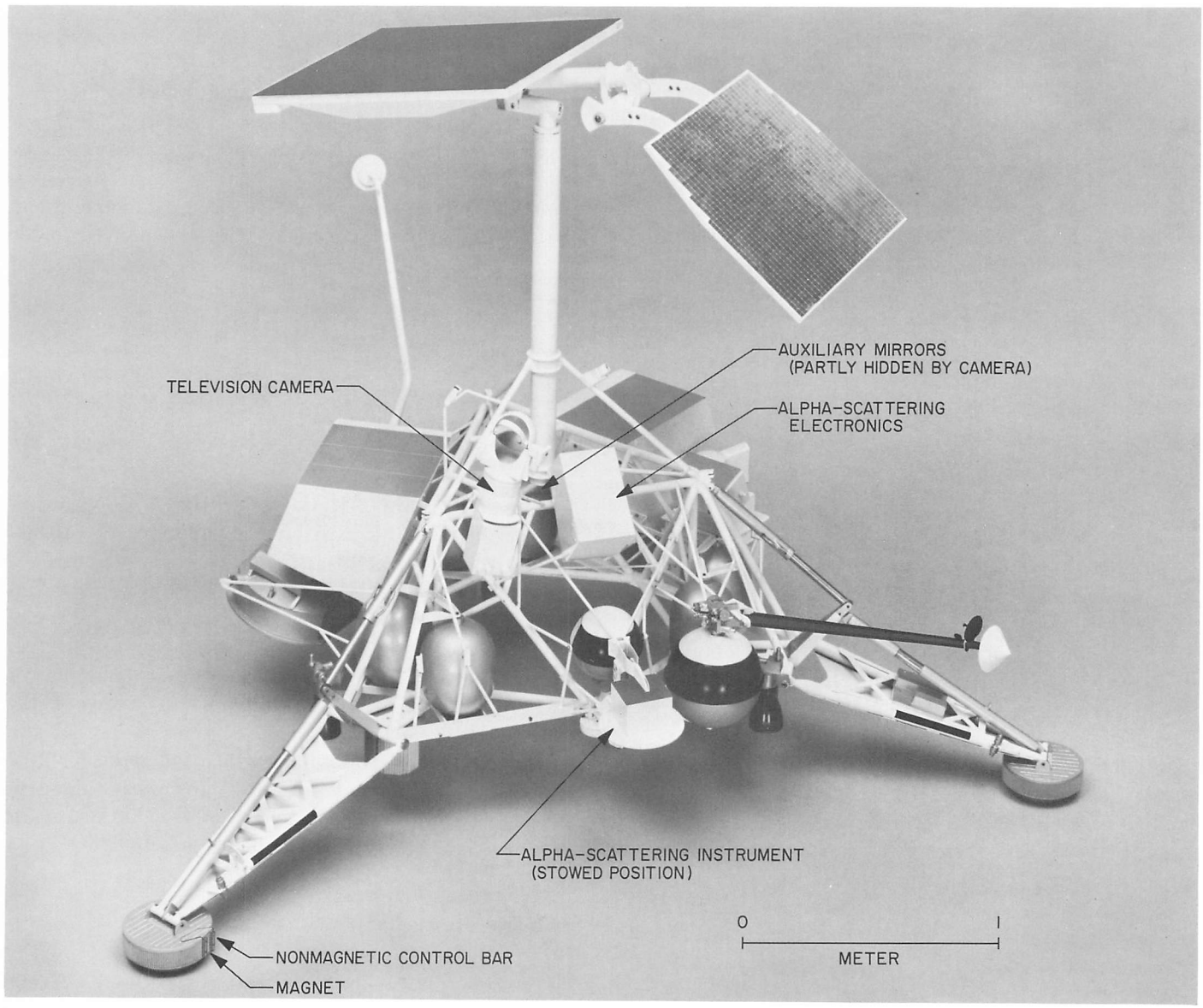

Fig. I-1. Model of *Surveyor VI* spacecraft in landed configuration.

surrounding lunar features, provided clearer views of the surface disturbances produced by the initial landing of the spacecraft, and furnished considerable information on the effects produced by firing the vernier rocket engines close to the lunar surface.

Surveyor VI transmitted 30,396 television pictures from November 10 to a few hours after local sunset on the spacecraft on November 24. These pictures included views of the undisturbed lunar surface and of the area disturbed by the initial landing and by the hop; views of the spacecraft, including the magnet assembly attached to one footpad; views of stars and earth; and views of the solar corona. The alpha-scattering instrument transmitted data for 30 hr on the chemical composition of the lunar surface. Good data on the temperatures of the surrounding surface area were obtained throughout the lunar day and for 41 hr after sunset. The magnet assembly supplied information on the presence of lunar material with a high magnetic susceptibility. During terminal descent, radar reflectivity data were obtained. The loads in the spacecraft legs were measured during initial touchdown and during the hop, thus providing information on the mechanical properties of the lunar surface material. A considerable quantity of doppler data was accumulated by the radio communication system after landing; these data should provide a selenodetic control point and information on lunar motions.

Surveyor VI was turned off for the lunar night on November 26. Spacecraft transmission was resumed for a short period on December 14, 1967.

Section II of this document, prepared by the *Surveyor* Scientific Evaluation Advisory Team, summarizes the principal science results of the *Surveyor VI* mission. More detailed information may be found in the subsequent sections, which were prepared by the *Surveyor VI* Investigator Teams and Working Groups. These sections have been written independently of one another; therefore, some differences in interpretation may exist among them. Because it was necessary to select values early in order to conduct calculations, some differences in numerical values may also occur among the sections.

Individual pictures taken by *Surveyor* may be obtained from the National Space Science Data Center, Goddard Space Flight Center, Greenbelt, Maryland. Individual pictures can best be identified by the day of the year and GMT at which they were taken. November 10 was Day 314; November 24 was Day 328. Mosaics are best identified by catalog number.

References

I-1. *Orthographic Atlas of the Moon, Supplement 1 to the Photographic Lunar Atlas,* compiled by D. W. G. Arthur and E. A. Whitaker, University of Arizona Press, Tucson, Ariz., 1961.

I-2. Jaffe, L. D., and Steinbacher, R. H., "Introduction," *Surveyor V Mission Report. Part II: Science Results,* Technical Report 32-1246, Jet Propulsion Laboratory, Pasadena, Calif., November 1, 1967.

Acknowledgment

R. H. Steinbacher and E. M. Christensen, JPL, conducted major portions of the organization and execution of the *Surveyor VI* science effort. J. N. Strand, JPL, was responsible for science aspects of the *Surveyor VI* television data handling.

(Blank Page)

II. Principal Science Results From *Surveyor VI*

L. D. Jaffe, S. A. Batterson, W. E. Brown, Jr., E. M. Christensen, S. E. Dwornik, D. E. Gault, J. W. Lucas, R. H. Norton, R. F. Scott, E. M. Shoemaker, R. H. Steinbacher, G. H. Sutton, and A. L. Turkevich

Surveyor VI landed on the flat surface of Sinus Medii near a mare ridge. The landing sites for the previous *Surveyor* spacecraft were:

(1) A flat surface inside a 100-km crater in Oceanus Procellarum (*Surveyor I*).

(2) Interior of a subdued 200-m crater, probably of impact origin, in Oceanus Procellarum (*Surveyor III*).

(3) A 10-m crater, which may be a subsidence feature, in Mare Tranquillitatis (*Surveyor V*).

All of these mare landing sites are very similar in topographic details; in the structure of the surface layer; in mechanical, thermal, and electrical properties; and, for *Surveyors V* and *VI*, in chemical composition and content of magnetic material. The resemblances of these sites to each other are striking. It is unlikely that sites on earth, thousands of kilometers apart and selected in a manner similar to the *Surveyor* landing sites, would be so much alike.

It is no longer possible, as it was after *Surveyor V*, to maintain that the chemical evidence of volcanic processes on the moon applies only to the *Surveyor V* site or only to Mare Tranquillitatis; these results must apply to a significant fraction of the mare surface of the moon.

The relatively minor differences among the sites have also proved significant in establishing some correlations that may have fundamental significance for the genesis of the outer layers of the maria. In this report, there is a significant new set of numerical values for the physical properties of the lunar surface. The increasing quantity of individual measurements has permitted new relationships to be established that better define numerical values.

As a result of the 2.4-m hop made by the spacecraft when the vernier engines were fired, pictures were taken of the lunar surface from perspective centers separated by as much as 2.4 m. Stereophotogrammetric reduction of these pictures will permit preparation of a large-scale topographic map of the surface extending about 50 m from the spacecraft in directions normal to the stereoscopic baseline. The hop also provided an opportunity to analyze significant properties of the lunar soil with a much higher level of confidence and permitted views of the imprints formed during the initial landing to be obtained, making it possible to obtain good measurements

of penetration of the lunar surface by the spacecraft and providing a clearer view of the character of the disturbed areas.

Based on data derived from *Surveyor VI* and the preceding missions, it can be concluded that there is a change in the properties of lunar surface material with depth: both bearing strength and density increase with increasing depth. The grain size, however, did not vary observably within a depth of several centimeters. The changes in the above parameters result in a decrease in porosity with the increase in depth.

The following range of values is representative of the mechanical properties at all landing sites:

Static bearing strength:

For upper few millimeters: $<10^4$ dynes/cm^2 (for 1-cm-diameter circular bearing area).[1]

At depth of approximately 2 cm: 2×10^5 dynes/cm^2 (for 20-cm-diameter circular bearing area).[2]

At depth of approximately 5 cm: 6×10^5 dynes/cm^2 (for average diameter of 25 cm).[3]

Bulk density (of undisturbed soil):

For upper few millimeters: 0.7 to 1.2 g/cm^3.

At depth of several centimeters: about 1.6 g/cm^3.

Assuming, from the results of the Alpha-Scattering Experiment, that the material is basalt with a grain density of about 3 g/cm^3, the porosity, including any vesicles within the grains, decreased from 0.8 to 0.5 over this depth. The lunar surface material was compressed inelastically, under pressures up to 5×10^5 dynes/cm^2, to a density of about 1.6 g/cm^3.

A value of adhesive strength of at least a few tens of dynes/cm^2, for lunar material thrown against and adhering to a photometric target, places a lower bound on the adhesion of the lunar soil. The value of 10^4 dynes/cm^2, for the bearing capacity of the upper few millimeters of surface, is indicative of a cohesion of the order 10^3 dynes/cm^2.

Damped oscillations of the spacecraft, after the initial landing and after the hop, indicate that the lunar surface material, as loaded by the footpads, had greater stiffness and contributed less damping at the second landing location than at the first. In both cases, estimates of elastic constants are approximately the same as those obtained for *Surveyors I* and *III*.

New information related to the grain size distribution near the surface is available from the results of firings of the vernier engines and attitude control jets and from the character of the various spacecraft imprints. A bright band of light observed along the horizon after sunset is apparently due to diffraction by small particles near or on the surface. These observations indicate a mean particle size of $<100\mu$.

Observations of the fine-grained parts of the lunar surface disturbed by the landing and liftoff of the *Surveyor VI* spacecraft, and by rolling fragments set in motion by the spacecraft, have shown that lunar material exposed at depths no greater than a few millimeters has a significantly lower normal albedo than the undisturbed surface. A similar abrupt decrease of albedo at depths of 3 mm or less was observed at the *Surveyor III* and *V* landing sites. The occurrence of this rather sharp contact of material with contrasting optical properties at widely separated localities on the lunar maria suggests that some process, or combination of processes, lightens the material at the lunar surface. If this is true, it may imply that a complementary process of darkening occurs at depths of a few millimeters and deeper, so that the abrupt albedo contact is not destroyed as a result of repetitive turnover of the lunar surface by solid particle bombardment.

The smallest blocky-rim craters observed on the mare floor around *Surveyor VI* are greater than 100 m in diameter; this shows that the layer of relatively fine-grained fragmental debris, or regolith, is considerably thicker (10 to 20 m) at the *Surveyor VI* site than at previous *Surveyor* landing sites. The depth of the debris layer was found to be 1 to 2 m thick at the *Surveyor I* site, and no more than 5 m at the *Surveyor V* landing site. The greater thickness at the *Surveyor VI* landing site is probably related to the greater age of the surface, which is indicated by a higher density of craters larger than 300 m in diameter on Sinus Medii as compared with most other mare surfaces. Blocky-rim craters 20 to 30 m in diameter occur on a mare ridge east of *Surveyor VI*. The debris layer is 8 to 10 m thick on the ridge; it may be thinner on the ridge than on the mare floor primarily as a result of gradual creep of fragmental material from the ridge to the floor.

The size-frequency distribution of the fragmental debris at the *Surveyor VI* landing site resembles that observed

[1]Based on tracks made by rolling stones.
[2]Based on imprint of crushable block.
[3]Based on *Surveyor I* footpad penetration.

at the *Surveyor V* site. Fewer fragments coarser than 1 to 2 cm in diameter were observed per unit area from *Surveyors V* and *VI* than from *Surveyor I*. These data suggest the average size of the grains resolvable by the *Surveyor* cameras is smaller on older mare surfaces with thicker debris layers and that the slope of the cumulative grain size-frequency distribution function increases with time.

From the Alpha-Scattering Experiment, it has been found that the elemental composition of the lunar surface sample examined at the Sinus Medii site is very similar to that found by *Surveyor V* in Mare Tranquillitatis. These results suggest that the elements present in lunar mare surface material are in the form of oxides and make up compounds and minerals well known on earth. The overall chemical composition is basaltic in character. It is not consistent with that of condensed solar material; extensive cosmochemical processing must have occurred if the chemical composition of the material from which the maria were formed originally resembled that of the atmosphere of the sun.

A low magnetic particle content in the Sinus Medii material is indicated by the *Surveyor VI* magnet test. Comparison of the *Surveyor V* and *VI* magnet data with laboratory studies suggests a magnetic particle content of $<1\%$ by volume at both landing sites. These results are consistent with a basaltic composition with little, if any, meteoritic iron addition.

Directional thermal emission from the lunar surface is indicated more clearly from preliminary analysis of *Surveyor VI* lunar day data than from that of *Surveyors I, III*, and *V*, and is in general agreement with earth-based (telescope) data. Preliminary analysis of lunar night data indicates an effective thermal parameter of about 500 in contrast to 1100 from earth-based data; this was also the case for *Surveyors I, III*, and *V*.

For the first time, measurements of polarization were made of the solar corona at distances of 10 to 30 solar radii from the sun, a range which is inaccessible to earth-based instruments.

(Blank Page)

III. Television Observations From *Surveyor VI*

E. C. Morris, R. M. Batson, H. E. Holt, J. J. Rennilson,
E. M. Shoemaker (Principal Investigator), and E. A. Whitaker

Surveyor VI landed on the lunar surface at 01:01:05 GMT on Day 314 (November 10, 1967) in the southwestern part of Sinus Medii near the center of the visible face of the moon. Over 30,000 pictures were transmitted from the spacecraft during the first lunar day of operation. The number of pictures taken by *Surveyor VI* almost equals the total number of pictures returned from the previous *Surveyor* missions combined. The pictures were received at the Goldstone, California; Canberra, Australia; and Madrid, Spain, Tracking Stations of the Deep Space Network.

A. Television Camera

The *Surveyor VI* television camera is similar to the cameras flown on *Surveyors I, III,* and *V* (Refs. III-1 and III-2). A redesigned mirror assembly, however, was installed on the *Surveyor VI* camera to improve the positioning accuracy of the mirror and to extend the limits of view of the camera (Figs. III-1 and III-2). The view in elevation was extended from 35 to 70 deg above the camera horizontal plane. This permitted wide-angle views of the earth to be obtained by rotating the mirror to a near-vertical position and looking past the mirror. The left and right stops on azimuthal rotation of the camera mirror were adjusted so that narrow-angle pictures could be taken over the complete 360-deg panorama. The new design also includes tongue and groove fit of the mirror to its housing so that the mirror could be closed completely during landing. This modification resulted in significantly less glare-producing contamination on the mirror than was observed on previous flights.

Included in the redesigned mirror assembly is a filter wheel with improved positioning accuracy of about 1 deg. This accuracy is required because of a change from three color filters to three polarizing filters for *Surveyor VI*. The new filters are glass-laminated, linearly polarizing dichroic-type (KN-36) filters with transmission axes oriented successively at 0, 45, and 90 deg when they are rotated into the optical path. The 0-deg filter transmission axis is parallel to the mirror surface and perpendicular to the plane containing the mirror normal and the camera optical axes. As the filter wheel is an integral part of the mirror assembly, the orientation of the polarizing filters remains fixed with respect to the camera mirror and rotates with respect to the picture format during azimuth rotation of the mirror assembly.

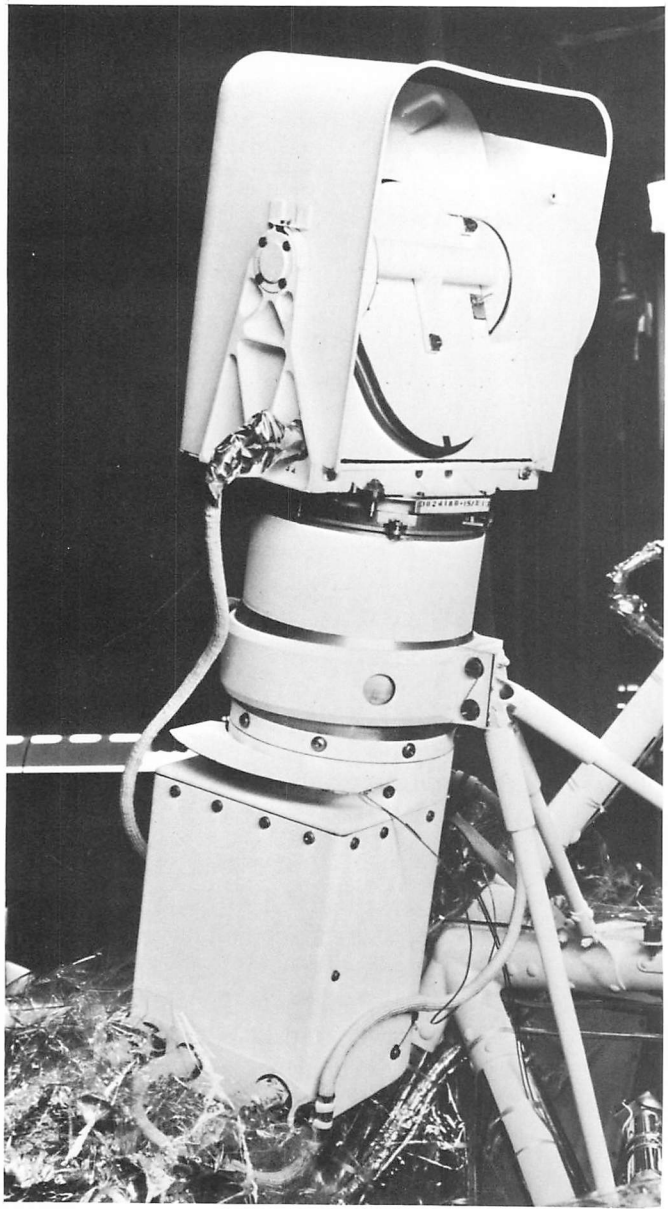

Fig. III-1. *Surveyor VI* television camera with redesigned hood and mirror assembly. The mirror is in the closed position. A tongue and groove fit of the mirror to its housing seals the optical elements of the camera from contamination during flight.

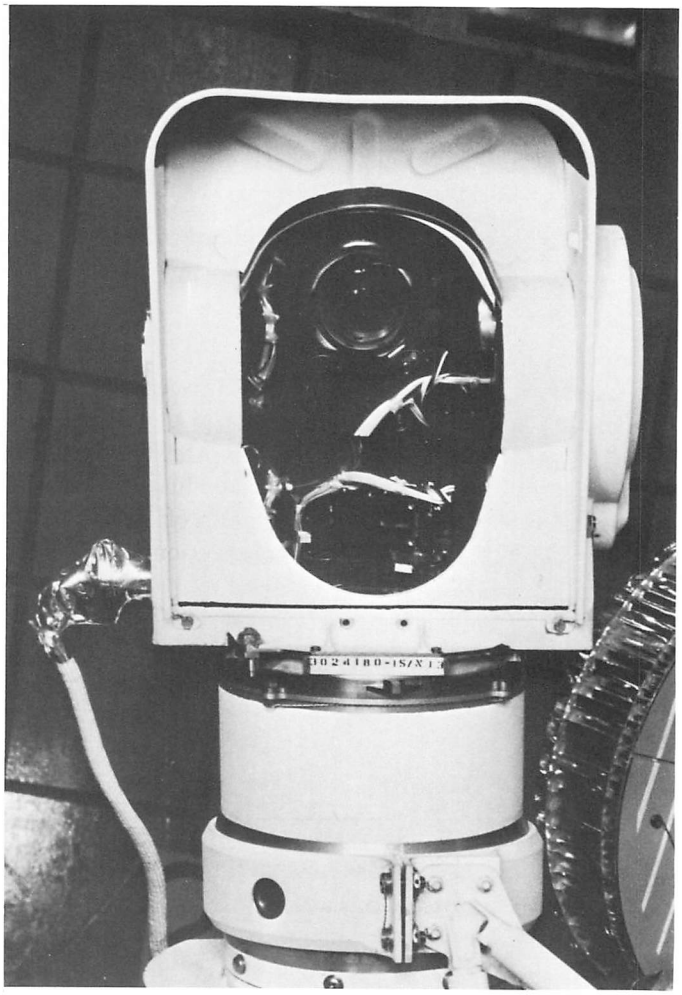

Fig. III-2. *Surveyor VI* television camera hood and mirror assembly. The mirror is open and reflects the image of the lens and filter-wheel assemblies. The hood, mirror, and filter-wheel assembly rotate in azimuth as a unit.

For a camera oriented vertically, the filter orientations are horizontal, at 45 deg, and vertical with respect to a level horizon projected onto the plane of the vidicon target. The fourth position of the filter wheel is occupied by a piece of optical glass with an Inconel coating of sufficient density that the transmission of the clear-filter position is equal to that of the polarizing filters. This was done in order that no iris changes would be required for pictures taken at different filter positions for a given field of view.

The dynamic range of the *Surveyor VI* television camera exceeded the dynamic range of the *Surveyor I, III,* and *V* cameras, but the overall sensitivity of the *Surveyor VI* camera was about one-half that of the *Surveyor V* camera and slightly less than *Surveyors III* and *I* because of the use of the neutral density coating on the clear filter. New intermediate iris positions were installed in the *Surveyor VI* television camera, providing a total of 12 separate iris positions from *f*/4 to *f*/22. The resolution of the *Surveyor VI* camera and the quality of the pictures transmitted by *Surveyor VI* are comparable to the resolution and quality of the pictures from *Surveyor V*.

B. Categories of Pictures Taken

As in previous *Surveyor* missions, television pictures were taken for a wide variety of purposes (Table III-I). Most of the pictures were taken for panoramic surveys of the area on the lunar surface visible to the camera. These surveys were taken at intervals throughout the lunar day to record the lunar surface under different angles of illumination. A special series of pictures was taken, using both the clear and polarization filters at selected azimuth and elevation positions, at each Goldstone pass of the moon. These pictures were taken to measure the photometric and polarization functions of the local lunar surface. Systematic focus-ranging surveys (Ref. III-3) were made to acquire topographic measurements of the lunar surface near the spacecraft. Pictures were taken of stars to determine the orientation of the camera and the spacecraft. Pictures were also taken of special areas on the spacecraft and parts of the lunar surface disturbed by the spacecraft, of the earth, of the solar corona, and of the lunar surface illuminated by earthlight after sunset.

Table III-1. Categories of pictures taken by *Surveyor VI* television camera

Survey type	Total number of pictures
Wide-angle panoramas	2,161
Narrow-angle panoramas	14,767
Photometric and polarimetric surveys	6,428
Focus-ranging surveys	2,222
Star surveys	357
Earth surveys	87
Solar corona surveys	147
Special area surveys and other pictures	4,227
Total	30,396

Early on November 17, 1967, upon command from earth, the vernier engines of *Surveyor VI* were ignited; the spacecraft lifted off the lunar surface and landed 2.4 m northwest of its original position. Over 13,850 pictures were taken before the spacecraft was moved, and more than 16,500 pictures were taken afterward. Pictures of the same areas taken immediately before and after the spacecraft was moved can be viewed simultaneously to provide a stereoscopic view of the landing site, and to make topographic maps of areas between 4 and 50 m from the camera. Approximately 1,000 narrow-angle and 100 wide-angle pictures were taken that are suitable for this purpose.

C. Location and Topography of Landing Site

Sinus Medii, the target area for *Surveyor VI*, is a relatively small mare plain, about 170 km across (Fig. III-3). It is bounded by highlands to the north and to the south, and to the northeast by another plain with a higher albedo and with a larger number of craters than is typical for the maria. The surface of Sinus Medii is broken by numerous small craters and by a system of mare ridges, the largest of which can be easily observed at the telescope.

1. Location of *Surveyor VI*

The best estimate of the landed position of *Surveyor VI*, derived from the pre-landing tracking data, was 0.42°N, 1.33°W. This location is about 2.5 km southeast of the nearest point of a fairly prominent mare ridge which crosses Sinus Medii in a general east-west direction (Fig. III-4). An early wide-angle panorama taken from the landed spacecraft, however, showed a ridge-like feature lying to the southeast. Details of the ridge were clearly visible in a narrow-angle panorama taken during the following Goldstone pass, by which time shadows had shortened sufficiently to facilitate the interpretation of horizon features with some confidence.

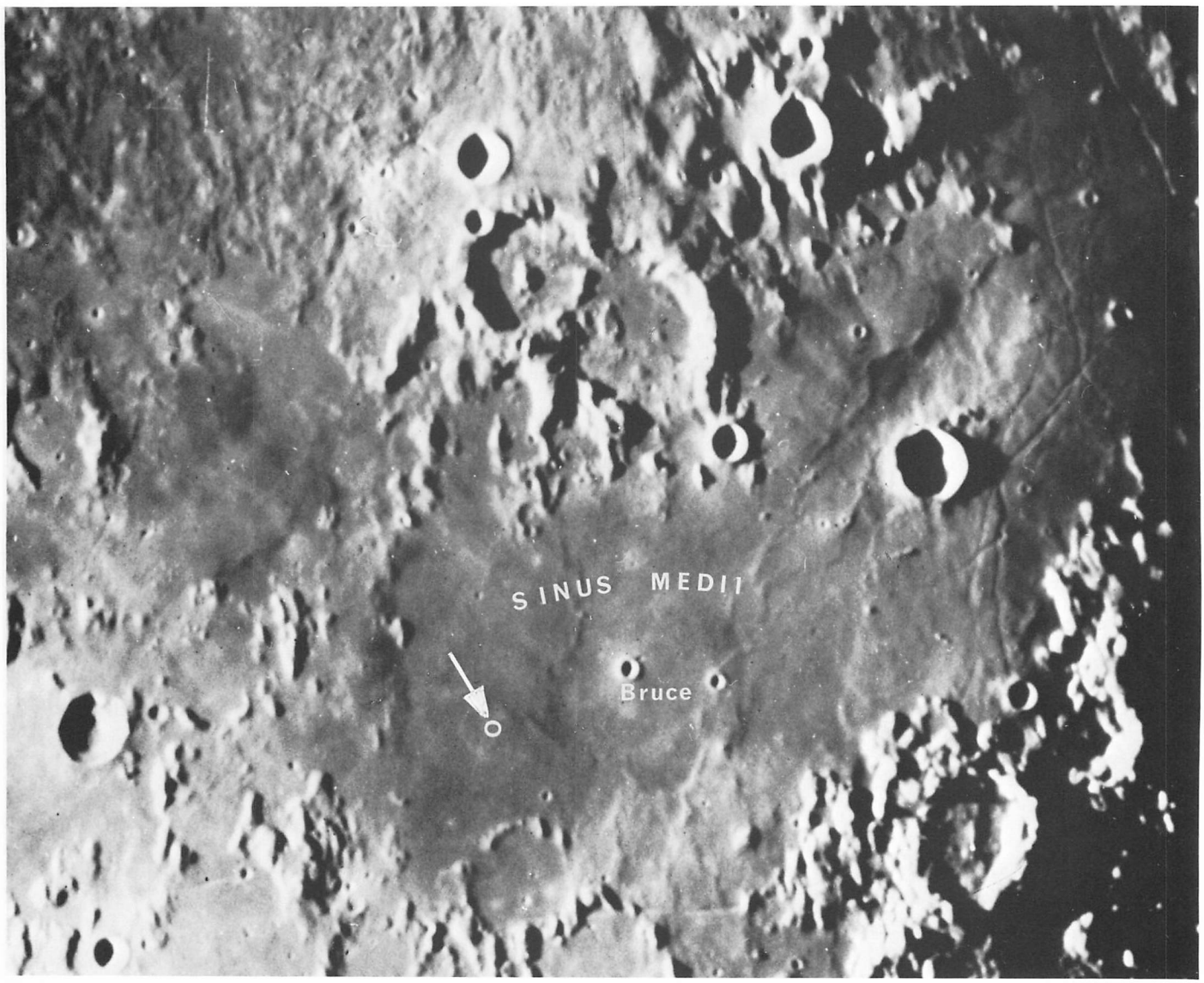

Fig. III-3. Photograph of the central region of the moon taken through the 100-in. telescope at Mt. Wilson Observatory, California. The white circle indicates the location of *Surveyor VI*, which landed in Sinus Medii at 0.49°N latitude, 1.40°W longitude.

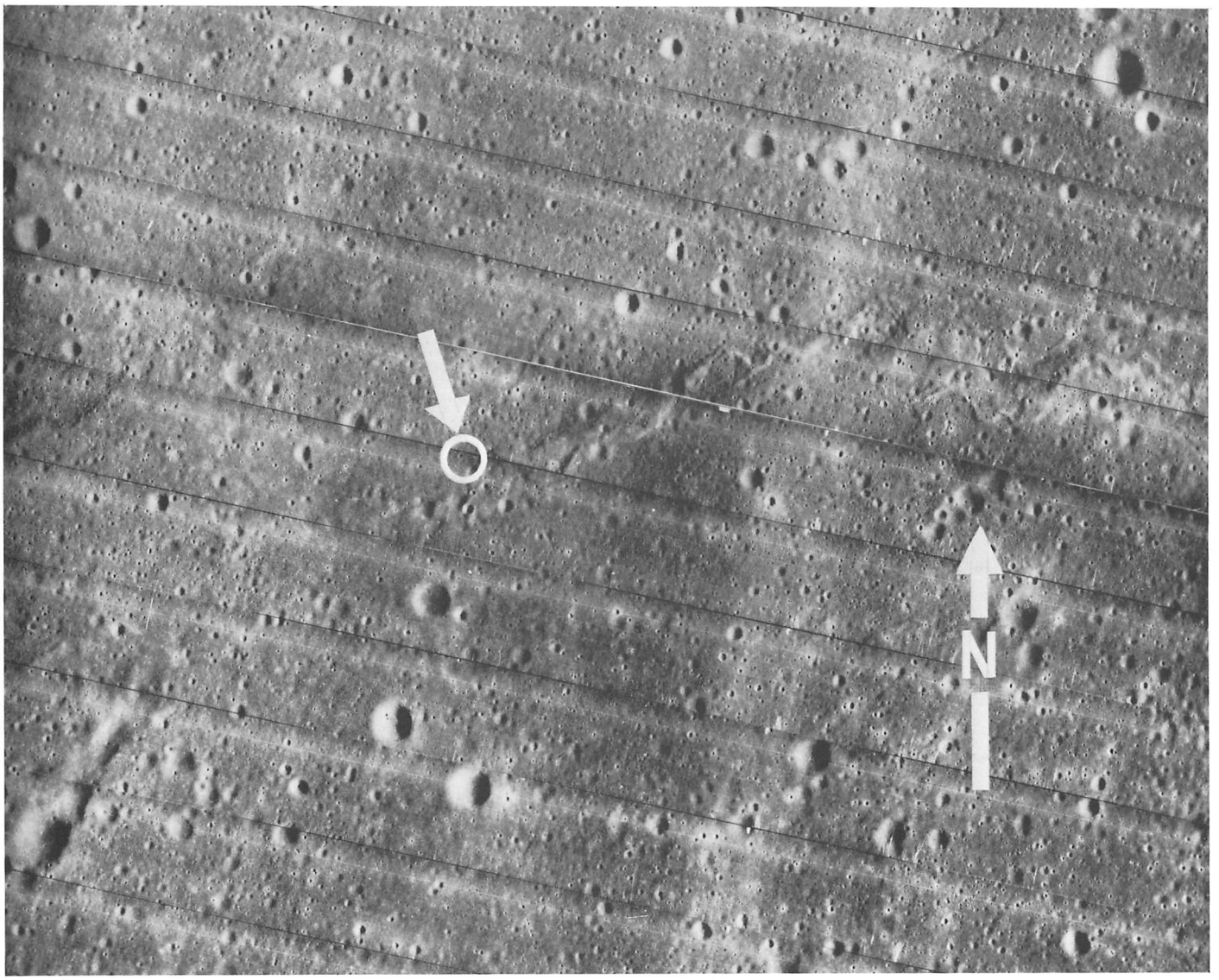

Fig. III-4. *Lunar Orbiter II* medium-resolution photograph M113 of Sinus Medii. *Surveyor VI* landing site is indicated by the white circle. A mare ridge, which passes just south of the *Surveyor VI* landing site, can be seen extending across the center of the picture.

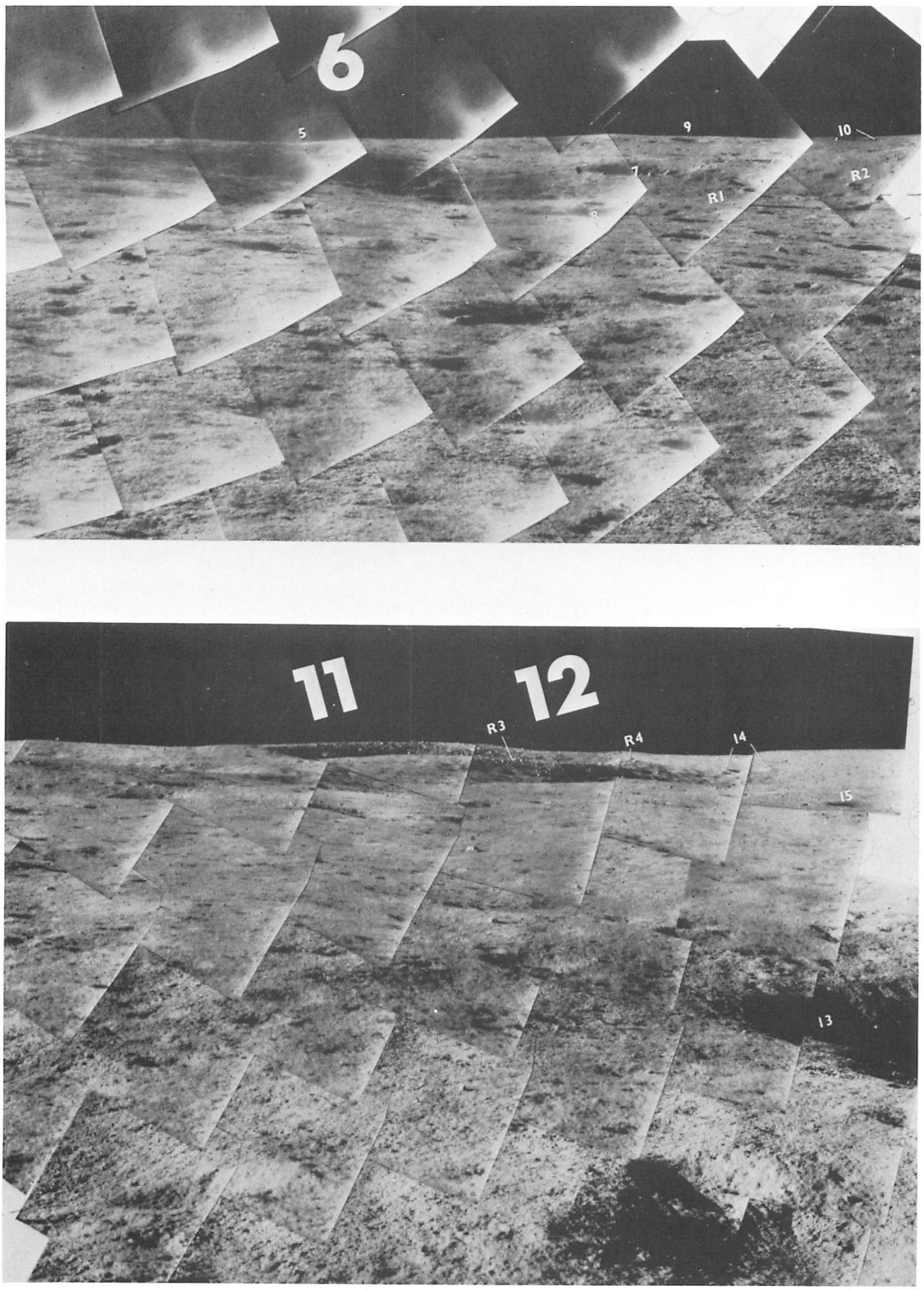

Fig. III-5. Mosaic of *Surveyor VI* pictures of a mare ridge southeast of the spacecraft. The numbered features were correlated with features on *Lunar Orbiter* photographs to accurately locate the *Surveyor VI* spacecraft in the *Lunar Orbiter* photographs (Day 315, 01:32:20 to 01:49:32 GMT).

Craters on the mare ridge (6, 11, and 12 in Fig. III-5) form a prominent group of landmarks; although their selenographic azimuths from *Surveyor VI* were known with adequate precision, their distances and, thus, actual dimensions could only be estimated. Crater 11 appeared to be unusual in having north and south walls that were higher than the east and west walls, and this proved to be the major clue in the eventual determination of the spacecraft's location on high-resolution photograph H114 from *Lunar Orbiter V*. *Lunar Orbiter II* photograph H121 covers this same general area with twice the resolution and was subsequently used; the relevant part of this photograph is reproduced in Fig. III-6.

After the tentative identification of crater 11, other correlations between features shown in the *Surveyor* panorama and photograph H121 from *Lunar Orbiter II* were gradually made and confirmed until the exact location of the spacecraft could be pinpointed. Some of the craters and large rocks that were correlated are numbered in Figs. III-5 and III-6.

Because of the possibility of cumulative errors in the available maps and charts of the region, the selenographic coordinates of *Surveyor VI* were determined by carefully plotting the latitude/longitude grid, as given in the Orthographic Atlas (Ref. III-4), onto *Lunar Orbiter IV* photograph H108, and reading off the pinpointed *Surveyor* position. The coordinates are 0.49°N latitude, 1.40°W longitude, about 3 km northwest of the pre-landing tracking position estimate. This position is about 60 km north of the southern border of Sinus Medii and 40 km east of the western border.

2. Orientation of Spacecraft

To determine the orientation of the spacecraft (Table III-2), pictures were taken of a number of stars and two planets. These observations were made both before and after the hop made by the spacecraft. In addition to the stars listed in Table III-2, fainter stars were seen on pictures exposed for the solar corona after sunset, using the camera integration mode. The sensitivity of the *Surveyor VI* camera in the integration mode is demonstrated in a picture taken of part of the constellation of Scorpio (Fig. III-7). This picture is a narrow-angle picture taken at *f*/4 and integrated for a time interval of 3 min. Stars as dim as 5.94 magnitude are recorded in the picture.

Table III-2. Celestial objects observed from *Surveyor VI*

Observations	Day	Name	Magnitude
Pre-hop	315	Sirius	−1.6
	315	Canopus	−0.9
	319	Jupiter	−1.7
Post-hop	324	Rigel	0.1
	324	Achernar	0.6
	326	Achernar	0.6
	326	Vega	0.1
	328	Antares	1.2
	328	Vega	0.1
	328	Deneb	1.3

The orientation of the spacecraft has been determined from position measurements on a few of the stars listed in Table III-2, together with orientation data derived from pointing of the solar panel and planar array antenna and from the attitude gyros. Prior to the hop, the spacecraft was tilted 2.3 deg at an azimuth of 243 deg from north; the $-Y$ axis of the spacecraft was oriented 115 deg from north. After the hop, the spacecraft was tilted 3.85 deg at an azimuth 260 deg from north and the $-Y$ axis was oriented 112 deg from north. Each of the estimated components of orientation may have an error as much as 1 deg.

3. Topographic Maps

Topographic maps of the *Surveyor VI* landing site are under preparation at several scales, using a combination of stereophotogrammetric methods, focus ranging, shadow measurements, and correlation with *Lunar Orbiter* photographs.

The successful hop by the *Surveyor VI* spacecraft permitted, for the first time, the acquisition of useful stereoscopic *Surveyor* television pictures of the lunar surface. These can be used, in conjunction with existing methods and instruments, to make highly detailed, large-scale maps of the lunar surface in the immediate vicinity of the spacecraft. Stereoscopic photogrammetric mapping is basically a method of triangulation. The pre- and post-hop positions of the *Surveyor VI* television camera are two vertices of a triangle; any object photographed from both camera positions is the third. If the distance between the two camera positions is known, the position of an object on the lunar surface can be computed from the horizontal and vertical angles to this object from each camera position. These angles can be determined from coordinates of the object in the television pictures, and from camera mirror orientation data, once the attitudes of the cameras have been found by star observations and by measurements of points on the horizon from each camera position.

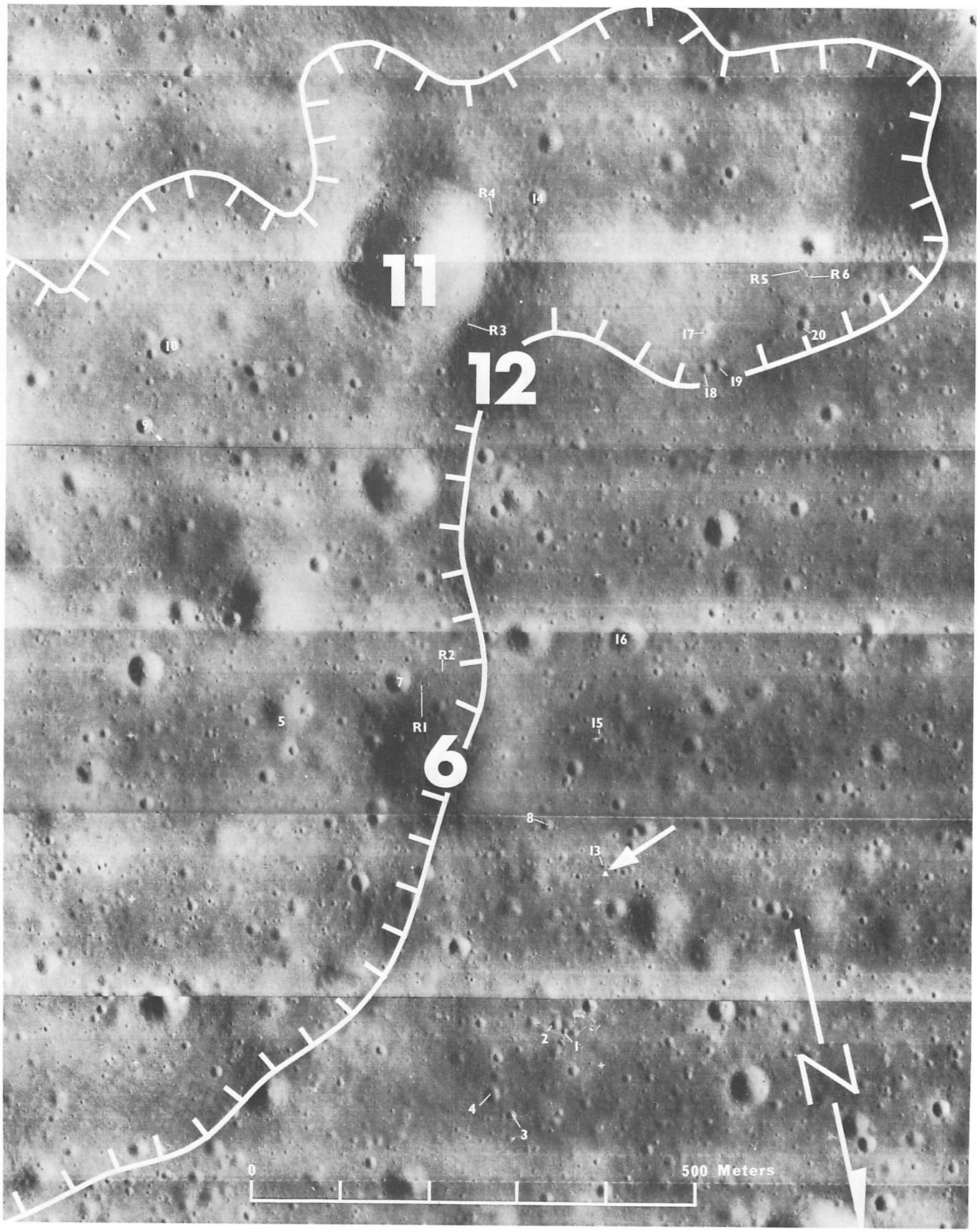
11
12
6
R4
14
R5
R6
R3
17
20
10
19
18
9
16
R2
7
5
R1
15
8
13
2
1
4
3
N
0
500 Meters

Fig. III-6. *Lunar Orbiter II* photograph H121 of the *Surveyor VI* landing site. The numbered features correspond to the numbered features on the mosaic of *Surveyor VI* pictures (Fig. III-5). These features were used to locate *Surveyor VI* on the *Lunar Orbiter* photographs.

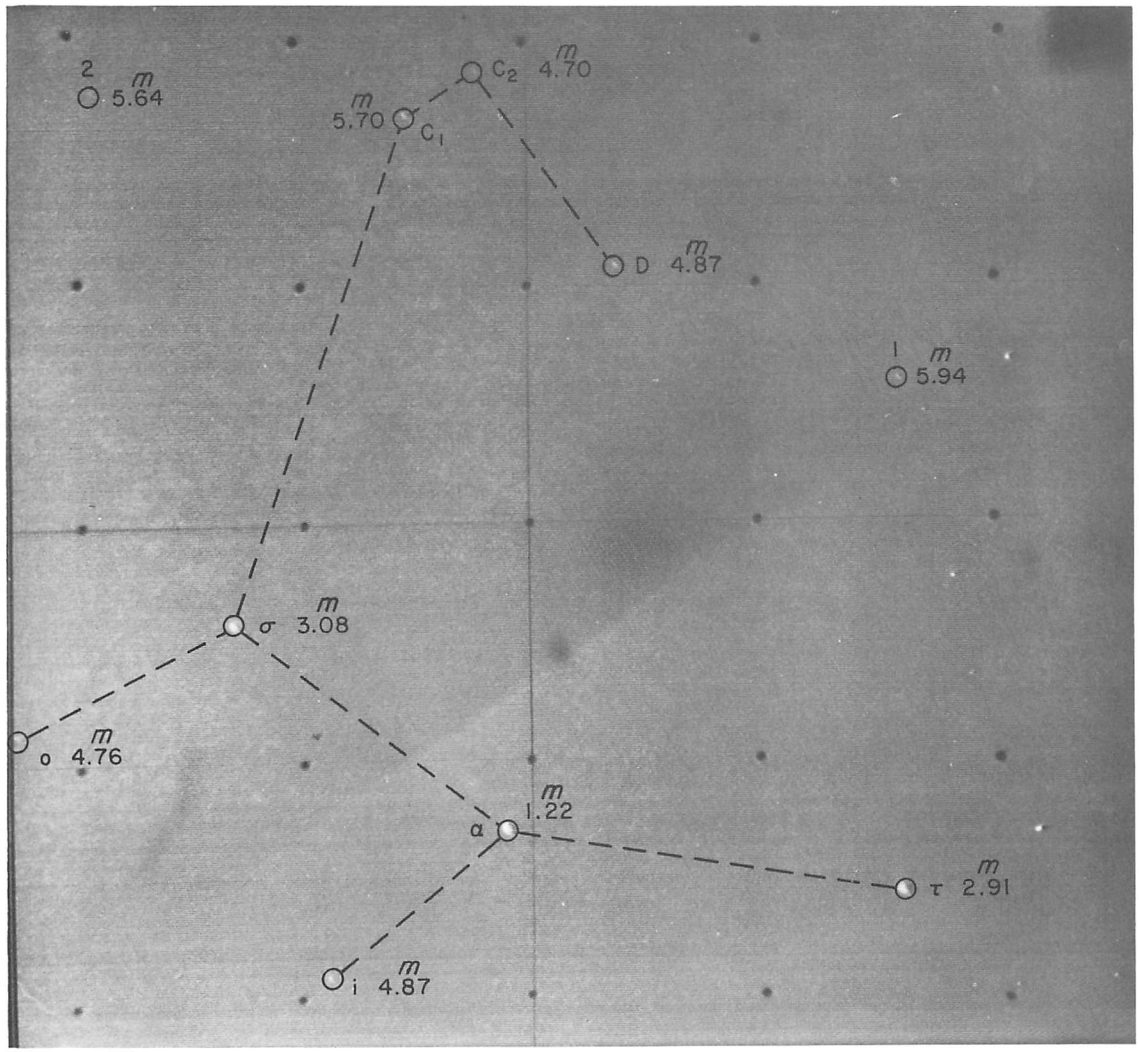

SCORPIO

Fig. III-7. *Surveyor VI* picture of part of the constellation Scorpio. Stars and their relative magnitudes are shown by circles. The exposure time was 3 min.

Rather than make individual computations of the object positions of thousands of points, stereoplotting instruments are used to make direct measurements of object positions from stereoscopic images. Most of these instruments, which have been designed for mapping from conventional aerial or terrestrial photographs, are restricted in their basic design to the use of stereoscopic pictures taken with parallel or slightly convergent axes that are nearly perpendicular to the stereoscopic baseline. Only a small percentage of the stereoscopic pictures taken by *Surveyor VI* meets this criterion. Most of the *Surveyor VI* mapping must be done, therefore, with an instrument specially designed to accommodate the wide variations in *Surveyor* stereoscopic geometry (Fig. III-8).

Although photogrammetric measurement is the most accurate available way to prepare large-scale topographic maps of the *Surveyor VI* landing site, it has some inherent limitations. Tests of the method have shown that stereoscopic mapping with *Surveyor* pictures is not feasible when the ratio between the effective camera baseline and the distance to the part of the surface to be

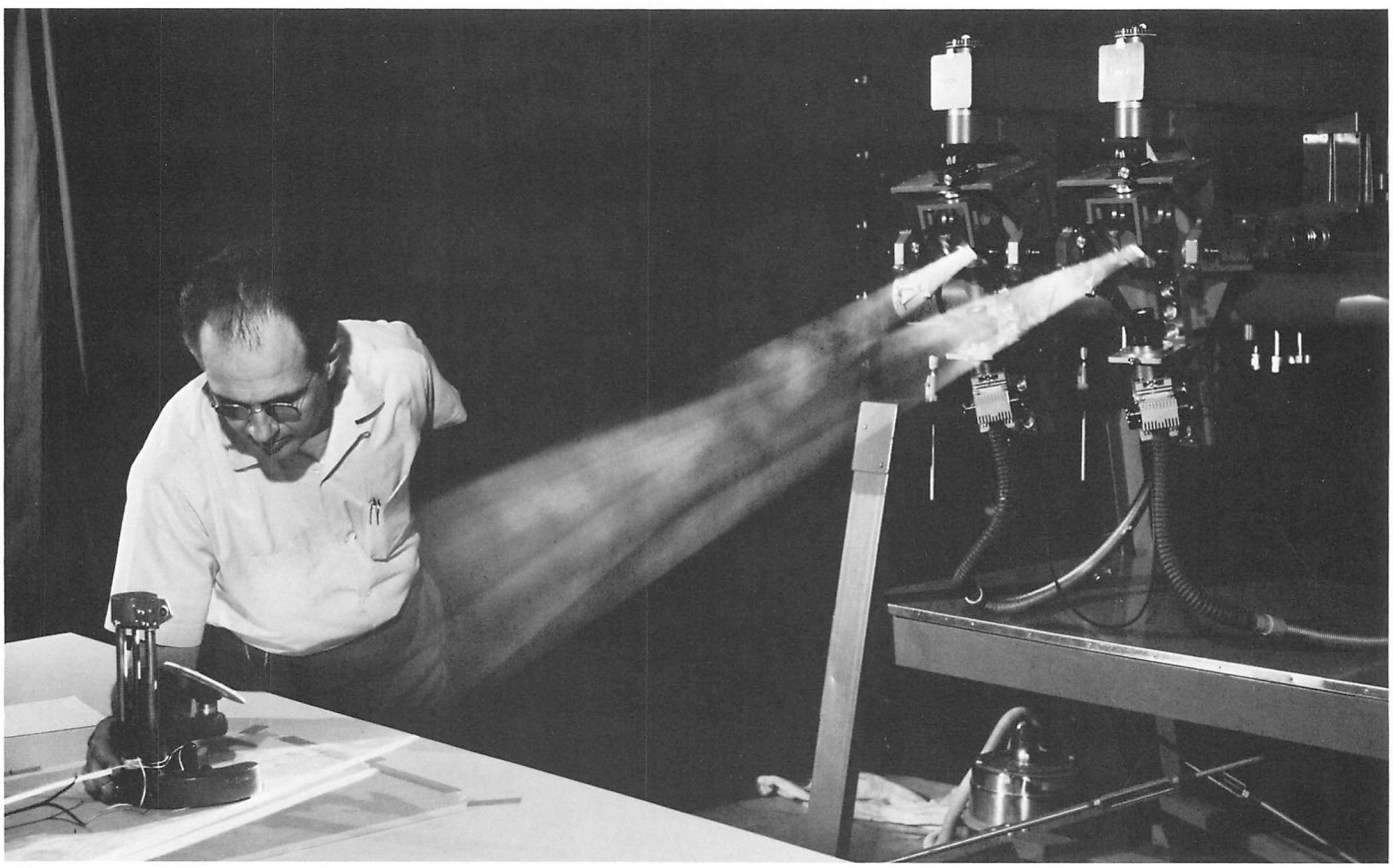

Fig. III-8. *Surveyor* anaglyphic stereoplotter. This instrument was originally designed to rectify monoscopic *Surveyor* pictures, but has been modified for use as a stereoplotter. Each projector is a geometric analog of the television camera. Glass transparencies, or "diapositives," made from stereoscopic pairs of pictures are used at each camera position. The projectors and projector mirrors are set in the same relative orientations as the camera at the time each picture is taken. One picture is projected with red light, and the other is projected with blue light. The overlapping images are viewed on a small, movable screen, or platen, in the center of which is a pinpoint of light. The operator wears spectacles with one red lens and one blue lens, enabling him to see the overlapping images as a single three-dimensional picture or model. As the platen is moved vertically or horizontally, the point of light at its center appears to float in the stereoscopic model. The horizontal position of the point of light is plotted on the map manuscript over which the platen carriage, or tracing table moves. The vertical position of the point of light can be read from a counter on the tracing table.

mapped is smaller than 0.05. The effective baseline becomes shorter than the line between the two camera positions where the objects to be measured lie along a line that is not perpendicular to the camera baseline (Fig. III-9). The baseline for the *Surveyor VI* stereo pictures is about 2.4 m; objects and surfaces lying as far as 48 m from the cameras in the direction normal to the camera baseline can be mapped. In other directions, the limiting distance is less. Along a line that makes a 30-deg angle with the camera baseline, for example, the effective baseline is only 1.2 m long, and photogrammetric measurement will not have acceptable accuracy beyond 24 m.

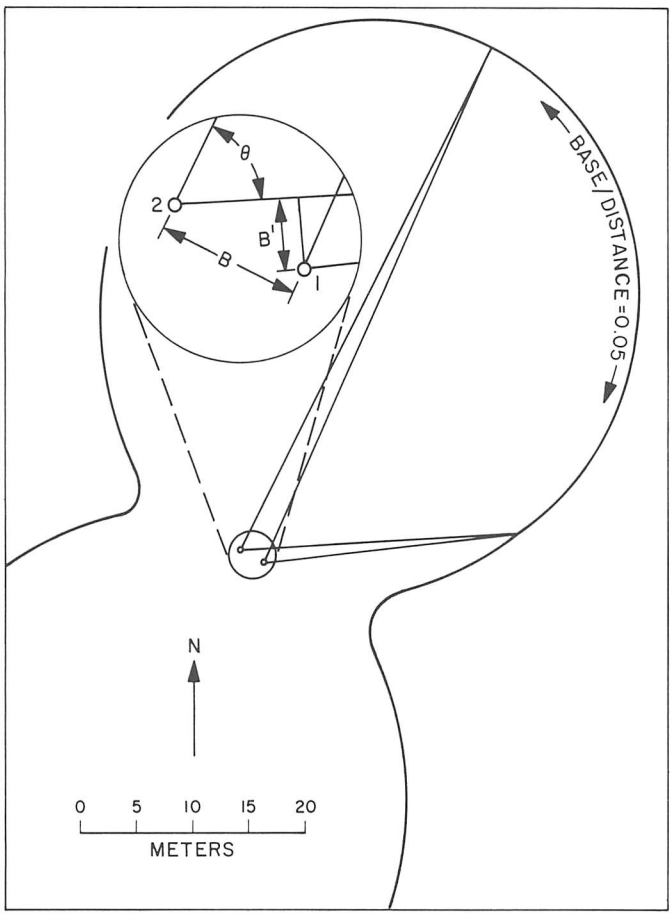

Fig. III-9. Geometry of *Surveyor VI* stereophotogrammetry. The hourglass-shaped figure encloses the area around *Surveyor VI* that could be mapped with a base/distance ratio of 0.05 or greater, on a level surface. For photogrammetric purposes, the length of the effective baseline, B′, is a function of the distance, B, between camera stations 1 and 2, and the angle θ, between the line of sight and a line perpendicular to B. Note that, if θ = 60 deg, B′ is only half as long as B. Since the camera is about 1.5 m above the lunar surface at each station, some stereoscopic effect is present even when θ = 90 deg.

As an illustration of the stereophotogrammetric method, a small area about 20 m from the spacecraft (Fig. III-10) was mapped in detail using the specially designed *Surveyor* stereoplotter. In this area is a crater about 1 m in diameter, the center of which is 19.8 m from the present position of the television camera. Narrow-angle stereoscopic pictures of this crater were used to make a contour map (Fig. III-11). A small-scale location map, shown in Fig. III-11, was made by graphical construction using horizontal angles from each camera position to the features shown.

The contour map shows the amount of detailed information that can be compiled on maps made by stereoscopic measurement of *Surveyor VI* pictures. At a distance of 20 m, the lunar surface can be mapped with a contour interval of 5 cm and at scales of the order of 1:25. Measurements of this type will permit a close study of the shapes of craters and other small features near the spacecraft and of the structure of the local lunar surface. Stereoscopic mapping of the *Surveyor VI* landing site is being accomplished with conventional first-order stereoplotting instruments, using the small number of stereoscopic pairs of pictures whose orientations are within the mechanical limitations of those instruments, and with the *Surveyor* stereoplotter when the pictures are not within the mechanical limitations of the conventional plotting instruments.

The preliminary determination of the baseline used for the map shown in Fig. III-11 was made by focus ranging and by triangulation. The pre-hop imprint of footpad 2 lies on one of the focus-ranging surveys taken after the hop. The distance to the footpad from the camera is thus known within 1 focus step, or about 0.2 m. The camera azimuth of the imprints of footpads 2 and 3 is known, as is the distance between them, providing two sides and an adjacent angle of a triangle. Solution of this triangle for the third side, the distance between the camera and the footpad 3 imprint, provides sufficient data to compute the location of the first camera position with respect to the second. The difference in horizontal angles before and after the hop to features on or near the horizon indicates that the spacecraft rotated a little more than 4 deg during the hop. The positions of the footpads, derived by focus-ranging, are consistent with this figure.

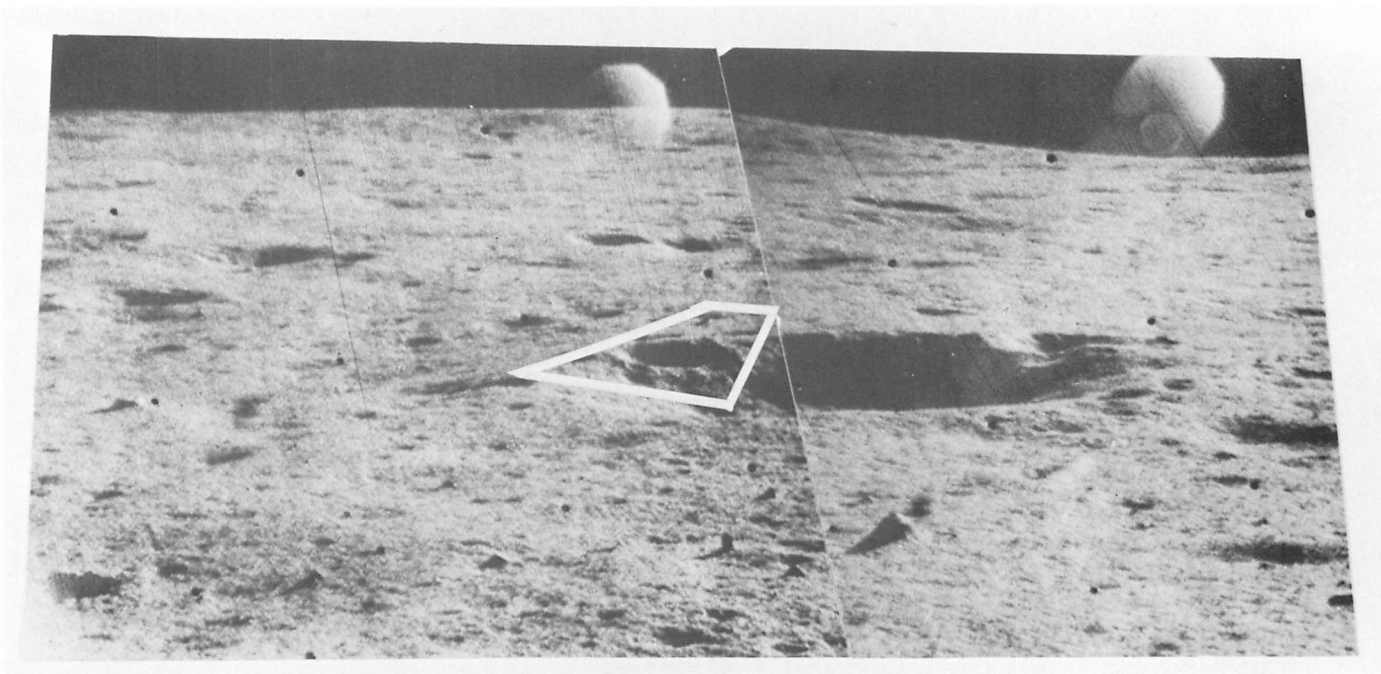

Fig. III-10. Crater, 1 m in diameter, which lies 20 m northeast of the *Surveyor VI* spacecraft. A detailed contour map of the area outlined was made with the stereoplotter (Day 315, 04:21:17 and 04:20:24 GMT).

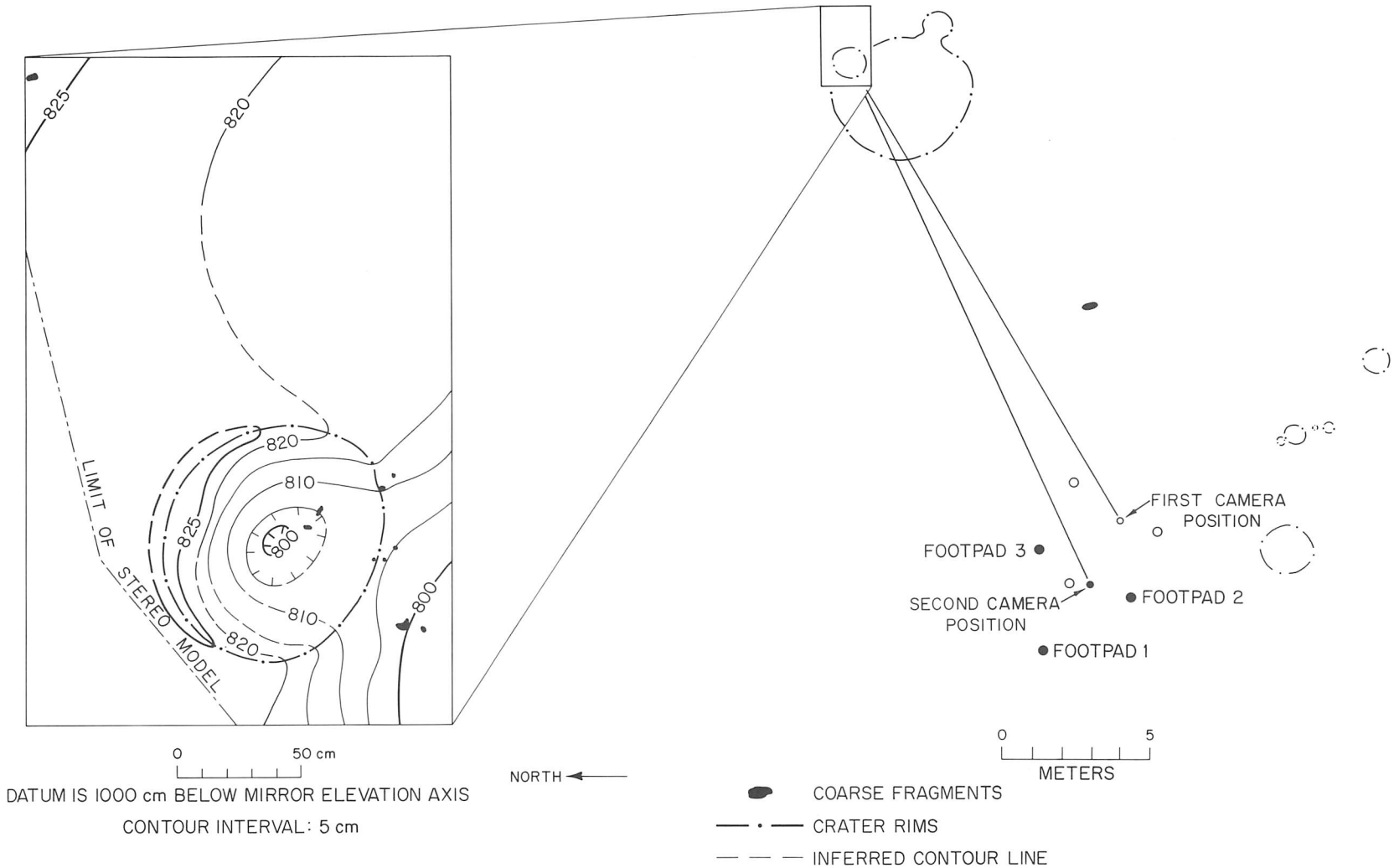

Fig. III-11. Maps prepared from stereoscopic *Surveyor* television pictures. The sketch on the right shows the position of the camera and spacecraft footpads before the hop (open circles) and after the hop (solid circles). A few craters and a prominent block (east of the spacecraft) were plotted graphically by triangulation. The contour map on the left was drawn from stereoscopic pictures with the *Surveyor* anaglyphic stereoplotter shown in Fig. III-8.

To facilitate the location of stereoscopic pairs of *Surveyor* pictures for general study as well as for preparation of maps, a chart (Fig. III-12) was prepared that shows the correlation of azimuth and elevation coordinates of picture centers of stereoscopic pairs. The chart was derived by correlation of the camera azimuths and elevations of 170 conjugate images on pre- and post-hop pictures. Azimuths and elevations (in the camera coordinate system) of the image points were measured from both camera positions, and the frame-center traces of the second camera station were plotted on a rectangular representation of the frame-center traces of the first camera position. The traces of frame centers for the second camera station are smoothed and generalized for legibility. The true, relative location of the frame centers varies with topography. At no point, however, do the generalized traces deviate more than 3 deg from their true positions, and in most areas the deviation is less than 1 deg.

Where stereoscopic measurement is not practical, other methods (Ref. III-5) are being used for making maps of the *Surveyor VI* landing site. The area within a few meters of the spacecraft, which was disturbed during the hop, cannot be mapped stereoscopically because conjugate images are not identifiable in pictures taken before and after the hop. Focus-ranging surveys (Ref. III-3) are being used to map this area. Measurement of the shadow of the spacecraft solar panel at several points along an east–west line through the spacecraft provides control points in areas where stereoscopic measurement is weak because of the small effective baseline. Correlation of features, identifiable on both *Surveyor* pictures and *Lunar Orbiter* photographs (Ref. III-2), will be used to map the area that is too far from the spacecraft to be measured stereoscopically.

D. Geology of Landing Site

Sinus Medii is underlain by an isolated patch of mare material located in a broad, shallow depression in the central highlands of the moon. It lies about 300 km east of the margin of the Oceanus Procellarum, about 250 km southeast of Sinus Aestuum, 250 km south of Mare Vaporum, and nearly 500 km west of Mare Tranquillitatis. The mare surface in Sinus Medii has a higher average albedo than most of the other maria and a significantly higher areal density of craters larger than a few hundred meters in diameter. The higher density of craters suggests the mare material exposed in Sinus Medii is older than most of the material exposed in the other maria. Comparative study of the crater populations in the various maria, in fact, suggests the surface of Sinus Medii is one of the oldest mare surfaces on the moon.

Bruce, the largest crater on Sinus Medii, is about 6 km in diameter and 55 km from the *Surveyor VI* landing site. The crater is surrounded by a bright halo and faint rays and is a potential, though likely to be a very minor, source of some fragments in the vicinity of *Surveyor*.

Two prominent and several subordinate sets of linear structures occur in the highlands north, south, and east of Sinus Medii (Refs. III-6 and III-7). The most conspicuous of these is expressed as a series of northwest-trending ridges, valleys, and segments of ancient crater rims, which are part of a regional pattern of linear features referred to as Imbrian sculpture. The second most prominent set of linear structures is a northeast-trending system of scarps and ridges. These two dominant structural patterns appear to be reflected in the detailed shapes and trends of the mare ridges and of local crater chains and small shallow trenches on Sinus Medii.

1. Mare Ridge Near *Surveyor VI*

The most prominent topographic feature in the vicinity of *Surveyor VI* is a sinuous mare ridge about 40 km long that trends generally east–west. This ridge is similar in form to other sinuous ridges that occur widely on the maria and have been observed at the telescope. The ridge near *Surveyor VI* is somewhat smaller than the ridges that have been studied through earth-based telescope, but it is the first such feature to be examined close at hand from a landed spacecraft.

As revealed in the *Lunar Orbiter* photographs of Sinus Medii, the mare ridge near *Surveyor VI* follows a zigzag course and is composed of two sets of nearly straight segments or elements, one set trending approximately N35°W to N40°W, and the other set trending about N60°E. The first set of ridge elements is roughly parallel with the Imbrian sculpture, and the second set is parallel with the other main trend of linear features in the adjacent highlands. Thus, in detail, the course of the ridge appears to be controlled by the regional geologic structure.

Individual ridge elements vary from about 300 m to 2 km in length and from 100 m to about 500 m in width. In places, ridge elements of a given set are grouped together in an echelon or a side-by-side cluster. At such places, the ridge is a composite structure, and the total width of the composite ridge may be as great as a kilometer. Where the ridge is composite, it is generally asymmetric in transverse profile, with the ridge crest close to one side of the ridge or the other. In some places, there are two distinct crests in the transverse profile.

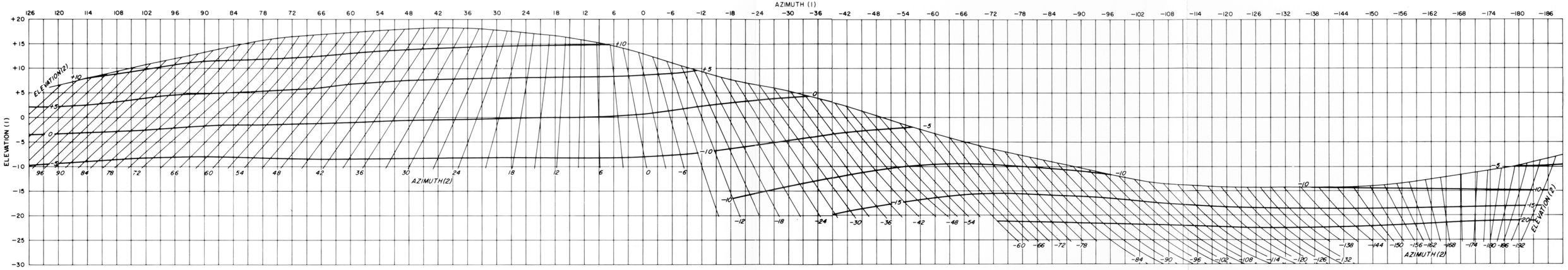

Fig. III-12. Correlation of centers of stereoscopic *Surveyor VI* pictures. This is a generalized chart for location of stereoscopic pairs of pictures. Azimuth (1) and elevation (1) are frame-center coordinates prior to spacecraft hop. Azimuth (2) and elevation (2) are frame-center coordinates after the spacecraft hop. A feature located near the center of a picture taken at azimuth −54 deg, elevation −10 deg, before the hop, for example, is located near the center of a picture taken at azimuth −51 deg, elevation −10 deg, after the hop.

(Blank Page)

In the vicinity of *Surveyor VI*, the ridge is composed of a long cluster of northeast-trending elements. The foot of the ridge lies 200 m from the spacecraft, at the nearest point, and the crest of the ridge lies about 700 m from the spacecraft, close to the far side. Craters 9 and 10 (Fig. III-6) lie nearly on the ridge crest.

At its nearest point, the crest of the ridge has an elevation about 30 m above the general level of the mare plain around *Surveyor VI*. The ridge gradually becomes lower to the southwest and dies out about 1 km southwest of the spacecraft.

The ridge is pockmarked by craters with about the same areal density as the nearby mare plain, and, as shown by the form and characteristics of the rims of the smaller craters, it is mantled with a layer of weakly coherent, fragmental debris, or a regolith, somewhat like that on the mare plain. Indeed, the surfaces of the ridge and the plain are so similar that it is difficult to locate the boundaries of the ridge on the high-resolution *Lunar Orbiter* photographs. Close inspection of the *Lunar Orbiter* photographs and *Surveyor* pictures, however, shows that a much greater number of coarse blocks occurs on the ridge than on the plains. In this respect, the ridge near *Surveyor VI* resembles many other mare ridges observed in high-resolution *Lunar Orbiter* photographs. In addition, study of the *Surveyor* pictures has revealed that smaller craters with blocky rims occur on the ridge than are found on the nearby mare plains. This indicates the debris layer is thinner on the ridge than on the plains.

Patterned ground (Ref. III-8) is more conspicuously developed on the ridge than on the adjacent mare plain around *Surveyor VI*. The patterned ground occurs both on the flanks of the ridge and, in places, on very gently sloping surfaces near the ridge crests. Low ridges and troughs in the patterned ground tend to be oriented at N30°W to N55°W and at N40°E to N50°E. Although the orientation of these linear elements in the patterned ground is variable, at least one set of elements tends to be roughly aligned with the Imbrian sculpture. The alignment suggests the development of the patterned ground is influenced by subsurface fracture or joint systems.

2. Craters

Most of the small topographic features near *Surveyor VI* are shallow craters with low, subdued rims; some craters are nearly rimless. The craters range from a few centimeters to about 200 m in diameter. They are mostly cup-shaped, with walls and floors concave upward. Some of the largest craters have a subdued terrace near the foot of the wall. No dimple-shaped craters, which were common at the *Surveyor V* site, have been observed close to *Surveyor VI*, although crater chains occur in the region. A series of subdued, northeast-trending troughs, 1 to 2 km in length, is present in the mare plain northeast of the landing site. The nearest of these is about 1 km away.

A number of irregular craters, lined with clods of fine-grained material, occur near *Surveyor VI* (Fig. III-13). They range in size from a few centimeters to several meters. Some are nearly filled with rubble. These craters are interpreted to be formed by impact of clods of weakly cohesive, fine-grained material ejected from nearby primary craters. Similar secondary impact craters have been observed around missile craters at White Sands Missile Range, New Mexico (Fig. III-14).

The size-frequency distribution of small craters ranging in size from 3 cm to 2 m was investigated in a 90-m^2 area close to *Surveyor VI*. There were 609 craters counted in *Surveyor VI* pictures. The cumulative size-frequency distribution of the small craters, normalized to 10^6 km^2, is closely similar to that found near *Surveyor I* (Fig. III-15). In both cases, the frequency distribution of small craters observed in the *Surveyor* pictures lies along the general distribution curve for craters on the lunar plains determined from *Ranger VII, VIII,* and *IX* pictures (Fig. III-15). The low frequency of craters in the size range of 3 to 12 cm in both the *Surveyor I* and *VI* curves, compared to the extrapolated curve derived from the *Ranger* pictures, is probably due to the observational difficulties of recognizing these small craters in an oblique view of the lunar surface, and not to an actual crater deficiency.

The cumulative frequency curve of craters ranging in diameter from 2 to 100 m, derived from measurements on a *Lunar Orbiter II* high-resolution photograph of the *Surveyor VI* landing site (Fig. III-15), lies somewhat below the *Ranger* curve. The discrepancy in crater frequency at the 2-m diameter between the curve derived from the *Surveyor* pictures and that derived from *Lunar Orbiter* photographs shows that the crater frequencies derived from the *Lunar Orbiter* photographs probably lie somewhat below the true frequencies. The combined crater size-frequency data from the *Surveyor* pictures and *Lunar Orbiter* photographs suggest that, at the *Surveyor VI* site, the frequency distribution of craters in the size range of a few centimeters to 100 m is very close to the average distribution for lunar plains. Only the craters larger than several hundred meters in diameter are more abundant on Sinus Medii than on other mare surfaces.

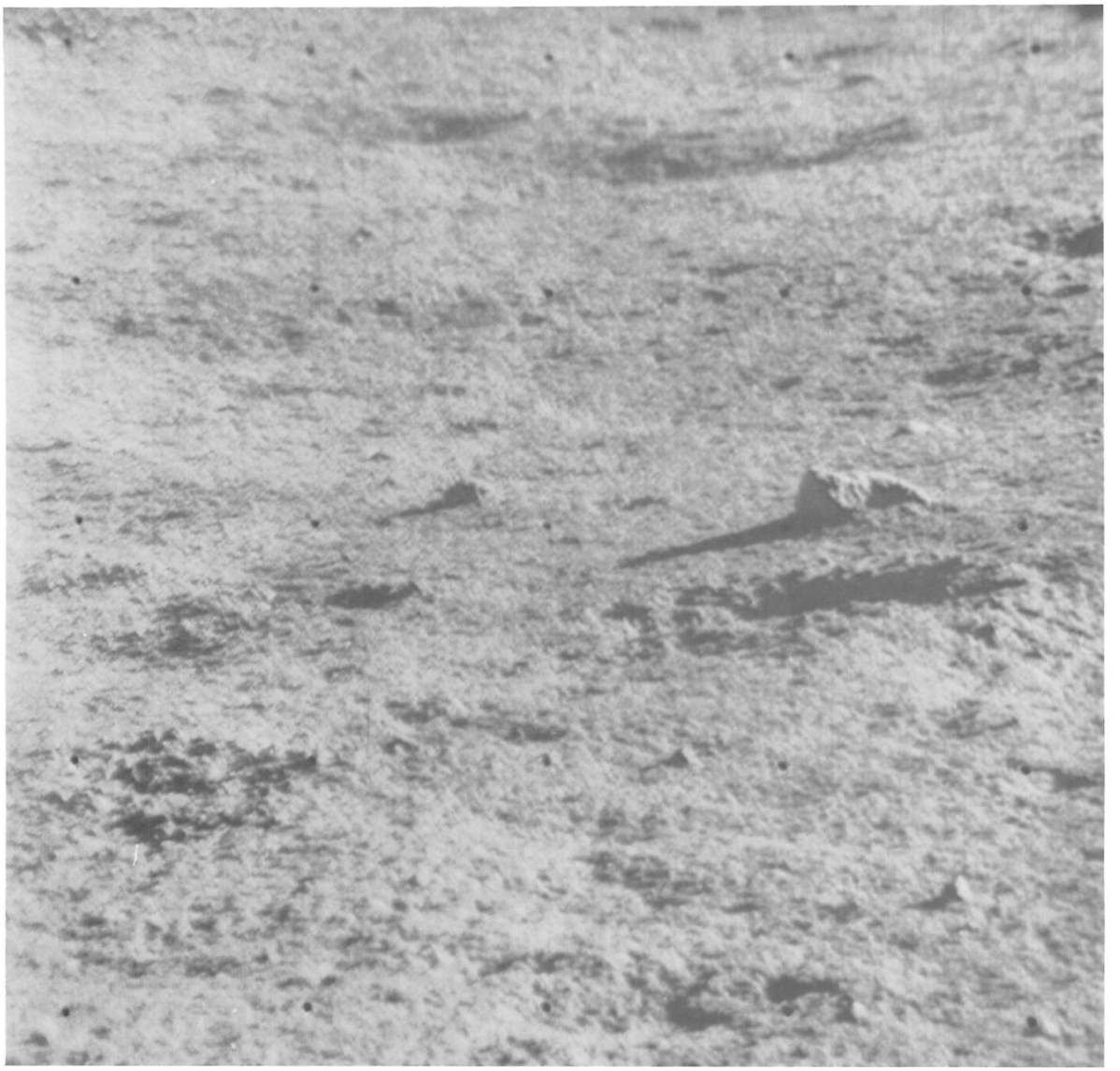

Fig. III-13. Narrow-angle picture showing several small, irregular, secondary impact craters about 15 to 30 cm in diameter with rubbly material on their floors and around their rims. Note the asymmetric shape of a 30-cm, secondary impact crater in the upper right of the picture (Day 315, 02:02:18 GMT).

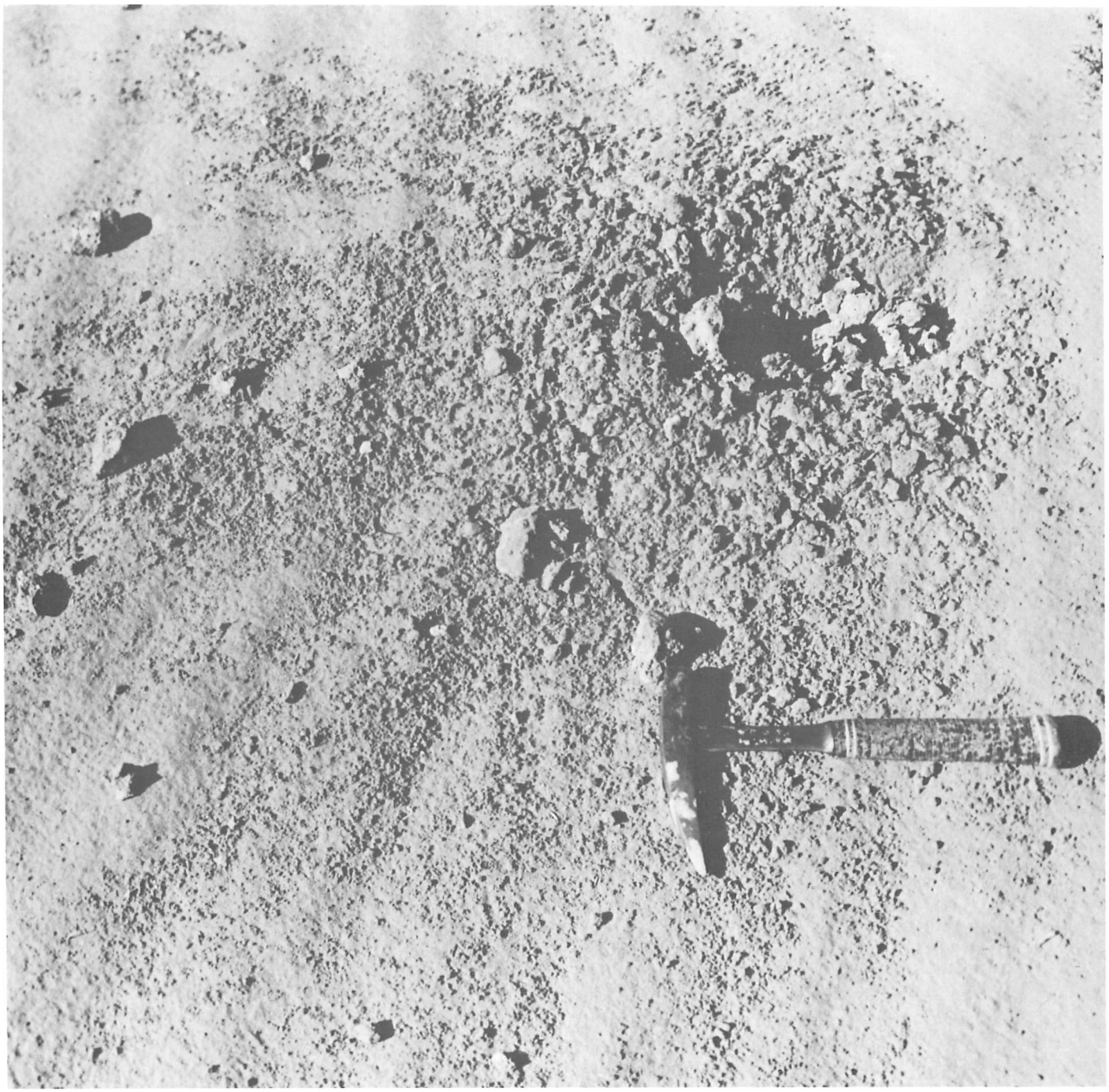

Fig. III-14. Secondary impact crater in moist sand, formed by a clot of weakly cohesive silty clay, ejected from a missile impact crater at White Sands Missile Range, New Mexico (H. J. Moore, personal communication, photograph courtesy of U. S. Army).

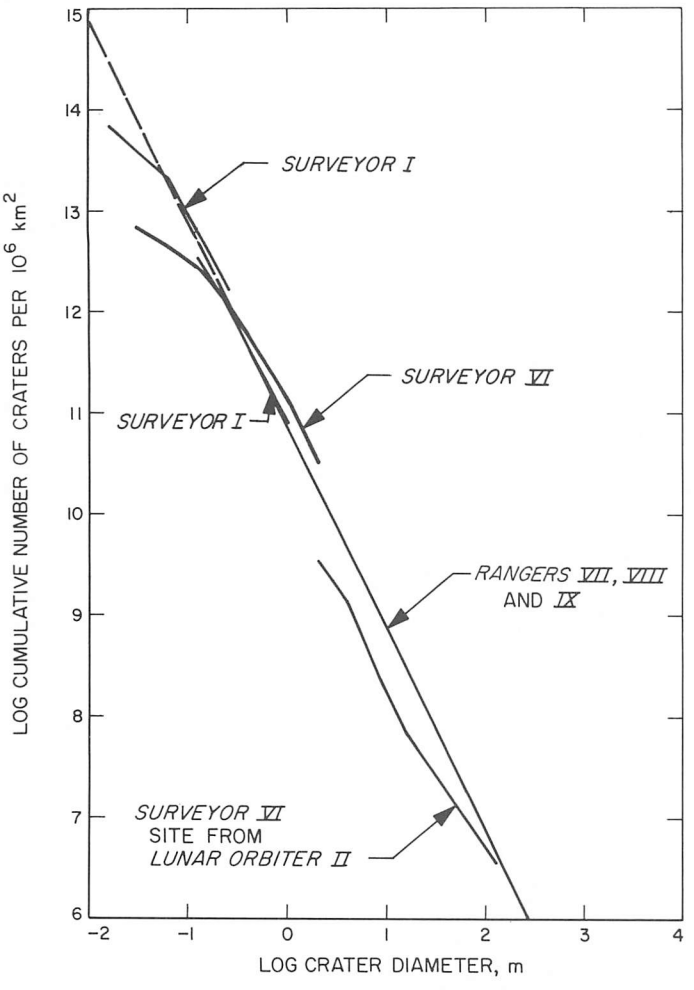

Fig. III-15. Cumulative size-frequency distribution of small craters determined from *Surveyor VI* pictures and *Lunar Orbiter II* photographs, compared with the cumulative size-frequency distribution of small craters determined from *Surveyor I* pictures and on the mare planes determined from *Ranger VII, VIII,* and *IX* photographs.

3. Fragmental Debris

As observed on the maria at the sites of the previously landed *Surveyors,* the mare surface of Sinus Medii around *Surveyor VI* is composed of fragmental debris. About 10 to 15% of the surface is occupied by fragments coarser than 1 mm, coarse enough to be resolved by the television camera on parts of the surface close to the spacecraft. Most of the resolvable fragments are significantly brighter, under all observed angles of illumination, than the unresolved fine-grained matrix of the debris.

Most of the coarser fragments observed near *Surveyor VI* are subangular to subrounded and, in some cases, are partly buried or covered by the fine-grained matrix material (Fig. III-16). Coarse blocks on the rims of craters on the mare ridge and in strewn fields of blocks on the ridge southeast of the spacecraft are more angular and faceted and appear to rest mostly on the surface. Some blocks near the spacecraft are tabular or platy, similar to the layered rocks observed near *Surveyor III* (Fig. III-17). In form, they resemble rock slabs derived from flow-banded lavas (Fig. III-18).

Nearly all the bright, rounded fragments have a knobby, pitted surface texture. This type of surface texture has been observed on most blocks at all *Surveyor* landing sites and is perhaps the most common surface texture developed on the coarse-grained, fragmental materials on the maria. Since the pitted texture is not present on highly angular, faceted blocks, it is inferred to be produced by the same processes that cause the rounding. The pits are probably produced by impact of small particles on the blocks.

The fragmental material ejected by the footpads of *Surveyor VI,* both during the initial landing and the landing after the hop, is composed mainly of clods or aggregates of fine-grained material (Fig. III-19), similar to the aggregates observed at the *Surveyor V* site (Ref. III-3). Many of the clods contain small, bright, rocky chips, and the surfaces of many of the clods have dark bumps, which are inferred to be slightly more coherent, small aggregates of fine-grained particles within the clods.

Fragments that are clearly aggregates also occur on the undisturbed mare surface. One fragment about 4 cm across containing bright, rocky chips (Fig. III-20) has a layered appearance, which may indicate that it has been compressed, perhaps by shock, during the formation of an impact crater.

The size-frequency distribution of the fragmental debris was determined for three sample areas in the immediate vicinity of *Surveyor VI.* A total of 1757 particles were counted, ranging in size from 2 mm to 25 cm. The sample areas are located on parts of the lunar surface undisturbed by the spacecraft. All recognizable fragments were counted in each area; some of the fragments counted may have been fine-grained aggregates. The estimated mean cumulative distribution of fragments on the lunar surface at the *Surveyor VI* site is shown by the heavy line in Fig. III-21. This line is the plot of the equation $N = 5 \times 10^6\ y^{-2.5}$, where N is the cumulative number of fragments per 100 m^2 and y is the diameter of fragments in millimeters.

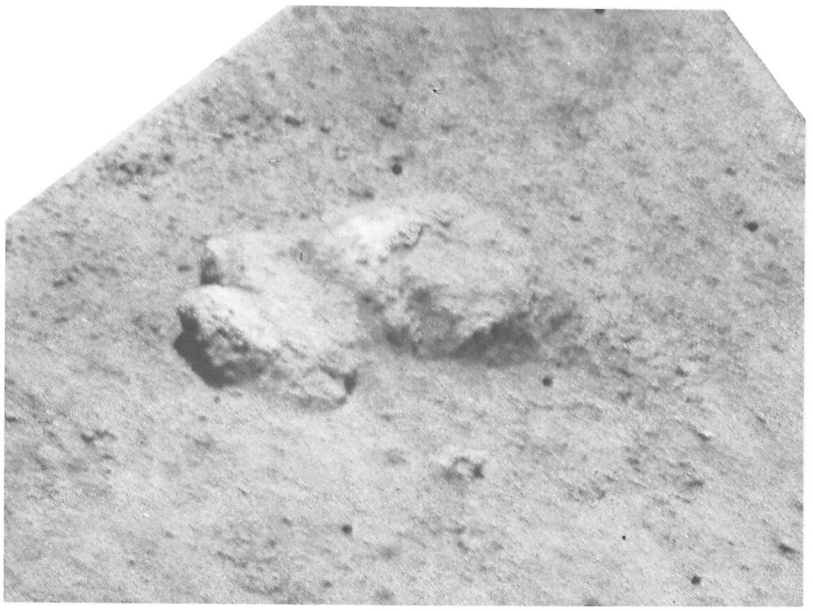

Fig. III-16. Narrow-angle picture showing fragment, about 15 cm across near *Surveyor VI*, which has been partially buried by fine-grained lunar material. Knobby, pitted surface texture on this fragment is typical of many rocks observed on the lunar surface (Day 321, 07:29:52 GMT).

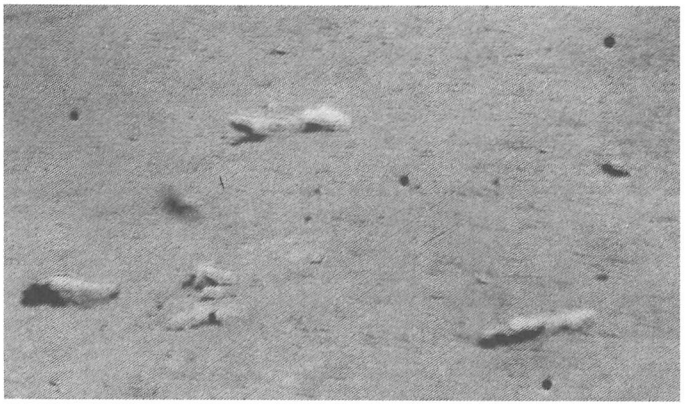

Fig. III-17. Narrow-angle picture showing slabby blocks 20 to 30 cm across near *Surveyor VI*. These blocks resemble tabular blocks near *Surveyor III* (Day 322, 03:18:52 GMT).

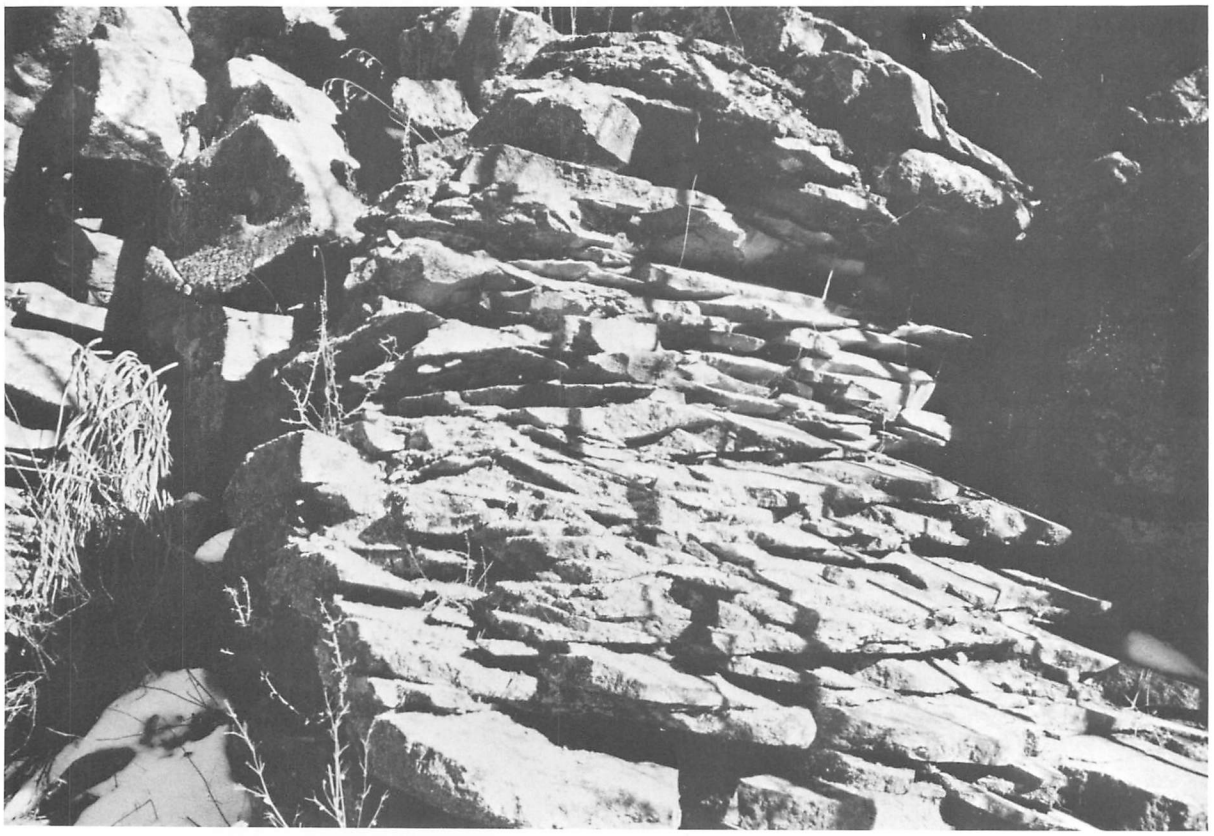

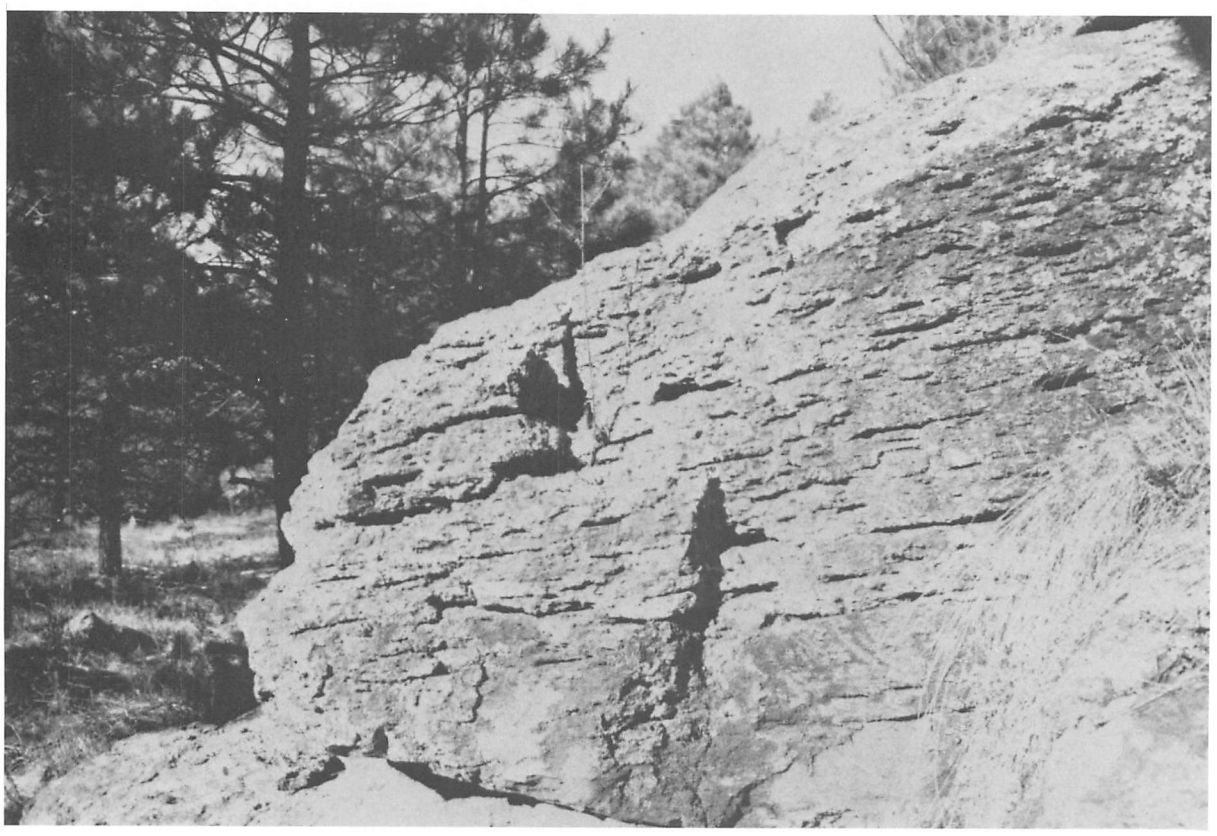

Fig. III-18. Photographs of flow-banded basalt lava flow near Flagstaff, Arizona. Layering, or banding in the lava flow, is due in part to laminar accumulations of gas bubbles in the fluid lava before it cooled. The basalt breaks along the planes of weakness caused by the layering.

Fig. III-19. Clods of fine-grained surface material disturbed by footpad 2 during landing after the hop made by *Surveyor VI* early November 17, 1967. Clods are composed of compacted, fine-grained material and bright, rocky chips (Day 323, 06:53:29 GMT).

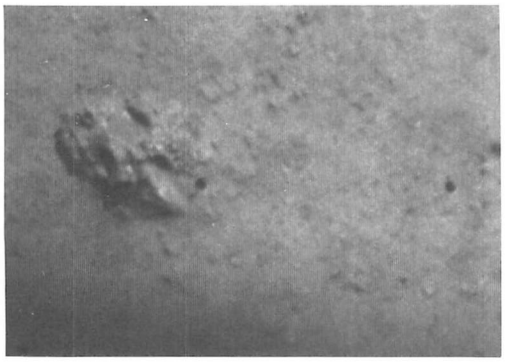

Fig. III-20. Fragment near *Surveyor VI* approximately 4 cm across, composed of an aggregate of fine-grained lunar surface material and bright, rocky chips. Fragment appears mottled and slightly layered, which may indicate it has been compacted and probably has been ejected from a nearby impact crater (Day 321, 07:23:27 GMT).

The size-frequency distribution curve for fragments on the mare plain around *Surveyor VI* has a steeper slope than the curve obtained for fragmental debris on the mare plain at the *Surveyor I* site (Fig. III-22). There are fewer fragments larger than 2 to 3 cm per unit area at the *Surveyor VI* site, and more fragments finer than 2 to 3 cm. Fragments larger than a few tens of centimeters are rare around *Surveyor VI*. The largest block observed within about 50 m of the spacecraft is about 50 cm across (Fig. III-23), and only six blocks larger than 20 cm across have been observed within this area.

Much coarser fragments occur on the nearby mare ridge than were observed on the plain. Blocks as large as 2.5 m across can be seen in the *Surveyor* pictures of the ridge (Fig. III-24), and blocks from 2 to 6 m across were found in the high-resolution *Lunar Orbiter* photographs.

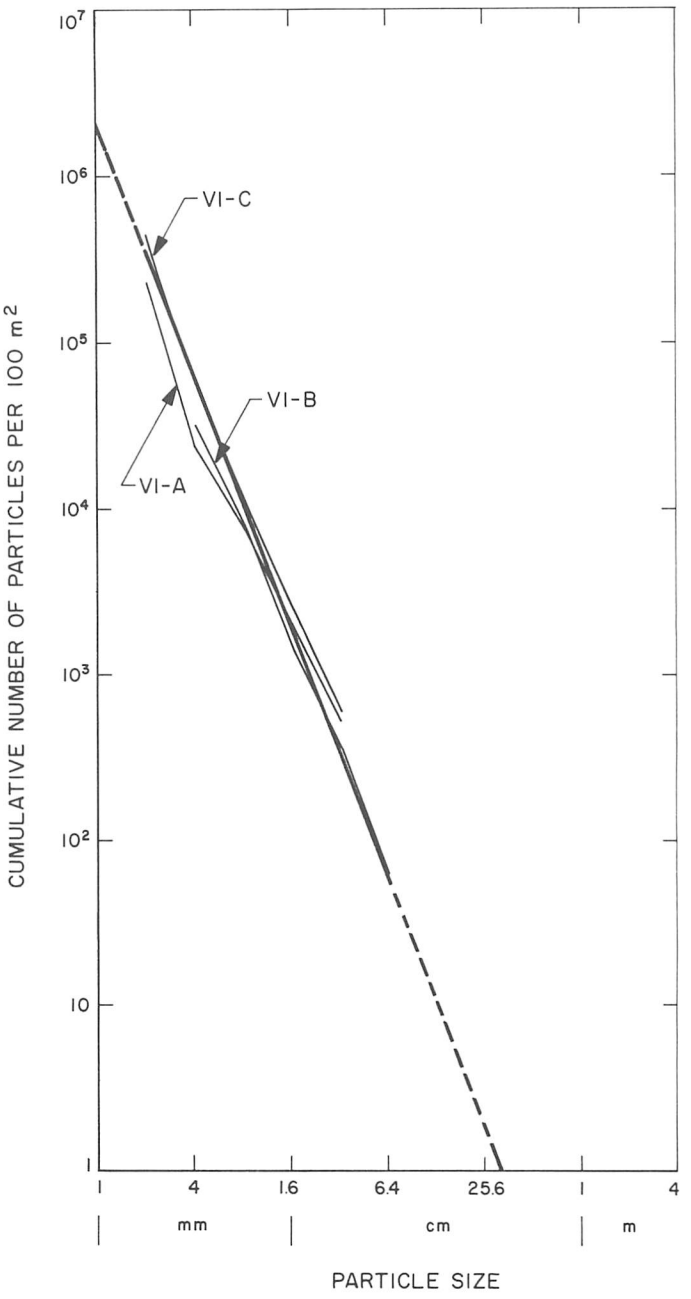

Fig. III-21. Cumulative size-frequency distribution of fragments determined for three sample areas from *Surveyor VI* pictures.

4. Thickness of Debris Layer

The debris layer, or regolith, at the *Surveyor VI* site is considerably thicker than at the previous *Surveyor* landing sites, as indicated by the depth of the smallest craters that have blocky rims (Refs. III-1 to III-3). The debris layer was found to be 1 to 2 m thick at the *Surveyor I* site and no more than 5 m at the *Surveyor V* site. At the *Surveyor III* landing site, the weakly coherent layer of fine-grained debris is, at most, a few meters thick on the rim of the main crater in which the spacecraft landed, but may be thicker beneath the floor of the crater. On the mare plain around *Surveyor VI*, the debris layer is more than 10 m thick, but the precise thickness is difficult to estimate.

On the mare plain, all craters that are visible from the *Surveyor VI* television camera have relatively smooth rims. The largest of these craters with smooth, raised rims are 20 to 30 m in diameter. The smallest, blocky-rim crater observed on the mare plain around the spacecraft

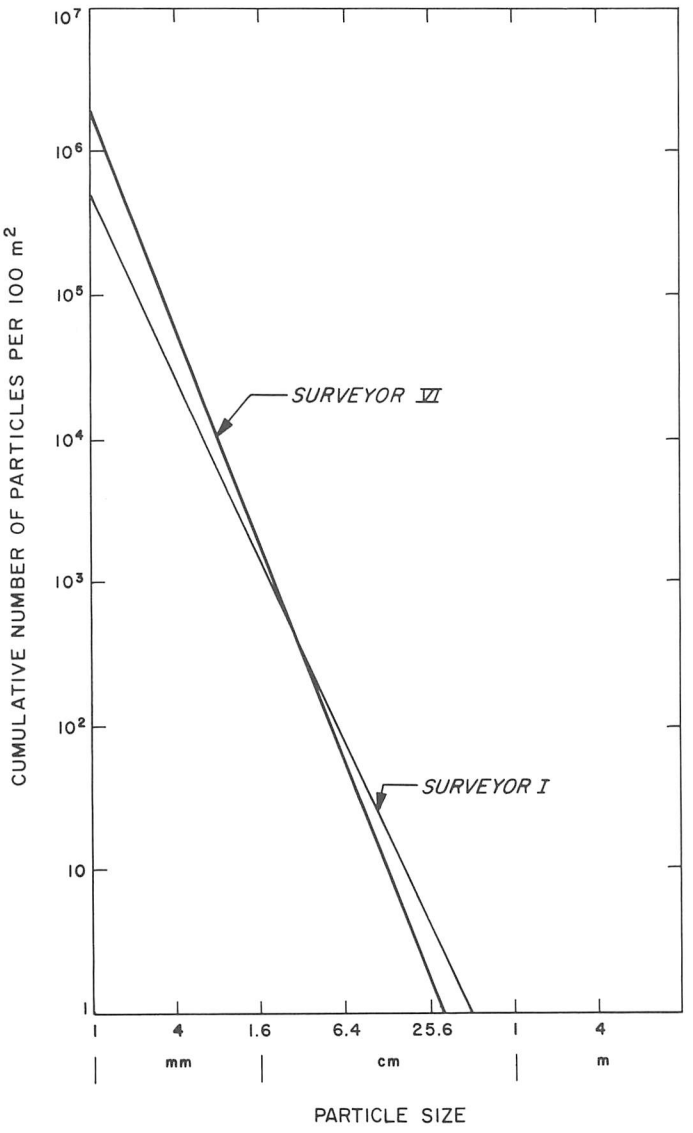

Fig. III-22. General size-frequency distribution of fragments on the lunar surface near *Surveyor VI* compared with the general size-frequency distribution of fragments on the lunar surface near *Surveyor I*.

is 150 m in diameter; the rim of this crater is not visible from the television camera, but the blocks are resolved on high-resolution *Lunar Orbiter* photographs. A pronounced terrace occurs on the wall of this crater at a depth of 20 to 25 m below the crater rim. If the level of the terrace corresponds with the contact of the weakly coherent debris layer on a more coherent substratum, its presence suggests the thickness of the debris layer on the mare plain around *Surveyor VI* is of the order of 20 m.

The debris layer on the mare ridge near *Surveyor VI* is thinner than on the mare floor around the spacecraft.

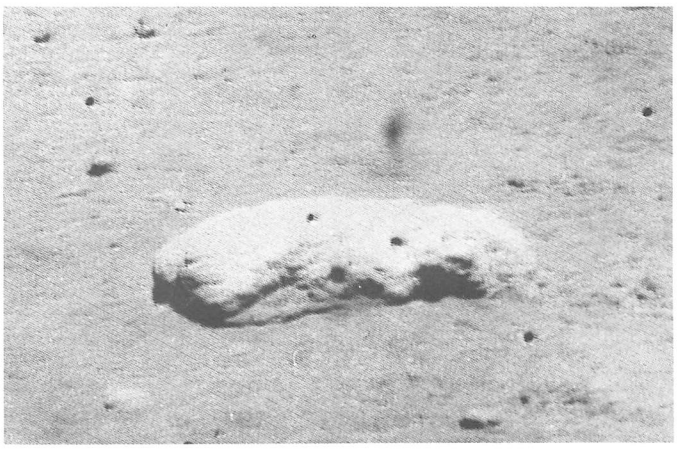

Fig. III-23. Block approximately 50 cm across, about 10 m from *Surveyor VI*; this is the largest block that lies within 50 m of the spacecraft. Knobby, pitted surface of the block is characteristic of many blocks seen at *Surveyor I, III,* and *V* landing sites. Pits may be caused by impact of small particles (Day 323, 03:41:59 GMT).

Lunar Orbiter II and *III* photographs of Sinus Medii and the *Surveyor VI* pictures show several strewn fields of large blocks and blocky-rim craters on the ridge. Two blocky-rim craters visible from the *Surveyor* camera (Fig. III-25), one 30 m in diameter on the flank of the ridge and the other 20 m in diameter near the crest of the ridge, indicate that the debris layer is no thicker than 8 to 10 m on the ridge.

5. Vertical Variations in Debris Layer

Vertical variations in both the photometric properties and strength of the upper part of the debris layer, or regolith, have been observed at each of the *Surveyor* landing sites. Wherever the upper few millimeters of the lunar surface have been disturbed, darker material is exposed beneath a light surface layer. The spacecraft footpads at each landing site kicked darker subsurface material onto the light uppermost surface layer. The soil mechanics surface sampler, carried on *Surveyor III*, exposed dark material beneath the surface, and the firing of the vernier rocket engines on *Surveyors V* and *VI* blew darker subsurface material onto the lighter uppermost surface. Small fragments, 1 or 2 cm in diameter, which have rolled across the surface and disturbed the uppermost layer, exposed darker material at a depth of only 1 or 2 mm (Fig. III-26). This was observed at the *Surveyor III* and at the *Surveyor VI* landing sites. In almost all observed cases, the subsurface material, at a depth of only a few millimeters, is at least 10 to 20% darker than the optically observed surface.

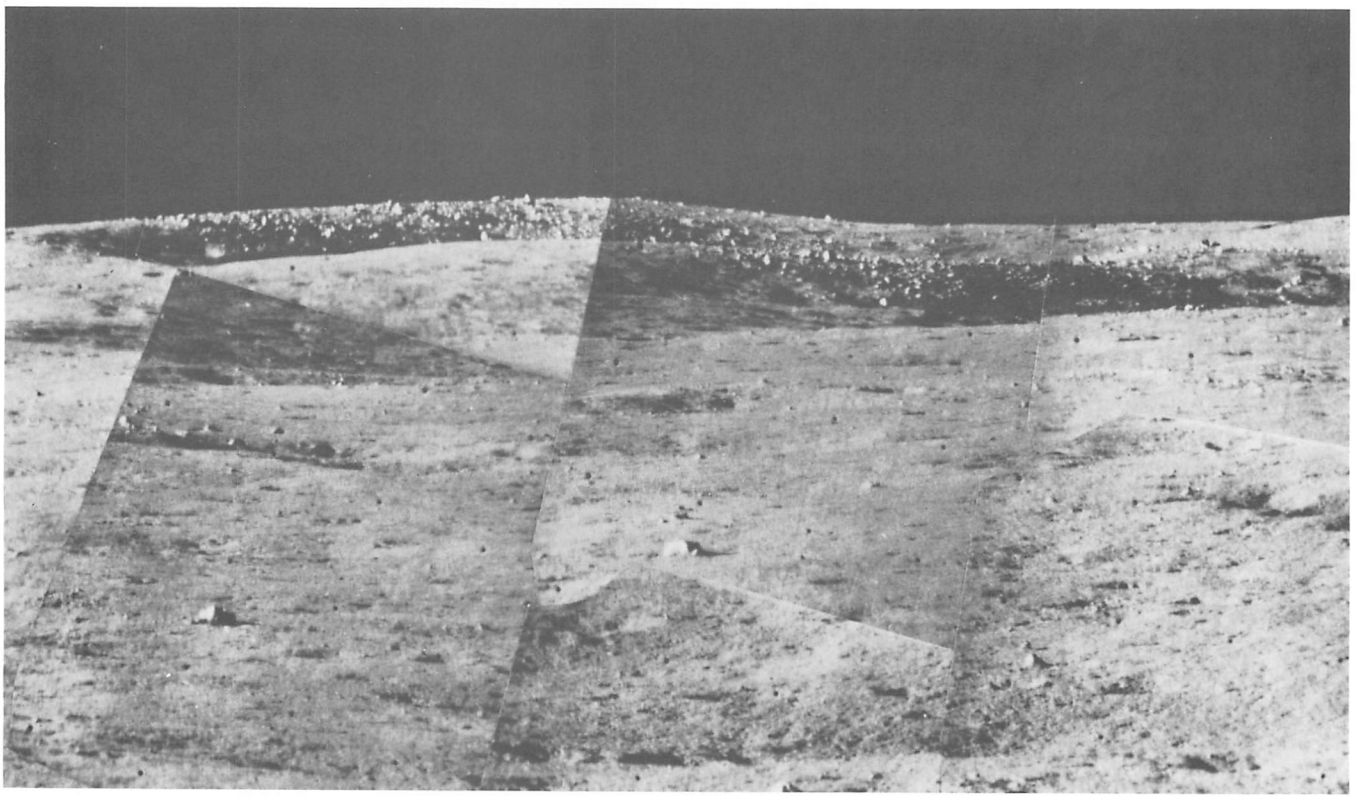

Fig. III-24. Mosaic of narrow-angle pictures taken by *Surveyor VI* of a ridge southeast of the landing site. A field of large blocks is strewn across part of the rim of a crater 180 m in diameter on the crest of the ridge. The largest blocks are 2 to 3 m across. The crest of the ridge at this point is approximately 650 m from the spacecraft.

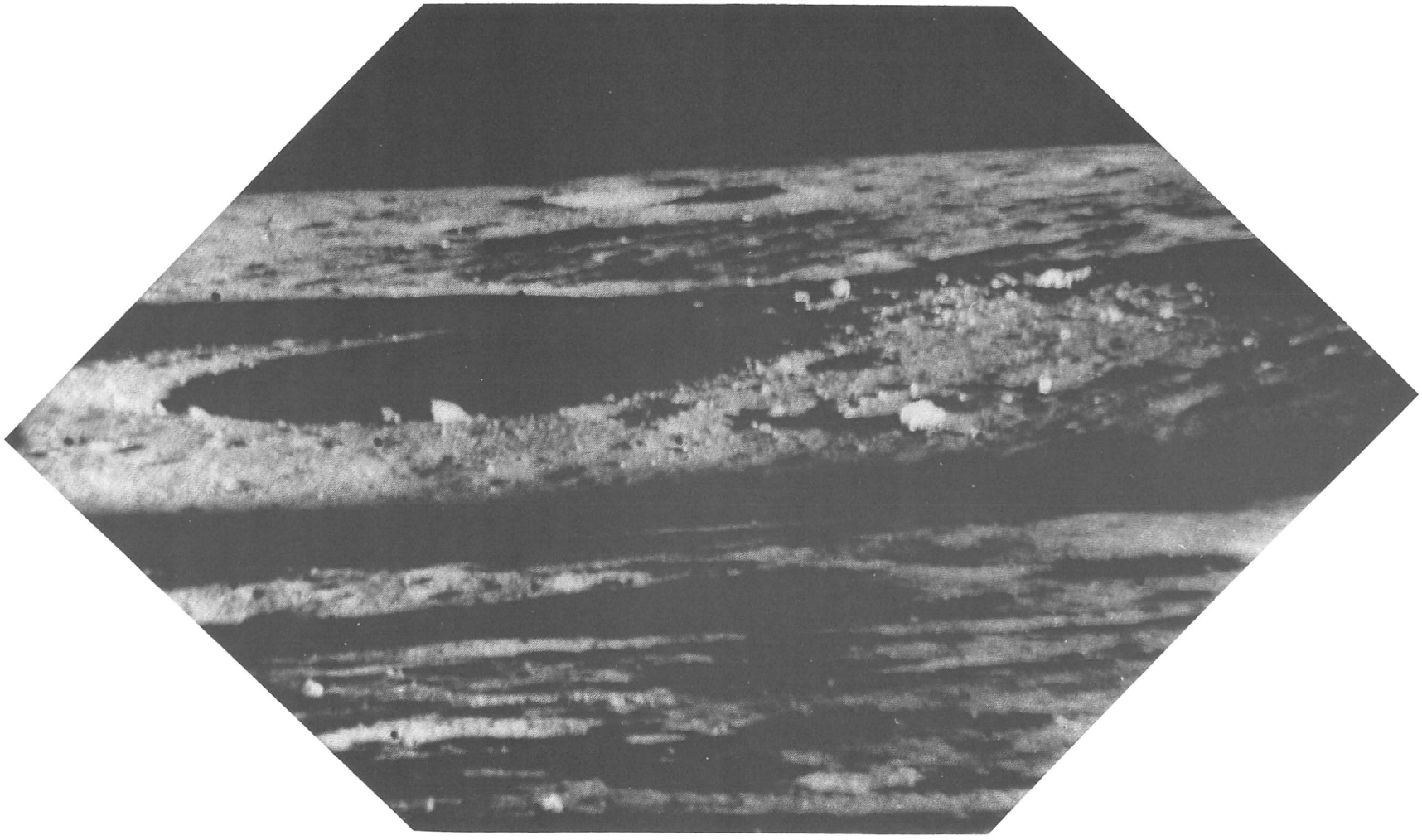

Fig. III-25. Narrow-angle picture looking northeast of the *Surveyor VI* landing site. Crater with the blocky, sharp, raised rim near the center horizon is about 22 m in diameter and 700 m from *Surveyor VI*. The crater with the blocky rim in the center of the picture is 30 m in diameter and 350 m from *Surveyor VI*. These craters lie on a ridge east of the spacecraft (Day 328, 11:47:30 GMT).

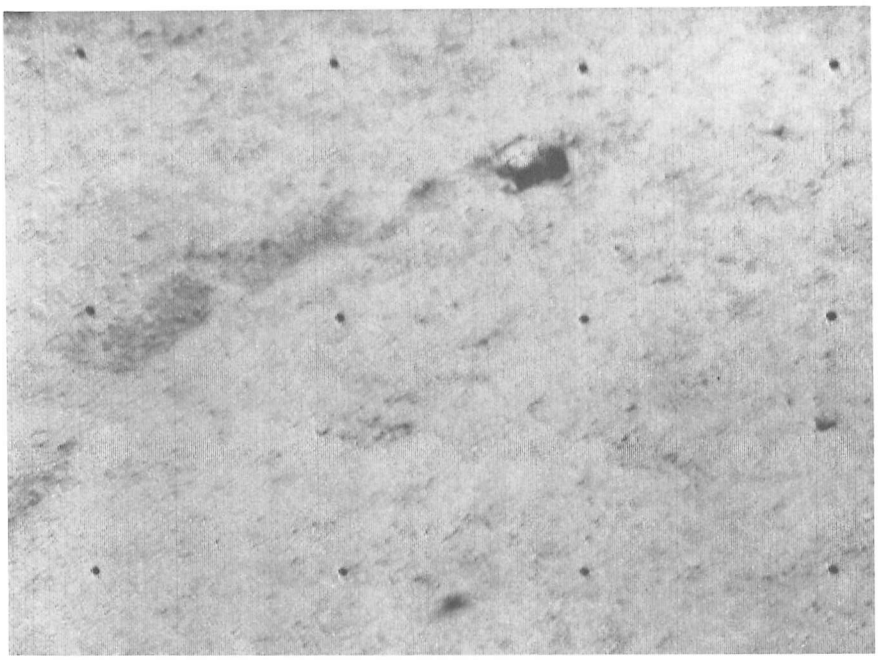

Fig. III-26. Track made by a 2-cm fragment rolling across the lunar surface near *Surveyor VI*. The fragment has disturbed a light, fragile layer of surface material and exposed darker material 1 or 2 mm beneath (Day 321, 07:13:54 GMT).

The strength of the surface material also varies with depth. The small fragment shown in Fig. III-26 is approximately 2 cm across, and the track made by the fragment rolling across the surface is a millimeter to a few millimeters deep. If the density of the fragment does not exceed 3 g/cm^3, the development of the tracks show that the bearing strength of the uppermost few millimeters of the fine-grained debris on the lunar surface is less than 10^4 dynes/cm^2, for surface areas of about 1 cm^2. The bearing strength of the debris layer at greater depths is considerably higher (see Section IV of this report).

6. Interpretation of Geologic Observations

The television observations made from *Surveyor VI* support the interpretation, made from previous *Surveyor* data (Ref. III-2), that the fragmental debris layer, or regolith, on the lunar maria has been derived primarily from bombardment of the lunar surface by solid particles. Because Sinus Medii appears to be a relatively old mare surface, the new observations from *Surveyor VI* are especially important in interpreting how the thickness, grain size distribution, and other characteristics of the debris layer have evolved in the course of time.

On the basis of the chemical analysis of the surface of the debris layer presented by Turkevich, et al. (see Section VII of this report) and the television observations of the coarser fragments around *Surveyor VI*, we infer that the bedrock beneath the debris layer in Sinus Medii consists of basaltic lava flows, which are locally flow-banded. At such localities, the bedrock tends to break into tabular, or slabby, fragments, some of which are scattered on the surface of the debris layer. As no vesicular fragments were observed, it seems likely that most of the bright, rocky fragments are pieces of relatively dense basalt.

The large majority of craters observed at the *Surveyor VI* landing site and elsewhere on Sinus Medii are inferred to be of impact origin. The size-frequency distribution of the craters smaller than a few hundred meters in diameter corresponds to that expected for a steady-state population of craters produced by prolonged, repetitive bombardment by meteoroids and by fragments of the moon itself (Refs. III-2 and III-9). It is significant, in this regard, that the frequency distribution of small craters is essentially the same, regardless of the population of large craters or of other differences in the mare surfaces.

The thickness of the debris layer on the relatively level mare plains is directly related to the abundance of large craters. In the western part of Mare Tranquillitatis, the areal density of craters 1 to 10 km across is about twice as great as on the Oceanus Procellarum in the vicinity of the *Surveyor I* landing site (Ref. III-8), and the thickness of the debris layer at the *Surveyor V* landing site in Mare Tranquillitatis is greater than that at the *Surveyor I* site. The thickest debris layer so far observed with *Surveyors* is on Sinus Medii, which has one of the highest densities of craters larger than a few hundred meters in diameter of all the mare surfaces so far studied on the moon.

The areal density, or frequency distribution of the larger craters, is interpreted here as a guide to the age of a given mare surface and to the total number of craters of all sizes that have been formed over the course of time (Ref. III-9). Thus, the higher the density of large craters, the higher total number of intermediate- and small-sized craters that have been formed and worn away again, and the greater is the depth to which the lunar surface will have been plowed, or turned over just once. This depth corresponds closely to the average depth of the largest craters that have been formed whose aggregate area is equal to the area of a given mare surface.

The size distribution of fragments in the debris layer is related in turn to its thickness. If the fragments are derived chiefly by impact comminution of coherent bedrock, coarse fragments will be abundantly strewn on the surface of the debris layer when it is at an early stage of development and very thin. At this stage, relatively coarse, blocky debris will be ejected from each relatively small crater that penetrates the debris layer, or regolith. As the debris layer matures and becomes thicker with age, as a result of deeper plowing by larger craters, the craters that penetrate the debris layer become more widely spaced, and fragments ejected from these craters are more widely spaced. Fragments formed early in the evolution of the debris layer, meanwhile, are broken and comminuted by repetitive bombardment by large numbers of small particles. Because the proportion of small meteoroids to the large meteoroids is greater than the proportion of small fragments to large fragments produced by impact in coherent rock, the proportion of fine-grained material in the debris layer tends to increase with time, and the proportion of coarse-grained material decreases. Thus, the size-frequency distribution of fragments in a mature, thick debris layer should have a steeper slope than the size-frequency distribution in a young, thin debris layer, as is observed.

This relationship between thickness and age of the debris layer and its grain size distribution leads to an apparent paradox in the selection of spacecraft landing sites on the moon. A landing site may appear very rough because of the number of large craters, but yet may be less hazardous than a younger surface because there are fewer coarse blocks. The implication is that older surfaces make better landing sites, if the larger craters can be avoided.

Finally, it is appropriate to inquire why the debris layer is thinner on the mare ridge near *Surveyor VI* than it is on the adjacent plains, and whether this observation has any bearing on the origin of the ridge.

There are at least two plausible hypotheses for the origin of mare ridges:

(1) The ridges are formed by buckling or deformation of the mare surface, and the buckling is partly controlled by regional structure.

(2) The ridges are formed by extrusion of lava that welled up along pre-existing fissures.

Under the second hypothesis, the ridges may overlie feeder dikes from which most of the flows on the maria issued.

The debris layer may be thinner on the ridge near *Surveyor VI* either because the ridge is younger or because part of the debris on the ridge has flowed onto the adjacent plain. The first explanation would lend support to the extrusion hypothesis for the origin of the ridge, whereas the second explanation would not favor either hypothesis.

No evidence was found in the crater density on the ridge to suggest the ridge is younger than the plain. The area of the ridge is so small, however, that population of craters large enough to determine the relative age of the ridge cannot be established with confidence.

Some evidence may be cited, on the other hand, that the debris layer on the ridge is actually flowing or has flowed downhill by slow mass movement or creep. The patterned ground on the ridge may be developed primarily as a consequence of mass movement. Possible terrestrial analogs of the patterned ground seen on sloping surfaces on the moon have been described[1] on large

[1] M. D. Crittenden, "Terrestrial Analogues of Lunar Mass Wasting," *Preliminary Geologic Evaluation and Apollo Landing Analysis of Areas Photographed by Lunar Orbiter III*, Langley Working Paper 407, pp. 125–127, Hampton, Va., June 1967.

expanses of debris at high elevations in the Uinta Mountains of Utah. There the patterned ground is developed on material undergoing mass movement. Patterned ground was also observed on the wall of the crater in which *Surveyor III* landed, and at that site the presence of fillets on the uphill sides of blocks suggested the debris layer is gradually flowing down the crater wall (Ref. III-2). The presence of fields of very coarse blocks observed in *Lunar Orbiter* photographs on the crests of other mare ridges suggests the finer-grained material in the debris layer has flowed away from these blocks, leaving them as a residual accumulation on the ridges. On balance, the evidence suggests to us that the debris layer is thinner on the mare ridge near *Surveyor VI* because of creep or mass movement rather than because the ridge is younger than the mare plain.

Observations of the fine-grained parts of the lunar surface disturbed by the initial landing and landing after the hop, and by rolling fragments set in motion by the spacecraft, have shown that lunar material exposed at depths no greater than a few millimeters has a significantly lower normal albedo than the undisturbed surface. A similar abrupt decrease of albedo at depths of 3 mm or less was observed at the *Surveyor III* and *V* landing sites. The occurrence of this rather sharp contact of material with contrasting optical properties at widely separated localities on the lunar maria suggests that some process, or combination of processes, lightens the material at the lunar surface. If this is true, it may imply that a complementary process of darkening occurs at depths of a few millimeters and deeper (Ref. III-2), so that the abrupt albedo contact is not destroyed as a result of

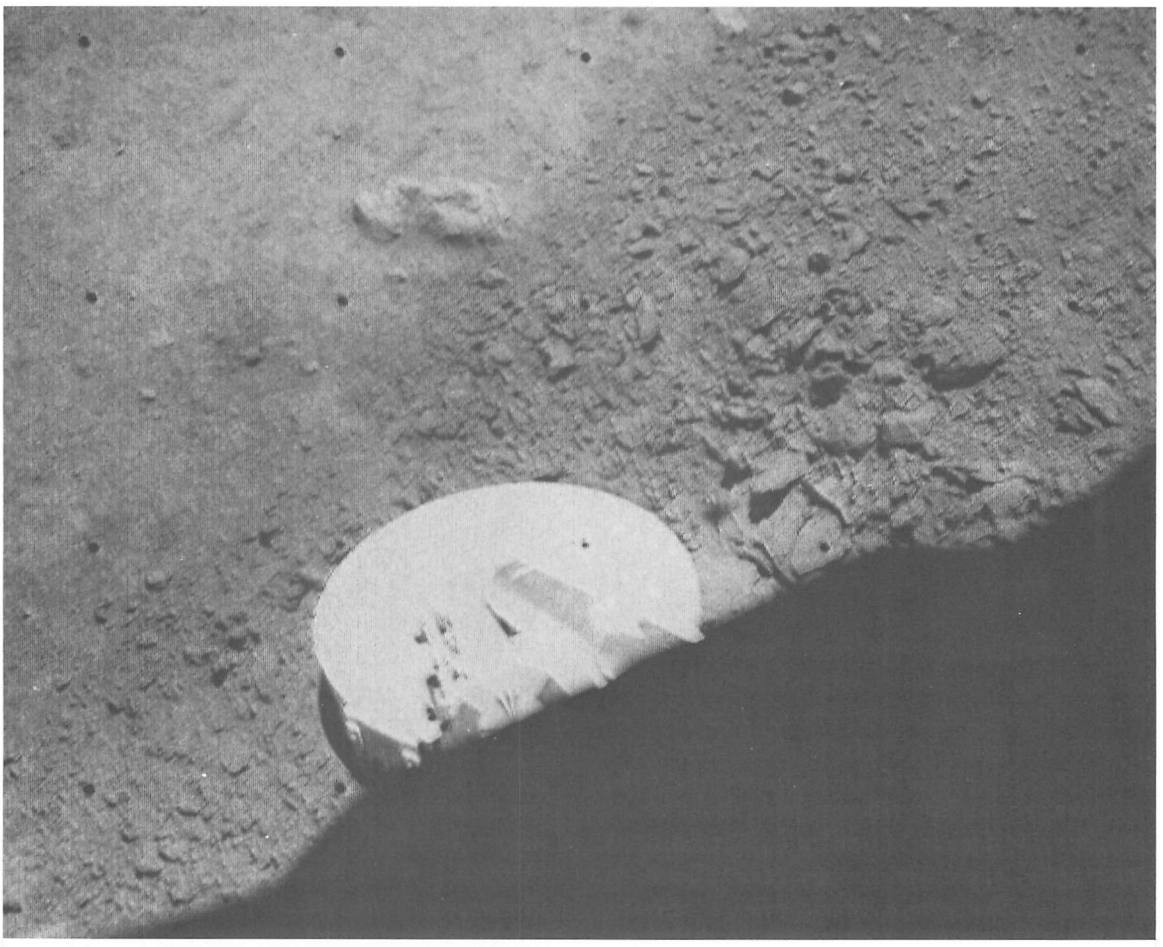

Fig. III-27. Wide-angle picture of dark material around footpad 2. The dark material was thrown out by the impact of the footpad after the spacecraft was hopped. The disturbed material is about 20% darker than the undisturbed material. The greatest contrast between this disturbed material and the undisturbed surface occurs during lunar noon (Day 322, 04:33:05 GMT).

repetitive turnover of the lunar surface by solid particle bombardment.

E. Photometric Observations

Preliminary photometric measurements have been made from the *Surveyor VI* television pictures of the undisturbed lunar surface; of disturbed, fine-grained material; and of material adhering to a photometric target mounted on the boom of one of the spacecraft omnidirectional antennas.

The estimated normal luminance (normal albedo) of the undisturbed, fine-grained surface material near the spacecraft is 8.2%, whereas the rock-like fragments scattered over the lunar surface are noticeably lighter and have estimated normal luminance factors ranging from 14 to 20%. The photometric function of selected areas around the spacecraft was sampled at 12 different angles of sun elevation and appeared similar to the photometric function observed at the other *Surveyor* landing sites.

The debris ejected by the spacecraft footpads is noticeably darker than the undisturbed surface (Fig. III-27) and its normal luminance factor is estimated to be 6.5%. The material, which adhered to the photometric target and was blown upward by vernier engine 3 during the hop, appears to have the same normal luminance factor as the material ejected by the footpads. The gray steps along the left side of the photometric target are faintly visible through a coating of lunar material under nearly normal solar radiance (Fig. III-28). The reflectance from the gray-step areas 5, 6, and 7 increased from the preflight calibration as a result of this coating, whereas gray steps 8 and 9 decreased in reflectance. Gray steps 7 and 8 bracket the reflectance of the lunar material; it has an estimated normal luminance factor of 6.5%. These photometric measurements are estimated to be within 10% of the true values.

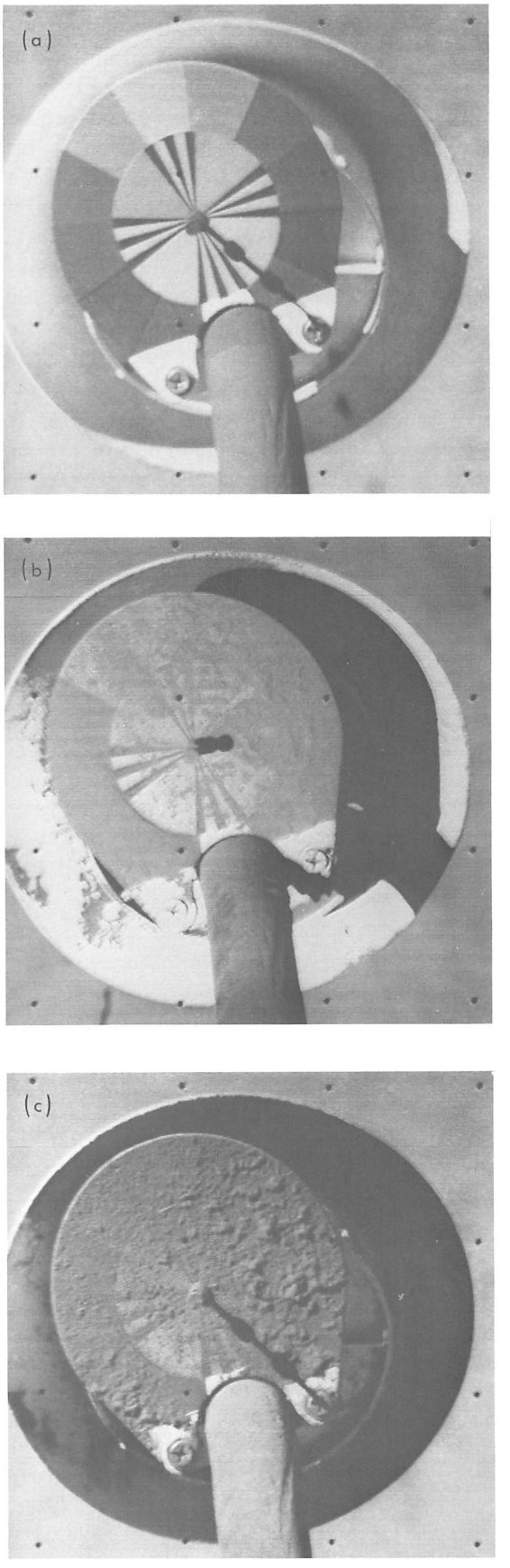

Fig. III-28. Photometric target on the boom of the omnidirectional antenna; the target was partially covered by lunar material blown by vernier engine 3 during the hop. (a) Target a few hours before the hop (Day 321, 09:37:05 GMT). (b) Target with the sun's rays incident at 17 deg on the surface of the target (Day 326, 06:47:06 GMT). (c) Target illuminated by the sun's rays at an angle of 70 deg to the surface of the target. More of the target can be seen under direct illumination (Day 321, 12:29:08 GMT).

An interesting and unexpected phenomenon was observed in television pictures taken after sunset. Approximately 1 hr after the sun's upper limb had set on the western horizon, a bright line with several pronounced bright beads was observed on the horizon in pictures exposed for the solar corona. Apparently, this bright line is caused by either the diffraction of sunlight by minute irregularities on the western horizon or by forward (Mie) scattering by particles above the surface, or possibly by both. The beads disappeared by groups as the sun dropped lower with respect to the horizon.

The bright line was observed in seven pictures (Table III-3). All pictures but one were exposed for several seconds by use of the integration mode of the camera. Integration of the light flux incident on the vidicon is obtained by sending a command to turn off the electron scanning beam, allowing the integration to proceed, then commanding a "start frame," which restarts the electron scanning beam and transmits the frame. Because the camera is not synchronized to the ground data system, the time at which the turnoff occurs is often somewhere in a frame. Part A of each frame listed in Table III-3 received less exposure than part B. Errors greater than 20% in the calculated exposure are possible for short (<5 sec) exposures if a constant integration time over the complete frame is assumed. Even taking the command times into account leaves an uncertainty in the position of the boundary between parts A and B of 0.1- or 60-sec television lines.

At the time of this report, the amplitudes of the video signal have been reduced to luminance values for only one picture showing the bright line. Frame 3 was selected for reduction and processed in a manner similar to that described by Shoemaker, et al. (Ref. III-2), for the analysis of eclipse pictures taken by the *Surveyor III* camera. From a digitized magnetic-tape record of the video signal, the parts of the frame containing the bright line (Fig. III-29) were introduced into the computer; the luminance was calculated for each picture element on the basis of pre-flight calibrations of the television camera.

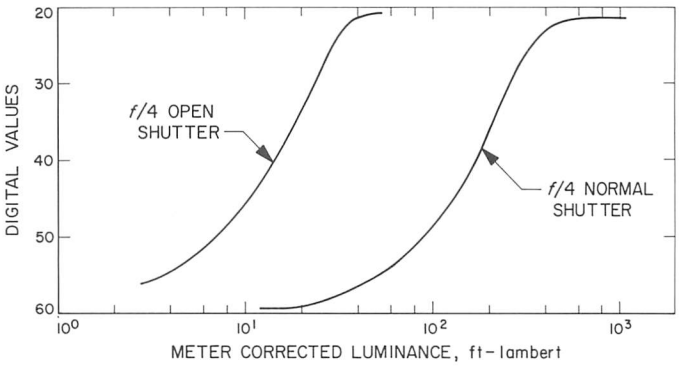

Fig. III-29. Digitized plot of the light-transfer characteristic of the *Surveyor* television camera in the part of the picture format that contains the right side of the sun's corona. The open-shutter data was obtained during pre-flight calibration at the f/8 iris position and extrapolated to f/4.

The angular position of the sun, with regard to the horizon at the time frame 3 was taken, is shown in Fig. III-30 and was obtained through identification of three stars in the constellation of Scorpio. The peak luminance of beads along the horizon decreases with angular distance from the sun (Fig. III-31). Vertical cross sections through two selected beads (Fig. III-32) show a rapid rise and fall of the luminance across the beads; the image of many of the beads close to the sun's position is saturated at the center of the bead, and the peak luminance cannot be measured.

Table III-3. *Surveyor VI* television pictures showing bright line on western horizon after sunset

Frame	GMT (Day 328)	Part A		Part B	
		Television lines	Exposure time, sec	Television lines	Exposure time, sec
1	14:15:26	360 to 600	6.8	0 to 360	8.0
2	14:21:50	540 to 600	11.9	0 to 540	13.1
3	14:25:25	240 to 600	61.8	0 to 240	63.0
4	14:36:41			0 to 600	1.2
5	14:38:06	60 to 600	61.5	0 to 60	62.7
6	14:42:21	480 to 600	61.0	0 to 480	62.2
7	14:56:02		27.6	0 to 600	28.8

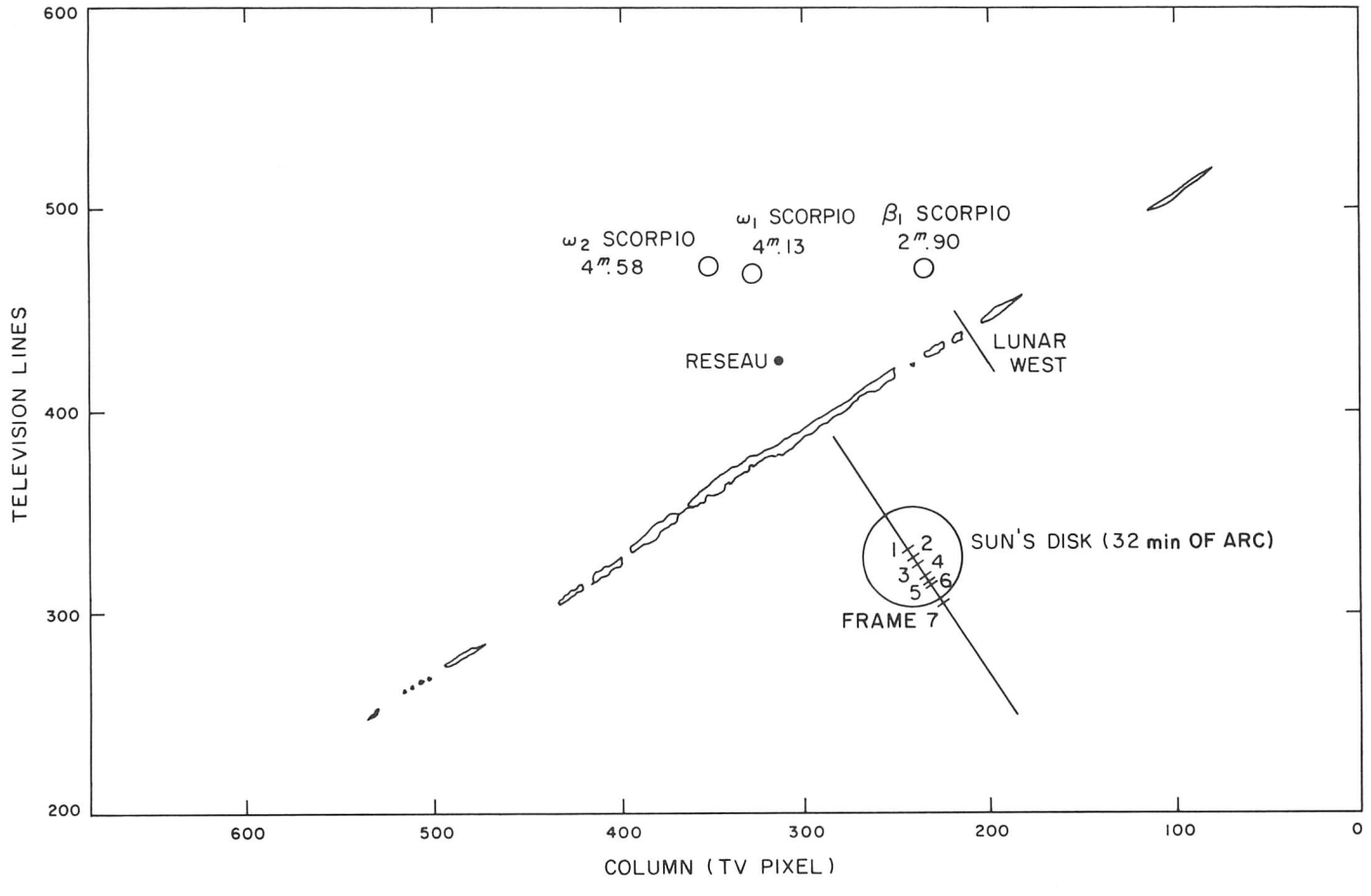

Fig. III-30. Diagram showing the position of the sun's disk in relation to the horizon and beads at 14:25:25 GMT on Day 328. The position of the center of the sun is also indicated for other frames showing the bright line on the horizon. The stars ω_1 and ω_2 Scorpio are those used to determine the sun's position. The magnitudes of these stars are indicated beside the circles. The grid coordinates refer to position in the digital frame.

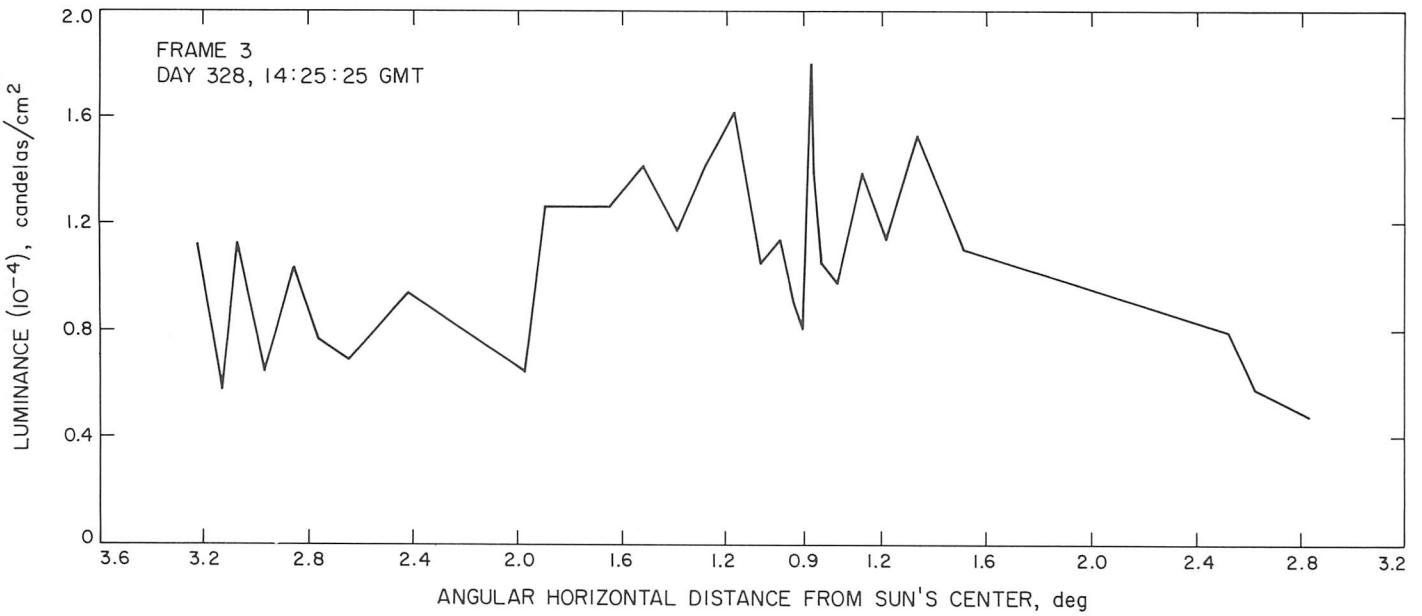

Fig. III-31. Luminance of beads on the horizon as a function of angular distance from the center of the sun's disk. The curve connects sample data points in the beads.

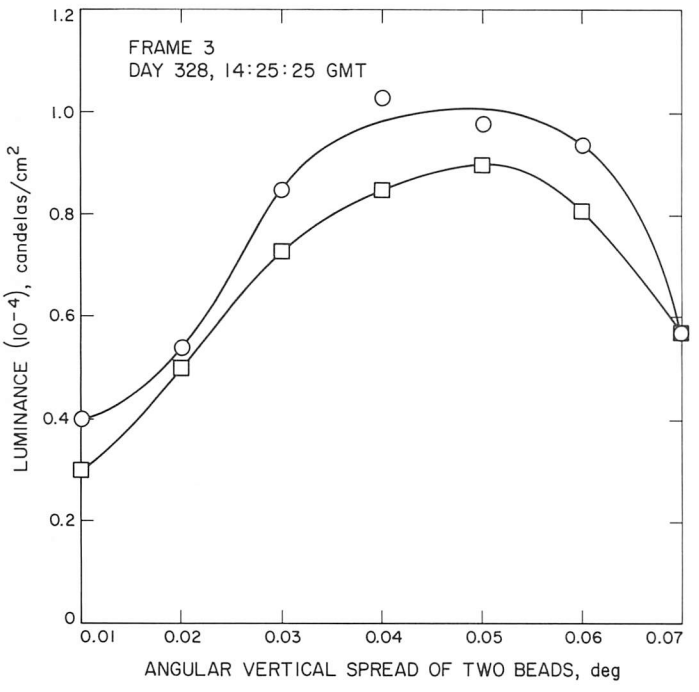

Fig. III-32. Luminance vs angular spread of two beads measured in frame 3. The photometric cross section of each bead was obtained along the vector from the bead to the sun's center, as shown in Fig. III-30.

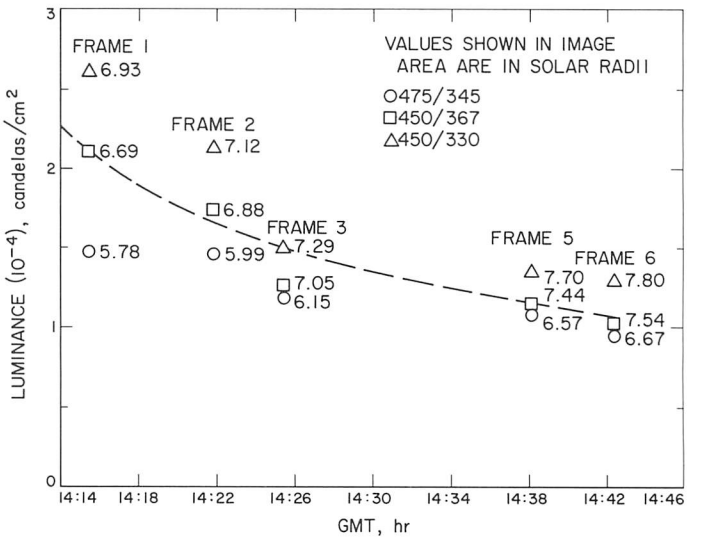

Fig. III-33. Luminance of the corona measured at three constant frame positions as a function of time. The distance of these positions from the center of the sun's disk is given in solar radii beside each data point. The curve is an indication of the trend of the data and does not represent absolute luminance values.

A check on the computed luminances was performed by reducing the digitized video signal for three constant positions in five out of seven frames as the solar corona moved through these positions. The luminance at each position falls off as the sun moves further below the horizon (Fig. III-33). The shape of the curve shown in Fig. III-33 is generally that expected for the solar corona, which increases confidence that the corrections for the different exposures in each frame are approximately correct.

F. Polarimetric Observations

Polarizing filters were mounted on the television camera to serve as analyzers for the detection and measurement of the linearly polarized component of the light scattered from the lunar surface. Pictures of selected areas of the lunar surface were taken through the polarizing filters during most Goldstone passes of the moon. Pictures for polarization measurements were usually taken about 25 hr apart, or at intervals of the sun's position at about 13 deg, in order to obtain measurements of the variation of the polarized component as a function of phase angle. After lunar sunset, pictures of the surface illuminated by earthshine were taken in order to measure the depolarization of earthlight scattered from the lunar surface.

Areas of the lunar surface around *Surveyor VI* were selected for polarimetric study according to their geometric orientation relative to the camera and sun. Numerous sample areas were selected along the east–west sun line in order to compare low-resolution telescopic measurements of polarized moonlight, made of areas of more than 100 km^2, to high-resolution *Surveyor* measurements, covering areas from 1 cm^2 to 1 m^2. Other sample areas were selected northwest, north, northeast, southeast, and south of the spacecraft to provide coverage to test for symmetry in the lunar polarization functions. Additional areas containing large fragments or swarms of small fragments were selected for special examination.

Areal variations were expected in the polarizing properties of the lunar surface corresponding with variations in the fine-scale surface texture and optical properties of the surficial materials. Near the spacecraft, the observed polarizing properties can be compared with resolved surface textures. At greater distances where the surface textures are indistinct or not resolvable, the polarizing properties may provide clues to help correlate the distant material with that observed near the spacecraft or to distinguish different materials.

1. Method of Polarimetric Measurements

Pictures of the lunar terrain were taken with the three polarizing filters rotated sequentially in front of the camera lens, while the aperture and other camera parameters were held constant. Variations in apparent radiance of an image element contained in the three pictures are due to a polarized component in the light incident on the filters. The greater the degree of polarization, or the percentage of linearly polarized light in the light scattered from the lunar surface, the greater the variation in apparent radiance. Laboratory tests indicate that the three-filter analyzer combined with a slow-scan television camera can be used to measure as little as 5% linearly polarized light in the total light incident upon the filters. Some variation in picture level could be detected for light with a 3 to 5% polarized component, but repeatable measurements could not be made. When the polarized light component was less than 3%, no change in picture level in response to analyzer rotation was detectable.

The orientations of the polarizing filters remain fixed with respect to the camera mirror, and consequently rotate with respect to the picture format. The camera was tilted approximately 16 deg from the lunar vertical during the first part of the lunar day and about 13 deg after the hop. Polarimetric measurements along the camera tilt plane have the polarization axis of filter 2 parallel to the horizon and the axis of filter 4 normal to the horizon. At other camera viewing positions, the axes of filters 2 and 4 are inclined to the left or right of these positions, reaching a maximum inclination at viewing positions normal to the camera tilt plane. Thus, the filter 2 axis of polarization, for example, rotated up to a maximum of 16 deg from the lunar horizontal before the hop and up to a maximum of 13 deg to the horizontal after the hop.

The plane of polarization of linearly polarized light scattered from the lunar surface, in most cases, tends to be parallel to the local surface element viewed. The best measurements of polarization are obtained when the plane of polarization is parallel to the mirror axis of rotation, which occurs when a level surface is viewed in the direction of the camera tilt plane. At other camera positions, it is difficult to apply a correction for the additional polarization introduced by the camera mirror, and the preliminary reduction of the data presented here does not contain any correction for this effect.

2. Preliminary Polarimetric Results

Light scattered by the lunar surface is partially plane-polarized at most phase angles. For a first approximate analysis, the degree of polarization, or percent of polarized light, was computed by dividing the difference between the luminances observed through filters 2 and 4 by the sums of the luminances. The percentage of polarized light estimated by this rough method of analysis and reported here includes polarization introduced by the camera mirror. Final corrections for the polarization

introduced by the camera mirror will be based on further tests of mirrors of the type used in the *Surveyor* television camera.

The degree of polarization of light scattered from the fine-grained parts of the lunar surface depends principally on the phase angle; inclination of the surface has a minor effect. At phase angles from 90 to 120 deg, as much as 18% polarization was observed, while at phase angles below 35 deg, the component of polarized light was reduced to only a few percent. About 8 to 11% polarization was observed at a phase angle of 155 deg. Sample areas toward the north and south appear to exhibit slightly lower maximum polarization than along the east–west sun line, which suggests that the polarization function is not symmetrical.

Some rocky surfaces exhibit slightly stronger polarizing effects. A maximum of 30% polarization was measured from the images of two surfaces, which suggests some specular reflection may be present. The polarization function of these rocks is apparently less symmetrical than that of the fine-grained material. The rocks exhibiting strong polarization effects have an estimated normal luminance factor (normal albedo) at least two times greater than the adjacent fine-grained material.

The polarization properties of the lunar material adhering to the photometric target were monitored during the lunar afternoon. Shortly after the material was blown on the target, 9% polarization was measured at a phase angle of 73 deg. The polarization decreased to 5% at a phase angle of 56 deg. When the phase angle decreased to 20 deg, barely detectable negative polarization was observed. These measurements of polarization more closely match the polarimetric function of the maria measured at the telescope (Ref. III-10) than most of our other measurements of the undisturbed lunar surface.

The few preliminary polarization measurements that have been reduced indicate that the degree of polarization measured from the *Surveyor* television pictures is greater than the degree of polarization measured at the telescope. This difference probably is due primarily to an increment of polarized light introduced by the camera mirror. The gross form of the polarization function of the fine-grained parts of the surface suggested by measurements from the television camera, however, is similar to the form of the telescopically measured function.

References

III-1. Rennilson, J. J., Dragg, J. L., Morris, E. C., Shoemaker, E. M., and Turkevich, A., "Lunar Surface Topography," *Surveyor I Mission Report. Part II: Scientific Data and Results*, Technical Report 32-1023, pp. 7–44, Jet Propulsion Laboratory, Pasadena, Calif., September 10, 1966.

III-2. Shoemaker, E. M., Batson, R. M., Holt, H. E., Morris, E. C., Rennilson, J. J., and Whitaker, E. A., "Television Observations from *Surveyor III*," *Surveyor III: A Preliminary Report*, Special Publication 146, pp. 9–60, National Aeronautics and Space Administration, Washington, D. C., 1967.

III-3. Shoemaker, E. M., Batson, R. M., Holt, H. E., Morris, E. C., Rennilson, J. J., and Whitaker, E. A., "*Surveyor V*: Television Pictures," *Science*, Vol. 158, No. 3801, pp. 642–652, November 3, 1967.

III-4. *Orthographic Atlas of the Moon, Supplement 1 to the Photographic Lunar Atlas*, compiled by D. W. G. Arthur and E. A. Whitaker, University of Arizona Press, Tucson, Ariz., 1961.

III-5. Batson, R. M., "*Surveyor* Spacecraft Television Photogrammetry," *Photogrammetric Engineering*, Vol. XXXIII, No. 12, pp. 1365–1372, December 1967.

References (contd)

III-6. Wilhelms, D. E., Geologic Map of the Mare Vaporum Quadrangle of the Moon, U. S. Geological Survey Misc. Geol. Inv. Map I-548, 1968 (in press).

III-7. Howard, K. A., and Masursky, H., Geological Map of the Ptolemaeus Quadrangle of the Moon, U. S. Geological Survey Misc. Geol. Inv. Map (in preparation).

III-8. Shoemaker, E. M., "Progress in the Analysis of the Fine Structure and Geology of the Lunar Surface from the *Ranger VIII* and *IX* Photographs," *Ranger VIII and IX. Part II: Experimenters' Analyses and Interpretations*, Technical Report 32-800, pp. 249–338, Jet Propulsion Laboratory, Pasadena, Calif., March 15, 1966.

III-9. Shoemaker, E. M., "Preliminary Analysis of the Fine Structure of the Lunar Surface," *Ranger VII. Part II: Experimenters' Analyses and Interpretations*, Technical Report 32-700, pp. 75–134, Jet Propulsion Laboratory, Pasadena, Calif., February 10, 1965.

III-10. Dollfus, A., "The Polarization of Moonlight," *Physics and Astronomy of the Moon*, pp. 131–159, edited by Z. Kopal, Academic Press, 1962.

Acknowledgment

We especially appreciate the efforts of L. Harold Allen, JPL, who initiated the work that led to the incorporation of the integration mode in the *Surveyor* camera. The integration mode has made possible the collection of much valuable scientific data, such as the positions of stars, the moon's surface by earthlight, and the sun's corona. Appreciation is also extended to Raymond Jordan and Jo Anne Jordan, U. S. Geological Survey, and Sayuri Harami and Patricia B. Conklin, JPL, for their assistance in the reduction of the television data.

(Blank Page)

IV. Lunar Surface Mechanical Properties

E. M. Christensen (Chairman), S. A. Batterson, H. E. Benson, R. Choate, R. E. Hutton, L. D. Jaffe, R. H. Jones, H. Y. Ko, F. N. Schmidt, R. F. Scott, R. L. Spencer, F. B. Sperling, and G. H. Sutton[1]

Information regarding the lunar surface mechanical properties[2] presented in this section is derived from telemetry data and studies of pictures showing surface disturbances caused by the spacecraft landings and the firing of the vernier rocket engines and the attitude control jets. Analyses and laboratory simulations were performed to assist in the interpretation of the observed results.

Surveyor VI (see Fig. I-1 of this report) made a normal landing on a generally level surface. About 7 earth days later, the spacecraft was hopped in the direction of leg 1, thereby providing good visibility of the initial landing imprints and stereoscopic pictures of the lunar terrain north and south of the spacecraft. Lunar soil erosion effects resulting from the vernier engine firings during the hop provided data on the lunar surface and a means of estimating expected soil erosion during a lunar landing of the *Apollo Lunar Module*. These data supplement lunar soil erosion results from *Surveyors III* and *V* (Refs. IV-1 and IV-2).

[1]The concurrence of all the authors was impossible to obtain because of the brief time available to prepare this report.

[2]In this section, centimeter-gram units are used. To convert to foot-pound units, the following factors apply: 1 m = 3.28 ft; 1 cm = 0.394 in.; 1 N (newton) = 10^5 dynes = 0.225 lb; 1 N/cm^2 = 1.45 lb/in.^{2}.

A. Spacecraft Landing

1. Description

The basic configuration and landing mechanism for *Surveyor VI* were essentially the same as for *Surveyors I, III,* and *V* (Refs. IV-1 to IV-3). During landing impact, the three landing legs rotate upward against the resistance of the shock absorbers. Following initial impact, the shock absorbers re-extend, returning the legs to their pre-touchdown positions. Additional capability for energy dissipation is provided by crushable honeycomb blocks mounted on the underside of the spaceframe, inboard of each leg, and by crushable footpads.

a. Initial landing. This description of *Surveyor's* initial landing is based on spacecraft telemetry data and analytical landing simulations. Included in the telemetry data (see Fig. IV-1) are continuous histories obtained at landing of the axial loads in the three shock absorbers. The maximum load in each shock absorber and the initial instant of contact for each footpad are given in Table IV-1.

Computer simulations using the time between the initial footpad contacts (Table IV-1) indicate that the angle between the spacecraft X–Y plane (Fig. IV-2) and a planar landing surface was approximately 2.3 deg at

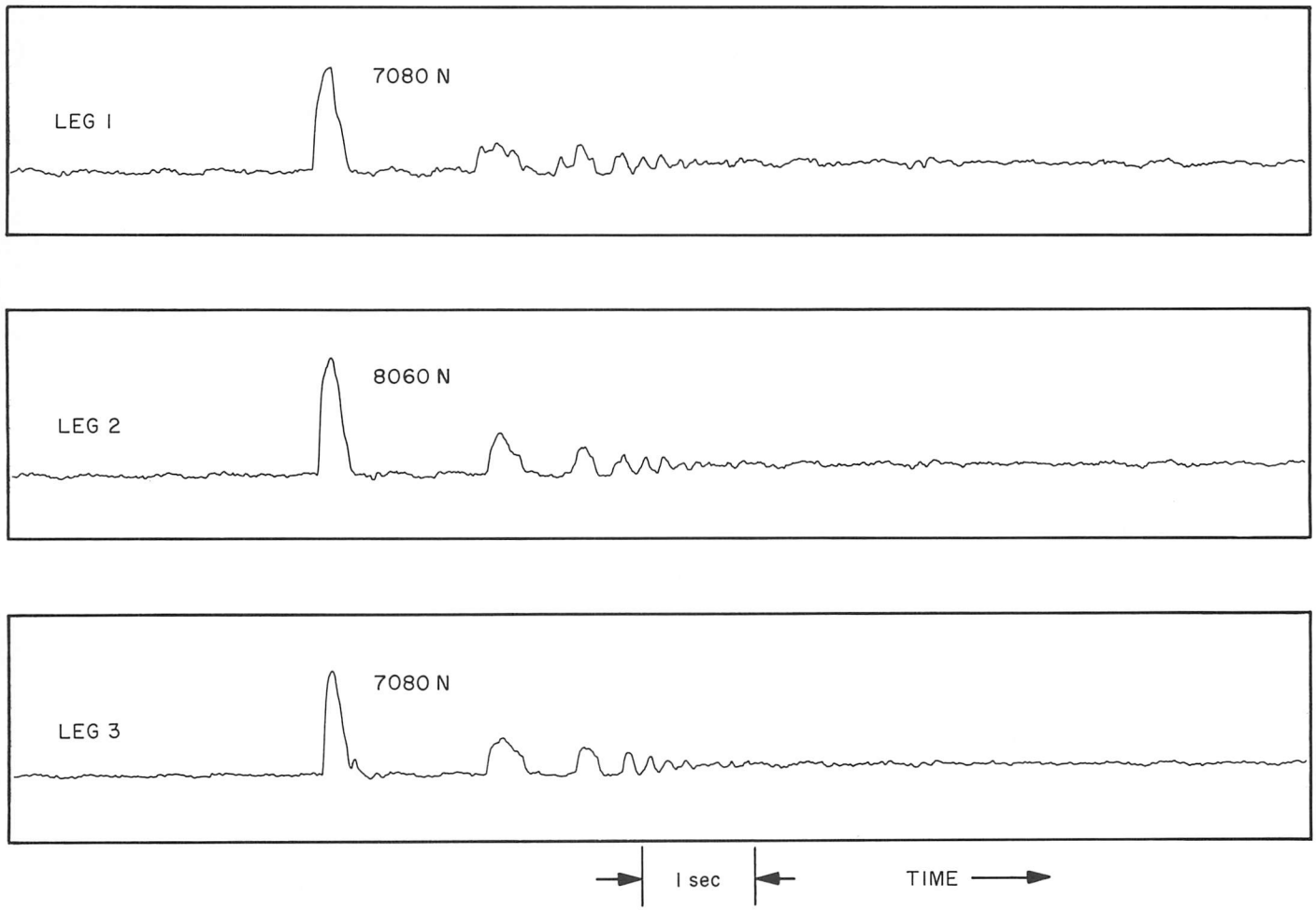

Fig. IV-1. Telemetry data showing shock-absorber axial load histories during initial landing.

the instant of footpad 1 contact. Based on post-landing antenna and solar panel position measurements and star surveys, spacecraft final tilt was determined to be < 1 deg. This would indicate that the initial contact angle was primarily a vehicle incidence angle (angle between a lunar horizontal plane and the plane of the spacecraft footpads). The direction of this incidence angle was such

Table IV-1. Maximum shock-absorber axial loads and times of initial ground contact (initial landing)

Leg	Maximum load, N	Time of impact after initial contact, sec[a]
1	7000±350	0
2	8000 ±400	0.023
3	7000 ±350	0.039

[a]Initial contact was on Day 314 at 01:01:05.467 GMT.

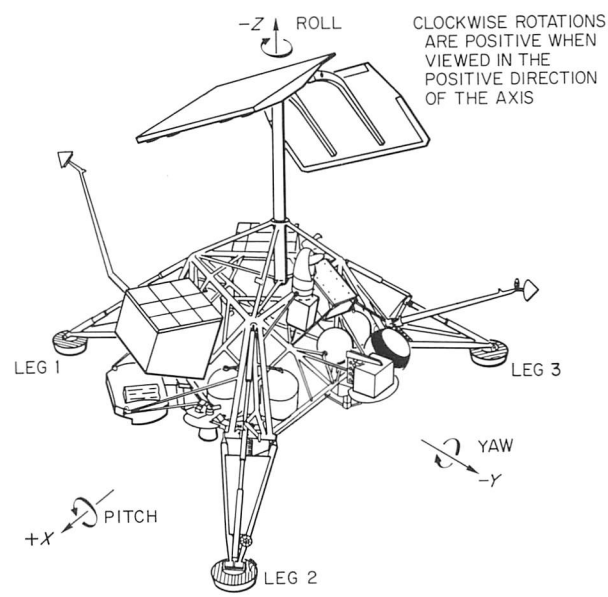

Fig. IV-2. *Surveyor* spacecraft configuration and coordinate system.

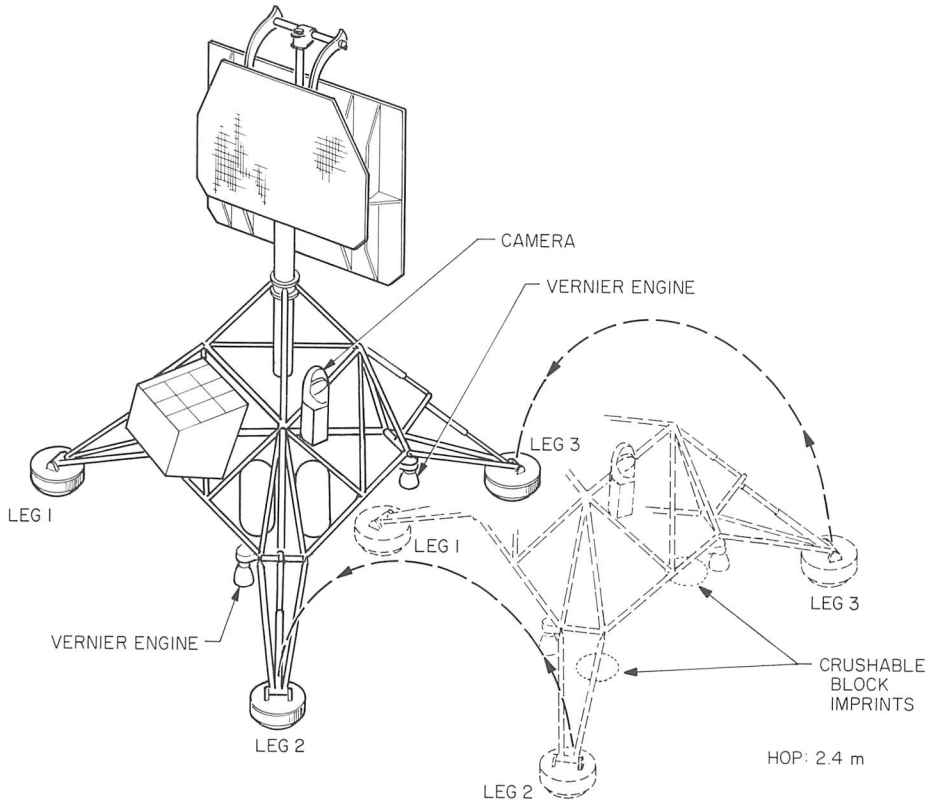

Fig. IV-3. *Surveyor* spacecraft trajectory during hop.

that leg 1 was tilted downward around a horizontal axis rotated clockwise 67 ±5 deg, from the direction of leg 1 (spacecraft viewed from above).

Telemetry data indicate that the vernier engines were cut off at an altitude of 3.00 ±0.1 m, while the spacecraft descended with the constant velocity of 1.4 m/sec. During the free-fall period following engine cutoff, the spacecraft vertical velocity increased to 3.4 ±0.1 m/sec by the time footpad 1 made the initial contact with the lunar surface. Considering the spacecraft incidence prior to engine cutoff, and the time of vernier engine thrust at this incidence, it is estimated that, at touchdown, the spacecraft had a horizontal velocity of 0.3 ±0.06 m/sec directed toward leg 1, normal to the spacecraft tilt axis.

Shock-absorber force histories (Fig. IV-1) show that the initial high loading, caused by the first impact, lasted approximately 0.2 to 0.25 sec. This was followed by a zero-force period lasting a little more than 1 sec, indicating that the spacecraft rebounded clear of the surface. A second impact then occurred, followed by a much shorter rebound period and a final low-energy impact. After the final impact, clearly defined oscillations could be seen. These oscillations are dependent upon the combined elastic properties of the spacecraft and the lunar surface. The spacecraft mass at touchdown was 299.6 kg.

b. Hop and landing. A hop was made by *Surveyor VI* when the vernier engines were fired on Day 321. The vernier engines could not be tilted; therefore, the flight control system was pre-set so that the spacecraft would acquire a +7-deg pitch attitude (leg 1 tilted downward) as soon as possible after liftoff. The vernier engines were ignited and commanded to sustain mid-thrust (a combined nominal thrust of 650 N ±20%) for 2.5 sec. The horizontal component of the tilted thrust provided the desired motion toward leg 1. The movement of the spacecraft during the hop is shown in Fig. IV-3.

The three strain gages, indicating the axial shock-absorber loads, were monitored, in addition to commutated gyroscope and other telemetry signals. The strain-gage histories are shown in Fig. IV-4. Liftoff and landing are clearly evident; vernier engine firing and shutoff were established from other telemetry data. Calculations, based on a reconstruction of the trajectory and telemetry data, indicated a vertical velocity at touchdown of 3.75 ±0.25 m/sec and a horizontal velocity in the direction of leg 1 of 0.55 ±0.06 m/sec. The maximum axial force in each shock absorber and the instant of each footpad contact are given in Table IV-2. The high force in leg 1, as compared with legs 2 and 3, is caused partly by the horizontal velocity in this direction. However, according to landing simulations, a very high friction

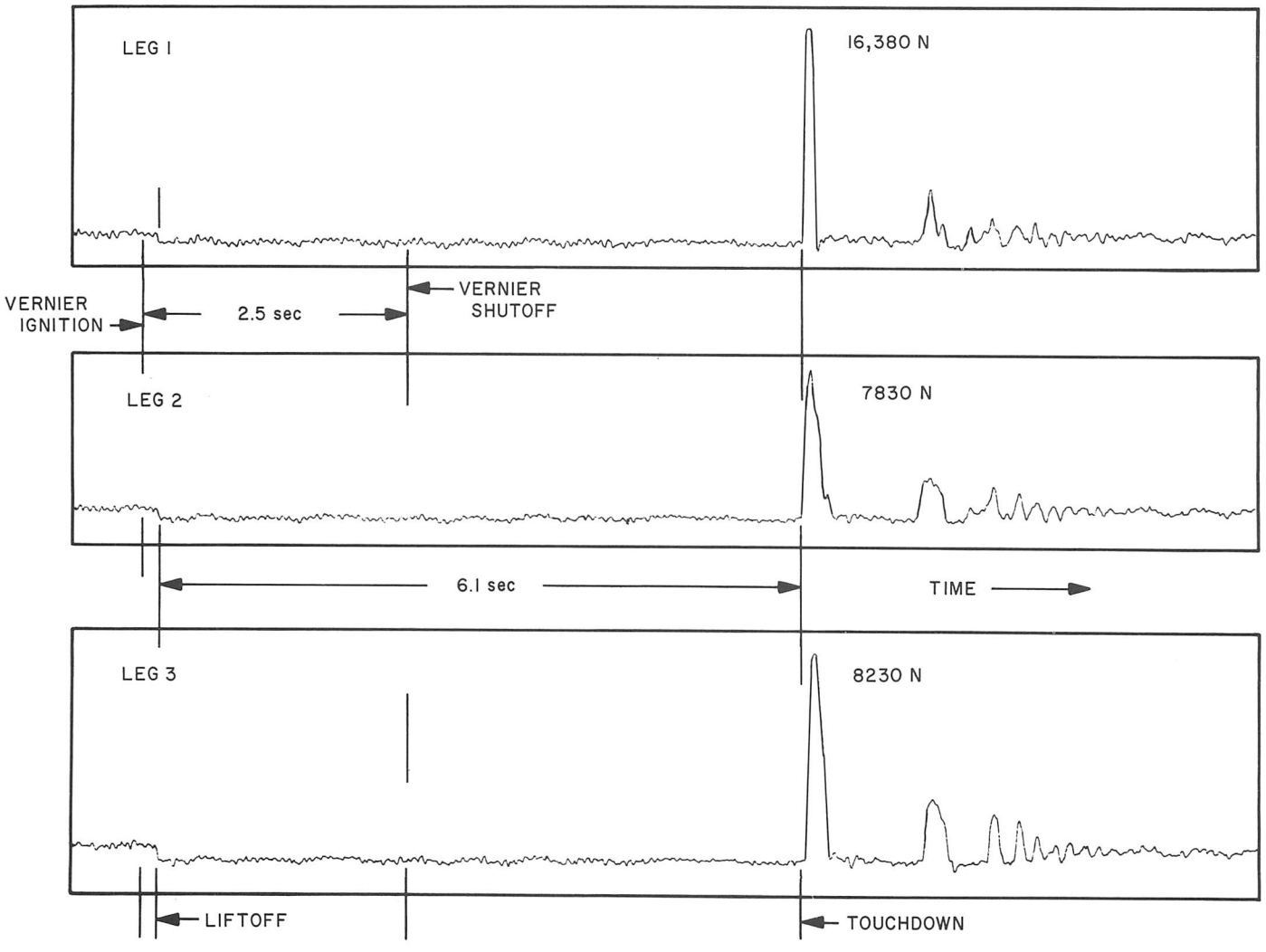

Fig. IV-4. Telemetry data showing shock-absorber axial load histories during hop.

Table IV-2. Maximum shock-absorber axial loads and times of initial ground contact (hop)

Leg	Maximum load, N	Time of impact after initial contact, sec[a]
1	14,900 ±700	0.018
2	7,800 ±400	0
3	8,600 ±400	0.042

[a]Initial contact was on Day 321 at 10:32:11.205 GMT.

force is required to obtain the shock-absorber force indicated. It is possible, therefore, that leg 1 may have encountered an obstruction that restricted its lateral motion. Figure IV-4 indicates that, following this first impact, the spacecraft rebounded and that final oscillations occurred which are similar to those observed during the initial landing.

Figure IV-5 is a post-hop mosaic showing the initial landing area. Figure IV-6 shows the spacecraft locations before and after the hop and indicates the various surface disturbances caused by the spacecraft.

2. Observations of Spacecraft/Soil Interactions

The hopping maneuver made it possible to obtain pictures of the first landing site from the position of the second site, in addition to the close-range pictures of spacecraft/soil interactions obtained at each landing site. Figure IV-6 shows that footpads 2 and 3 made two distinct overlapping imprints each during the first landing; these imprints are visible in the narrow-angle pictures (Figs. IV-7 and IV-8) taken from the second landing site.

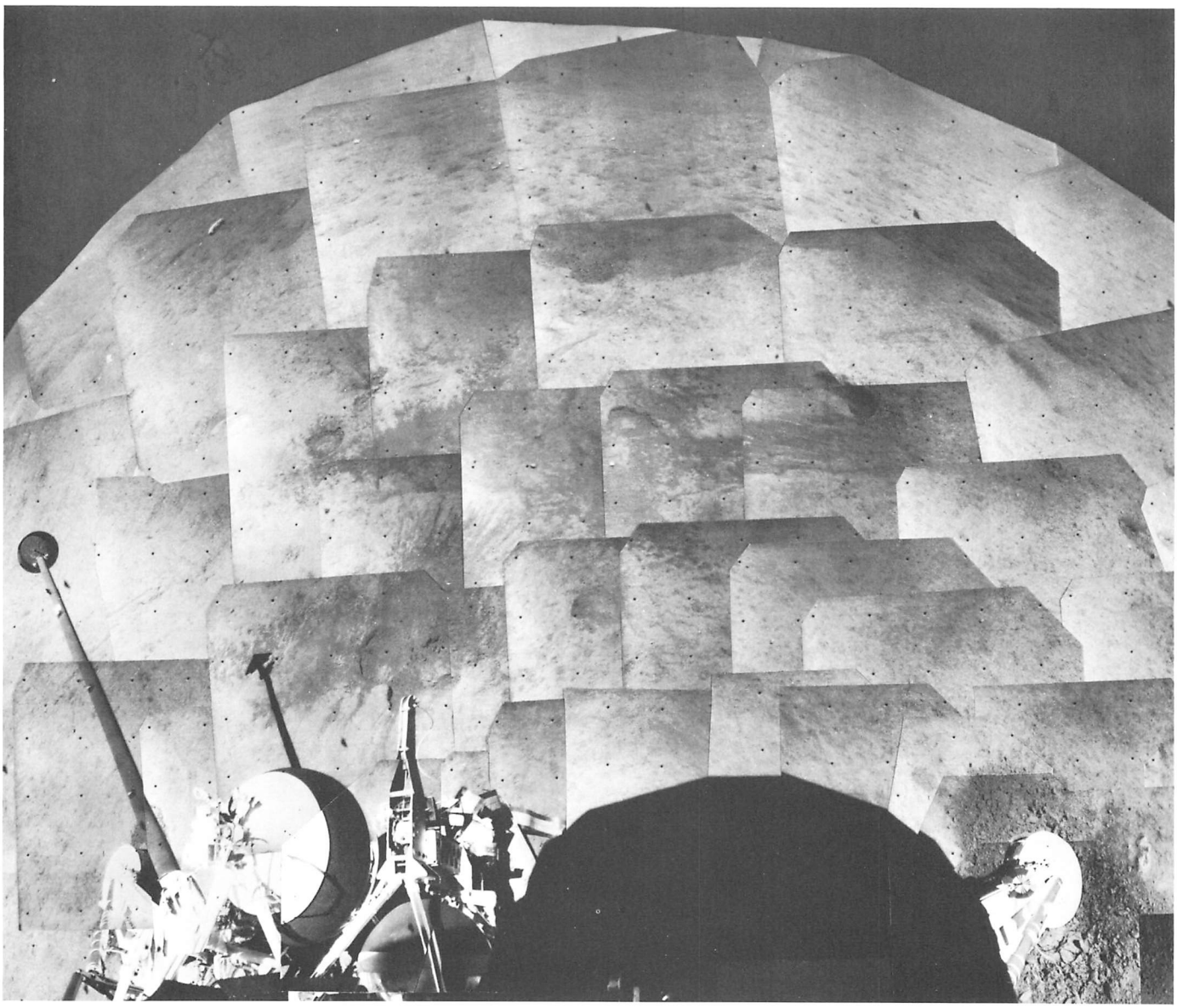

Fig. IV-5. Wide-angle mosaic showing the surface disturbances caused by the landings and the firing of the vernier engines during the hop. The original landing imprints of footpads 2 and 3 and the three crushable blocks are visible (Day 321, Catalog 6-SE-9).

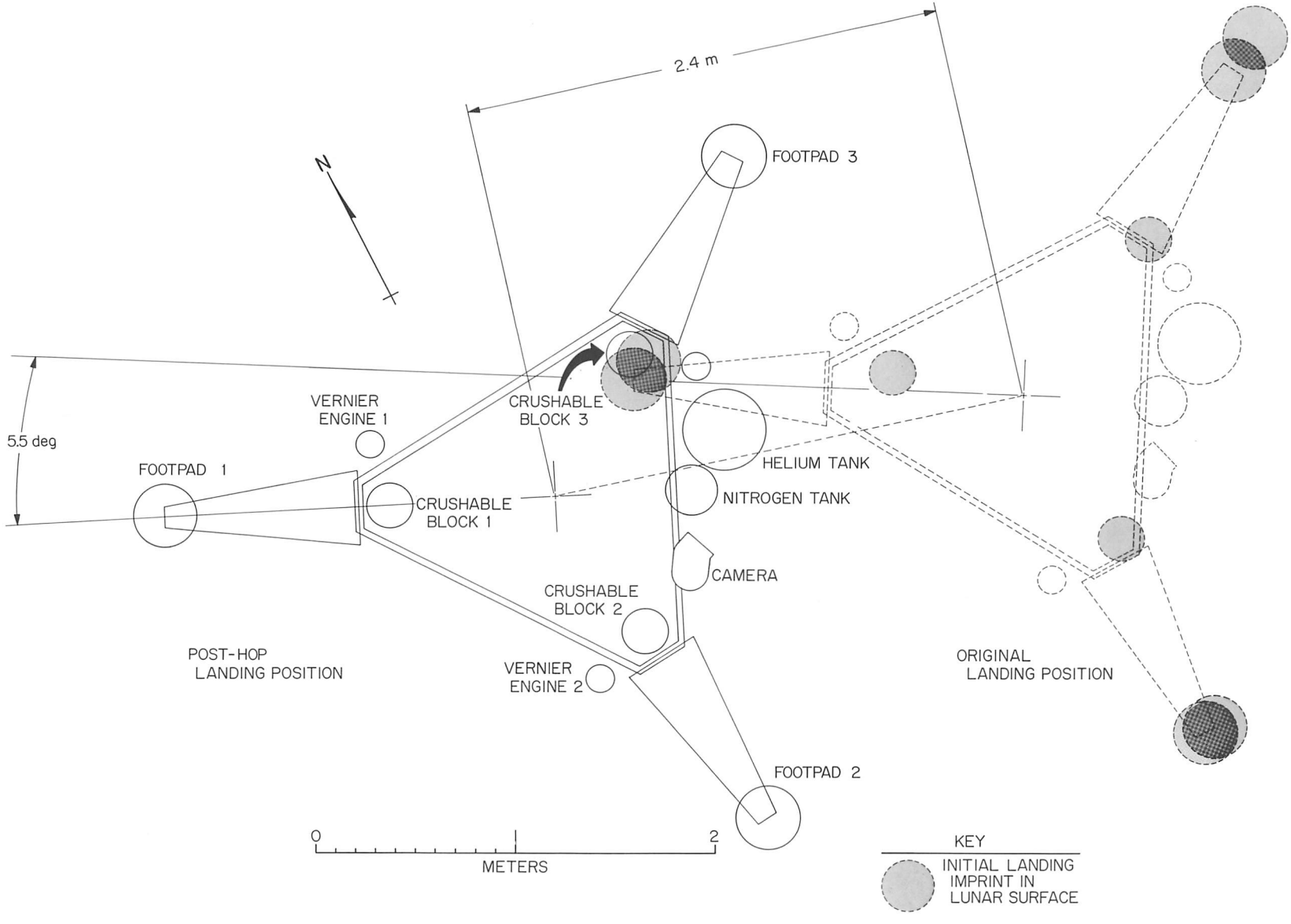

Fig. IV-6. Spacecraft location before and after hopping and the locations of the various surface disturbances shown in Fig. IV-5.

During the first landing, the second impact of foodpads 2 and 3 occurred in the flat-bottomed imprint formed during the initial impact. The mark made by the second impact in the disturbed soil does not have a raised rim, although some disturbance outside the mark is visible. This is an indication that the near-surface soil has been compressed under the footpad rather than laterally displaced by the footpad. Material ejected by the first impact covers the surrounding area to such an extent that the relative amounts of compression and displacement are difficult to estimate. In addition, it is possible that the contours of the initially disturbed areas were changed by the firing of the vernier engines. Part of this second imprint shows a waffle pattern (Fig. IV-7), indicating that the patterns of the conical surface of the footpad were reproduced on the lunar surface material through the thin aluminum sheet that covers the footpad.

Figures IV-9 and IV-10, taken before the hop, show the footpad 2 and 3 ejecta caused by the initial landing. The ejected material, which appears darker than the undisturbed surface, extends for approximately 50 cm from footpad 2 and 40 cm from footpad 3. Part of the imprint made by footpad 2 can be seen in the narrow-angle picture in Fig. IV-11 in which the surface material appears both compressed and displaced. There are no large clods or soil clumps, as have been observed in previous missions.

Figures IV-12 and IV-13 show the surface disturbances and ejecta around footpads 2 and 3 caused by the landing after the hop. The ejecta around footpad 2 extend about 90 cm; around footpad 3, about 30 cm. Part of the first impression made by footpad 2 can be seen in Fig. IV-14. The footpad appears to have made two adjacent imprints, finally coming to rest between them. These pictures also show that many large clods or soil clumps resulted from this landing. Figure IV-14a and b shows that parts of some of these clumps along the upper ridge have sufficient cohesion to overhang the underlying clumps in a cantilevered fashion.

Figure IV-15 shows crushable block 3 and the impression made by it during the first landing. These pictures were obtained before the hop at various sun angles. Depth of the impression is about 3 cm, and a mound of soil between 1 and 2 cm high can be seen in the center. The top edge of the imprint is fairly sharp; there is no apparent raised rim or surface disturbance that can be attributed to its formation. This would indicate, as in the case of the footpad imprints, that the material is inelastically compressible. Figure IV-16 is a calibration picture, taken before launch by the *Surveyor* television camera. The surface directly below crushable block 3 is indicated by the larger circle which has been positioned to simulate a 7.6-cm footpad penetration.

The imprint formed on the moon by the crushable block has the appearance of a natural depression; the floor does not have a smooth, compressed surface as do the bottoms of the footpad imprints. This could have been the result of lunar material that adhered to the block, was pressed between the block and its thermal shield, or was pressed into the core of the block, and was then shaken loose during rebound. There is no apparent change in albedo in the imprint such as observed around and in the footpad imprints. A discussion of the mound in the center of the imprint appears in Section IV-A-4-b.

3. Simulation of Landings and Hop

Computer simulation studies of landings, using several analytical soil models, are being performed to estimate the mechanical properties of a surface material that will yield penetrations and shock-absorber axial loads similar to those obtained during the *Surveyor VI* landings. In order to calculate the pressures exerted on the lunar surface by the engine exhaust plumes during the hop, the spacecraft flight control and propulsion characteristics have been mathematically modeled to obtain vernier engine thrust histories.

a. Initial landing. Using the compressible soil model described in Ref. IV-2, the best simulation of the strain-gage time history achieved to date for *Surveyor VI* has been for a 3.4-N/cm^2 static bearing strength soil (averaged for the entire depth of penetration). Figure IV-17 shows a comparison of these results with the flight data. The impact velocities used in the simulation are 3.4 m/sec vertical and 0 m/sec lateral, with the spacecraft tilted at a 3-deg angle relative to the surface. Leg 1 is oriented 12 deg clockwise from the line of greatest surface slope (viewed from above). The initial and final soil densities used in this homogeneous compressible soil model were 1.20 g/cm^3 and 1.6 g/cm^3, respectively. The penetrations of footpads 1, 2, and 3 obtained in this simulation are 6.6 cm, 6.9 cm, and 6.9 cm, respectively. Using this compressible soil model, the best analytical reproduction of strain-gage time histories for *Surveyors I* and *III* was obtained with these same values of strength and density (Refs. IV-3 and IV-1); lower values were used for *Surveyor V* to obtain the best agreement (Ref. IV-2).

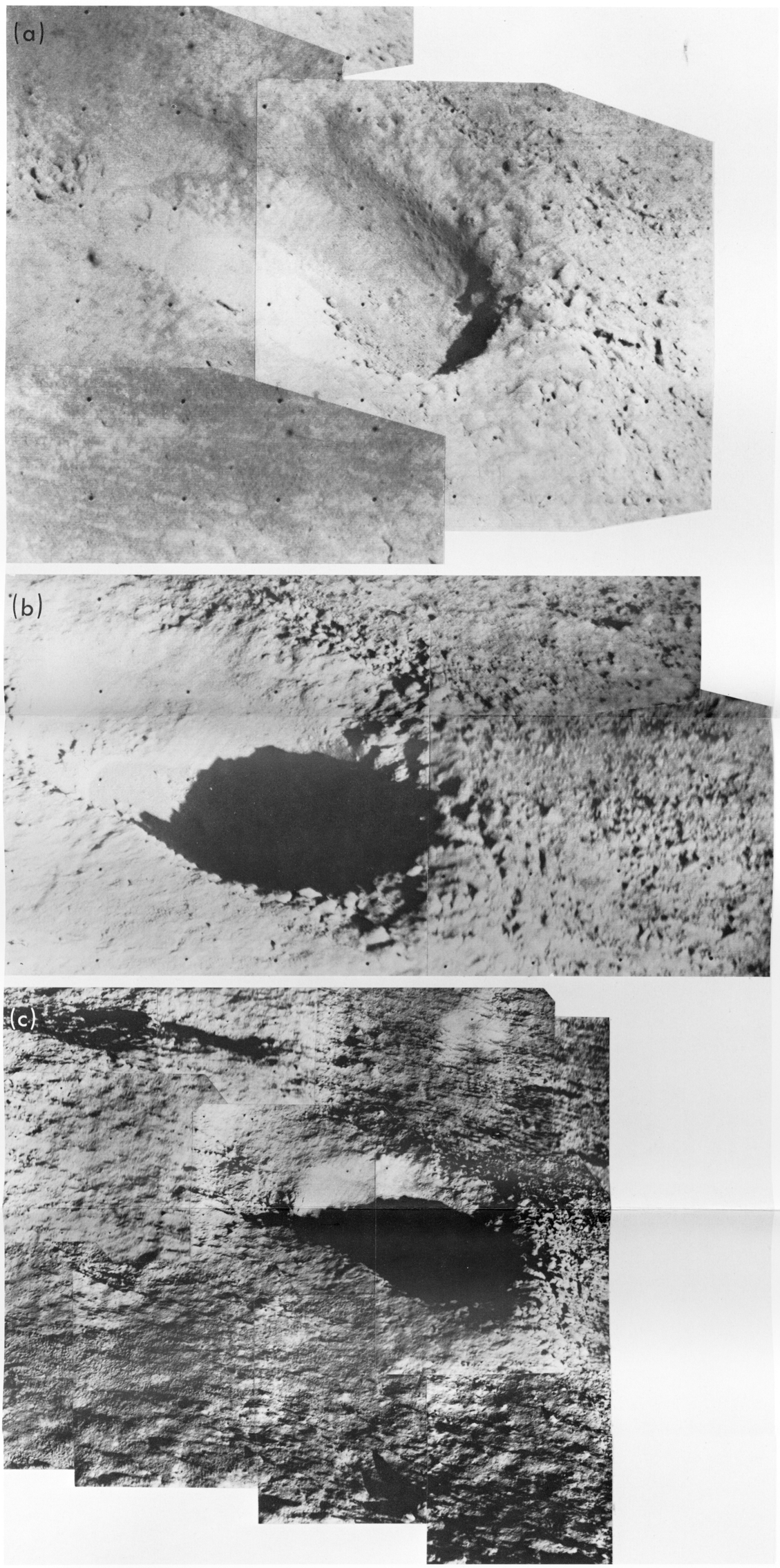

Fig. IV-7. Post-hop, narrow-angle mosaics of the double imprint caused by footpad 2 during the initial landing. (a) Sun elevation angle of 70 deg (Day 323, Catalog 6-SE-39). (b) Sun elevation angle of 28 deg (Day 326, Catalog 6-SE-40). (c) Sun elevation angle of 18 deg (Day 327, Catalog 6-SE-17).

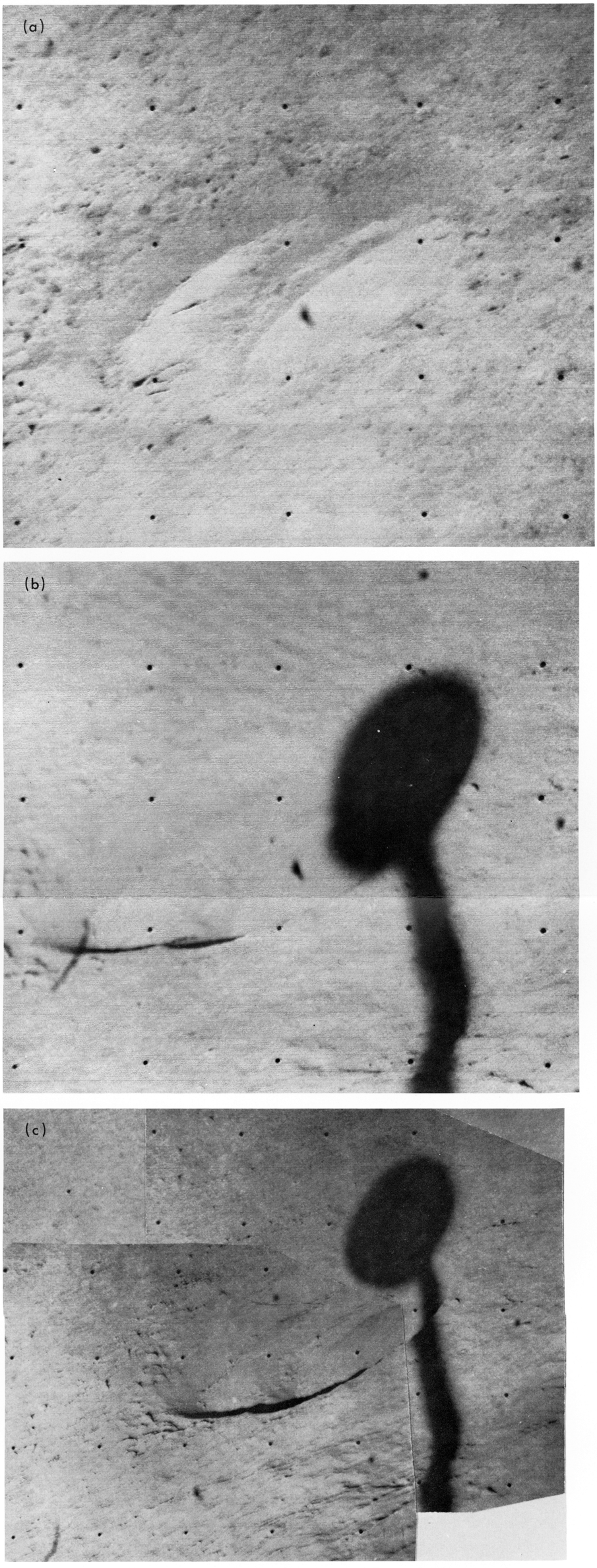

Fig. IV-8. Post-hop, narrow-angle mosaics of the double imprint caused by footpad 3 during the initial landing. (a) Sun elevation angle of 88 deg (Day 321, 11:49:38 GMT). (b) Sun elevation angle of 30 deg (Day 326, 10:39:55 GMT). (c) Sun elevation angle of 27 deg (Day 326, Catalog 6-SE-38).

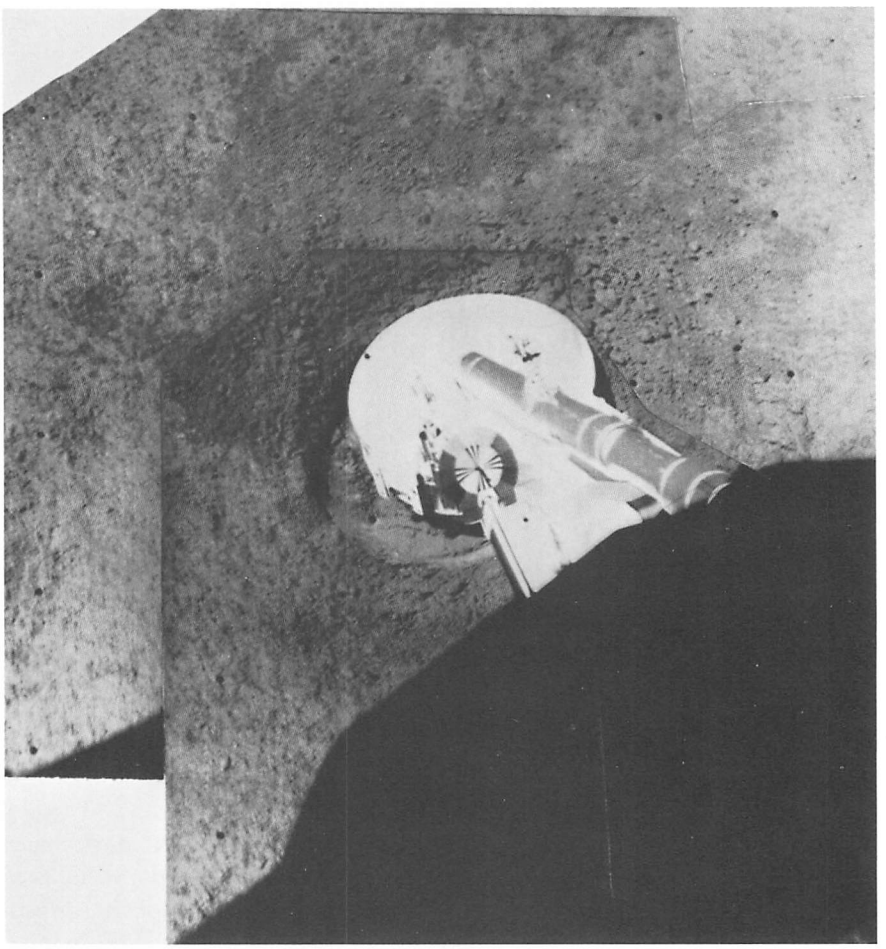

Fig. IV-9. Wide-angle mosaic showing the darker area of ejected material disturbed by the initial landing of footpad 2 (Day 319, Catalog 6-SE-25).

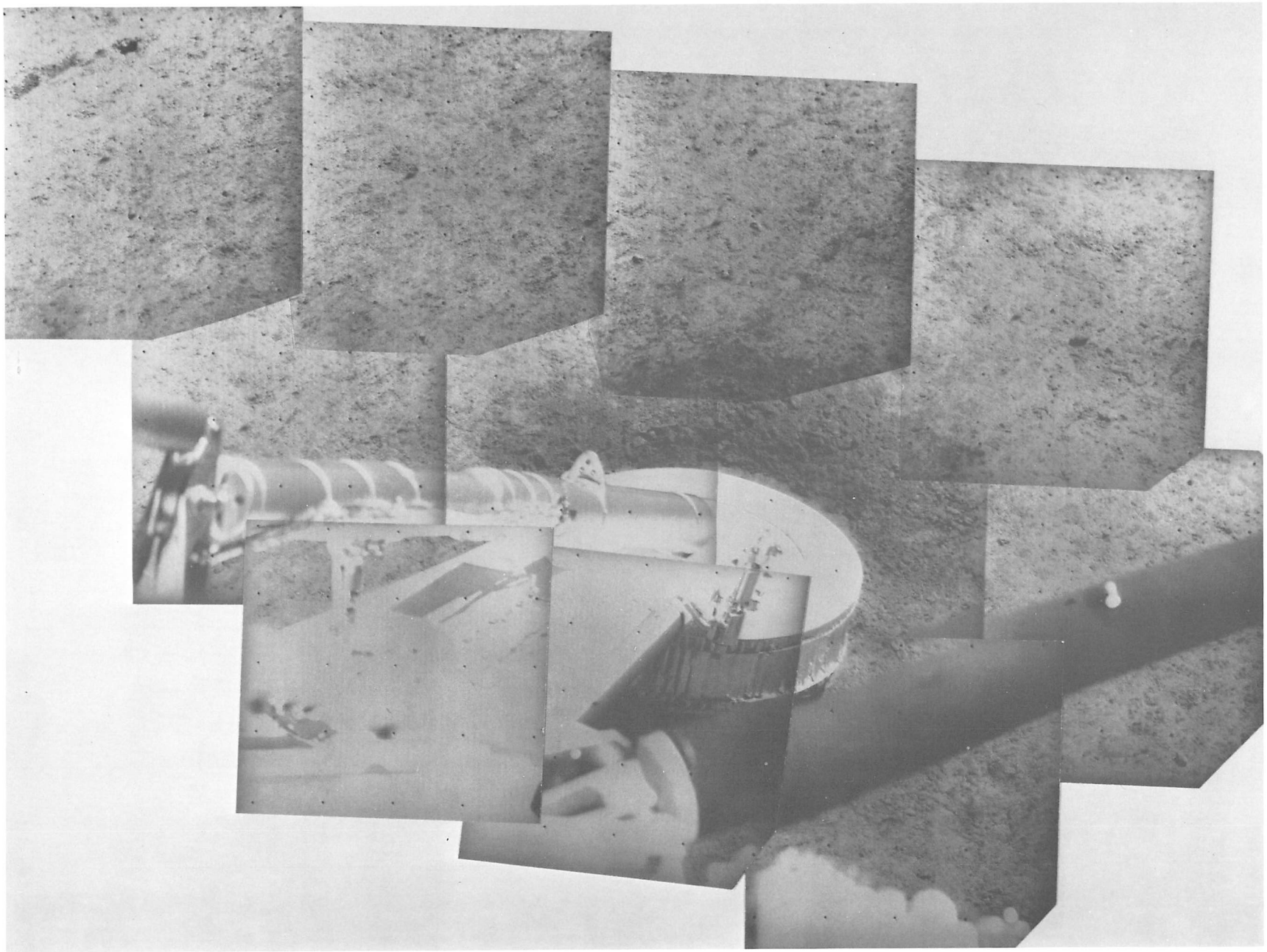

Fig. IV-10. Narrow-angle mosaic showing soil disturbance around footpad 3 after the initial landing (Day 319, Catalog 6-SE-19).

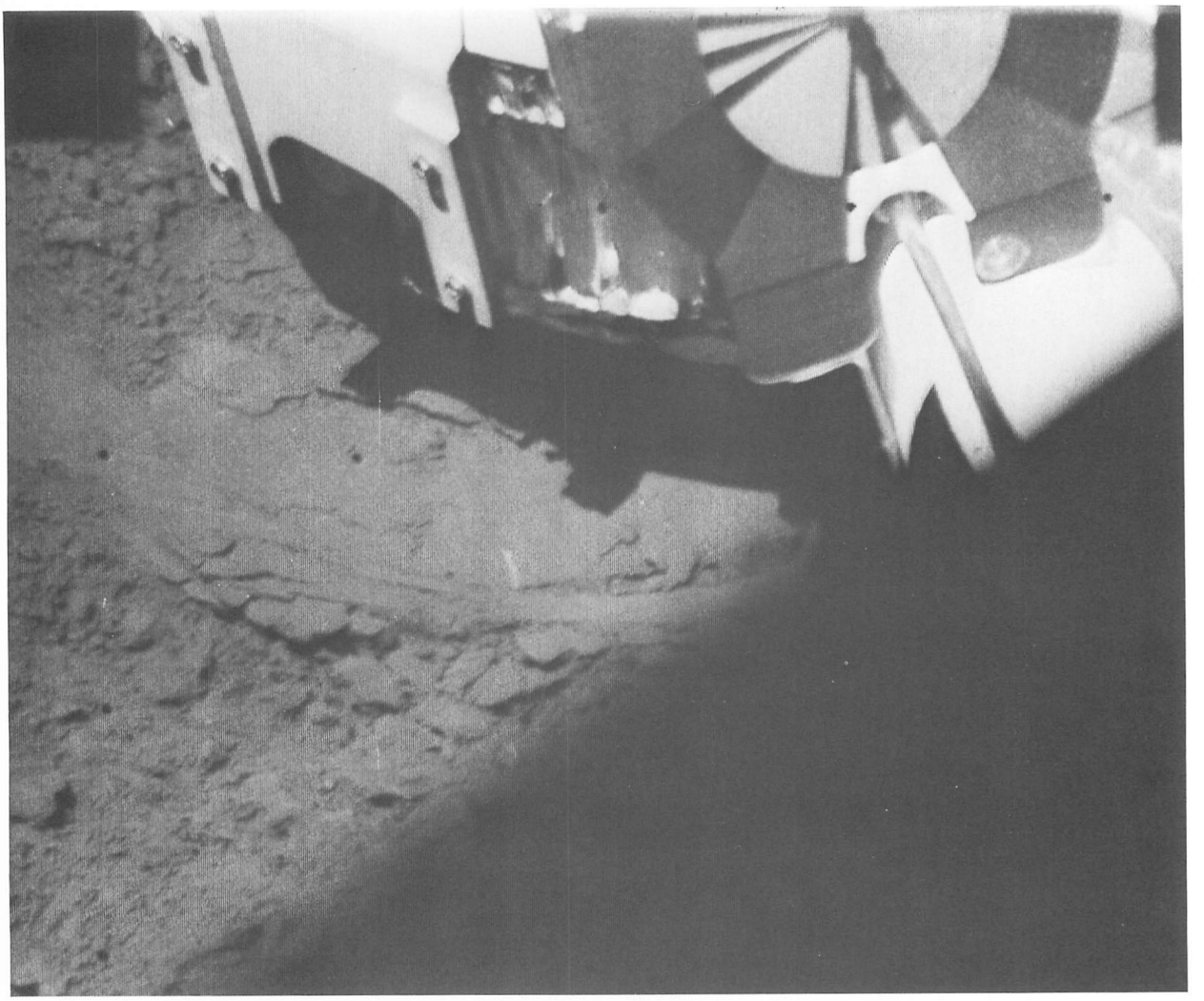

Fig. IV-11. Compressed lunar soil in the bottom of the footpad 2 imprint made during the initial landing (Day 320, 03:35:09 GMT).

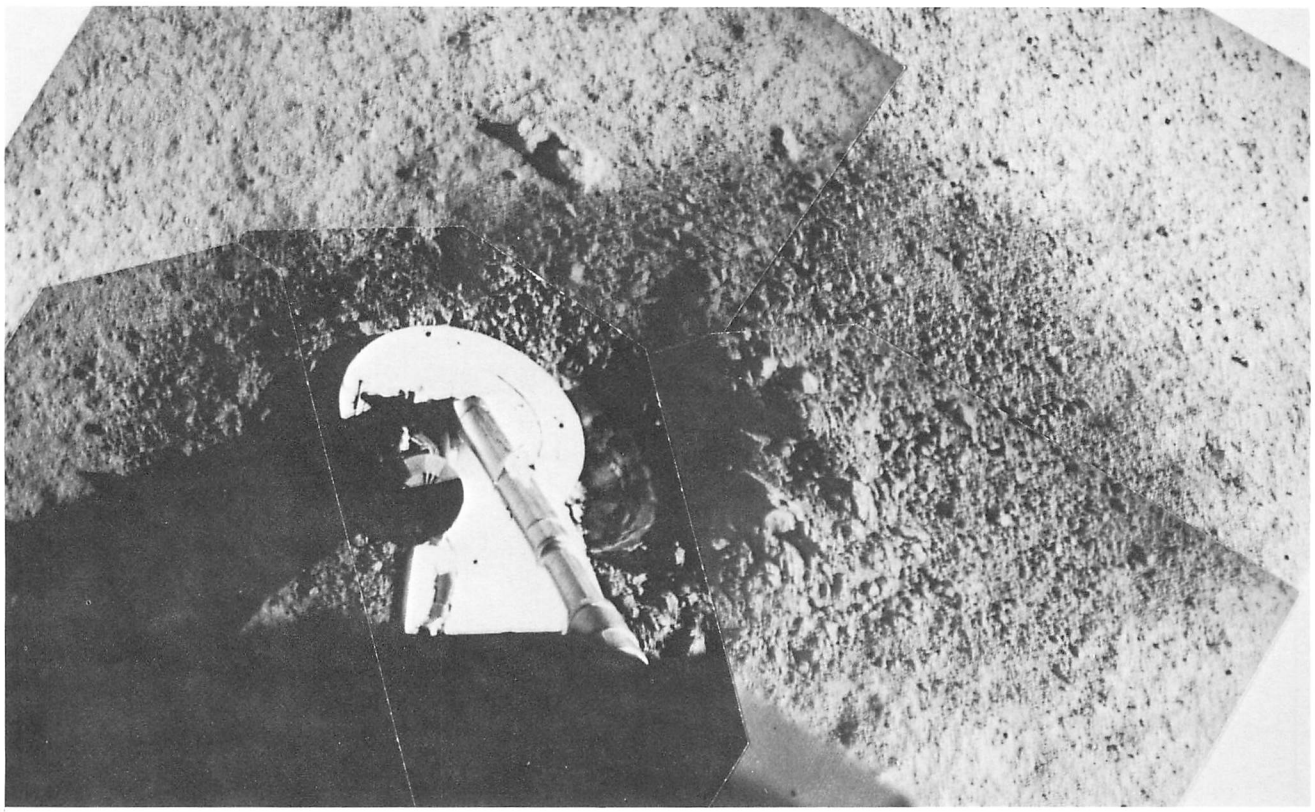

Fig. IV-12. Wide-angle, post-hop mosaic of footpad 2. The darker material was ejected by the footpad during the landing (Day 326, Catalog 6-SE-20).

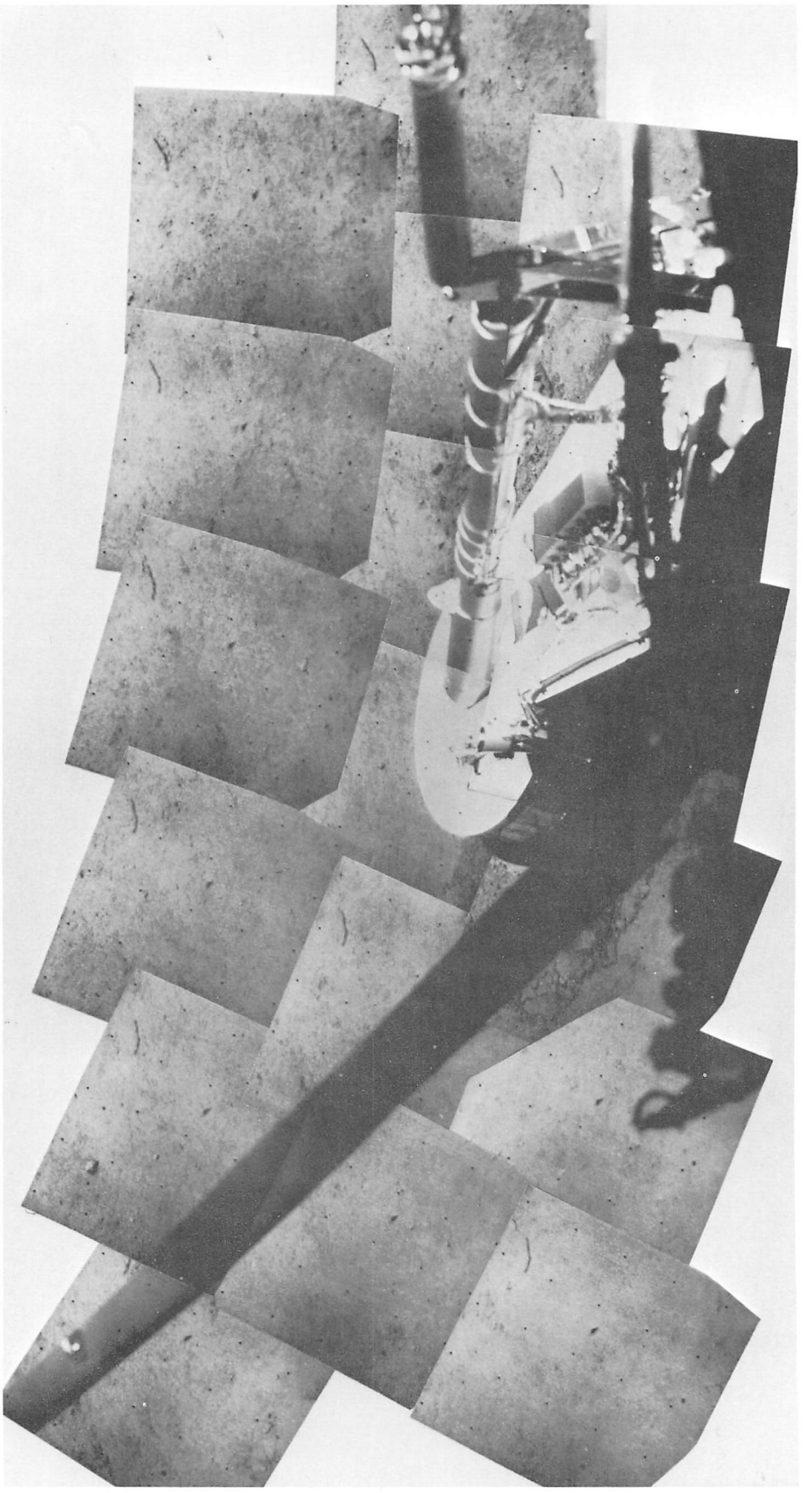

Fig. IV-13. Narrow-angle mosaic of footpad 3 and the material disturbed by the landing after the hop (Day 322, Catalog 6-SE-24).

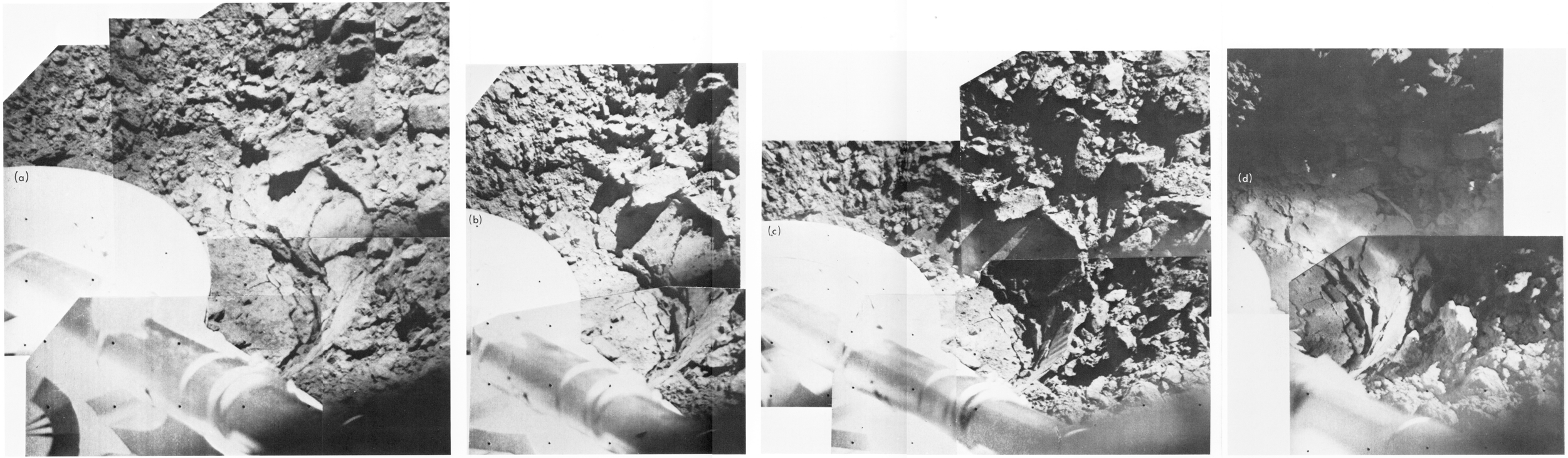

Fig. IV-14. Narrow-angle, post-hop pictures of the disturbed material around footpad 2. Note the large clump overhanging the imprint edge and the compressed soil in the imprint bottom. A honeycomb pattern imprint from the conical lower section of the footpad can be seen in the lower right area of b and c. (a) Day 321, Catalog 6-SE-41. (b) Day 323, Catalog 6-SE-37. (c) Day 324, Catalog 6-SE-42. (d) Day 326, Catalog 6-SE-35.

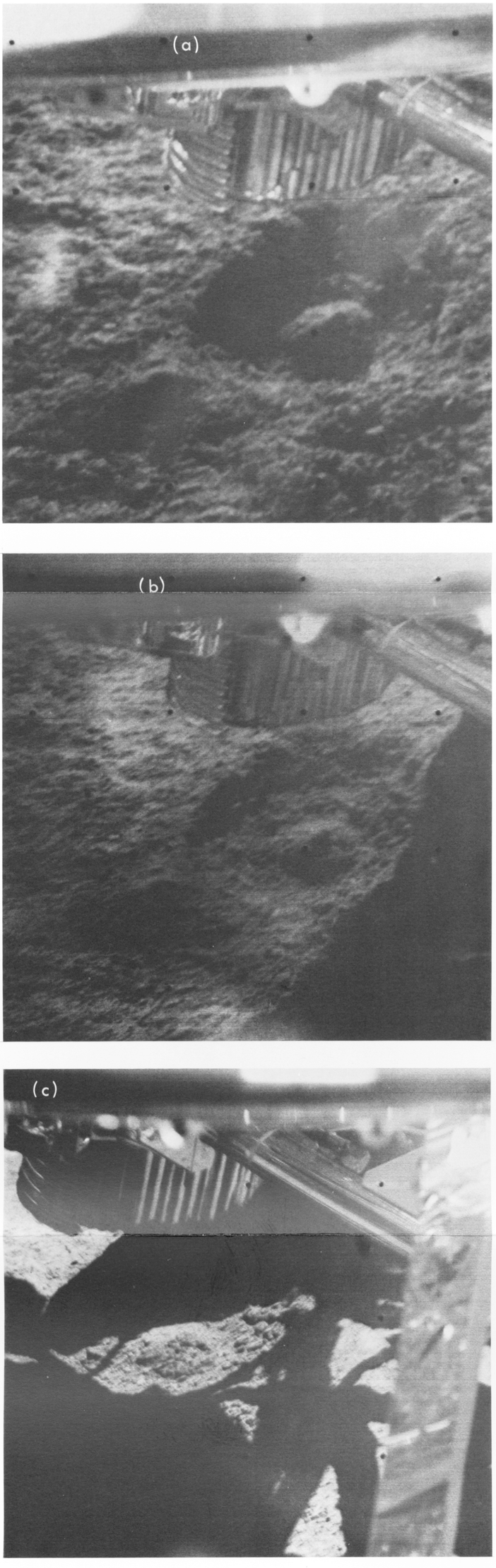

Fig. IV-15. Narrow-angle pictures of crushable block 3 and its impression on the lunar surface. Pictures were taken through the auxiliary mirrors at different sun elevation angles. (a) Sun elevation angle of 15 deg (Day 315, 01:28:20 GMT). (b) Sun elevation angle of 30 deg (Day 316, 07:08:08 GMT). (c) Sun elevation angle of 65 deg (Day 319, 03:57:13 GMT).

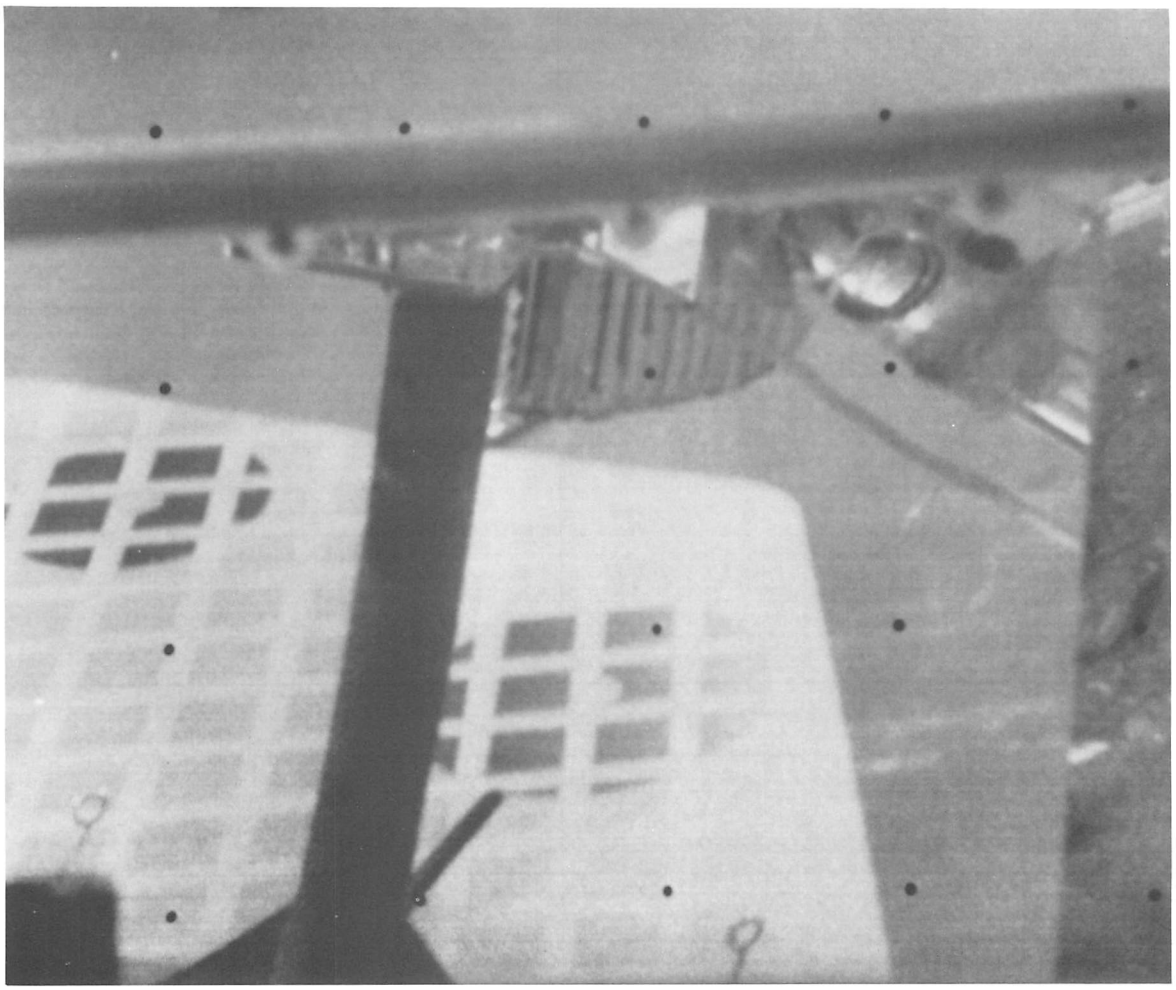

Fig. IV-16. Reference picture taken by the *Surveyor VI* television camera after final calibration and alignment before launch. Crushable block 3 can be seen near the top of the auxiliary mirror image. The large circle, indicating the area directly below the crushable block, has been positioned to simulate a 7.6-cm footpad penetration. (The black vertical post in the center of the picture is a support used during pre-launch checkout.)

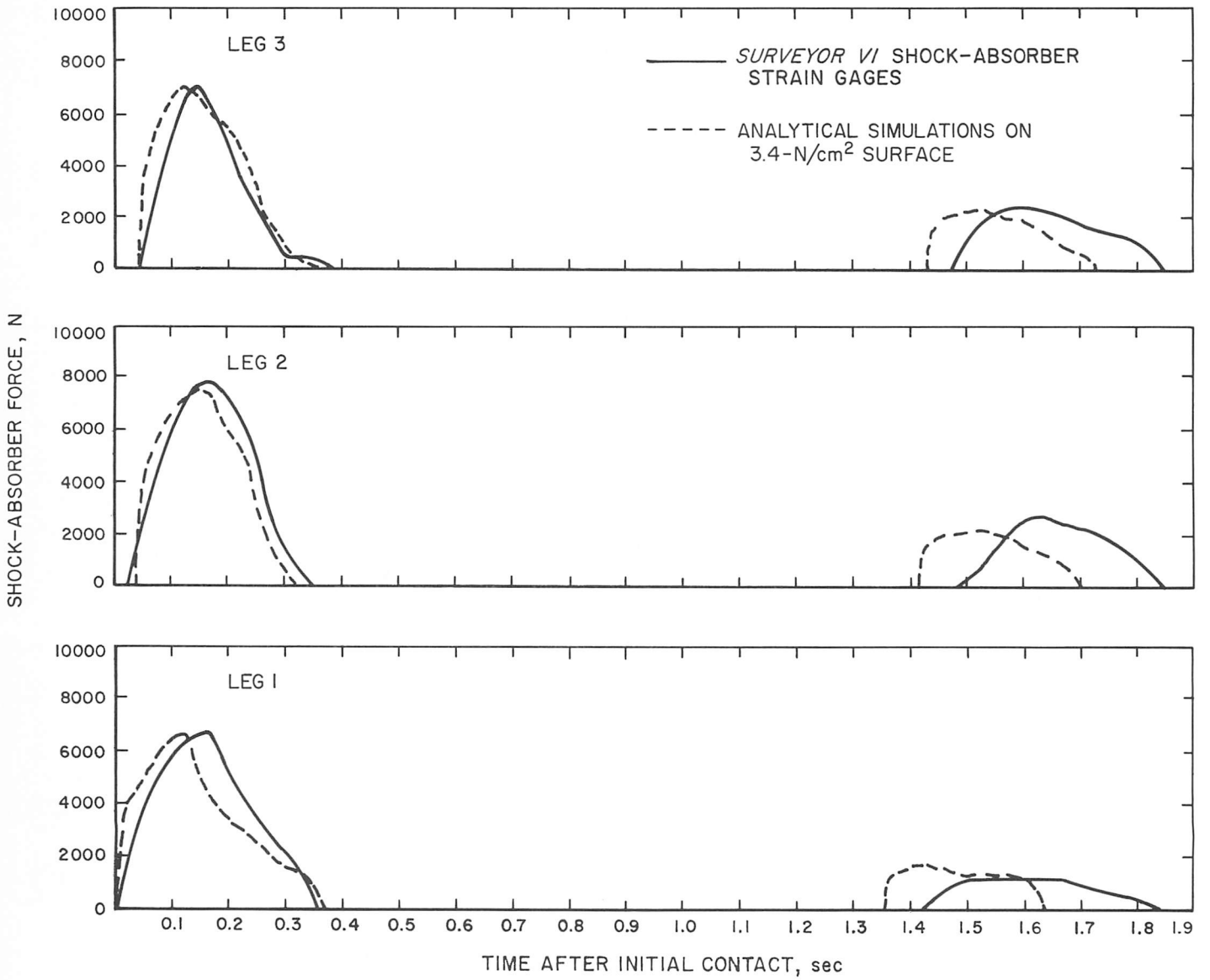

Fig. IV-17. Initial landing data and analytical shock-absorber force/time histories.

b. Hop and second landing. Computer simulations incorporating models of the spacecraft flight control system and propulsion system have been made in an effort to duplicate the hopping maneuver of *Surveyor VI*. Parameter variations during the first 2.0 sec of flight, for the simulation that is considered the best representation of actual conditions, are shown in Figs. IV-18 to IV-20. For this simulation, the hop distance achieved was 2.2 m with impact velocities of 3.7 m/sec vertical and 0.5 m/sec horizontal. Figures IV-18 and IV-19 show time histories of the spacecraft center-of-gravity vertical motion, pitch rotation, and yaw rotation. From these quantities, the variation of vernier engine nozzle height above the lunar surface was calculated. Figure IV-20 shows the time histories of vernier engine thrust levels. From these two figures, time histories of surface pressure levels have been calculated. The time histories shown in Figs. IV-18 to IV-20 show good correlation with flight data obtained from flight control gyroscopes and vernier engine strain gages. Because of uneven engine cutoff, the pitch motion was reversed after engine thrusting and a negative yaw motion was introduced, which resulted at touchdown in a +2-deg pitch and a −3.5-deg yaw position with respect to the pre-hop attitude of the spacecraft. Also, a negative roll motion was introduced, resulting in a relative roll angle of −4.3 deg.

To identify the lunar surface markings and to determine the pre- and post-hop positions from the pictures, a full-scale spacecraft model was used in the *Surveyor* Experiment Test Laboratory (SETL). The camera was set to the azimuth and elevation values at which lunar surface disturbances had been observed by the *Surveyor VI* television camera. The location of these disturbances within particular lunar pictures was then compared to disks located on the laboratory floor and photographed by the television camera on the model. Distances between critical points could then be measured directly. The spacecraft model was tilted to account for the difference in tilt of the *Surveyor VI* spacecraft before and after the hop.

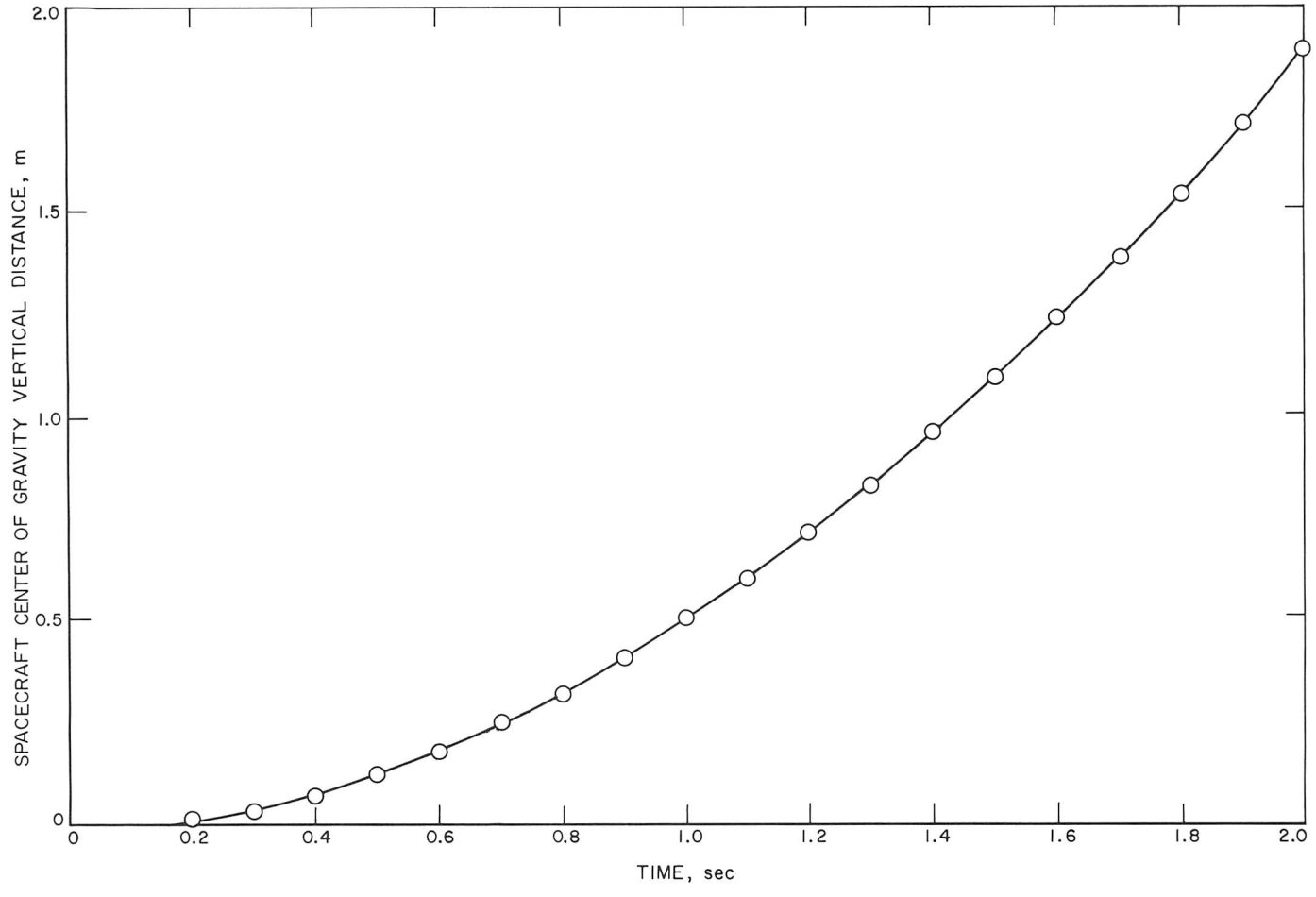

Fig. IV-18. Change of vertical height with time during the hop.

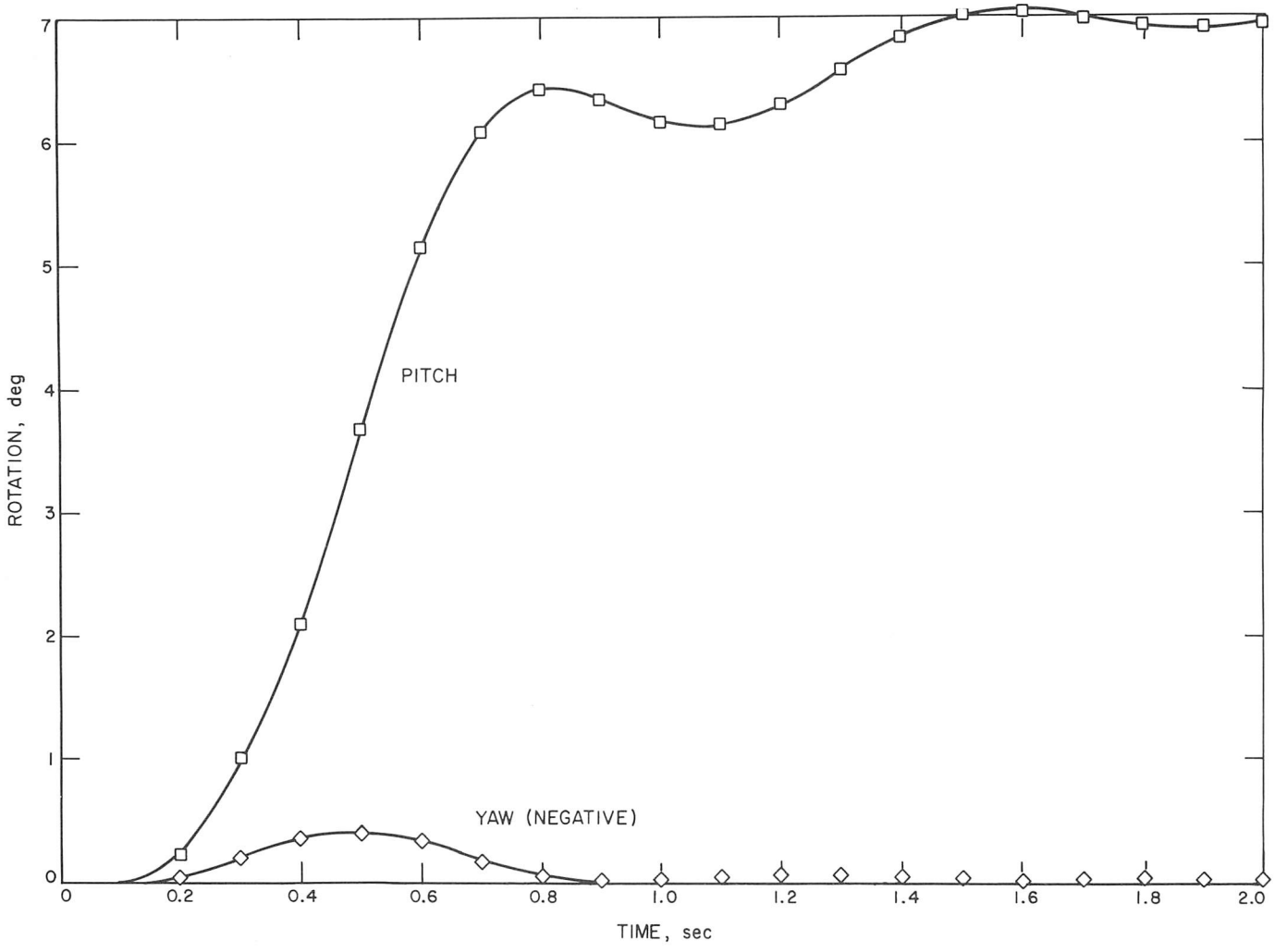

Fig. IV-19. Change of rotational position with time during the hop.

The combined tilt was 3 deg downward at an azimuth of 8.25 deg clockwise from the $+X$ axis. The tilt was simulated by raising footpad 3 by 13 cm. With the spacecraft model in this configuration, the footpad imprint locations checked satisfactorily. The other imprints seen in the *Surveyor VI* pictures were then located and appear to correlate well with the crushable block imprints made during the *Surveyor VI* initial touchdown. Figure IV-6 shows the results of these simulations, which indicate the following:

(1) The spacecraft was moved horizontally 2.4 m in a direction slightly north of west.

(2) As a result of the hop, the spacecraft rolled 5 deg in the negative direction (gyro telemetry indicated a −4.3-deg roll).

(3) Footpad 1 imprints from the initial landing are located under the present location of crushable block 3.

(4) Imprints in Fig. IV-5 correlate with the location of the crushable blocks at the time of initial touchdown.

(5) Two imprints appear in the pre-hop location of crushable block 1. Although it is possible that crushable block 1 impacted twice, one of the imprints may have been a natural depression.

c. Footpad penetrations. Two methods of analysis were used to determine the depth of footpad penetrations during the spacecraft landings. The first method consisted of imprint simulations made by reconstructing footpad disturbances in the SETL. A *Surveyor* footpad and

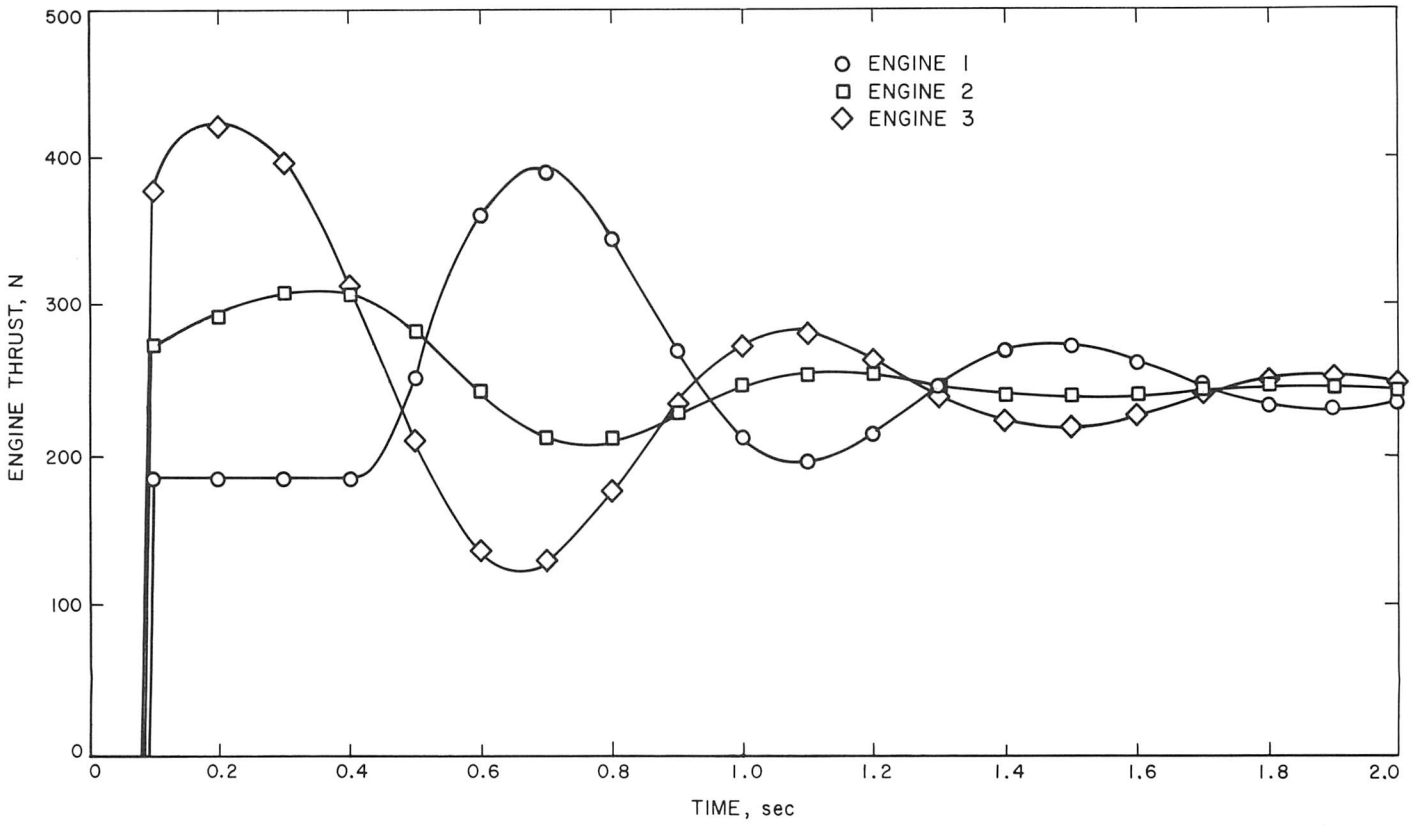

Fig. IV-20. Variation of vernier engine thrust with time during the hop.

crushed basalt soil material were used. The lighting angles were adjusted to match the sun's position during the lunar observations; a prototype television camera on the full-scale *Surveyor* model was used to view the results. The footpad position data from these tests were used to help construct the sketch in Fig. IV-6.

The second method used for penetration determination was an analysis of spacecraft shadows as described in Ref. IV-4. This approach estimates the location and height of the lunar material around the footpads relative to the footpad and makes use of a series of television pictures taken at different sun angles. By combining the results of both methods, the general features of a footpad impression can be reconstructed and the vertical dimensions of the imprint can be determined.

The position of footpad 2 after the initial landing is represented by Fig. IV-21. The footpad was tilted downward at an angle of approximately 10 deg, which produced a nonuniform penetration. The average depth of the bottom of the footpad relative to the nearby lunar surface is estimated to be 7 to 9 cm. The adjacent ridge of material rises to within 2 cm of the footpad top. The large, apparent penetration suggests that footpad 2 impacted in a small, natural depression. This is evident in pictures taken under low sun angle (Fig. IV-22). Thus, the actual penetration is believed to be less than 7 or 9 cm.

Figure IV-23 shows a profile of the position of footpad 2 after the hopping maneuver. The average penetration depth is estimated to be 5 to 7 cm. The ridge of ejected material rises 2 to 3 cm above the undisturbed surface. Here again, the footpad is tilted so that the penetration is not uniform.

Data for footpad 3 are limited; the average penetration for both landings is estimated to be from 2 to 3.5 cm. Footpad 1 cannot be seen by the television camera.

4. Interpretations of Lunar Soil Properties

As a result of the hop, the footpad penetrations during the first landing can be estimated within smaller limits than those of previous *Surveyors*. The lower portion of the footpad has the shape of a truncated cone with the dimensions shown in Fig. VI-2 of Ref. IV-3. Since, most probably, the maximum vertical load on the footpad is developed at the time of maximum penetration, it is

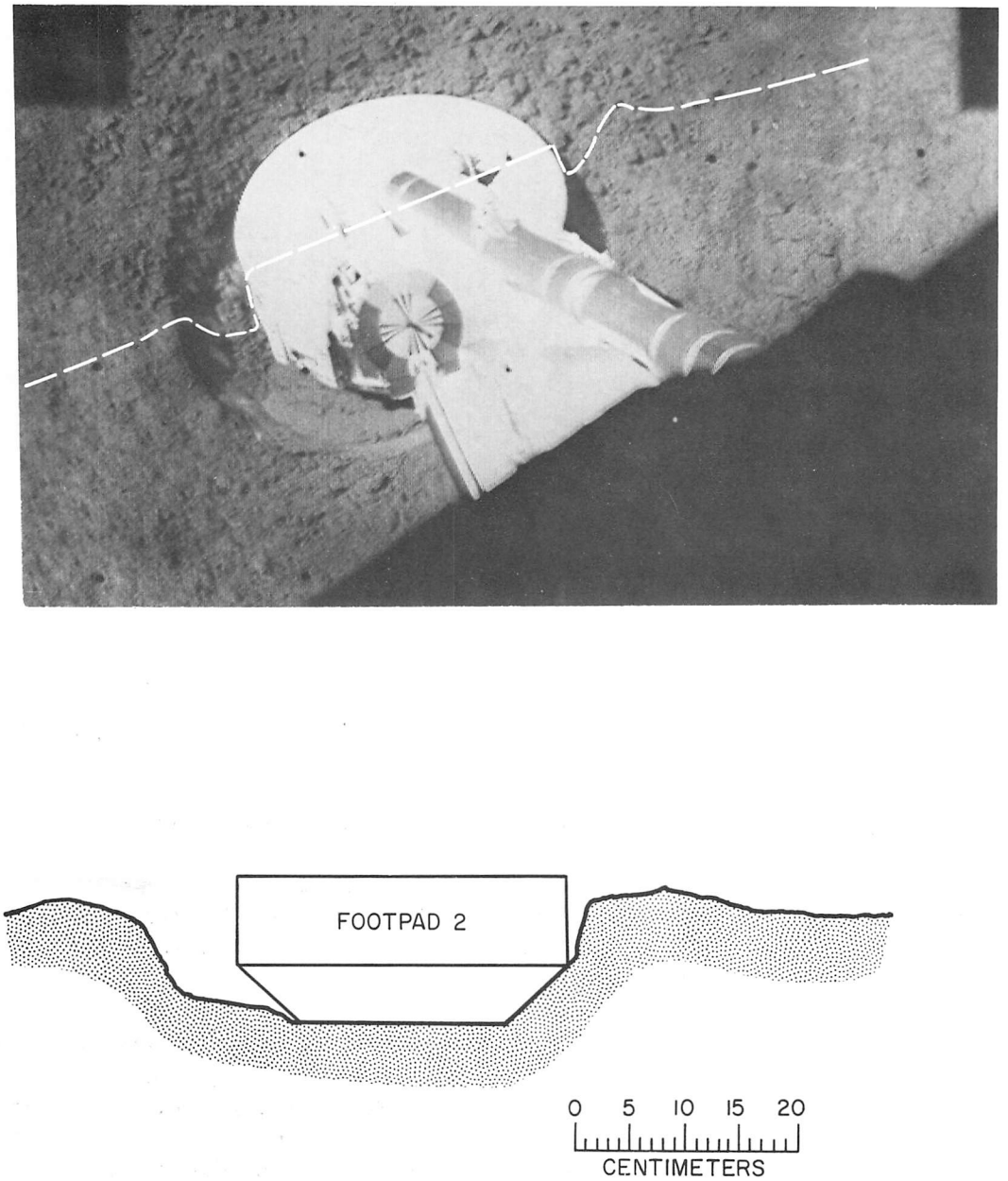

Fig. IV.-21. Penetration of footpad 2 during the initial landing. The profile was drawn parallel to the footpad hinge line, as shown by the dashed line.

possible to calculate the foodpad bearing area at the instant of maximum load with a higher degree of confidence than on the previous *Surveyor* missions. Computer simulations of the landing indicated that the maximum vertical load on footpad 3 was 2.7×10^8 dynes; therefore, the maximum dynamic bearing pressure on the footpad was 5.2×10^5 dynes/cm^2.

a. Variation of soil properties with depth. The bearing strength, density, and porosity of the upper few centimeters of the lunar surface appear to vary with depth. A landing simulation study performed for the *Surveyor I* landing (Ref. IV-5) used a soil representation that simulated a static bearing strength that linearly increased with depth, and a dynamic effect proportional to the square of the footpad penetration velocity. Simulated landings were performed on a variety of soils, with constant to increasing bearing strength profiles, and dynamic coefficients with bulk densities up to 1.5 g/cm^3. The *Surveyor I* landing could best be duplicated using a soil with a bearing strength below 1.4 N/cm on the surface, increasing to a value between 4.1 and 5.5 N/cm^2 at a depth of 5 cm.

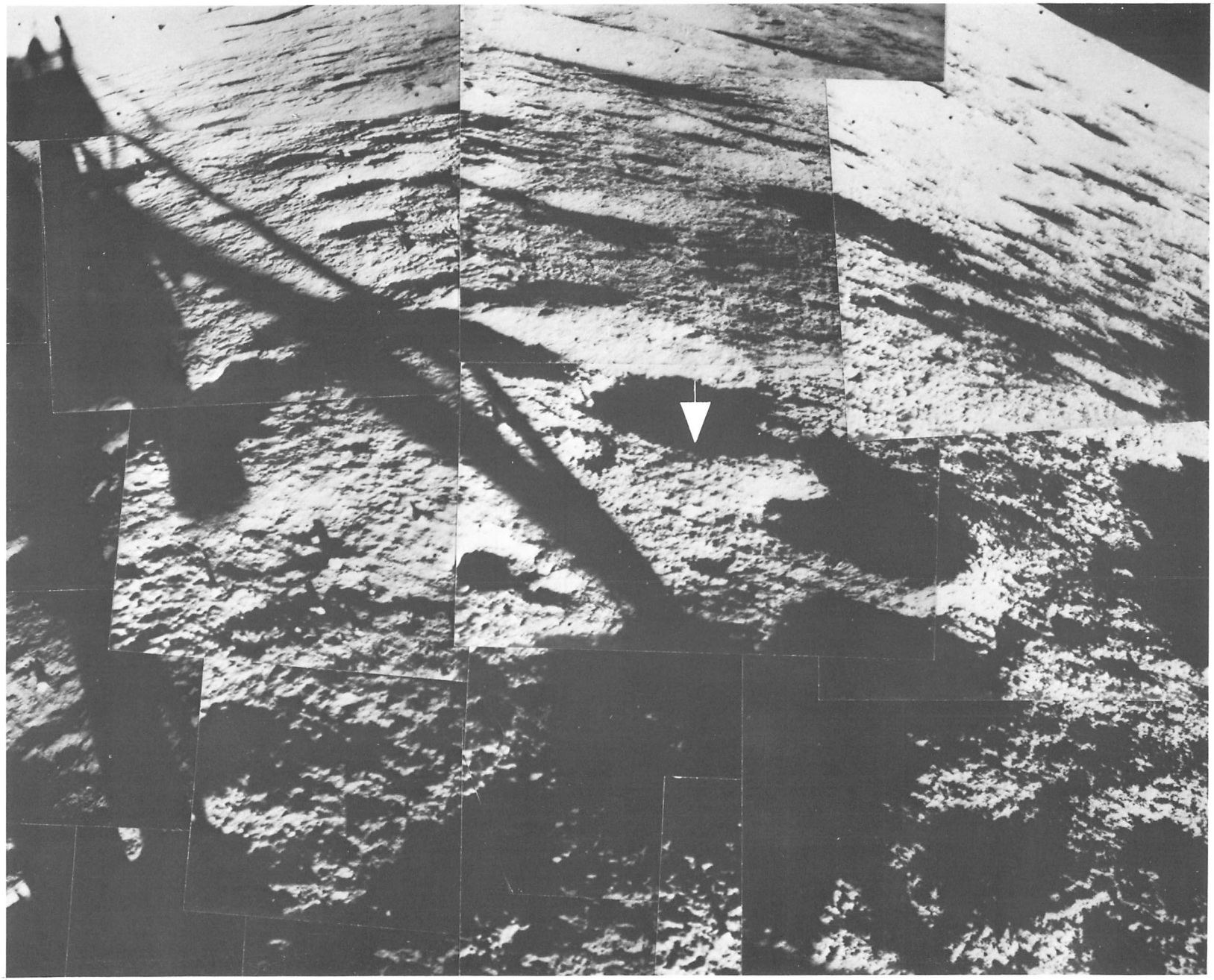

Fig. IV-22. Wide-angle mosaic of the initial landing imprints of footpad 2 (indicated by arrow) and surrounding area, at a sun elevation angle of 7 deg (Catalog 6-SE-11).

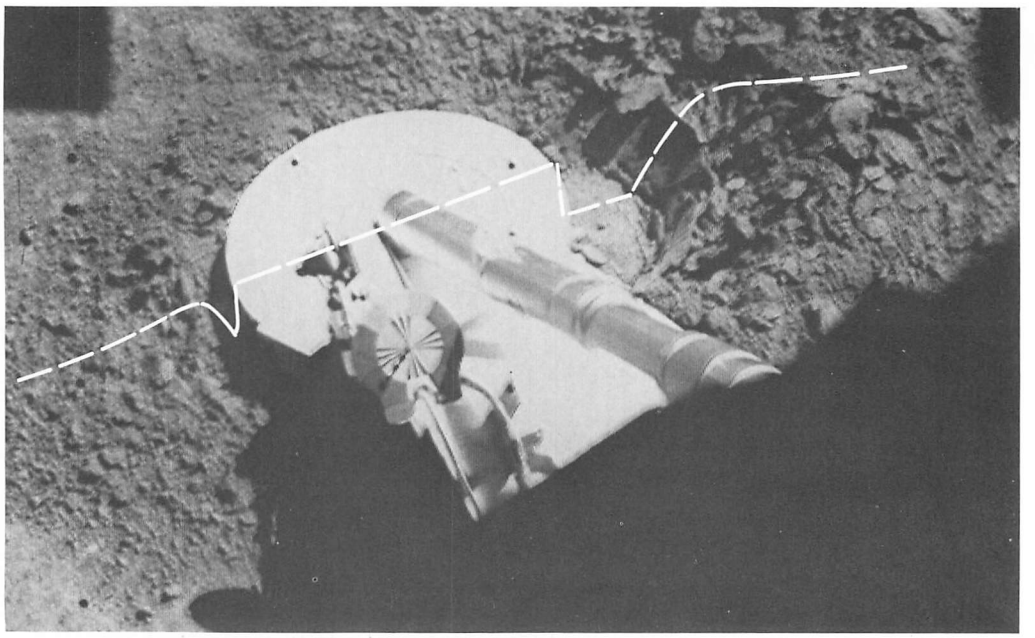

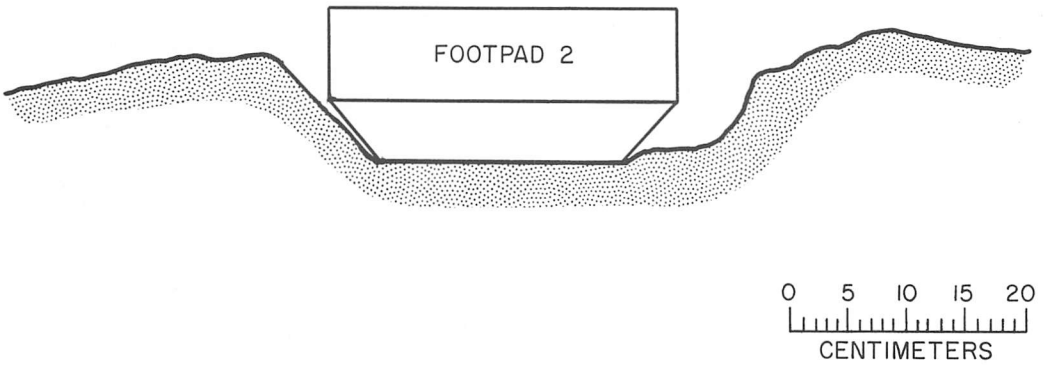

Fig. IV-23. Penetration of footpad 2 after the hop. The profile was drawn parallel to the footpad hinge line, as shown by the dashed line.

For *Surveyors I, III,* and *VI,* the most representative simulation at this time is for a bearing strength of approximately 3.4 N/cm^2 (averaged for the entire depth of footpad penetration). For the compressible soil model simulations, typically, the footpad penetrations have been less than the actual penetrations. It is conjectured that more accurate footpad penetrations would result from use of a soil model that varies with depth.

The *Surveyor III* soil mechanics surface sampler (SMSS) performed bearing and impact tests on undisturbed lunar material and on the bottom of a 5- to 7.5-cm-deep trench excavated by the SMSS (Ref. IV-6). The undisturbed material was penetrated 1.9 to 2.5 cm in the bearing tests and 6.3 cm in the impact tests. On the trench bottom, for corresponding tests and loadings, penetrations of 0.6 and 1.3 cm, respectively, were produced. This

indicates a substantial increase in bearing strength with depth even in material which was not compressed by a footpad impact. The SMSS did not detect "an extremely soft upper layer" in the vicinity of *Surveyor III*. However, a weak upper surface was indicated at the landing site of *Surveyor V* by tracks of fragments that rolled on an undisturbed surface. Here, the bearing strength of the upper few millimeters was estimated to be less than 0.1 N/cm^2 for a bearing area of 1 cm^2 (Ref. IV-7). A similar track was noticed at the *Surveyor VI* landing site (see Section II of this report). Later in this section, the variation with depth is used as an explanation of some observed soil erosion effects.

b. Cohesion, density, and porosity. Calculations presented in Ref. IV-3 for the *Surveyor I* landing, and in Ref. IV-1 for the *Surveyor III* landing, as well as similar calculations made for the *Surveyor VI* landing, assumed that the failure mode of the top layer of surface material (<0.5 cm) is primarily local shear. The following calculations, which were made to determine the upper bounds of cohesion and density of the top surface material, follow the same methods.

For a frictionless material that fails in local shear, the upper bound for cohesion is about one-fourth of the bearing strength. The resistance to penetration, P_i, of a soil that fails in local shear is given in Ref. IV-8 and by Chandeysson[3] as

$$P_i = \frac{\rho_2\rho_1}{\rho_2 - \rho_1}(\dot{h}^2 + h\ddot{h}) \qquad (1)$$

where

ρ_1 = density of undisturbed soil

ρ_2 = density of soil after local shear

h = depth of penetration

When $h = 0$ (initial surface contact), the velocity $\dot{h}$, at initial surface contact, is 336 cm/sec, and $\dot{h}^2$ is 1.1×10^5 cm^2/sec^2. At this instant, $P_i < 1.3 \times 10^5$ dynes/cm^2, the upper bound of cohesion for a frictionless soil that fails in local shear.

Therefore, from Eq. (1), for $h = 0$:

$$\frac{\rho_2\rho_1}{\rho_2 - \rho_1} < \frac{(5.2 \times 10^5)/4}{1.1 \times 10^5} = 1.2 \text{ g/cm}^3 \qquad (2)$$

[3]Unpublished work, 1966.

If $\rho_2 = 1.6$ g/cm^3, the value determined for the assumed soil model used in the computer simulations, is substituted in Eq. (2), then $\rho_1 < 0.7$ g/cm^3.

For a soil derived from basalt, as indicated by the Alpha-Scattering Experiment for the *Surveyor V* and *VI* landing sites, the average grain density would equal 3.0 g/cm^3. Thus, if it is assumed that the bulk density of the undisturbed soil ranges from 0.7 to 1.2 g/cm^3 at the top to < 1.6 g/cm^3 at a depth of a few centimeters, the porosity could range from 0.8 to 0.5, respectively (based upon assumed soil models).

c. Tests and analyses: crushable block imprints. Tests and analyses have been conducted to substantiate the assumption that the deformation of the surface beneath crushable block 3 was actually caused by impact of the crushable block. Analytical simulation of the initial landing indicated a 5.8-cm (assuming a planar surface) penetration by crushable block 3. The additional tests and analyses described are primarily intended to explain the small mound of soil in the bottom of the imprint and to present the implications relative to surface bearing strength.

The presence of the mound can be explained by the construction of the crushable block, which has an 8-cm-diameter vertical hole through the center (Fig. IV-24). The bottom of the entire block is covered by a thin sheet of corrugated aluminum (Figs. IV-25 and IV-26), which presumably ruptured when the crushable block impacted the lunar surface. The mound could have been stamped into the soil following fracture of the thin metal cover; or it could have been formed by soil that was forced into the hole, adhered to the inner walls of the block, and then was shaken out during the rebounding of the spacecraft. During the SMSS Experiment on *Surveyor III* (Ref. IV-8), the lunar surface material exhibited similar adhesive properties.

In one direction, the center portion of a bottom sheet provides little resistance to any pressure exerted on the sheet because the corrugations will easily deform, as shown in Fig. IV-24. However, in the perpendicular direction, the sheet is put into tension, and a much greater resistance is present.

A test was performed to determine the pressure required on the sheet to rupture the unsupported area. Pressure loads were applied evenly over the total unsupported area in increments of 0.35 N/cm^2 beginning at 0.35 N/cm^2. Small deformations in the sheet occurred

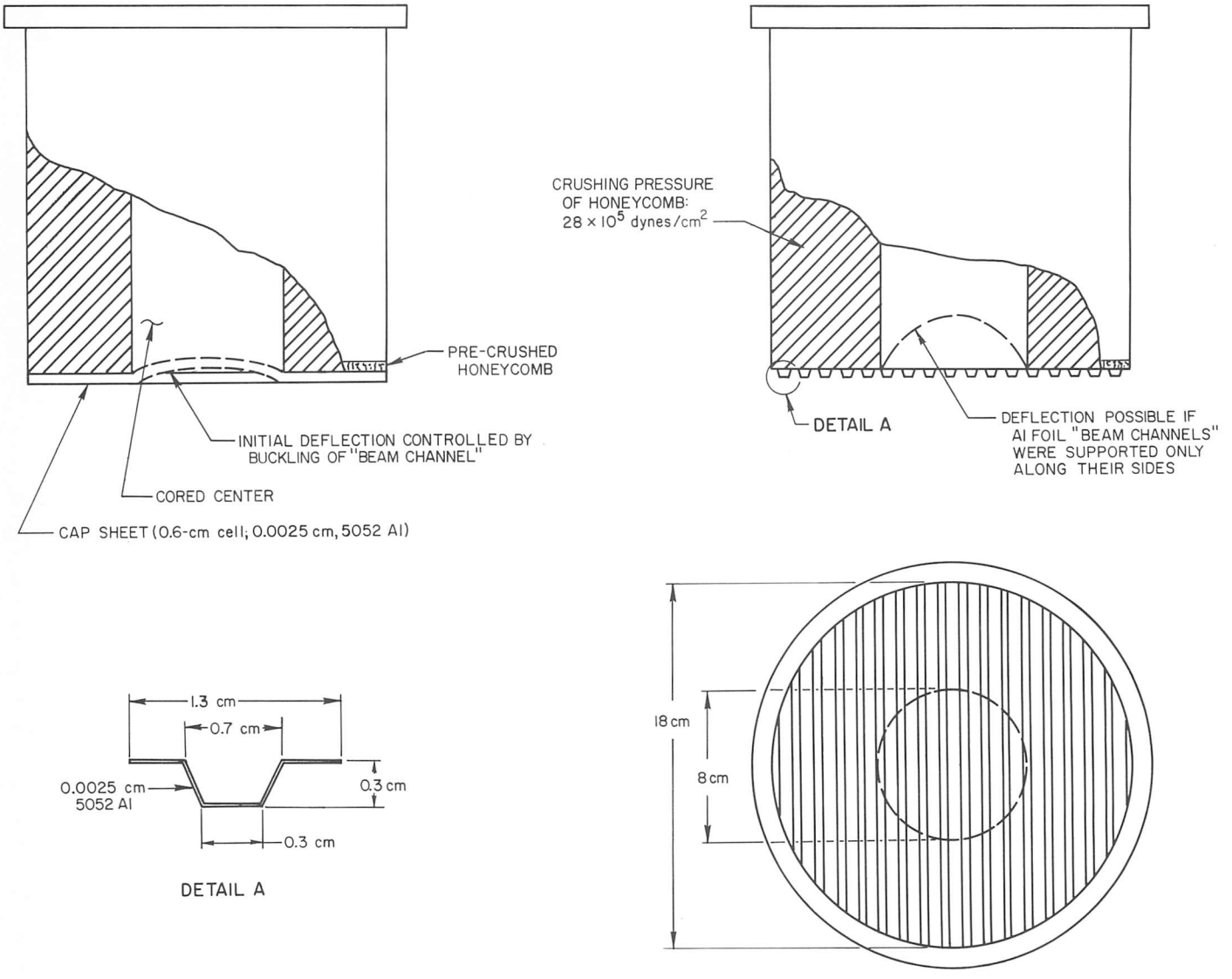

Fig. IV-24. Drawings and construction details of a *Surveyor* crushable block.

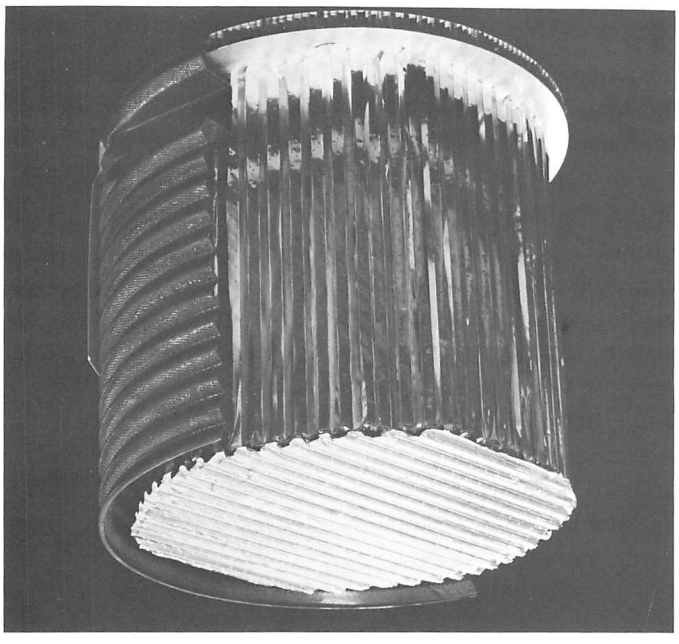

Fig. IV-25. A crushable block, with corrugated thermal shield.

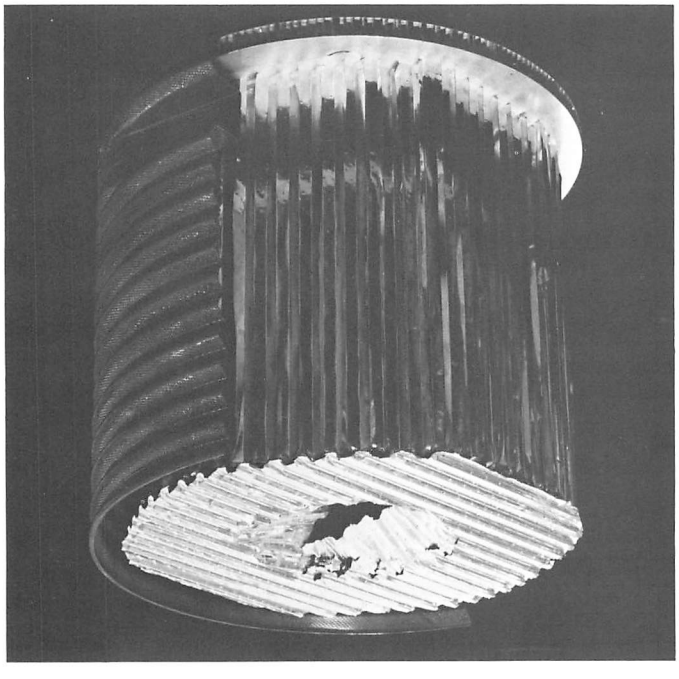

Fig. IV-26. The aluminum bottom sheet of the crushable block was stressed until it ruptured into the hollow center of the block.

during application of a 2.4-N/cm^2 load, and failure occurred at the 2.8-N/cm^2 level. Figures IV-25 and IV-26 show the crushable block before and after the bottom was fractured. From this test, it can be concluded that a surface dynamic bearing pressure greater than 2.4 N/cm^2 would be necessary to rupture the sheet and leave a residual soil mound, as observed in the imprint of Fig. IV-15.

A simplified analysis was performed to determine the rupture pressure. In the analysis, the bottom sheet was considered as a series of parallel beams, as shown in Fig. IV-25. The beams, spanning the cored-out center of the crushable block, have varying lengths up to a maximum of 8.1 cm. The beam assumption is justified even though the bottom sheet is extremely thin (0.0025 cm), since both tensile and compressive failures were apparent in the described tests. The beams are assumed to have fixed ends, because the sheet is bonded to the block. Using the associated beam formulas, $My = \sigma I$ and $M = 1/12\, pbl^2$, where

M = bending moment

I = second moment of area

σ = stress in filament

y = filament distance from neutral axis

p = applied pressure

b = beam width

l = beam length

the substitution of appropriate values yields $pl^2 = 147$ N. The relationships between p and l, which satisfy the equation, are:

l (cm)	2.5	5.0	7.5	8.1
p (N/cm^2)	23.5	5.9	2.6	2.2

Thus, a fracture would be expected when the applied pressure reaches 2.2 N/cm^2. Once the fracture is initiated, it would propagate so that fracture of chordwise elements, < 8.1 cm long, would occur at a pressure near that causing initial fracture.

Analytical and test results indicate that fracture of the sheet can be expected for applied pressures of approximately 2.4 N/cm^2. Landing dynamic simulations have shown that crushable block 3 impacted the surface at approximately 1.5 m/sec; at the moment of fracture, 2.4 N/cm^2 was the total pressure exerted on the lunar surface. In Figs. IV-17 and IV-18 of Ref. IV-2, a hypothetical soft surface model is described, and a relationship between dynamic pressure, static pressure, and

densities of undisturbed and compressed soils is presented. The dynamic and static pressures of this soil model are functions of the densities of the undisturbed and of the compressed soils. Therefore, for specific densities that are compatible with Ref. IV-2, a resulting total pressure can be calculated. For lunar soil initial and compressed densities of 0.9 g/cm^3 and 1.4 g/cm^3, respectively, the total pressure exerted on the crushable block would be approximately 2.4 N/cm^2. The static bearing pressure, or strength portion of the relationship, would be approximately 1.8 N/cm^2. This static bearing strength determination is for a lunar surface penetration of 1 to 2 cm; i.e., the depth, below the adjacent surface, of the center mound in the imprint formed by crushable block 3.

Additional evidence that the crater below crushable block 3 was formed by the block is the correlation of dimensions of the crater to the block and to the thermal shield, which partly encircles it. Figure IV-27 shows the center of the small cone in the crater, aligned with the center of the hole in the crushable block. Dimensions of the crater and cone were measured from narrow-angle *Surveyor VI* pictures using, as a reference scale, pictures taken before launch, but after final alignment of the television camera (Fig. IV-16). As shown in Fig. IV-27, the depth of the imprint is 3 cm.

d. Elastic properties of the lunar soil. Oscillations can be seen on the strain-gage records (Figs. IV-1 and IV-4) following the final impact of both the initial landing and the hop. Similar oscillations were observed in previous landings (Refs. IV-1 to IV-3); however, they can be read more clearly in the *Surveyor VI* records. The frequency of the oscillations can be related to the combined elastic properties of the spacecraft and the lunar soil; estimates of the elastic properties of the lunar soil can be made provided that the constants for the spacecraft are known. In addition, the rate of decay of the oscillations provides data for an estimate of the dissipative (anelastic) properties of the soil. At present, the appropriate elastic constants (for small oscillations) of the spacecraft are not accurately known, nor are the dissipative constants. Tests are planned to determine the desired constants by using a duplicate spacecraft.

For a single mass-spring system with viscous (velocity) damping, the free oscillations are of the form [$f(t)$ = deflection]

$$f(t) = C\, e^{-\gamma\omega_0 t} \sin\left[\omega_0^2\,(1-\gamma^2)\right]^{1/2} t \qquad (3)$$

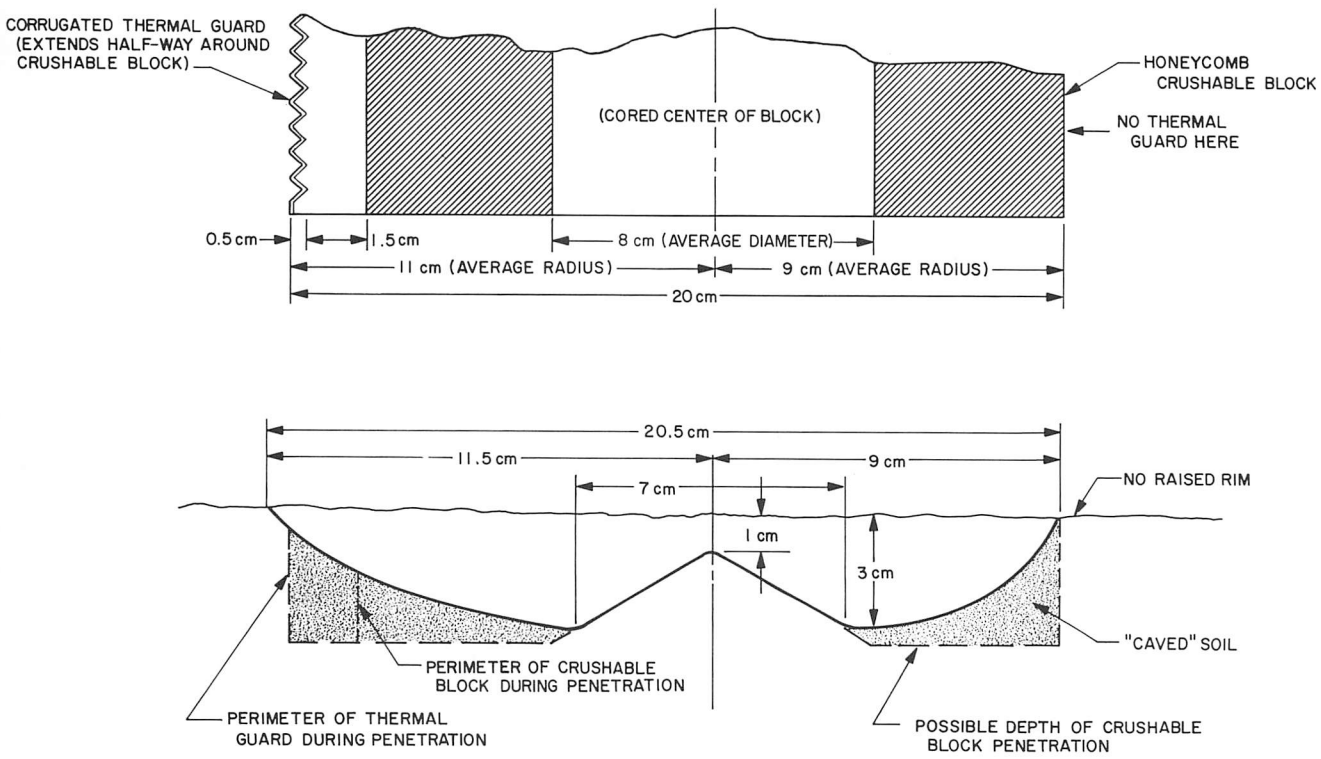

Fig. IV-27. Section through the 20-cm-diameter crater visible through the large auxiliary mirror in pre-hop pictures. The center of the cone in the crater is aligned with the center of the crushable block to show size correlations.

where γ is the fraction of critical damping and ω_0 is the undamped, angular resonant frequency.

The quality factor, Q, of a resonant system is $Q = 1/(2\gamma)$. For large Q, i.e., small γ, the damped frequency is approximately equal to ω_0. As an example, if $Q = 2.5$, then $\gamma = 0.2$, and the damped frequency is 0.98 ω_0. For a spacecraft on the lunar surface, ω_0 and γ depend upon the stiffness and damping of the lunar surface material as well as those of the spacecraft.

The observed oscillations in each of the legs, as in *Surveyors I* and *III*, were of the same frequency and in phase, indicating a vertical mode of vibration. During the oscillations, the maximum force developed in each leg was about 620 N, which is equivalent to about 1-mm displacement of the spacecraft center of gravity. For such a small motion, linear approximations for the spacecraft motion appear justified. However, there is some dispersion in the oscillations, with the frequency increasing slightly with decreasing amplitude. The reason for this dispersion, which is neglected in the present analysis, is not known. It may be caused by nonlinearities in the system.

For the initial landing, the average frequency of the observed oscillations is 6.3 Hz and Q is about 9; for the post-hop landing, the frequency is 6.9 Hz and Q about 12. An approximate analysis indicates a frequency of 8.0 Hz $\pm 10\%$ for the oscillation of a spacecraft sitting on a rigid surface. Provided that the constants of the spacecraft were essentially the same in both cases, this observation indicates that the lunar surface material, as loaded by the footpads, had greater stiffness and contributed less damping at the second landing location than at the first landing location. For *Surveyors I* and *III*, the observed frequency was about 6.5 Hz; and an estimate of Q has not yet been obtained.

In the absence of damping, the effective stiffness of the lunar surface material under one footpad is approximately

$$K_m = \frac{4\pi^2 M f_s^2 f_m^2}{f_s^2 - f_m^2} \tag{4}$$

where M is one-third of the spacecraft mass; f_s is the resonant frequency for the spacecraft on a rigid surface, and f_m is the observed frequency.

The rigidity modulus, μ, for the lunar material can be estimated using the relation (Ref. IV-9)

$$\mu = \frac{2K_m(1 - \nu)}{\pi^2 r} \tag{5}$$

where r is the radius of the loaded area and ν is Poisson's ratio. Since ν lies between 0 and 0.5 for all common materials, this relationship provides an estimate of μ. Then, the shear wave velocity of the lunar soil, V_s, can be estimated for a given value of μ and various assumed values of bulk density, ρ, since $V_s = (\mu/\rho)^{1/2}$. In addition, the compressional wave velocity, V_p, can be obtained from the relation

$$V_p^2 = \frac{V_s^2\, 2(1 - \nu)}{1 - 2\nu} \tag{6}$$

For *Surveyor III*, the oscillation frequency was 6.5 Hz, which results in $K_m = 4.9 \times 10^8$ dynes/cm. This implies a rigidity modulus range from 3.9×10^6 to 7.8×10^6 dynes/cm^2, for ν varying from 0.5 to 0, respectively, and a shear wave velocity of 16 to 28 m/sec for a bulk density of 1.0 to 1.5 g/cm^3. For Poisson's ratio less than 0.45 and the same range of density, a compressional wave velocity of 33 to 70 m/sec is obtained (Ref. IV-1).

Using the frequencies from the *Surveyor VI* landing, the value for K_m would be reduced by about 10% from that given above for 6.3 Hz and increased by about 60% for 6.9 Hz. Corresponding changes in the velocities would be -5% and $+30\%$, respectively.

The estimated seismic velocities are considerably lower than those expected for terrestrial soils with the other mechanical properties as described in this report. Until tests on a spacecraft have been performed, these results should be considered as preliminary estimates only.

B. Lunar Soil Erosion: Vernier Engine Firing

1. Test Explanation

Possible soil erosion caused by the rocket engine exhaust gas impingement on the surface during the hop is of three basic types, which might occur in combination, although one mode probably would predominate. (Additional explanations of these erosion phenomena are given in Ref. IV-2.)

(1) Viscous erosion (Refs. IV-10 and IV-11): erosion by entrainment of soil particles as the gas flows over the surface.

(2) Gas diffusion erosion (Ref. IV-12): movement of the soil caused by the upward flow of gas through the pores of the soil during and after the firing.

(3) Explosive cratering (Ref. IV-13): rapid cratering caused by the exhaust gas pressure on a surface exceeding the bearing capacity of the lunar surface. (With the full expansion of the *Surveyor* or the *Apollo Lunar Module* exhaust plumes as they can occur on the moon, little of this type of erosion would be expected.)

The firing of the vernier engines during the *Surveyor V* mission was primarily intended to determine the diffused gas eruption effects resulting from rapid engine shutdown. This eruption did occur, as did viscous erosion during the firing of the engines. However, neither of these effects caused a functional degradation of the spacecraft. The vernier engines on *Surveyor V* were fired for 0.5 sec at a thrust level near that required to lift the spacecraft off the surface. For a supplemental erosion test, it was desirable to fire the *Surveyor VI* engines at a higher thrust level and for a longer time to emphasize the viscous erosion effects.

The hop made by *Surveyor VI* increased the viscous erosion effects, minimized the possibility of diffused gas eruption, and provided good visibility of the erosion effects. It was reasoned that correlation of the results of the two tests (*Surveyors V* and *VI*) should be realistic because of the general similarity of the soils at the four *Surveyor* mare landing sites (more similar than would be expected at four earth sites).

2. Observations

During liftoff for the hop, the exhaust gases from the vernier engines caused erosion of a shallow layer of lunar soil beneath, and adjacent to, the spacecraft. This soil was redeposited up to several meters away from the spacecraft. Figures IV-28 through IV-31 are controlled mosaics (frame orientation and center location are correct) showing the lunar surface near *Surveyor VI* before and after the hop. These mosaics are annotated to identify features pertinent to the analysis of the erosion test.

Figure IV-28 is a controlled mosaic of narrow-angle pictures taken the day before the hop. The mosaic represents 165 deg of camera azimuth and shows most of the lunar surface close to the spacecraft that can be seen by the camera.

Figure IV-29 is a controlled mosaic of narrow-angle, post-hop pictures looking toward the original landing site. This mosaic, which extends in camera azimuth for 87 deg, shows much of the soil disturbance caused by the spacecraft's first landing and by the vernier engines during the hop.

Figure IV-30 is a post-hop, controlled mosaic identifying imprints made during the original landing by the footpads and crushable blocks, as well as the approximate locations of the vernier engines after the spacecraft came to rest. Shown in the mosaic are the double imprints of footpads 2 and 3 during the first impact and the subsequent, short bounce of the spacecraft. Also identified are the single imprints made by crushable blocks 2 and 3 during the first impact of the initial landing. The craters beside the crushable block 1 imprint were probably formed by vernier engine 1 exhaust during the hop. The original landing imprint of footpad 1 is beneath the spacecraft in its present position and cannot be seen by the camera. Also shown are the approximate pre-hop locations of the vernier engines. Figure IV-6 is a scaled drawing of the positions of these landing imprints.

By comparing the pre- and post-hop mosaics (Figs. IV-28 and IV-29), rocks that were not moved by the vernier engine firing can be seen; they are identified with the lowercase letters a through y. These rocks are used as reference points for determining erosion effects caused by the firing. Approximately the same area of the lunar surface is included in each of the mosaics.

Of interest is rock g near the alpha-scattering instrument sensor head in the pre-hop mosaic of Fig. IV-28. It appears to be in the same location after the hop (Fig. IV-29), although its shape is not unique enough to positively identify it. The vernier engine forces were three times greater for the *Surveyor VI* firing than they were for the *Surveyor V* static firing, and rocks of this size and at this distance were moved by the *Surveyor V* firing.

Several of the larger rocks or soil fragments moved by the firing are identified with arabic numerals in Figs. IV-28 and IV-29. Positive identification of movement of fragments is much more difficult for the *Surveyor VI* firing. *Surveyor V* did not move; pre- and post-hop camera locations for *Surveyor VI* are offset by the lateral movement of 2.4 m. Therefore, camera angles for the pre-hop position are different from those for the post-hop position. In addition, many small surface features close to the spacecraft, which could be seen in pre-hop pictures, are below the camera resolution in its post-hop position.

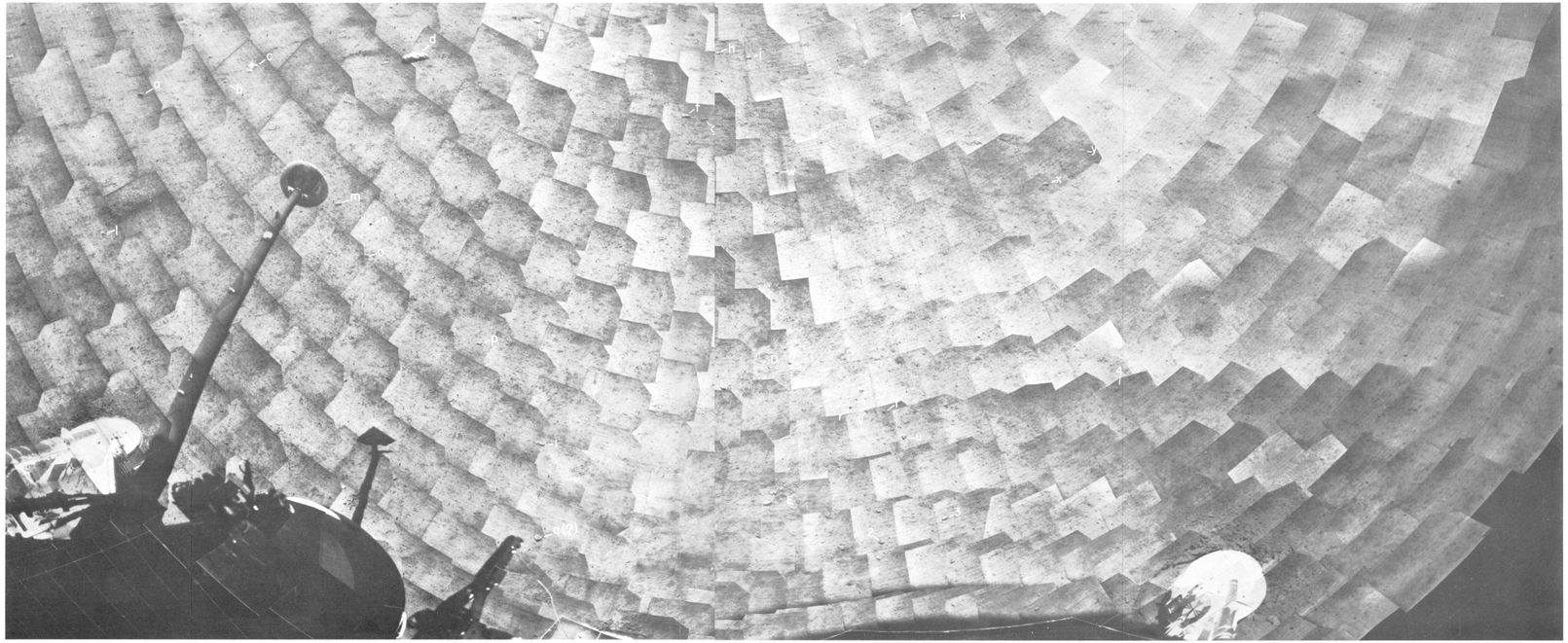

Fig. IV-28. Controlled pre-hop mosaic of narrow-angle pictures extending from footpad 3 (on the left) to footpad 2 (on the right). View is to the east. Locations of representative rocks that were not moved by the vernier engine firing are identified with lowercase letters; rocks that were moved are identified with arabic numerals. Capital letters identify areas in Fig. IV-31 (Day 320, Catalog 6-SE-26).

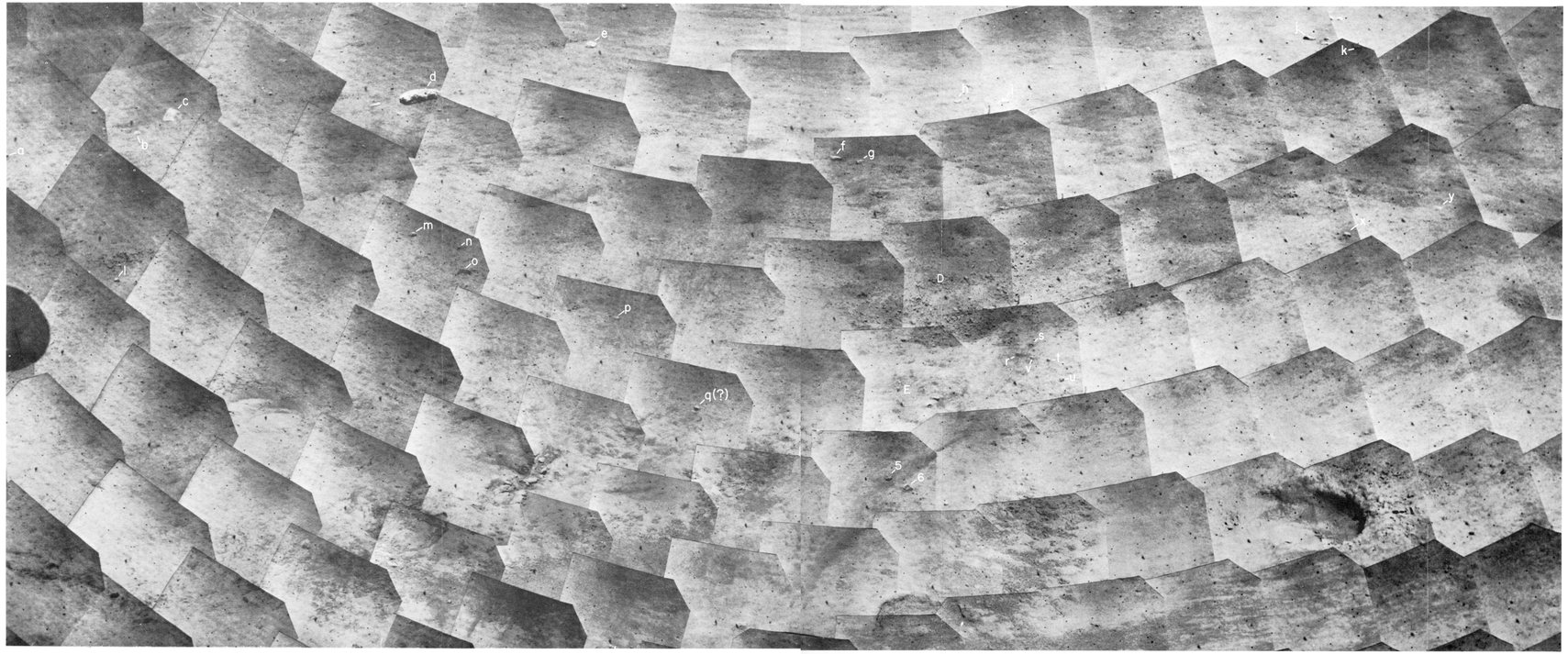

Fig. IV-29. Controlled post-hop mosaic of narrow-angle pictures. View is to the east toward the original landing site. Locations of those rocks which were not moved by the vernier engine firing (identified in Fig. IV-28) are identified by lowercase letters. Two rocks moved by the firing are identified with arabic numerals (Days 321 and 322, Catalog 6-SE-22).

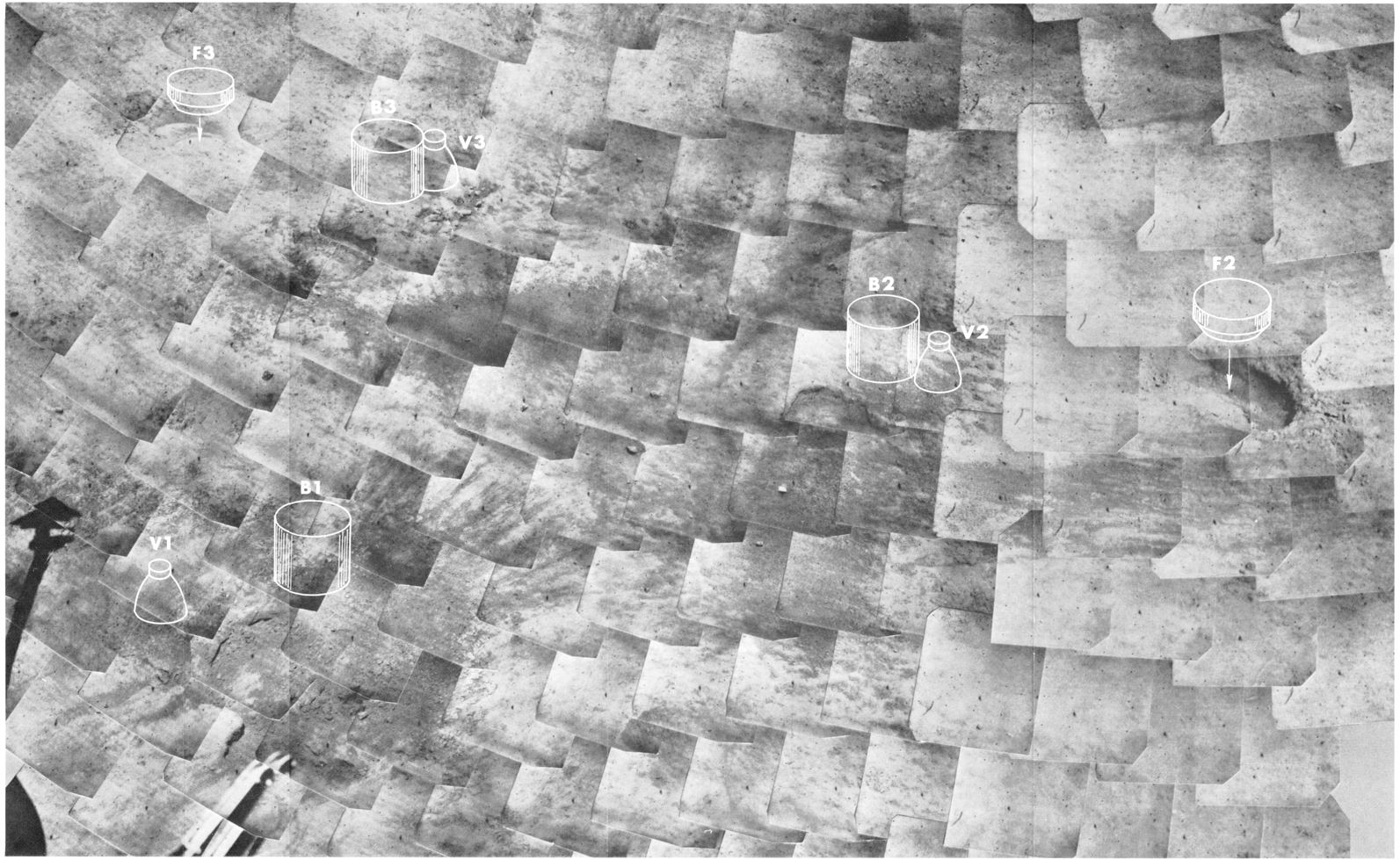

Fig. IV-30. Post-hop mosiac showing most of the lunar surface disturbance caused by the initial landing and by the vernier engine firing during the hop. Approximate locations are shown for the crushable blocks and vernier engines before liftoff for the hop. Images of footpads are shown above the final imprints made during the original landing. F = footpad, B = crushable block, V = vernier engine; 1, 2, and 3 denote the landing legs (Days 321 and 322, Catalog 6-SE-23).

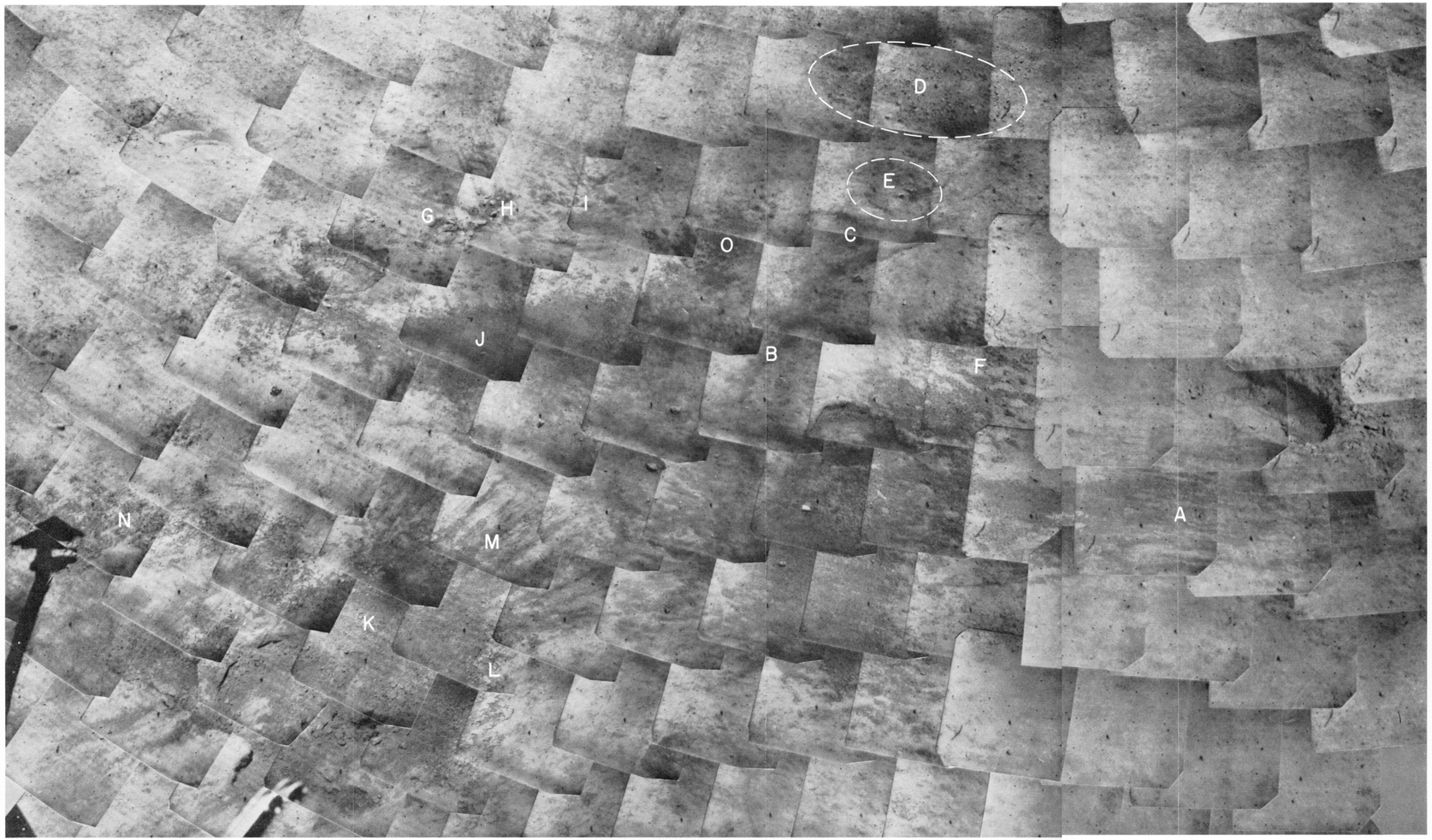

Fig. IV-31. Areas of erosion (capital letters) caused by the vernier engine during liftoff for the hop (Days 321 and 322, Catalog 6-SE-23).

Figure IV-31 is a post-firing mosaic in which several surface areas disturbed by the vernier engine firing are identified with uppercase letters.

The vernier engines were pre-commanded to fire so that the spacecraft would rise off the surface; with engines 2 and 3 firing at higher thrusts than engine 1, it would tilt the spacecraft's vertical axis approximately 7 deg in order to travel to the west. Because of the spacecraft tilt, vernier engine 1 rose from the ground slower than did engines 2 and 3 and was expected to cause more erosion. Also, because of the tilt, it was expected that soil eroded by the engines would be primarily ejected away from the engines toward the east. The combined vertical and tilt motions caused all three engine nozzle heights to increase continuously during the powered phase, as shown in Fig. IV-32. It is recognized that any of the three engines could contribute to any of the erosion features; however, presumably, the engine closest and immediately west of each feature was primarily responsible for the erosion.

a. Vernier engine 2 area. Examination of the surface features surrounding vernier engine 2 indicates that the erosion was primarily viscous; i.e., soil was removed in a thin sheet from the area surrounding the engine and redeposited at distances ranging up to several meters. The lunar surface material beneath, and adjacent to, the engines has been eroded by the exhaust gases; however, the depressions caused by this erosion are too irregular and shallow to be called craters. Figure IV-33 indicates that, at liftoff, the center of vernier engine 2 was above an area to the right and below the imprint of crushable block 2. No erosion depression below vernier engine 2 can be seen in this area.

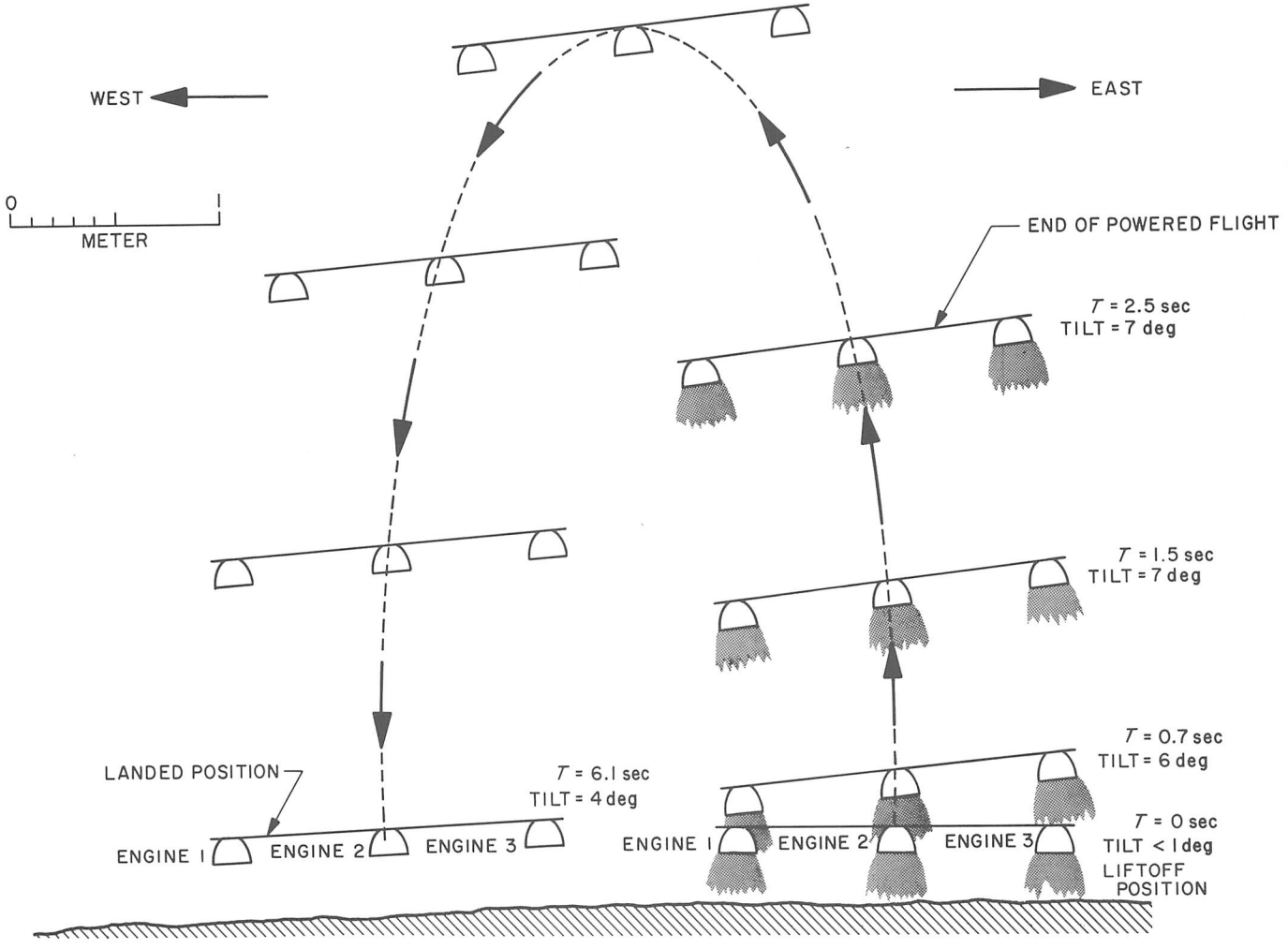

Fig. IV-32. Time sequence of vernier engine positions during liftoff for the hop. View is perpendicular to direction of hop.

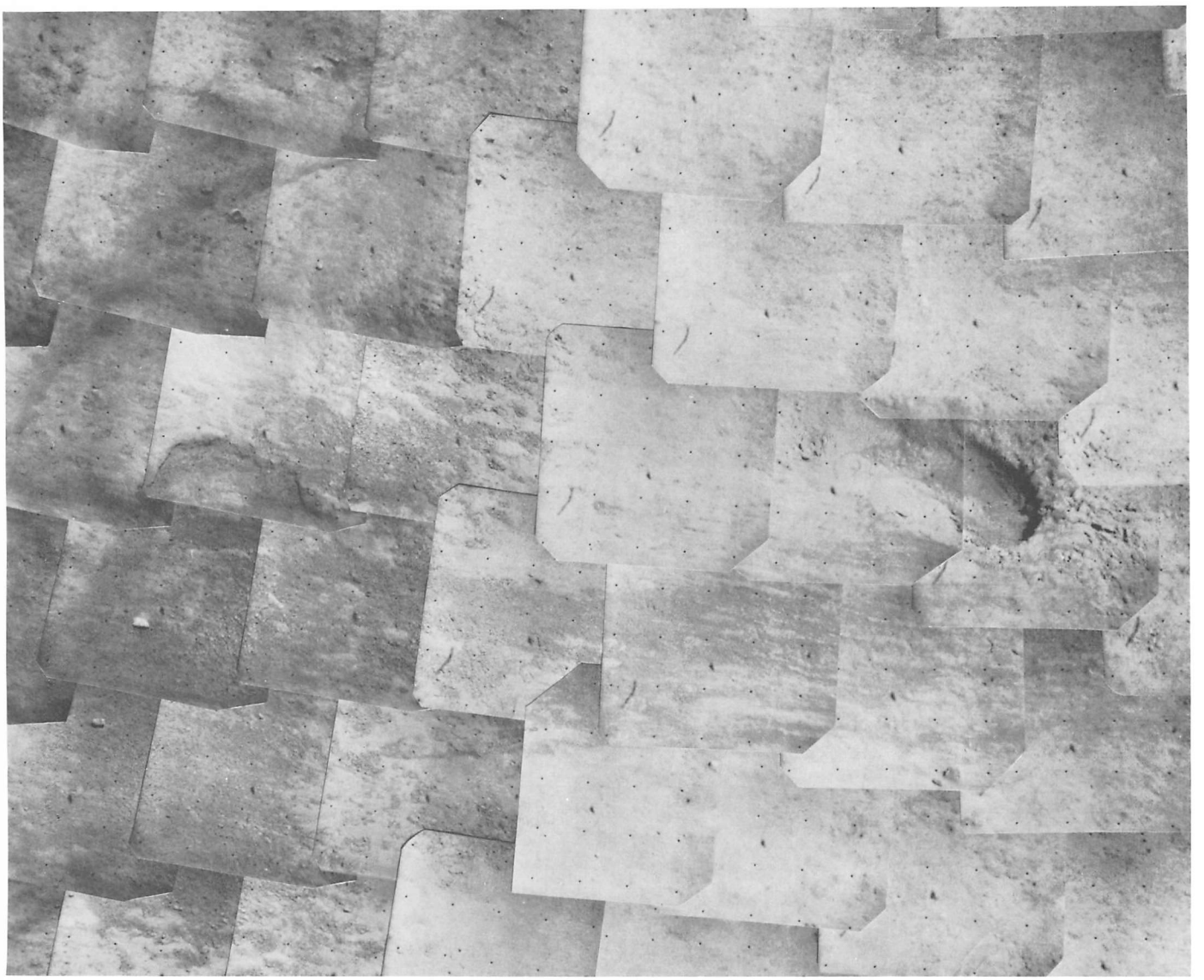

Fig. IV-33. Portion of the mosaic of Fig. IV-31 showing rays of fine, dark soil deposited by vernier engine 2 during the hop (Days 321 and 322, Catalog 6-SE-23).

Area A contains a broad band of fine, dark soil deposited in parallel rays that extend from below the vernier engine 2 position at liftoff, toward and beyond the footpad 2 imprint. Area B is a narrow, dark ray of fine soil that starts below the crushable block imprint and curves smoothly around it. To the east, ray B broadens into a fan-shaped ray at C. Rays A, B, and C are almost certainly deposition, rather than erosion, features. These rays occur on the boundaries of the zone disturbed by engine 2, where surface pressures of the exhaust gases were greatly reduced compared to the center of the disturbance. The rays represent fine soil deposited after being propelled laterally along the surface by the exhaust gases. Rayed soil in areas A, B, and C forms an open bow around the vernier engine 2 liftoff point.

Further to the east, ray C joins a circular zone of deposition (area D), which is entirely covered by agglomerated soil fragments and small rocks, as well as by fine, dark soil. The pre-firing mosaic (Fig. IV-28) and individual, narrow-angle pre-hop pictures show that most of these fragments were not present in area D before the hop. Rock w and the distinctive pattern made by rocks r through v aid in locating area D in pre-hop pictures. Area D is approximately 60 cm in diameter with its center 3.8 m from the vernier engine 2 liftoff position.

Ejecta fragments within area D range in size up to 1.5 cm in diameter. Ejecta seen in area D grade into finer material (both to the north and south) containing numerous dark rays that point back toward the spacecraft. Pre- and post-firing details in area D are shown in Fig. IV-34a and IV-34b.

Area E in pre-hop pictures (Fig. IV-31) is a small depression, partly filled with coarse fragments. In post-hop pictures, most of the depression has been filled with fine soil through which two fragments protrude slightly (Fig. IV-35a and IV-35b).

Fine soil has also partially coated the five small fragments, r through v, and has buried them to a slightly greater depth (Fig. IV-36a and IV-36b). Much of the fine, light-appearing soil eroded from the surface close to vernier engine 2 maintained its light appearance after deposition, e.g., in area E and in the vicinity of fragments r through v.

Area F is a zone of disturbed soil directly in line with the vernier engine as its exit plane tilted 7 deg during the firing. The irregular surface here, with its numerous small depressions bottoming in dark soil, indicates that much of the surface soil in area F was eroded by the firing. Much of the coarst ejecta seen in area D in post-hop pictures probably came from area F.

The probable relationships of erosion and deposition by vernier engine 2 are summarized in Fig. IV-37. Most of the fine, eroded soil probably was swept along the surface in a turbidity-like current of exhaust gases that were deflected into a horizontal sheet bounded by the shock front beneath the vernier engine. Many of the large fragments, eroded from the immediate vicinity of the vernier engine, were probably ejected into high ballistic trajectories.

b. Vernier engine 3 area. Soil erosion associated primarily with vernier engine 3 can be seen in Fig. IV-31 and in Fig. IV-38. At liftoff, vernier engine 3 was to the right of the crushable block 3 imprint and above the disturbed soil marked area G. Soil disturbance at area G was caused by the vernier engine firing; it is not present in pre-hop pictures taken through the large auxiliary mirror (Fig. IV-15a and IV-15b). Soil erosion at G primarily consists of a small, irregular, shallow crater that contains several slightly displaced soil clumps up to 7 cm long. A similar, but possibly smaller clump, probably ejected from this area, struck the photometric target on one of the omnidirectional antenna booms, causing a thick layer of soil to adhere to the target (Fig. IV-39b).

The irregular surface in area I has a rippled appearance (Fig. IV-40). Because this is not typical of the lunar surface, it is thought to be a result of the vernier engine erosion. This effect has been observed in laboratory tests in which a slightly cohesive soil begins and continues to erode differentially. That is, once erosion is initiated at several points, it progresses rapidly. Loose soil fragments initially picked up by the exhaust gases impact and loosen adjacent soil fragments.

Area J, a substantially disturbed region, though closest to vernier engine 2, is between all three engines. Thus, all engines probably contributed to the formation of the area of dark soil which is believed to be due to deposition rather than erosion.

c. Vernier engine 1 area. At liftoff, Vernier engine 1 was above a point to the left and below the crushable block 1 imprint (Figs. IV-30, IV-31, and IV-41). The more extensive soil erosion beneath vernier engine 1, compared with engines 2 and 3, has two explanations: (1) Liftoff of engine 1 during the hop was slower than for vernier engines 2 and 3; therefore, erosion beneath engine 1 occurred for a longer period of time. (2) Vernier engine 1 fired directly into the crushable block 1 imprint as the spacecraft tilted to the west. Soil, previously loosened by the impact of the crushable block, was more easily eroded than the undisturbed soil, and probably caused further erosion by a saltation-type process (individual soil particles, accelerated by exhaust gases, acted as miniature excavation tools as they struck the sides of the imprint). Such erosion probably accounts for the irregular depression below the imprint (Figs. IV-31 and IV-41). Most of the coarse fragments initially present in the crushable block imprint have been broken up; the resulting fine soil was deposited in area K. This blanket of fine soil at area K grades into coarser fragments along its margin at area L (Fig. IV-42) and extends into a wide fan of fine, dark rays at area M (Fig. IV-43). Area N is a fairly extensive zone of disturbance caused in part by impact of many coarse fragments (Fig. IV-44). Some fragments which have penetrated into the dark, subsurface soil still lie in their small, dark depressions.

d. Sensor head area. Area O in Fig. IV-31 shows the lunar surface region where the sensor head of the alpha-scattering instrument rested before the hop. Figure IV-28 indicates that some lunar soil was displaced by the sensor head during deployment, and the instrument made a circular imprint in the lunar soil. Since an examination of area O does not disclose any impressions made by the alpha-scattering instrument, it is concluded that they must have been obliterated by vernier engine erosive action.

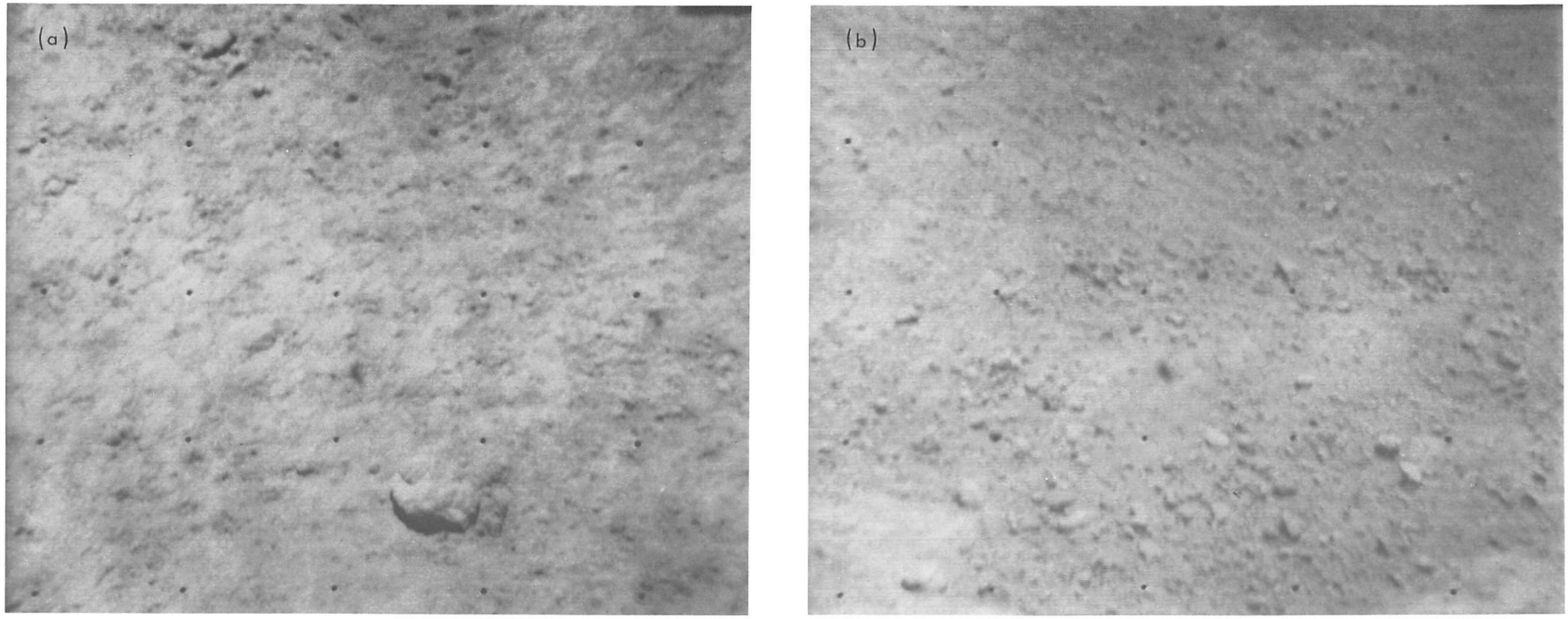

Fig. IV-34. Narrow-angle pictures of parts of area D (see Fig. IV-31) showing the extent of fine soil and fragments ejected by the vernier engine firing. Area shown in (a), the pre-hop picture, is part of (b), the post-hop picture. Texture of the lunar surface in area D has been changed by the firing, especially by addition of a large number of coarse fragments. (a) Pre-hop (Day 320, 05:59:44 GMT). (b) Post-hop (Day 321, 11:34:40 GMT).

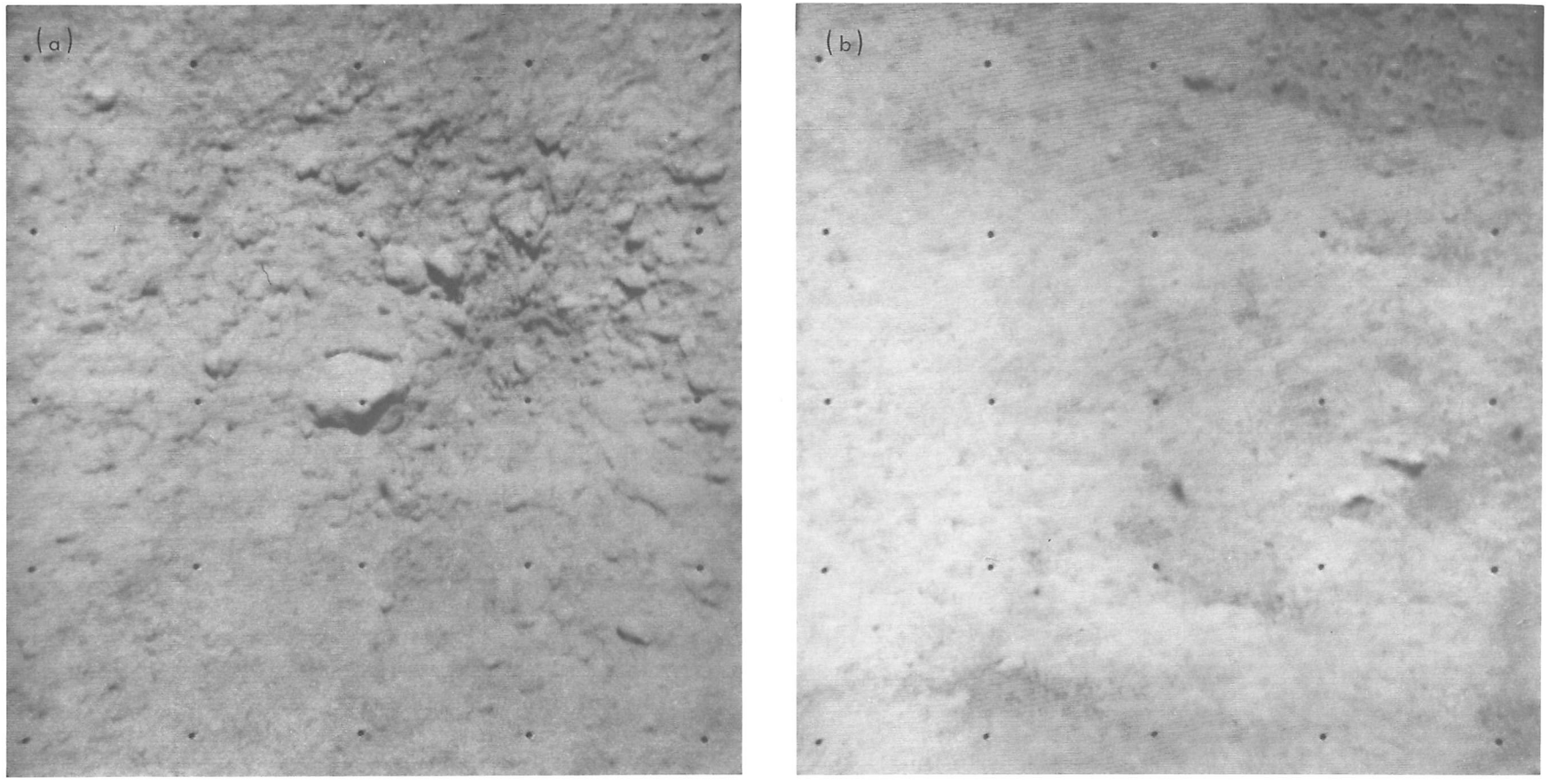

Fig. IV-35. Narrow-angle pictures of area E. The depression containing a number of fragments before the hop is shown partly filled with fine soil after the hop. (a) Pre-hop (Day 320, 05:58:04 GMT). (b) Post-hop (Day 321, 11:34:04 GMT).

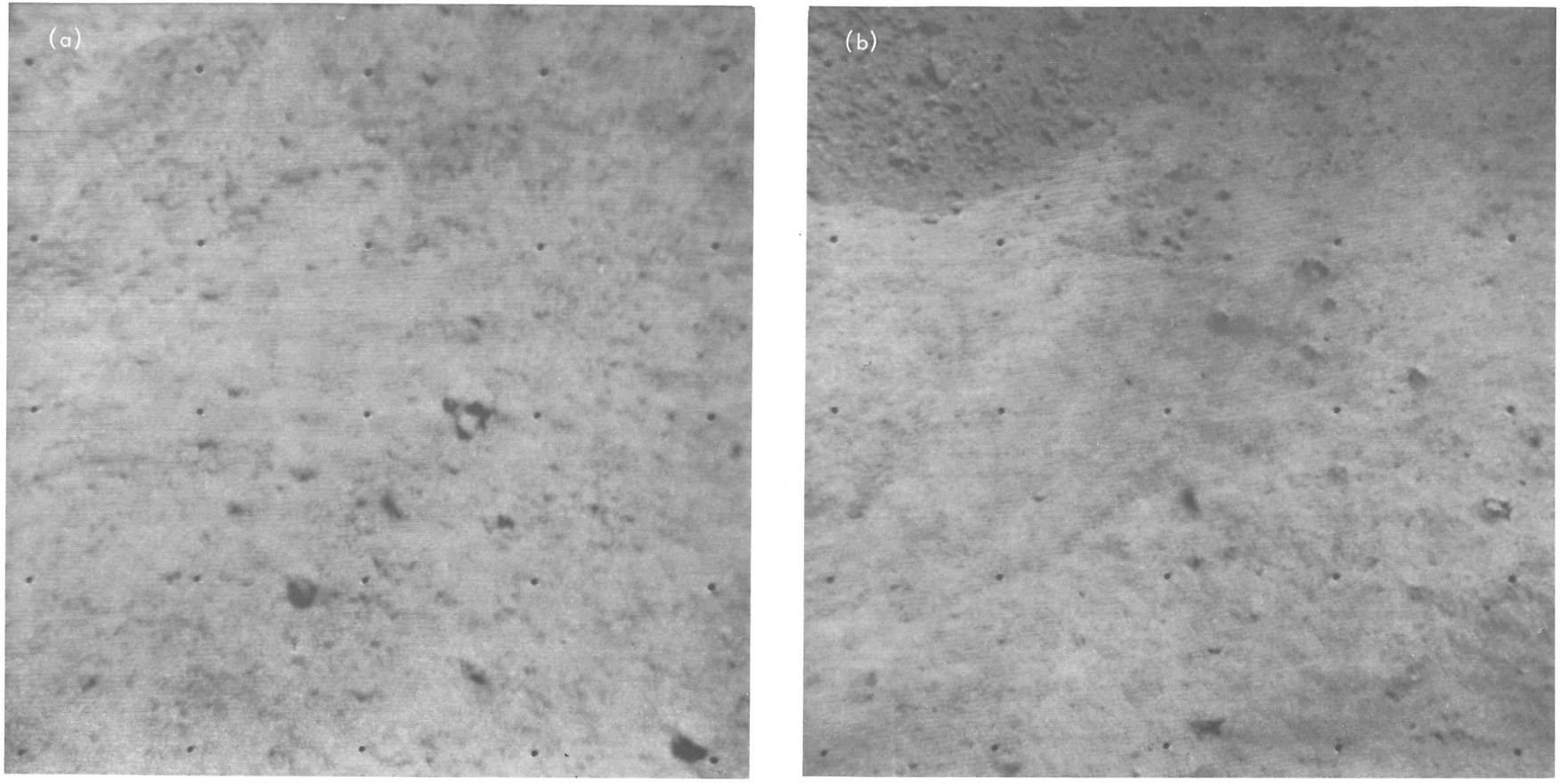

Fig. IV-36. Narrow-angle pictures taken of rocks r, s, t, and v; rock u can also be seen in the post-hop picture. These rocks were buried somewhat deeper and partially coated with fine soil because of the vernier engine firing. (a) Pre-hop (Day 320, 05:48:37 GMT). (b) Post-hop (Day 321, 11:34:00 GMT).

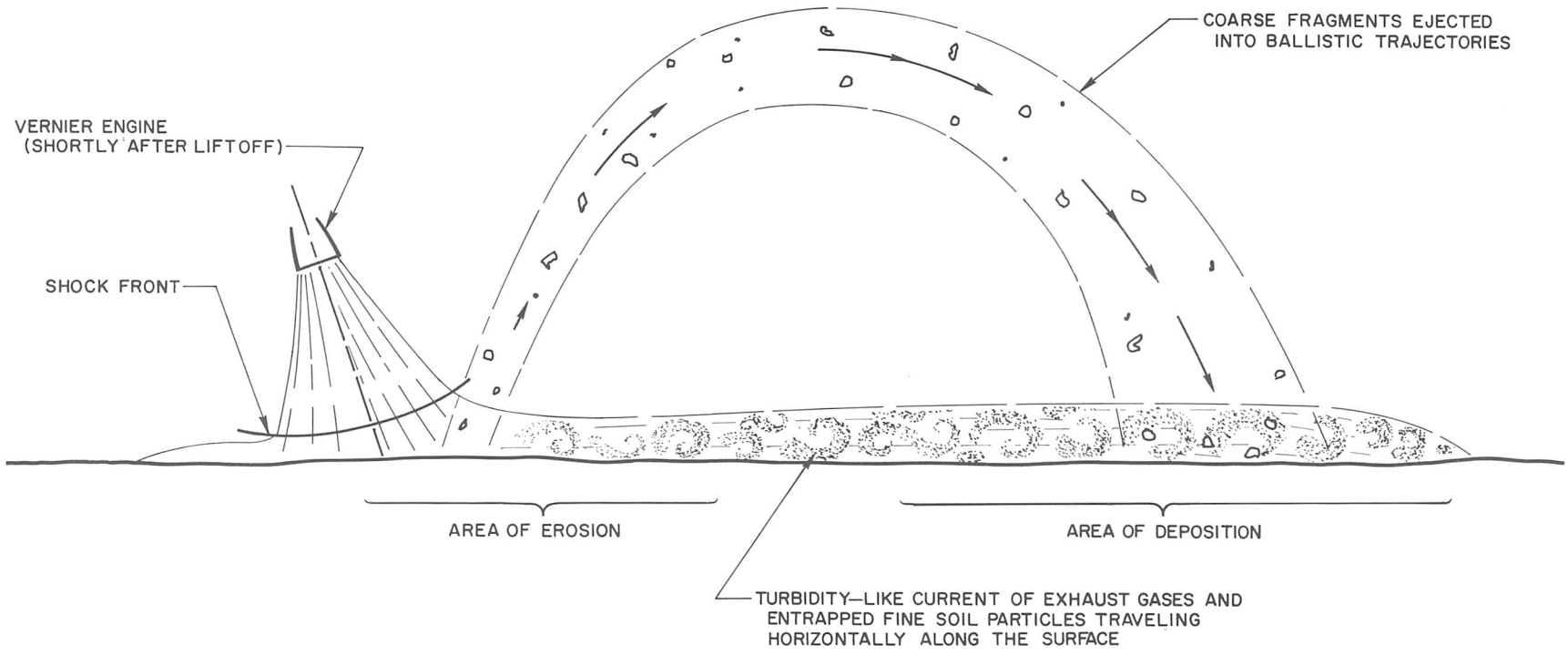

Fig. IV-37. Probable history of erosion in vernier engine 2 area during hop.

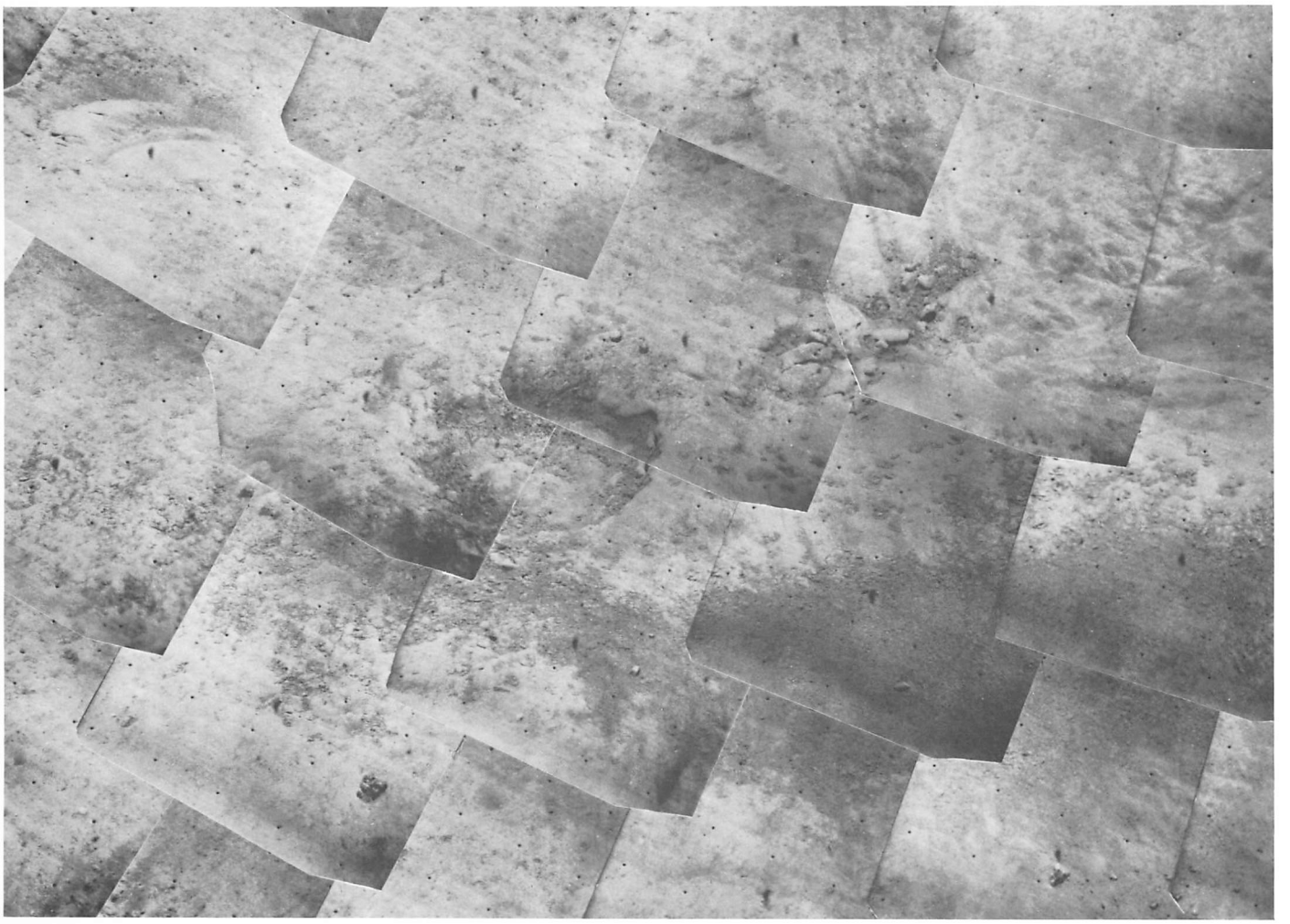

Fig. IV-38. Enlargement of part of Fig. IV-31 showing imprints of footpad 3 and crushable block 3 and area below vernier engine 3 (Days 321 and 322, Catalog 6-SE-23).

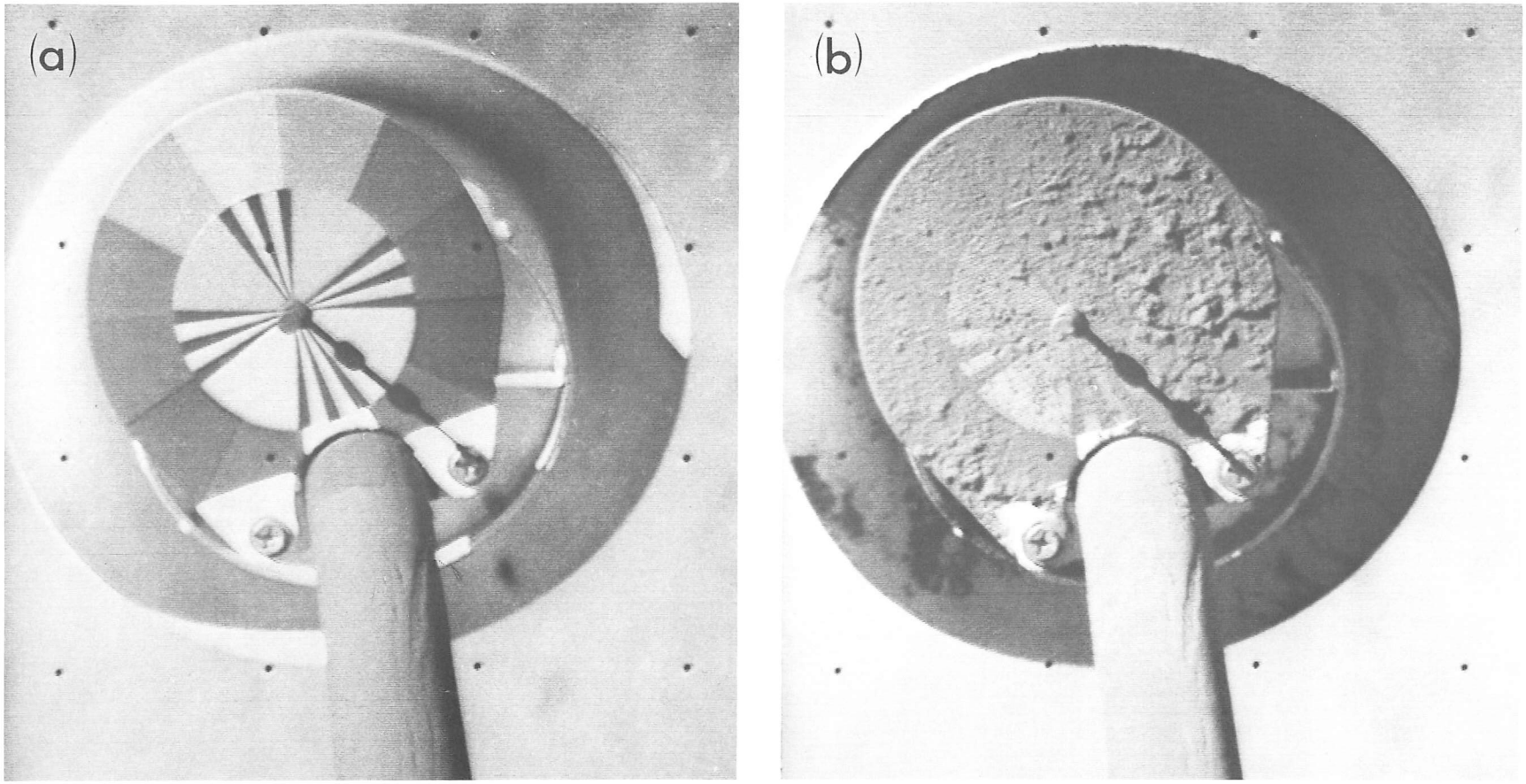

Fig. IV-39. Photometric target on omnidirectional antenna boom: (a) before, and (b) after, the vernier engine firing. Before the firing, the target is clean; after the firing the target is coated with a layer of soil up to 0.9 mm thick. The coating probably was caused by impact of a soil clump on the target during the firing. (a) Day 321, 09:37:11 GMT. (b) Day 321, 12:30:00 GMT.

Fig. IV-40. Narrow-angle picture of part of area I (see Fig. IV-31) showing rippled appearance of the surface after vernier engine firing (Day 321, 11:34:18 GMT).

Fig. IV-41. Enlargement of a portion of Fig. IV-31 showing the crushable block 1 impact area and soil disturbance caused by vernier engine 1 during the hop (Days 321 and 322, Catalog 6-SE-23).

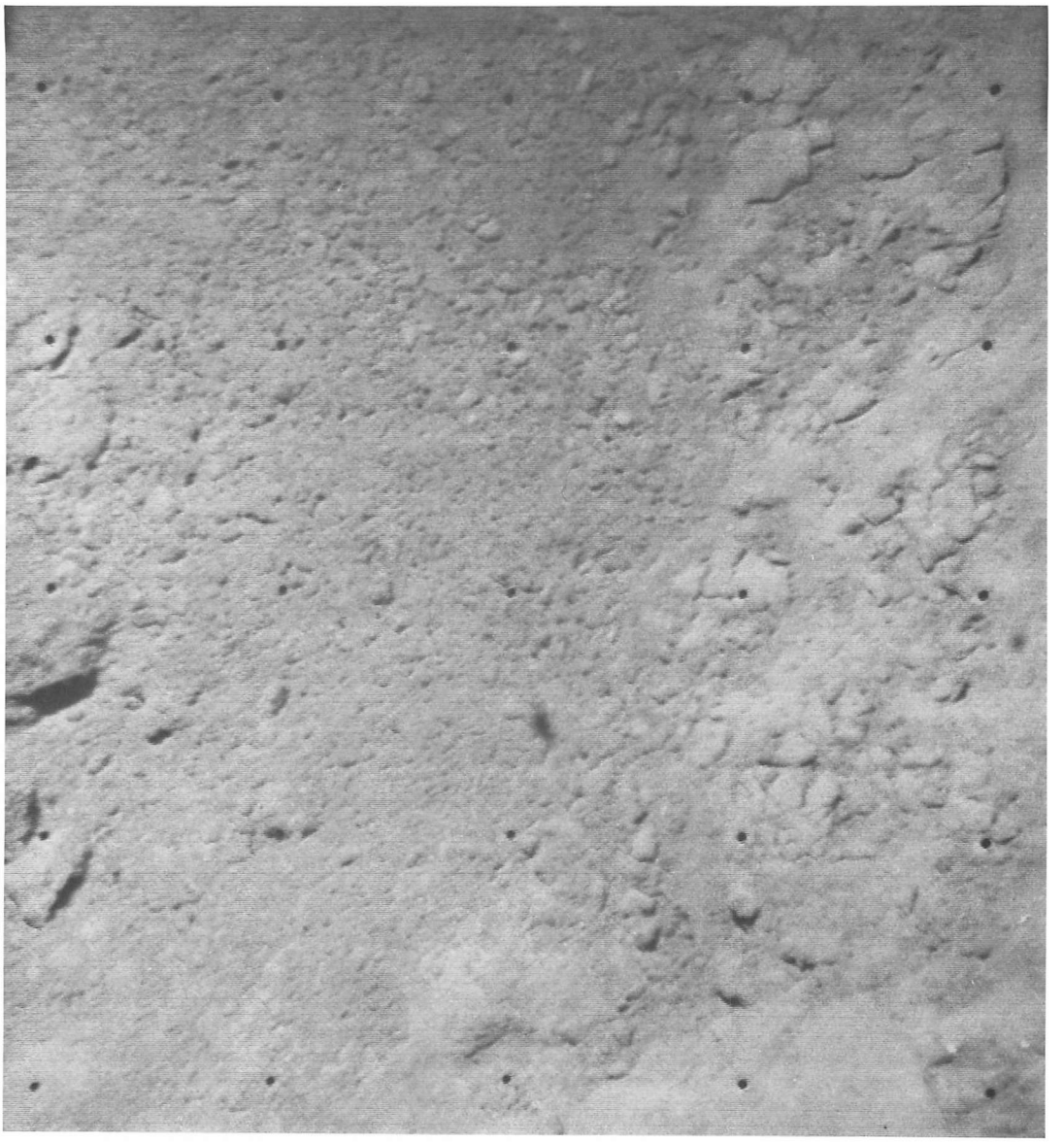

Fig. IV-42. Soil disturbed by vernier engine 1 firing. Soil fragments seen in area L probably have been moved along the surface without being overturned because their tops are formed of light-colored surface soil (Day 321, 11:47:26 GMT).

Fig. IV-43. Rays of fine, dark soil ejected by vernier engine 1 during hop (Day 321, 11:32:52 GMT).

Fig. IV-44. Shallow depressions (area N) in dark, subsurface soil formed by impact of fragments ejected by vernier engine 1 during hop (Day 321, 11:48:31 GMT).

e. Contamination of spacecraft by vernier engine firing. The coating of soil adhering to the photometric target (Fig. 39b) seems to have been an anomalous effect of the vernier engine firing. Probably this soil coating was caused by impact of a clump of soil on the target. The rest of the spacecraft remained relatively clean and free of contamination. The top of footpad 2 shows only a few small, scattered soil fragments along its edge; footpad 3 is completely clean (Fig. IV-45a and IV-45b). Only a few scattered soil fragments lie on the electronic compartment tops (Fig. IV-45c).

3. Analysis

The irregular and shallow depressions caused by the *Surveyor VI* vernier engine firing cannot be compared exactly with the expected theoretical craters because the lunar surface is undulating, with the top few centimeters more porous and less dense than the lunar material below the depth of erosion. These conditions permit the flowing gases to exert greater forces on the more exposed, uppermost lunar material. Also, material is probably moved by the saltation process. It is

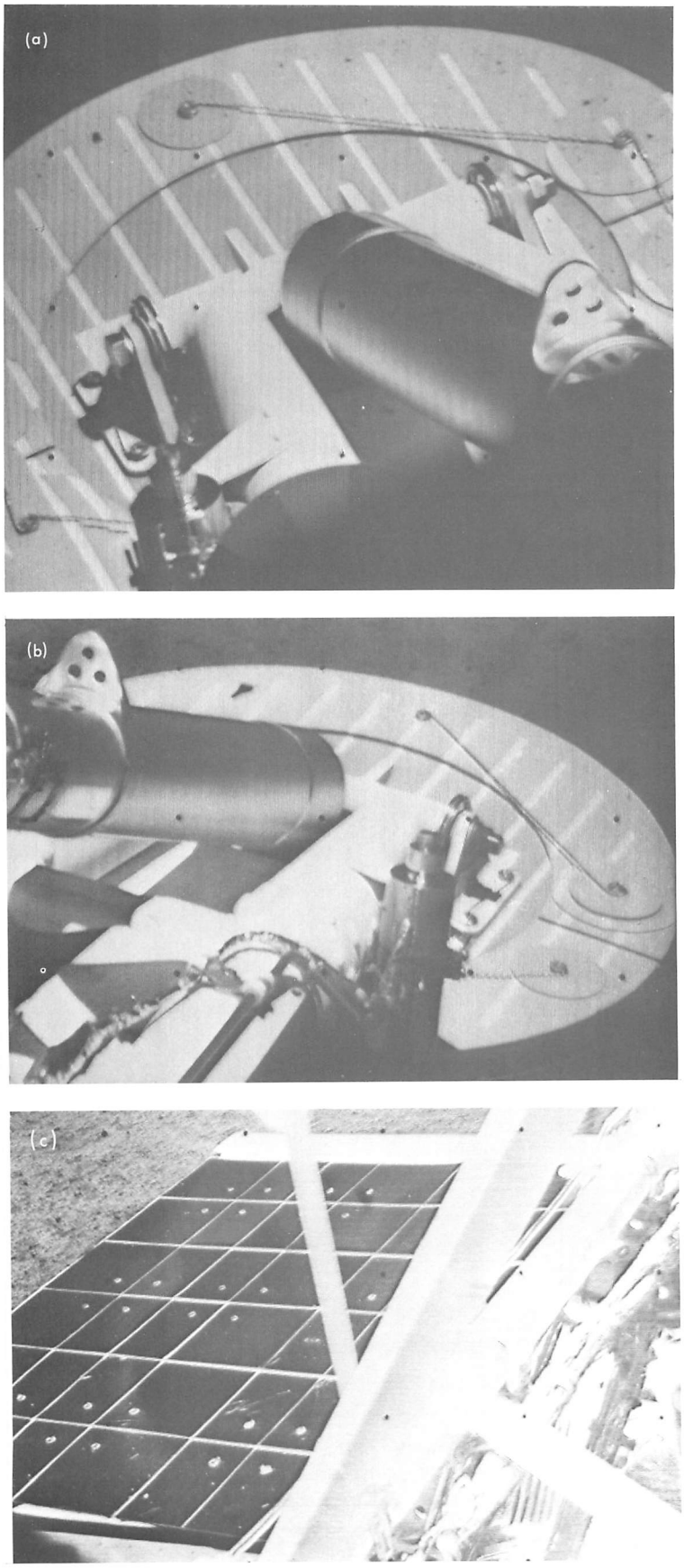

Fig. IV-45. Pictures showing relative lack of contamination on the spacecraft after the vernier engine firing. (a) Top of footpad 2; note the few particles along the top edge (Day 323, 04:51:01 GMT). (b) Top of footpad 3 (Day 321, 12:23:13 GMT). (c) Top of electronic compartment A (Day 324, 06:04:56 GMT).

possible, however, to obtain a limited amount of surface mechanical property data by examination of the theory.

a. Exhaust gas forces. The viscous erosion studies use the theoretical flow field along the lunar surface and the associated surface loadings determined from Roberts' theory (Refs. IV-10 and IV-11). Table IV-3 lists the engine parameters used in the theoretical computations of surface loading and associated soil erosion. The initial nozzle heights of the vernier engines used in the analysis were taken to be 32 cm, which corresponds to footpad penetrations of about 5 cm. (After these calculations were performed, the pre-hop height of vernier engine 3 above the lunar surface was determined to be 35 ± 1 cm.) The subsequent nozzle heights were determined from the vertical and tilt motions shown in Fig. IV-18. Engine thrust levels used in the computations are shown in Fig. IV-20, while Fig. IV-46 shows the relation between engine thrust and chamber pressure. Figures IV-18 and IV-20 show that the engine thrust began a little before $t = 0.1$ sec and the spacecraft started to ascend shortly after; the engines were commanded on at $t = 0$. Vernier engine 3 developed the maximum thrust level of about 66 N at $t = 0.2$ sec. At this time, the spacecraft had moved upward about 1 cm and pitched about 0.25 deg.

Table IV-3. Vernier engine parameters used in theoretical calculations

Nozzle exit radius	6.46 cm
Exit Mach number	5.2
Gas constant	366 m^2/sec^2 °K
Gas specific heat ratio	1.313
Chamber gas temperature	2950°K
Chamber gas viscosity	1.17×10^{-6} dynes/sec/m^2

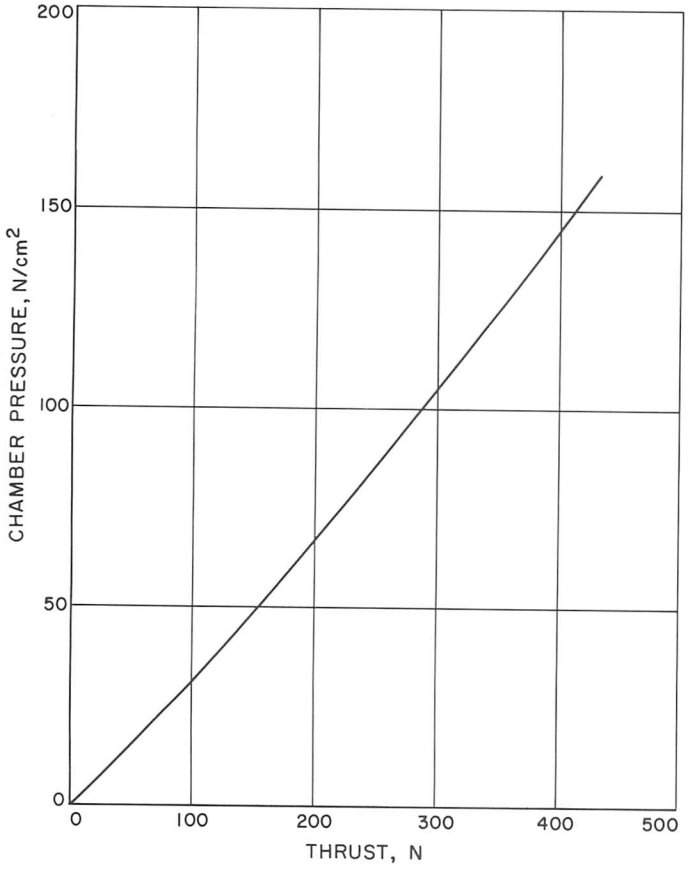

Fig. IV-46. Variation of vernier engine thrust with chamber pressure.

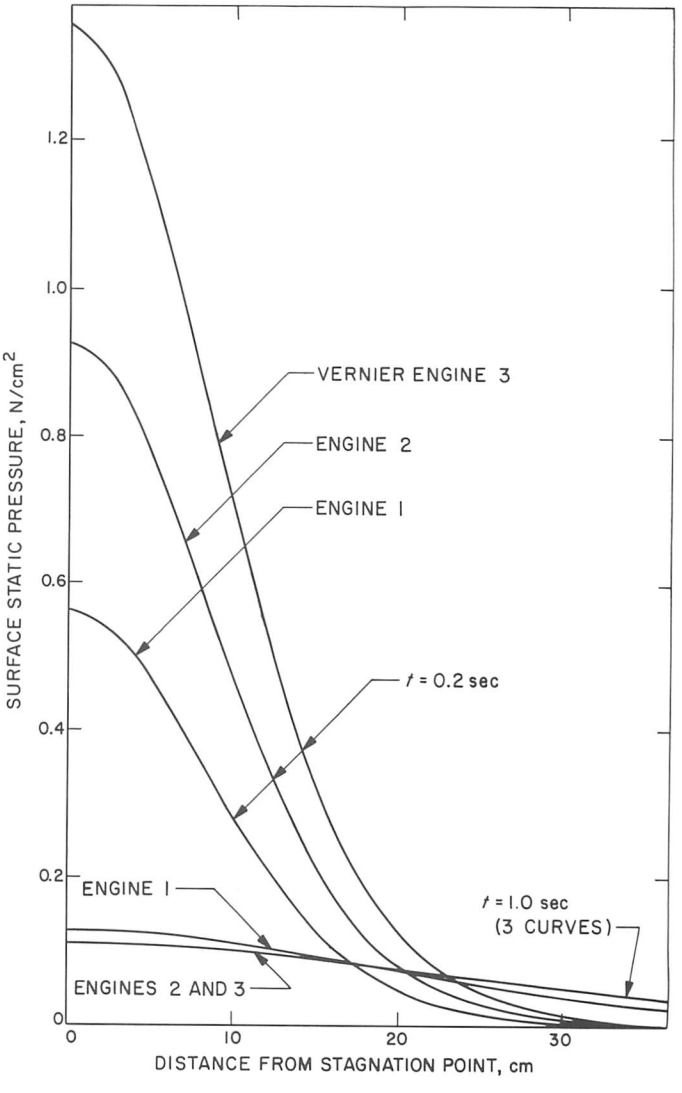

Fig. IV-47. Theoretical static pressure along a surface parallel to the engine nozzle exit plane 0.2 and 1.0 sec after initiation of the hop.

Figure IV-47 shows the variation with distance of surface static pressure at $t = 0.2$ and at 1.0 sec for vernier engines 1, 2, and 3, respectively. The maximum pressure loading for vernier engines 2 and 3 occurred at $t = 0.2$ sec. The maximum pressure loading for engine 1 occurred at about $t = 0.6$ sec. However, the surface loading is only a little higher than at $t = 0.2$ sec. The stagnation pressure under vernier engine 3 was 1.35 N/cm^2 at $t = 0.2$ sec. Surface erosion of the explosive cratering and diffused gas types depends on these static pressure soil surface loadings.

Theoretical dynamic pressures (defined as $\rho u^2/2$, where ρ is the gas density and u is the gas radial velocity along the surface), for all three engines at times $t = 0.2$ and 1.0 sec, are shown in Fig. IV-48. Vernier engine 3 developed the maximum dynamic pressure, which was 0.56 N/cm^2 at $r = 13.4$ cm and $t = 0.2$ sec (Fig. IV-48).

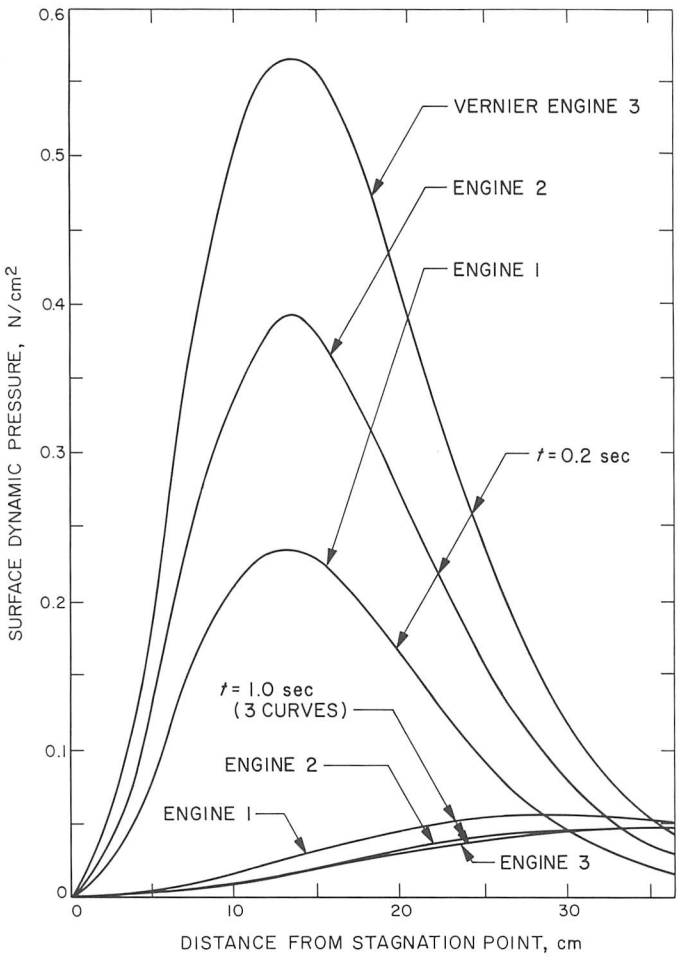

Fig. IV-48. Theoretical dynamic pressure, developed by the three vernier engines, along a planar surface parallel to the engine nozzle exit plane 0.2 and 1.0 sec after initiation of the hop.

Surface erosion of the viscous type depends on the dynamic pressure along the surface.

b. Lunar soil cohesion. According to the theory advanced in Refs. IV-10 and IV-11, soil erosion will occur when the shear stresses acting on the soil surface (equal to the gas dynamic pressure multiplied by a friction coefficient) exceed the resistance to shear offered by soil cohesion and soil frictional forces. Since viscous erosion occurred during the hop, viscous erosion theory can be used to make an upper-bound estimate of soil cohesion. This estimate is the value of cohesion for which incipient erosion occurs when subjected to the maximum erosive shear stress.

The maximum erosive shear stress occurs at the point of maximum dynamic pressure and is dependent on the effective value of the friction coefficient. Soil erosion data obtained by the Langley Research Center from soils having an initial flat surface indicated the effective friction coefficient, C_f, to be about 0.2, which is the value recommended in Ref. IV-11. For the irregular, undulating surface existing at the *Surveyor VI* landing site, the friction coefficient should be higher than 0.2. In the upper-bound estimate made here, C_f is taken as 0.4. According to Fig. IV-48, the peak dynamic pressures under vernier engines 1, 2, and 3 are 0.24, 0.39, and 0.56 N/cm^2, respectively. These peak values are the maximum dynamic pressures caused by engines 2 and 3; the maximum pressure (0.3 N/cm^2) caused by engine 1 occurred at $t = 0.6$ sec. Hence, for a friction coefficient of 0.4, the lunar surface was subjected to maximum shearing stresses of 0.12, 0.16, and 0.23 N/cm^2 for vernier engines 1, 2, and 3, respectively.

The resistance of the soil surface provided by the frictional forces between soil grains is negligible for the small-diameter particles at the *Surveyor VI* landing site. As a result, upper-bound estimates of soil cohesion are equal to the maximum values of applied shearing stress. Since each vernier engine caused some soil erosion, the minimum value for an upper-bound soil cohesion estimate is the shear stress caused by vernier engine 1. This value gives 0.12 N/cm^2 as the upper-bound estimate of soil cohesion.

During the hop, the maximum static pressure loading on the lunar surface occurred under vernier engine 3 about 0.2 sec after the initiation of the maneuver. Figure IV-48 indicates that the corresponding stagnation pressure was about 1.35 N/cm^2.

Apparently, an explosive type of soil cratering did not occur during the hop. Under the assumption that Terzaghi's bearing capacity theory is applicable for this type of surface loading, estimates are made of the minimum value of soil cohesion needed to prevent a bearing-capacity failure for various values of soil density and internal friction angle.

In Ref. IV-14, the constant pressure loading, acting on a circular region of radius, a, at which failure occurs, is given as

$$p = 1.3\, N_c\, \tau_{coh} + 0.6\, wa\, N_\gamma \tag{7}$$

where N_c and N_γ are nondimensional constants depending on the soil internal friction angle; w and τ_{coh} are the soil weight density and cohesion, respectively.

The values of the nondimensional constants read from Fig. IV-39 in Ref. IV-9 are

$$\begin{aligned} &\phi = 35 \text{ deg}; \quad N_c = 58, \quad N_\gamma = 42 \\ &\phi = 30 \text{ deg}; \quad N_c = 37, \quad N_\gamma = 20 \end{aligned} \tag{8}$$

so that the loading at which a penetration occurs is

$$p = \begin{cases} 75.4\, \tau_{coh} + 25.2\, wa, & \phi = 35 \text{ deg} \\ 48.1\, \tau_{coh} + 12.0\, wa, & \phi = 30 \text{ deg} \end{cases} \tag{9}$$

To apply Terzaghi's theory to the pressure loading in Fig. IV-48, an equivalent constant pressure and radius over which it acts must be introduced. This is accomplished by assuming that the loading is equal to the maximum loading (the stagnation pressure) and determining the equivalent radius of loading such that the total force acting on the surface is equal to that caused by the theoretical pressures. According to this equivalence, the stagnation pressure acting over a circular area of radius

$$R = z \left(\frac{2}{2 + k} \right)^{1/2} \tag{10}$$

produces the same total force on the surface as that caused by the theoretical pressure loading. The engine parameter k (Ref. IV-10) is defined as:

$$k = \gamma (\gamma - 1)\, M_e^2 \tag{11}$$

where γ is the gas specific heat ratio and M_e is the exit mach number. For *Surveyor* vernier engines, $k = 11.1$. The corresponding nozzle height, z, for the pressure loading shown in Fig. IV-47 is 33 cm; thus, $R = 13$ cm. Taking this radius as an approximation to the radius a in Eq. (9) and p to be the stagnation pressure, $p_s = 1.35$ N/cm², Eq. (9) becomes

$$\omega(\text{N/cm}^3) = \begin{cases} 0.00413 - 0.230\, \tau_{coh}, & \phi = 35 \text{ deg} \\ 0.00865 - 0.308\, \tau_{coh}, & \phi = 30 \text{ deg} \end{cases} \tag{12}$$

Equation (12) is plotted in Fig. IV-49, which shows those values of soil cohesion and weight density for which the loading given in Fig. IV-47 is just sufficient to produce a soil bearing-capacity failure for internal friction angles of 30 and 35 deg. For a soil weight density of 2.4×10^{-3} N/cm³ (mass density is 1.5 g/cm³), a soil cohesion greater than 0.0073 N/cm², as indicated in Fig. IV-49, would be sufficient to prevent a bearing-capacity failure for a soil with a 35-deg internal friction angle. For a friction angle of 30 deg, the required value of cohesion is 0.020 N/cm². Since no such failure was observed during the hop, this procedure provides an estimate of the soil cohesion lower bound of 0.0073 N/cm².

c. Lunar soil adhesion. As shown in Fig. IV-39, lunar material (apparently a clump) ejected by the exhaust from a vernier engine during the hop, struck and adhered to the photometric target. This permits an estimate of a value for the adhesion of lunar surface material to spacecraft surfaces.

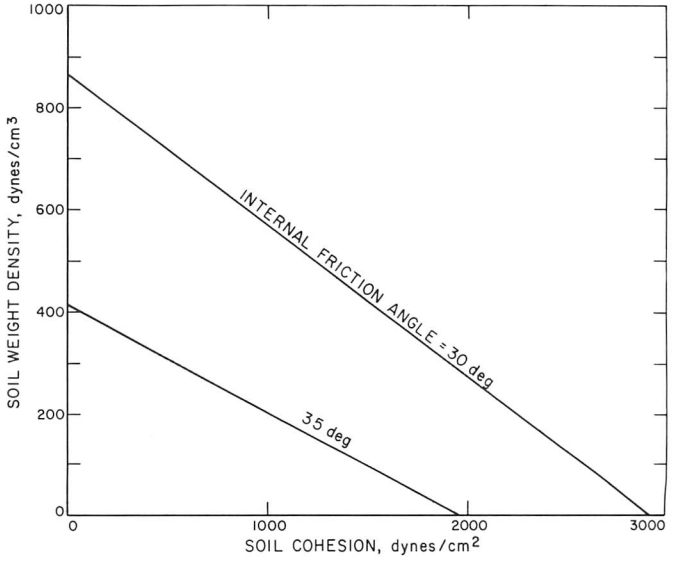

Fig. IV-49. Values of soil cohesion and weight density for which the maximum loading under vernier engine 3 is equal to the soil bearing capacity.

In Fig. IV-37, the longest shadow of material adhering to the target is 3 mm; the sun was approximately 17 deg from the plane of the photometric target. Thickness of the material casting this shadow was 0.9 mm. For a density of 1 to 2 g/cm^3, the corresponding unit weight is 14 to 28 dynes/cm^2. The plane of the target is about 75 deg from the horizontal; therefore, the surface material is supported by adhesion, not friction. Thus, the adhesion must be at least 10 dynes/cm^2. The 10^4-dyne/cm^2 bearing capacity of the upper few millimeters of the lunar surface is consistent with a cohesion greater than 3×10^3 dynes/cm^2. Adhesion must be less than cohesion or soil would stick to spacecraft parts touching the lunar surface. Thus, the adhesion is probably not more than approximately 10^3, and possibly not more than 10^2, dynes/cm^2.

The estimated lower bound is for adhesion of lunar surface material to the silicate-base paint with which the epoxy-glass photometric target was coated. Moreover, it is for material thrown against the target at a velocity of a few meters/second, as discussed below. Adhesion of surface material lightly pressed against the spacecraft is apparently lower. The control bar for the magnet and its support bracket, coated with a similar paint, remained clean after the hop.

The surface material continued to adhere to the photometric target despite the loads imposed by the landing after the hop. However, these loads were smaller at the target than at the main spaceframe because of the attenuation provided by the omnidirectional antenna boom.

An estimate was determined of a minimum velocity with which the clump struck the target. The height of the target is about 1 m; thus, the initial velocity of the clump must have been sufficient to carry it at least 1 m above the surface. An examination of the lunar surface indicated that some debris was deposited at least 2.4 m from an area directly below the vernier engines. For an initial velocity, v_0, and an initial angle, θ, from the lunar surface, the range, R, is

$$R = \frac{v_0^2 \sin 2\theta}{g} \tag{13}$$

and the vertical height is

$$h = \frac{v_0^2 \sin^2 \theta}{2g} \tag{14}$$

from which

$$\tan \theta = 4 \left(\frac{h}{R}\right) \tag{15}$$

Assuming that the range is 2.4 m and the maximum height is 1.0 m, the initial angle at which the soil particles left the surface is about 60 deg; the initial velocity is about 2.1 m/sec. Thus, the horizontal component of the velocity is 1.0 m/sec and represents the maximum velocity of impact on the target.

According to the theory in Refs. IV-10 and IV-11, it is possible that such a velocity was imparted to soil particles below vernier engine 3 at $t = 0.2$ sec. In the theory, the surface is assumed to be flat; actually, the undulating lunar surface contains particles of various sizes which were ejected from the region of the footpad and crushable block impacts. Thus, because of the undulating surface, it is possible that some particles departed from the surface at an angle as large as 60 deg without the necessity of first developing an erosion crater with 60-deg sloping sides. In tests conducted at the Jet Propulsion Laboratory, fragments as large as 3 cm were ejected at velocities of 6 m/sec at high angles. Although a definite point of origin of the lunar material deposited on the photometric target has not been determined, it is believed that viscous erosion could have caused the transfer of lunar material onto the target.

C. Lunar Soil Erosion: Attitude Control Jet Firing

1. Test Explanation

A cold nitrogen gas jet is mounted on each spacecraft leg (Fig. IV-50) to control the spacecraft attitude during unpowered flight; these jets can be commanded to operate for durations longer than 0.5 sec after the spacecraft has landed.

Since the attitude control jet mounted on leg 2 has its axis pointing in a downward direction (Fig. IV-50), the gas flow from the nozzle of the jet could change the lunar surface, permitting an estimate of soil cohesion and other properties of the surface material. Any such disturbance of the soil was expected to be small; therefore, good photographic coverage of the jet impingement area at a low sun angle was necessary to obtain useful results from the test.

The jet on leg 2 is inclined at an angle of 24 deg (Fig. IV-50) from the spacecraft vertical axis. The conical

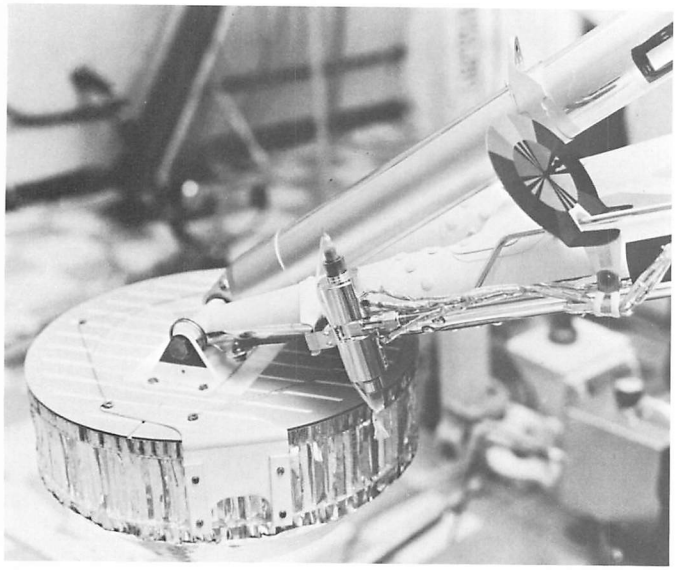

Fig. IV-50. A *Surveyor* leg 2 assembly showing the attitude control jet mounted between the footpad and the photometric target.

nozzle of the jet has an 0.1-cm-diameter throat and an 0.35-cm-diameter exit plane. Nominally, the jet operates at a chamber pressure of 27.5 N/cm^2 and produces an 0.31-N thrust. The gas flow rate is nominally 0.024 m^3/min at a 27.5-N/cm^2 chamber pressure.

On Day 315, the leg 2 jet was operated for 4 sec; 25 min later, it was operated for 60 sec. Pictures were taken before, during, and after the jet operations. The sun was approximately 16 deg above the horizon.

2. Observations

Displacement of fine grains of soil, individual clumps, and partial erosion of some of the larger fragments occurred during both the 4- and 60-sec firings of the attitude control jets. Gross surface features were not altered by either firing; i.e., there has been no cratering, nor have small holes been filled with soil. Distance from the attitude control jet centerline intercept with the lunar surface to the farthest point of known soil disturbance is 15 cm for the 4-sec firing and 25 cm for the 60-sec firing. The largest fragment moved is 1.5 cm long and 1.0 cm in diameter.

The extent of soil movement is shown in Figs. IV-51 through IV-55. Figure IV-51 is a wide-angle view of leg 2, footpad 2, the attitude control jet, and the impingement area. Figures IV-52 and IV-53 are, respectively, pre- and post-firing, narrow-angle mosaics of the 4-sec firing; Figs. IV-54 and IV-55 are pre- and post-firing mosaics of the 60-sec firing. Some soil fragments moved or altered by the firings are circled on each mosaic; those on pre-firing mosaics (Figs. IV-52 and IV-54) represent fragments, blown away or eroded, that can not be seen in post-firing pictures. Circled portions on the post-firing mosaics (Figs. IV-53 and IV-55) represent fragments that arrived at their present sites because of the firings. Each of the mosaics consists of three rows of pictures, representing the three lowest rows in elevation which can be taken by the television camera, looking toward leg 2, and which include lunar surface features.

The most interesting disturbance caused by the jet impingement is the pair of protrusions marked A and B in Figs. IV-52 and IV-54. Originally, they were located at a distance of about 12 to 15 cm from the center of impingement. During the 4-sec operation of the jet, protrusion A was broken and apparently landed at A′ in Fig. IV-53. In Fig. IV-51, which was taken near the end of the 4-sec firing, A can still be seen in its original position. But in Fig. IV-53, taken after the firing, A has been moved to A′. This indicates that the disturbance of A did not occur at the instant the jet was turned on; several seconds of loading from the jet gases were required before the protrusion broke. During the 60-sec firing, protrusion B was broken off and landed at B′ in Fig. IV-55. A′ and B′ are in a depression below the original positions of A and B.

Most of the soil disturbance was caused by the 4-sec firing of the jet, although the 60-sec firing produced some disturbance, notably that of protrusion B mentioned above and in the area directly below the jet. It appears that most of the jet gases impinged into a small depression, as indicated by the large number of displaced particles it originally contained (Figs. IV-52 to IV-55).

Some of the disturbance caused by the jet impingement appears to have been on soil clumps, which were formed by the footpad 2 landing. For example, the clumps sitting on top of the rim of the depressed area under footpad 2 appear to have been made up of disturbed soil even before the jet firings. However, most other material blown away by the actual jet firings seemed to come from the undisturbed lunar surface. The jet impingement area was about 2.4 m from the camera. Sizes of particles on the lunar surface and their displacements can be estimated from the scale provided by the 5.1-cm-diameter inner circular area on the nearby photometric target, which is about 2.1 m from the camera.

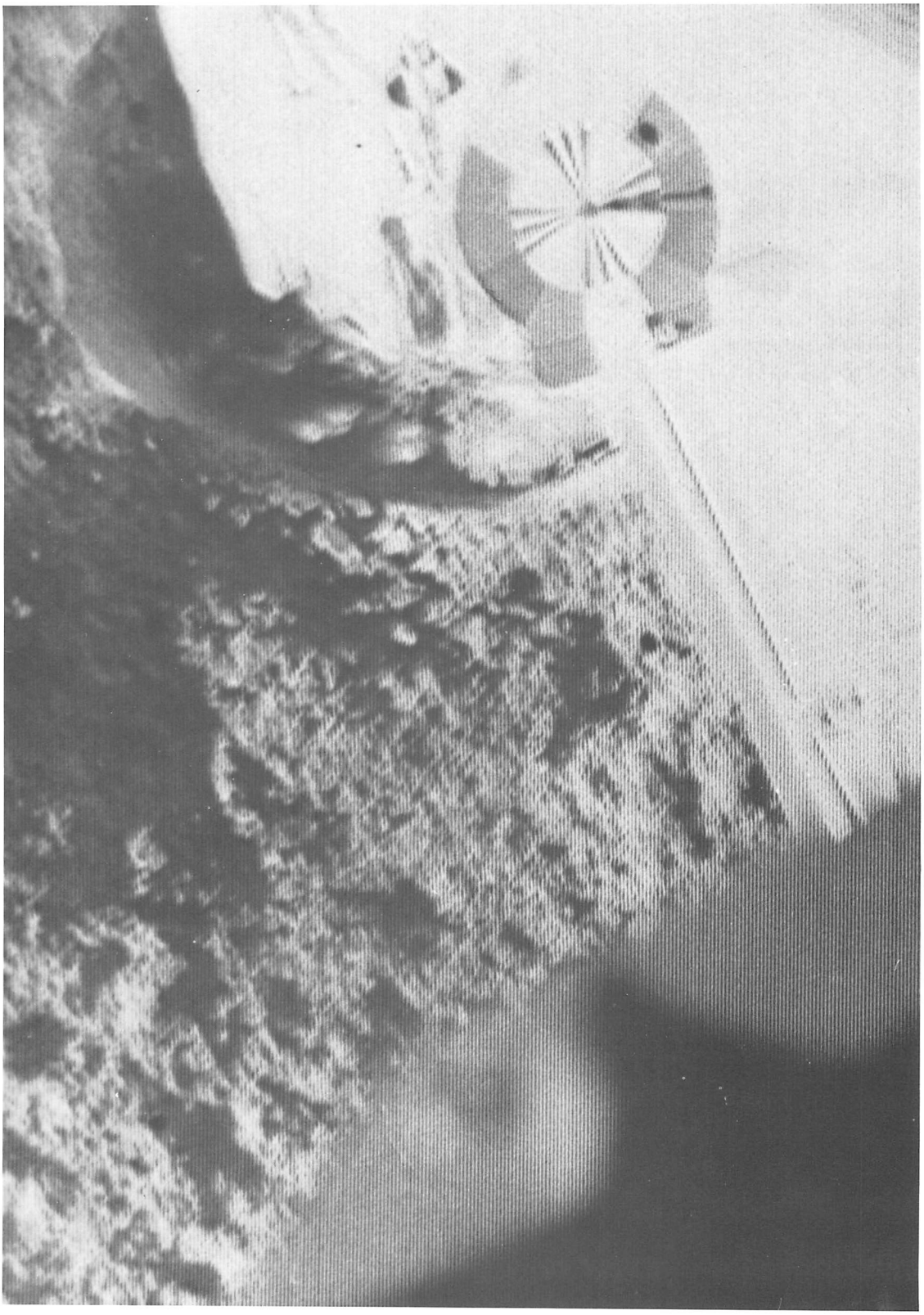

Fig. IV-51. Portion of a wide-angle picture of footpad 2 and attitude control jet taken during the 4-sec firing (Day 315, 03:22:49 GMT).

Fig. IV-52. Mosaic of narrow-angle pictures taken just prior to the 4-sec firing of the attitude control jets. Representative fragments, shown by later post-firing pictures to have been moved or partially eroded by the firing, are circled. The dark area cutting diagonally across each picture is caused by the camera housing. A line extending through the center of the attitude control jet is shown by the arrow. The approximate point where this line intercepts the lunar surface is shown by an X (Day 315, Catalog 6-MP-1). →

Fig. IV-53. Mosaic of pictures taken just after the 4-sec firing of the attitude control jets. Representative fragments that arrived at their present sites because of the firing are circled (Day 315, Catalog 6-MP-2). →

Fig. IV-54. Mosaic of the same pictures used in Fig. IV-53; however, the fragments circled are those fragments shown by later pictures to have been moved by the 60-sec attitude control jet firing (Day 315, Catalog 6-MP-2). →

Fig. IV-55. Mosaic of pictures taken after the 60-sec attitude control jet firing. Fragments circled have arrived at their present sites after the 60-sec firing (Day 315, Catalog 6-MP-3). →

Fig. IV-52.

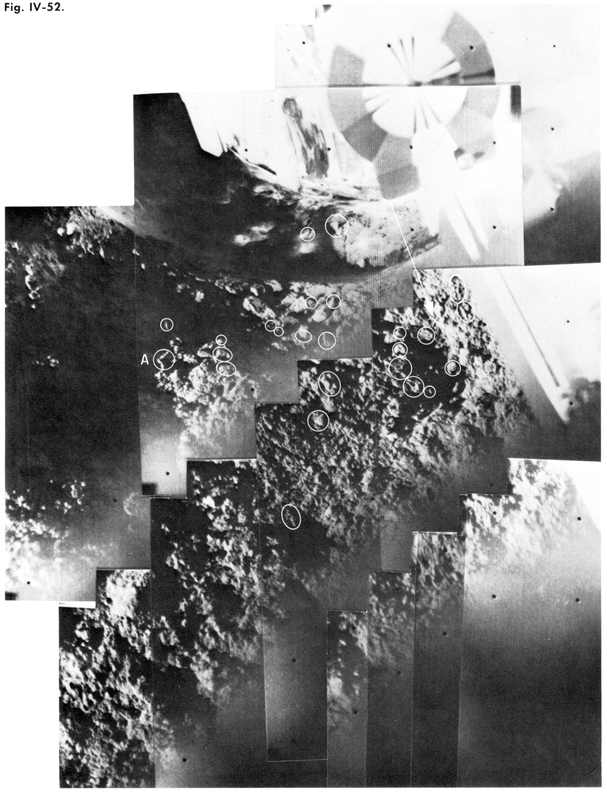

Fig. IV-53.

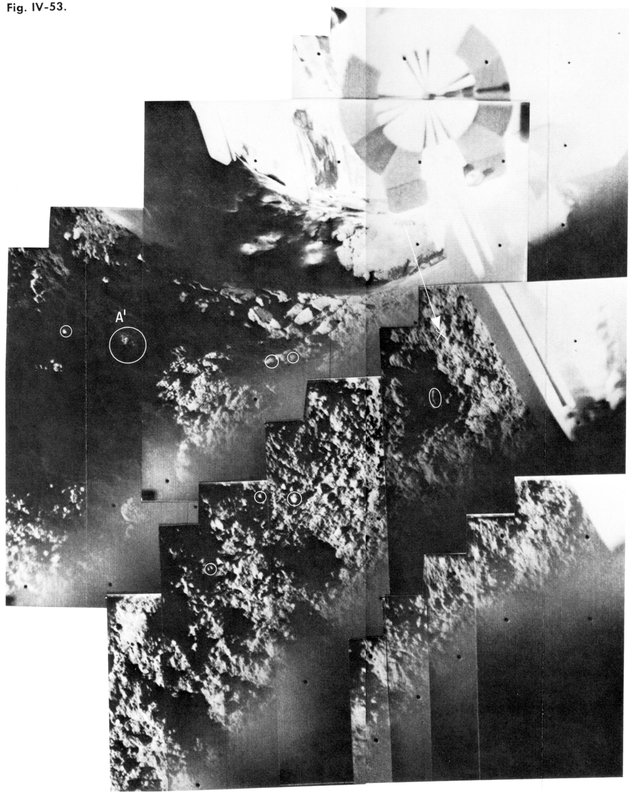

Fig. IV-54.

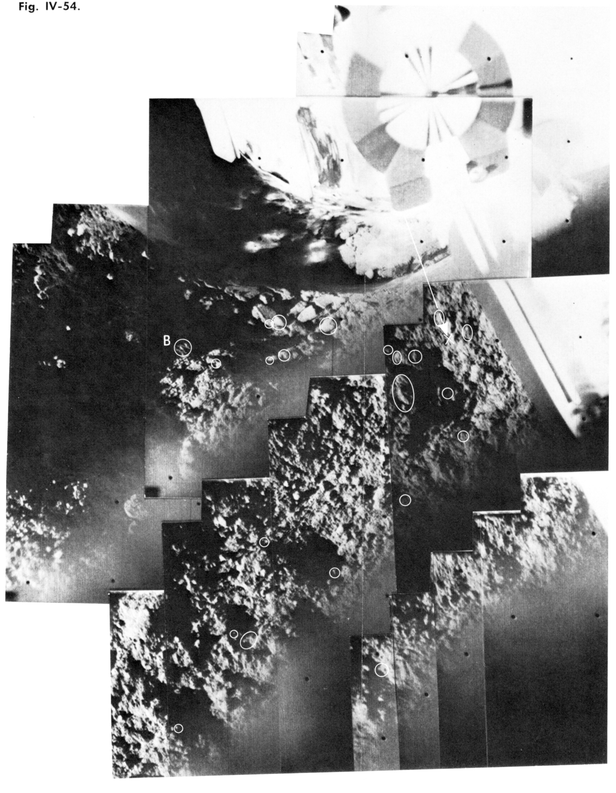

Fig. IV-55.

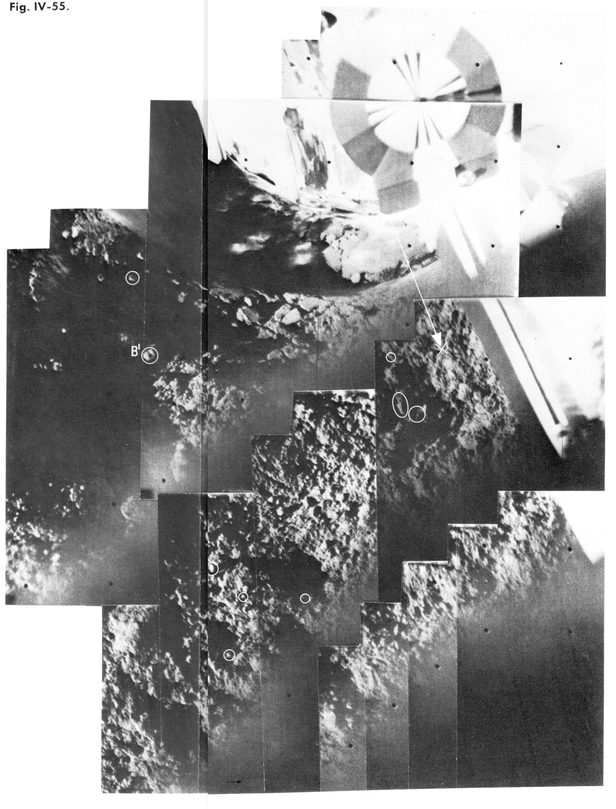

(Blank Page)

3. Simulation and Analysis

Before the *Surveyor VI* launch, tests were conducted at the Jet Propulsion Laboratory in which an attitude control jet was fired in a vacuum chamber with an ambient pressure of 10^{-5} mm of mercury and the exhaust gases impinged normally onto a flat plate.[4] The pressure profiles on the plate were measured for two different nozzle heights: 7.7 and 15.4 cm. The results are shown in Fig. IV-56, together with the theoretical surface pressure calculated from Roberts' theory for a thrust level of 0.31 N and other parameters as listed in Table IV-4. The correlation between measured and calculated pressure profiles indicates that the theory provides reasonable estimates of the surface loading. The theoretical static and dynamic pressures on a flat surface are shown in Fig. IV-57 for the *Surveyor VI* jet 2 inclined at an angle of 24 deg from a normal to the lunar surface and at a nozzle height of

[4]H. Y. Ko and E. M. Christensen, unpublished report.

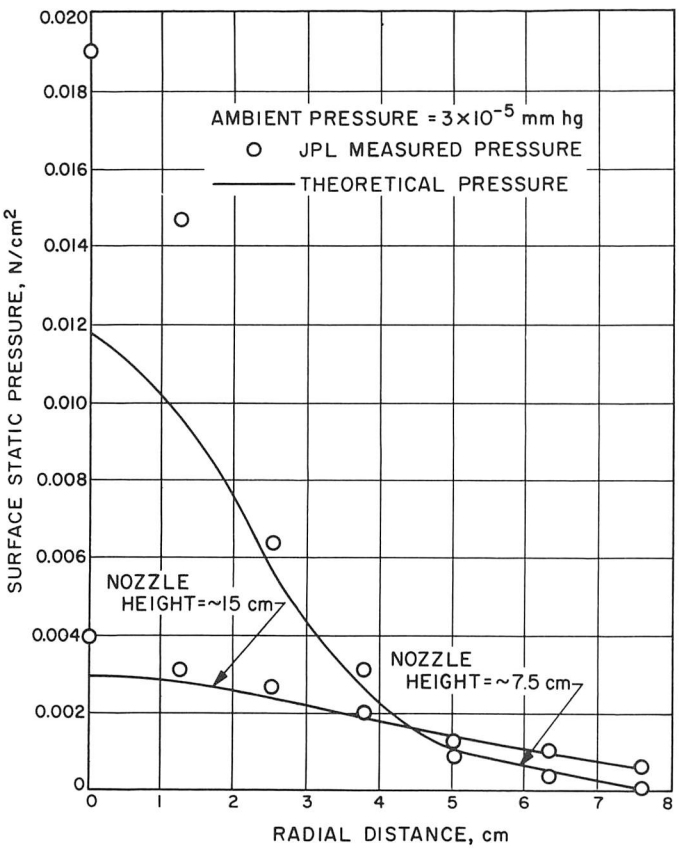

Fig. IV-56. Comparison of theoretical and measured static pressures along a planar surface parallel to the attitude control jet exit plane; thrust = 0.31 N, vacuum chamber pressure = 3 × 10^{-5} mm Hg.

Table IV-4. Attitude control jet parameters used in calculations

Nozzle exit radius	0.176 cm
Exit mach number	4.2
Gas constant	297 m²/sec² °K
Gas specific heat ratio	1.4
Chamber gas temperature	296°K
Nozzle height	10.4 cm
Thrust axis tilt	24 deg
Engine thrust	0.31 N
Chamber pressure	27.6 N/cm²

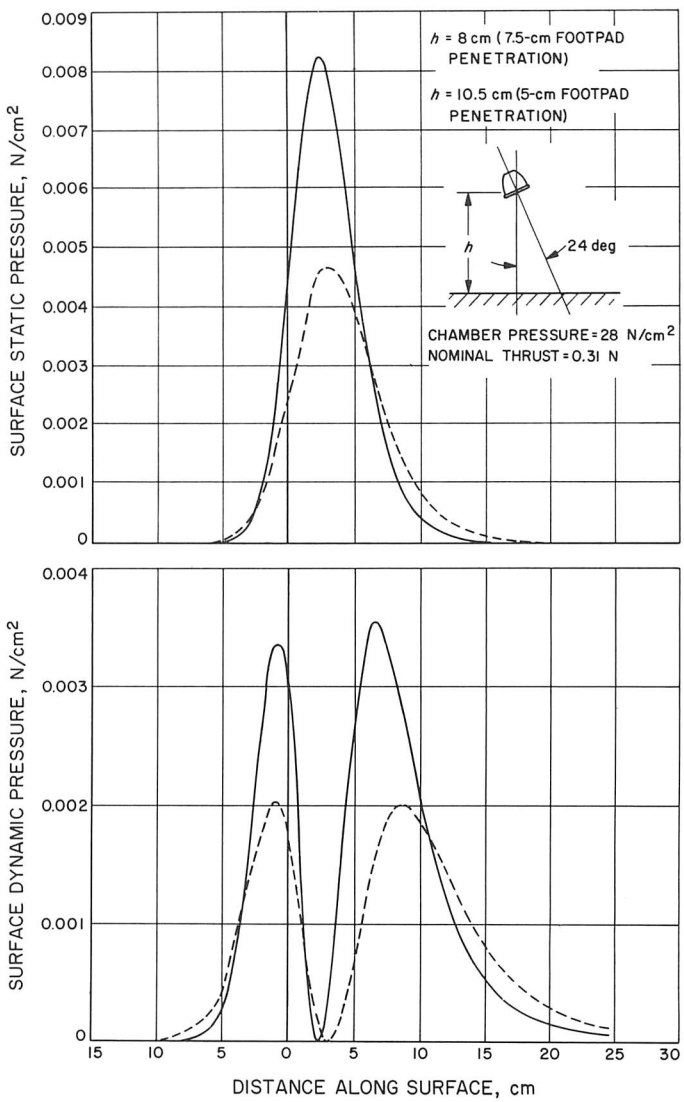

Fig. IV-57. Theoretical static and dynamic pressures along a planar surface produced by the attitude control jet with its 24-deg tilt; thrust = 0.31 N.

10.6 cm. This nozzle height is based on a 5-cm penetration for footpad 2.

Jet firing tests on soil beds were also conducted under vacuum conditions prior to the *Surveyor VI* launch.[4] The soils used were sandy silts and were prepared with different amounts of cohesion by mixing the soil with water and slowly baking off the moisture. When the jet was fired normally onto the prepared soil surface for different durations and nozzle heights, various amounts of soil disturbance were observed, depending on the duration of firing and the soil cohesion. In these tests, and also on the moon, the soil erosion that occurred appeared to be of the viscous type; a diffused gas surface eruption did not take place. It was generally found that no soil erosion occurred whenever the soil cohesion exceeded some limiting value, irrespective of the duration. For the soils used and for a nozzle height of 15.2 cm, samples with a cohesion greater than 0.17 N/cm^2 did not erode.

For soils with a cohesion less than 0.05 N/cm^2, soil fragments were blown away, leaving an irregular hole in the soil surface within 4 sec. However, symmetrical craters with diameters greater than 10 cm were formed in cohesionless soils in less than 1 sec. The major limitations of these tests performed to date is that the soil surface was flat and the ambient pressure was 10^{-3} mm Hg, i.e., the jet plume did not achieve full expansion. It is believed that erosion should be less on the moon because the plume would be less concentrated; however, significantly less erosion occurred during tests performed in the atmosphere than when performed at 10^{-3} mm of mercury. Nevertheless, it is believed that the terrestrial tests provide an estimate for lunar soil cohesion values.

D. Summary and Preliminary Conclusions

Surveyor VI executed a nominal landing on a gently undulating lunar surface; the spacecraft tilt after landing was less than 1 deg. After the initial landing, the spacecraft was commanded to hop by firing the vernier rocket engines for 2.5 sec. After the 2.4-m (horizontal distance) hop, most of the spacecraft/ground contact areas of the original landing were exposed to the camera, as well as areas that were eroded by vernier engine exhaust gases during liftoff.

A first evaluation of photographic and telemetry data, aided by analytical and laboratory simulations performed thus far, has provided the following preliminary conclusions.

(1) The soil is predominantly fine-grained and granular, similar to that found at the previous *Surveyor* landing sites.

(2) Subsurface soil is darker than the undisturbed soil at the surface, as shown by erosion effects created by the initial landing and by the firing of the vernier engines.

(3) Footpad and crushable block imprints of the original landing indicate that the soil is compressible.

(4) Static bearing strength increases with depth as follows:

  (a) In the upper few millimeters: <0.1 N/cm^2 (imprints of small rolling fragments).

  (b) At a depth of approximately 2 cm: 1.8 N/cm^2 (imprint of crushable block).

  (c) At a depth of 5 cm: 5.5 N/cm^2 (*Surveyor I* footpad penetration).

(5) An average lunar surface static bearing strength of 3.4 N/cm^2, determined for *Surveyor VI* footpad penetration into an assumed compressible soil model, is similar to that observed in the *Surveyor I* and *III* landings.

(6) Dynamic bearing stress developed on crushable block 3 exceeded 2.4 N/cm^2 during penetration to a 3-cm depth, as evidenced by the rupture of the aluminum sheet on the bottom of the crushable block.

(7) Soil density of the surface is estimated to be between 0.7 and 1.2 g/cm^3; corresponding porosities, for an assumed grain density of 3 g/m^3, are 0.8 and 0.6. An estimate of soil density a few centimeters lower beneath a footpad is 1.6 g/cm^3; corresponding porosity would be 0.5 (based upon assumed soil models).

(8) Estimate of the soil shear wave velocity is between 15 and 36 m/sec, and of the compressional wave velocity between 31 and 91 m/sec. These estimates, based on oscillations in the spacecraft landing leg forces during touchdown for both landings, are lower than those expected for terrestrial soils with mechanical properties as listed in this report.

(9) Viscous soil erosion occurred during the vernier engine and attitude control jet firings, i.e., erosion by the entrainment of soil particles as gas flows over the surface.

(10) Soil disturbed by the spacecraft's original landing was more readily eroded by the engine exhaust gases than was the undisturbed soil.

(11) A diffused gas eruption of the soil did not occur during the vernier engine firing because the surface gas pressure decreased slowly during spacecraft lift-off. In contrast, although the surface pressure was less than one-third of that during the *Surveyor VI* firing, diffused gas surface eruption occurred during the *Surveyor V* rapid engine shutdown.

(12) Most of the fine soil eroded during the vernier engine firing was picked up by exhaust gases moving in a horizontal sheet along the lunar surface and was redeposited at distances up to several meters.

(13) Some soil clumps and fragments ejected from the exhaust gas impingement areas rose at least 1 m above the lunar surface and traveled at least 4 m. One such clump impacted and partially adhered to the photometric target.

(14) With the exception of the photometric target, very little spacecraft contamination was caused by the surface erosion. No degradation in any spacecraft functions was observed.

(15) Adhesive strength of lunar material impacting and adhering to the photometric target is estimated to be between 10 and 100 dynes/cm^2. Lunar material pressed against spacecraft parts apparently did not adhere.

(16) Estimated soil cohesion was determined as follows:

(a) From vernier engine firings: 0.007 to 0.12 N/cm^2.

(b) From attitude control jet firing: 0.05 to 0.17 N/cm^2.

References

IV-1. Christensen, E. M., Batterson, S. A., Benson, H. E., Choate, R., Jaffe, L. D., Jones, R. H., Ko, H. Y., Spencer, R. L., Sperling, F. B., and Sutton, G. H., "Lunar Surface Mechanical Properties," *Surveyor III Mission Report. Part II: Scientific Results,* Technical Report 32-1177, pp. 111–153, Jet Propulsion Laboratory, Pasadena, Calif., June 1, 1967.

IV-2. Christensen, E. M., Batterson, S. A., Benson, H. E., Choate, R., Hutton, R. E., Jaffe, L. D., Jones, R. H., Ko, H. Y., Schmidt, F. N., Scott, R. F., Spencer, R. L., and Sutton, G. H., "Lunar Surface Mechanical Properties," *Surveyor V Mission Report. Part II: Science Results.* Technical Report 32-1246, pp. 43–88, Jet Propulsion Laboratory, Pasadena, Calif., November 1, 1967.

IV-3. Christensen, E. M., Batterson, S. A., Benson, H. E., Chandler, C. E., Jones, R. H., Scott, R. F., Shipley, E. N., Sperling, F. B., and Sutton, G. H., "Lunar Surface Mechanical Properties," *Surveyor I Mission Report. Part II: Scientific Data and Results,* Technical Report 32-1023, pp. 69–85, Pasadena, Calif., September 10, 1966.

IV-4. Spencer, R. L., *Determination of Footpad Penetration Depth from Surveyor Spacecraft Shadows,* Technical Report 32-1180, Jet Propulsion Laboratory, Pasadena, Calif., 1967.

IV-5. Sperling, F., and Garba, J., *A Description of the Surveyor Lunar Landing Dynamics and an Evaluation of Pertinent Telemetry Data Returned by Surveyor I,* Technical Report 32-1035, Jet Propulsion Laboratory, Pasadena, Calif., 1967.

References (contd)

IV-6. Scott, R. F., and Roberson, F. I., "Soil Mechanics Surface Sampler: Lunar Surface Tests, Results, and Analyses," *Surveyor III Mission Report, Part II: Scientific Results,* Technical Report 32-1177, pp. 69–110, Jet Propulsion Laboratory, Pasadena, Calif., June 1, 1967.

IV-7. Shoemaker, E. M., Batson, R. M., Holt, H. E., Morris, E. C., Rennilson, J. J., and Whitaker, E. A., "Television Observations from *Surveyor V*," *Surveyor V Mission Report. Part II: Science Results,* Technical Report 32-1246, pp. 7–42, Jet Propulsion Laboratory, Pasadena, Calif., November 1, 1967.

IV-8. Scott, R. F., *Problem of the Penetration of a Projectile into Soil or Soil-like Medium, or Compressible Rock,* four reports to Space-General Corporation, El Monte, Calif., 1962 (copies available from author).

IV-9. Timoshenko, S., and Goodier, D., *Theory of Elasticity,* p. 367, second edition, McGraw-Hill Book Co., Inc., New York, 1951.

IV-10. Roberts, L., "The Action of a Hypersonic Jet on a Dust Layer," presented at the Thirty-First Annual Meeting of the Institute of the Aerospace Sciences, January 1963.

IV-11. Roberts, L., "The Interaction of a Rocket Exhaust with the Lunar Surface," presented at a Specialists' Meeting on Fluid Dynamic Aspects of Space Flight, under the sponsorship of the Fluid Dynamics Panel of the Advisory Group for Aeronautical Research and Development, Marseilles, France, April 20–24, 1964.

IV-12. Scott, R. F., and Ko, H. Y., "Transient Rocket-Engine Gas Flow in Soil," to appear in *AIAA J.*

IV-13. Alexander, J. D., Roberds, W. M., Scott, R. F., "Soil Erosion by Landing Rockets," Final Report 1301, Hayes International Corporation, July 15, 1966.

IV-14. Terzaghi, K., "Theoretical Soil Mechanics," John Wiley & Sons, Inc., New York, Ninth Printing, Article 46, June 1959.

Acknowledgment

Appreciation is extended to the numerous individuals at many organizations (especially JPL and HAC) who designed, built, tested, and operated the spacecraft and the associated launch vehicle and ground stations; to Charles Goldsmith, William Peer, Alex Irving, Albert Plescia, and Lloyd Starks, JPL, for spacecraft shadow predictions, assembly of the mosaics, and the operation of the full-scale model spacecraft in the SETL; and to Dave Conaway, Margaret Dove, and John Hinchey, HAC, for assisting in the landing dynamic simulations.

V. Lunar Surface Temperatures and Thermal Characteristics

G. Vitkus, R. R. Garipay, W. A. Hagemeyer, J. W. Lucas (Chairman), and J. M. Saari

Surveyor VI landed on a primarily level area of the lunar surface at 01:01:05 GMT on Day 314 (November 10, 1967), at selenographic coordinates of 1.40°W longitude, 0.49°N latitude; the sun was approximately 3.5 deg above the eastern horizon. The spacecraft temperature data were obtained until Day 330 (November 26) at 06:41 GMT, or about 41 hr after sunset.

The spacecraft had no specially designed instrument for measuring lunar surface temperatures or thermal characteristics. Following the analyses of the data received from *Surveyors I, III,* and *V* (Refs. V-1 to V-3), outboard-face temperatures of compartments A and B were used to derive lunar surface brightness temperatures. The derived temperatures after sunset were used to estimate the thermal parameter, γ, of the lunar surface.

A. Thermophysical Properties of Landing Site, as Determined From Earth-Based Observations

The albedo and temperature measurements for the *Surveyor VI* landing site were determined from earth-based (telescope) results (Ref. V-4) to a resolution of 18 km. Thus, it is possible for the characteristics of the surface viewed by the compartments to be considerably different from those determined from earth.

The total solar albedo, A, was determined in a manner described in Ref. V-2 to be 0.084. This albedo was used to calculate Lambertian temperatures, T_L, of the surface during illumination by use of the following expression:

$$\sigma T_L^4 = S_1 (1 - A) \tag{1}$$

where S_1 is the solar insolation on the surface and σ is the Stefan-Boltzmann constant. By this definition, T_L is the temperature that a completely Lambertian surface with unity emissivity would have if it absorbed the same amount of radiation as the lunar surface under consideration. Now

$$S_1 = S_0 \sin \theta / R^2 \tag{2}$$

where S_0 is the solar constant, taken to be 1394 W/m² (2.00 cal/cm² min), θ is the elevation angle of the sun to the surface, and R is the distance from the moon to the sun in astronomical units. Lambertian temperatures were calculated for values of R appropriate for the first lunar day after landing. The results are plotted in Fig. V-1 (solid curve).

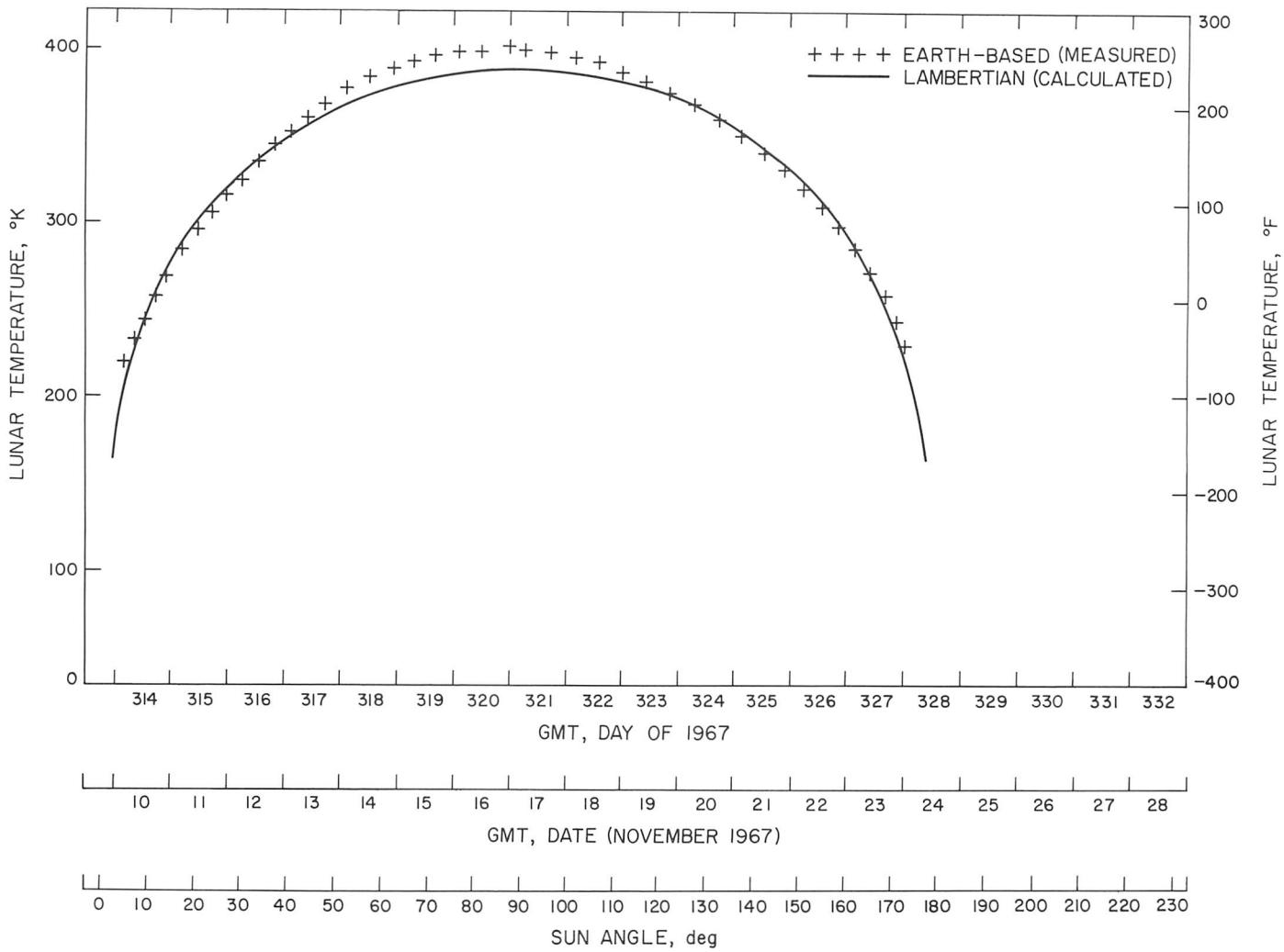

Fig. V-1. Earth-based (measured) and Lambertian (calculated) temperatures for *Surveyor VI* landing site region.

Also shown in Fig. V-1 are the temperature measurements at the landing site made from earth (plus curve). Each value has been plotted at that time in November 1967 when the elevation angle of the sun was the same as when the measurement was made. Additionally, each temperature was corrected to the appropriate moon/sun distance at each time in November. These results show the directionality of lunar infrared emission: near local noon, when the surface was observed from the same general direction as the sun, the measured temperatures were higher than the Lambertian temperatures.

The lunar surface temperatures during a lunation for the homogeneous model depend upon the thermal parameter, defined as $\gamma = (kpc)^{-1/2}$, where k is thermal conductivity, ρ is density, and c is specific heat. Lunar surface brightness temperatures for an equatorial site have been calculated by Jones (Ref. V-5) for a homogeneous model and are shown in Fig. V-2 for γ of 500, 800, and 1000 (in centimeter-gram-second units). Note that only after sunset is it possible to distinguish between different values of γ. There is considerable evidence supporting the fact that the thermal conductivity is actually represented by the expression $k = K_0 + K_1 T^3$ (where K_0 and K_1 are constants); calculations are underway to consider the effects of the temperature dependency on the lunar surface model. However, in this report, γ is used as an average property for the purpose of data comparison.

Earth-based measurements of the *Surveyor VI* landing site during the lunar night have not been made. However, eclipse observations, made by scanning the entire lunar disk (Ref. V-6) show that the site has the highly insulating property of the typical lunar surface; the temperature obtained during totality is comparable to that for a homogeneous model with a γ of 1100. The isotherms obtained during totality (Fig. V-3) reveal the area to be relatively bland.

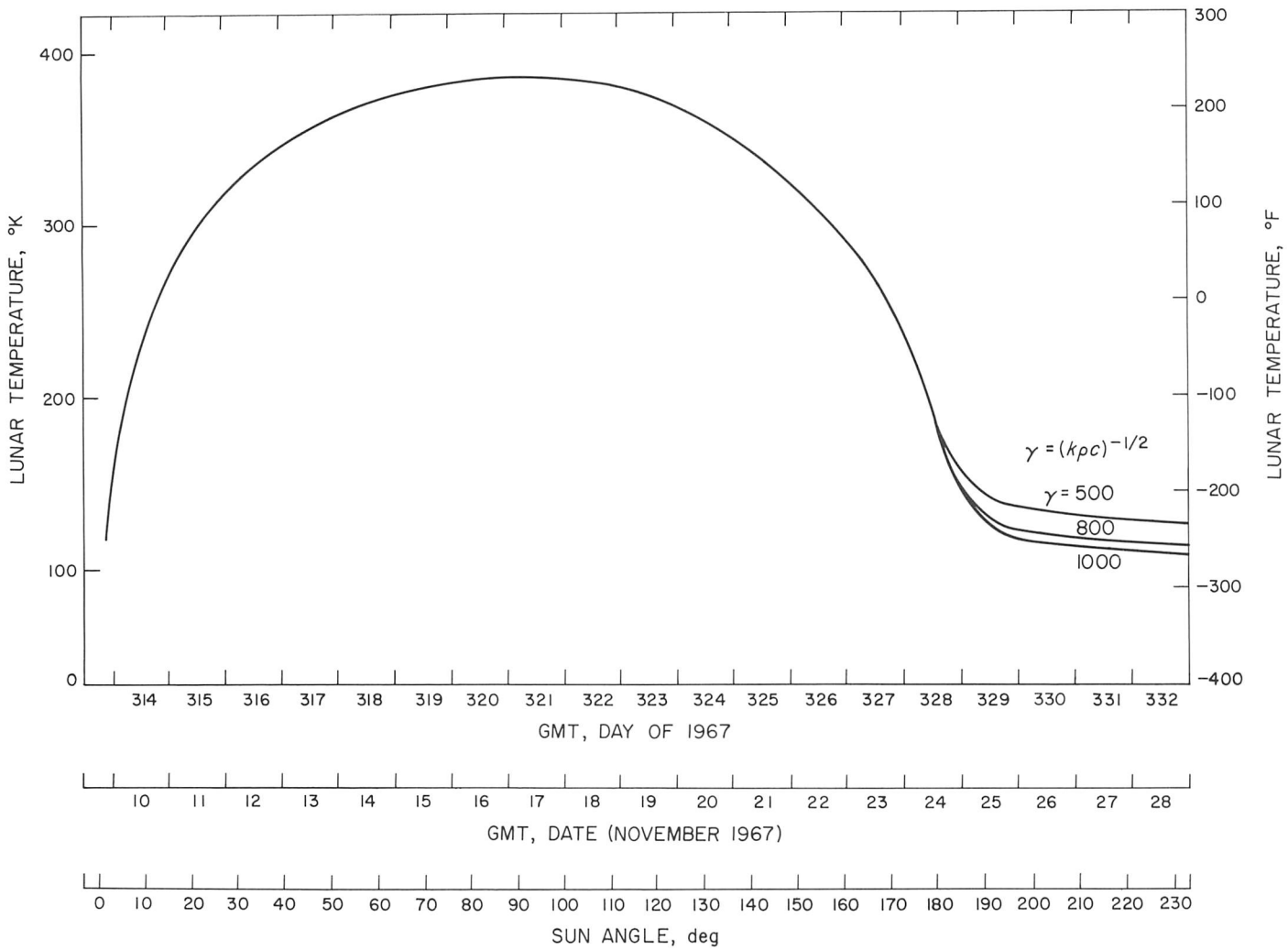

Fig. V-2. Lunar surface brightness temperatures on the lunar equator assuming homogeneous model.

B. Spacecraft Description

Surveyor VI is similar in structural and thermal design to *Surveyors I, III,* and *V*. The basic frame (Fig. V-4) is tubular aluminum, which serves as a tetrahedral mounting structure for the electronic gear and propulsion system. The three spacecraft legs are attached at the three corners of the base. The planar array antenna and solar panel, mounted on a mast approximately 1 m above the apex of the structure, cast varying shadow patterns on the spacecraft and on the lunar surface throughout the lunar day. Changes in shadow patterns occur as a result of the intermittent repositioning of the planar array antenna and solar panel and from the 0.5-deg/hr apparent movement of the sun.

Generally, the spacecraft in the sun-illuminated areas has white-paint surfaces which provide a low-solar-absorptance and high-infrared-emittance thermal finish. The polished aluminum underside greatly isolates the spacecraft from the lunar surface temperature effects.

The temperature data of various points in the spacecraft are provided by platinum resistance temperature sensors. Each sensor is calibrated individually to $\pm 1°C$; other nominal system inaccuracies degrade the overall accuracy to $\pm 3°C$.

Compartments A and B house the spacecraft electronics and battery. A blanket of superinsulation surrounds each compartment and, in turn, is covered with an aluminum panel. A temperature sensor is bonded to the polished-aluminum inner surface of the outboard face (i.e., the surface facing the superinsulation) of each compartment.

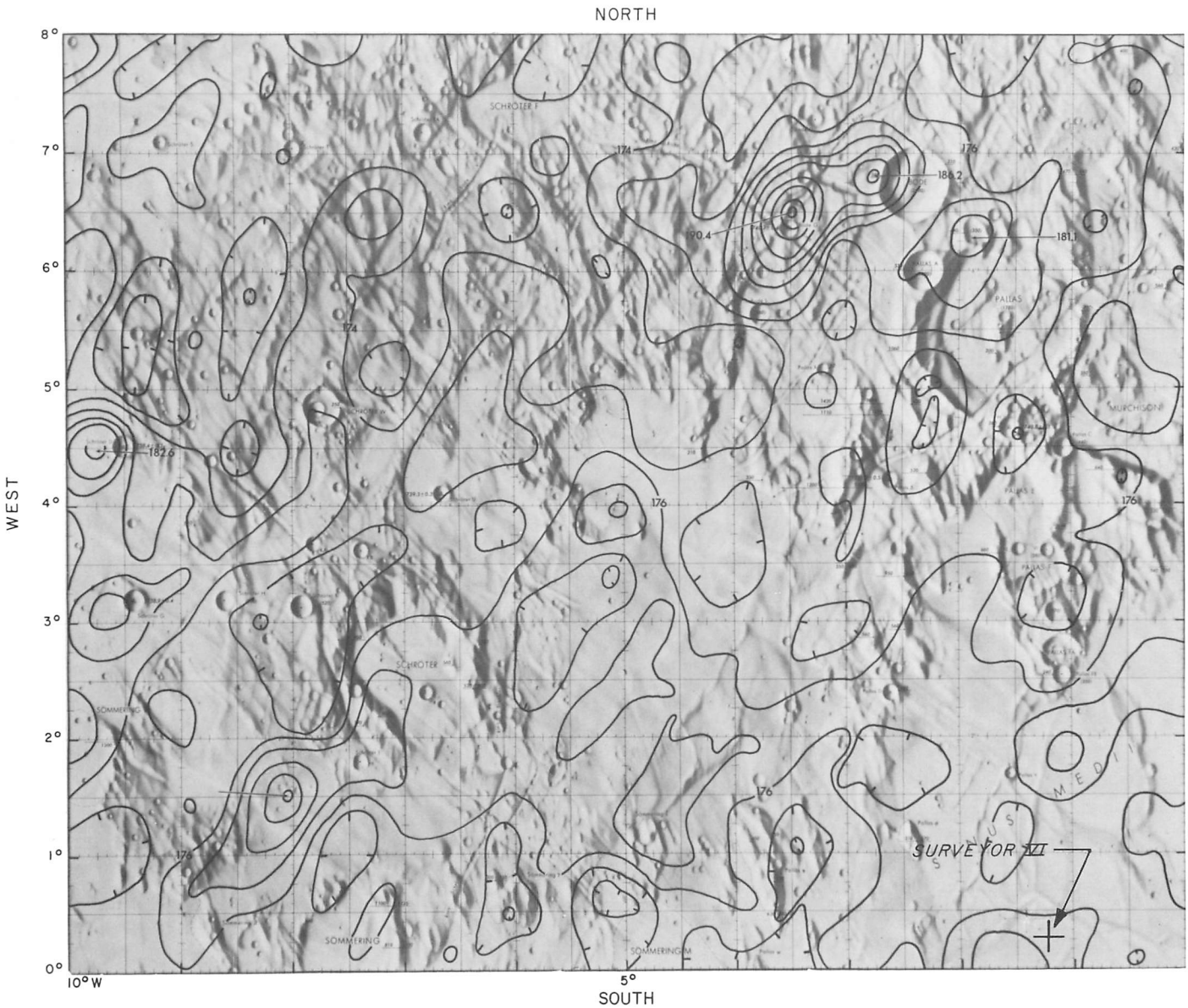

Fig. V-3. Isothermal contours (°K) for landing site region obtained during totality of lunar eclipse of December 19, 1964.

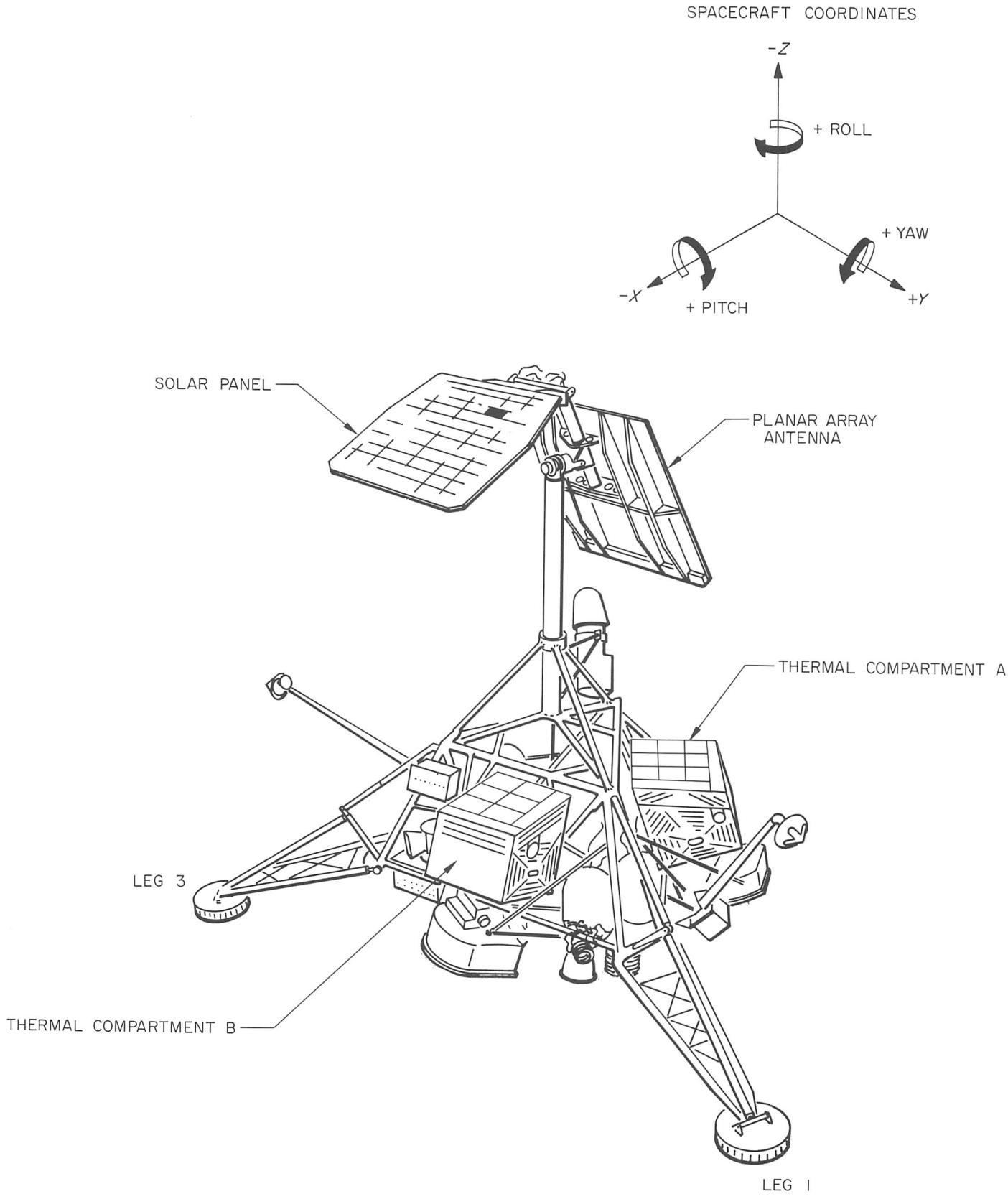

Fig. V-4. *Surveyor* spacecraft configuration.

The superinsulation isolates the panels from the inside of the compartments so that heat flux across that boundary is negligible during the lunar day; this, however, is not valid during the lunar night. Since the outboard faces of the compartments have a strong coupling to the lunar surface, but are virtually shielded from view of other spacecraft components, they allow a convenient analysis of lunar surface brightness temperatures. The parameters needed to obtain lunar surface brightness temperatures of the compartment outboard faces by the methods described in this section are:

(1) Angle between normal to outboard face and spacecraft $-Z$ axis.

  (a) Compartment A: 69° 58′.

  (b) Compartment B: 69° 30′.

(2) Properties of the outboard faces before launch.

  (a) Material: 2024 aluminum, 0.4-mm-thick panel with corrugations, coated with inorganic white paint.

  (b) Solar normal absorptance: $\alpha_s = 0.20 \pm 0.02$.

  (c) Infrared hemispherical emittance: $\epsilon_H = 0.87 \pm 0.02$.

C. Spacecraft View of Lunar Surface

Surveyor VI, after initial landing and later after the hop, landed on a generally level, smooth lunar surface. The hop occurred at 10:32 GMT on Day 321 (November 17) when the vernier engines were fired for 2.5 sec, causing the spacecraft to rise and land 2.4 m from the original landing point. The assumed orientation of the spacecraft with respect to the lunar coordinates is shown in Fig. V-5; the values were chosen on the basis of solar panel position data and were used in all calculations in this section. Compartment A looks in a southwest direction, with a view factor of 0.321 to the lunar surface after the initial landing and 0.350 after the hop. Compartment B looks toward the north, with a view factor of 0.318 to the lunar surface after the initial landing and 0.316 after the hop.

D. Compartment Data

The angle, β, between a normal to the compartment outboard faces and the sun vector is presented in Fig. V-6. The temperatures of the compartment A and B outboard faces are presented in Fig. V-7. Note that compartment A registered sudden changes in temperatures.

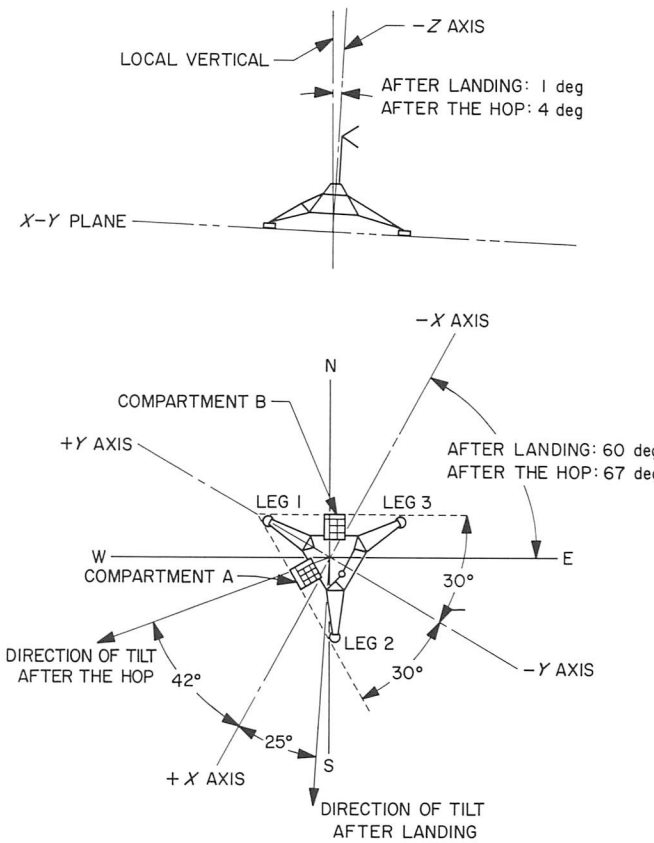

Fig. V-5. *Surveyor VI* orientation.

Fluctuations in temperatures of the outboard faces during a portion of the lunar day are caused by the shading produced by the solar panel and planar array antenna. The percentages of shadow on the outboard faces of compartments A and B are shown in Fig. V-8.

The view factor from compartment A to the shaded portion of the lunar surface is plotted in Fig. V-9; that from compartment B is negligible.

E. Lunar Surface Brightness Temperatures

Lunar surface brightness temperatures were obtained from the following heat-flux density balance equation (Ref. V-2) of the outboard faces:

$$\sigma T_2^4 = \frac{\sigma T_1^4}{\epsilon_2 (F_{12} - F_{13})} - \frac{F_{13}}{F_{12} - F_{13}} \sigma T_3^4 - \frac{\alpha_{1s} S}{\epsilon_1 \epsilon_2 (F_{12} - F_{13})} [(F_{12} - F_{13}) \rho_2 \sin \phi + \cos \beta] - \frac{\dot{q}}{\epsilon_1 \epsilon_2 (F_{12} - F_{13})} \quad (3)$$

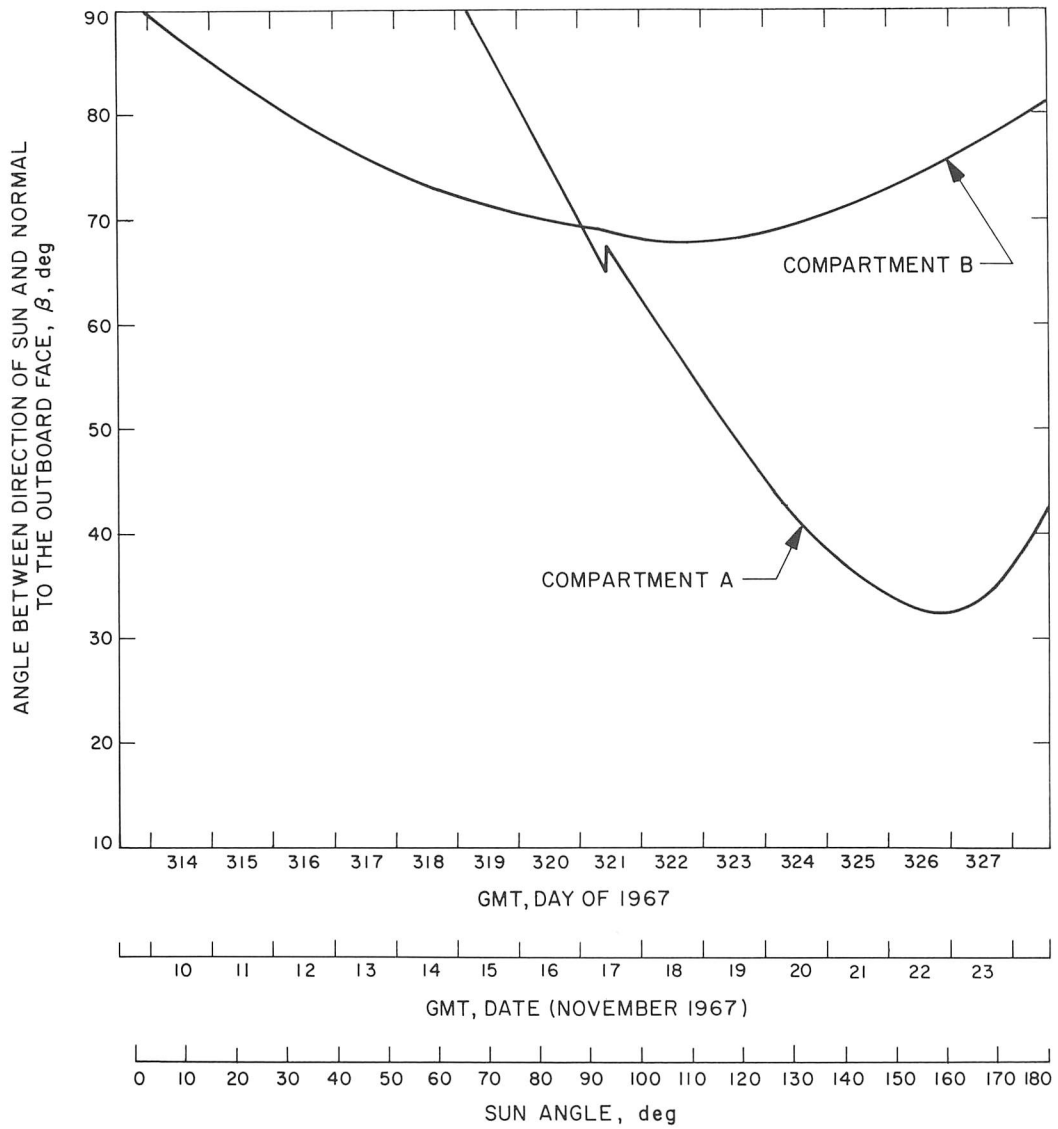

Fig. V-6. Angle between direction of sun and normal to outboard faces of compartments A and B.

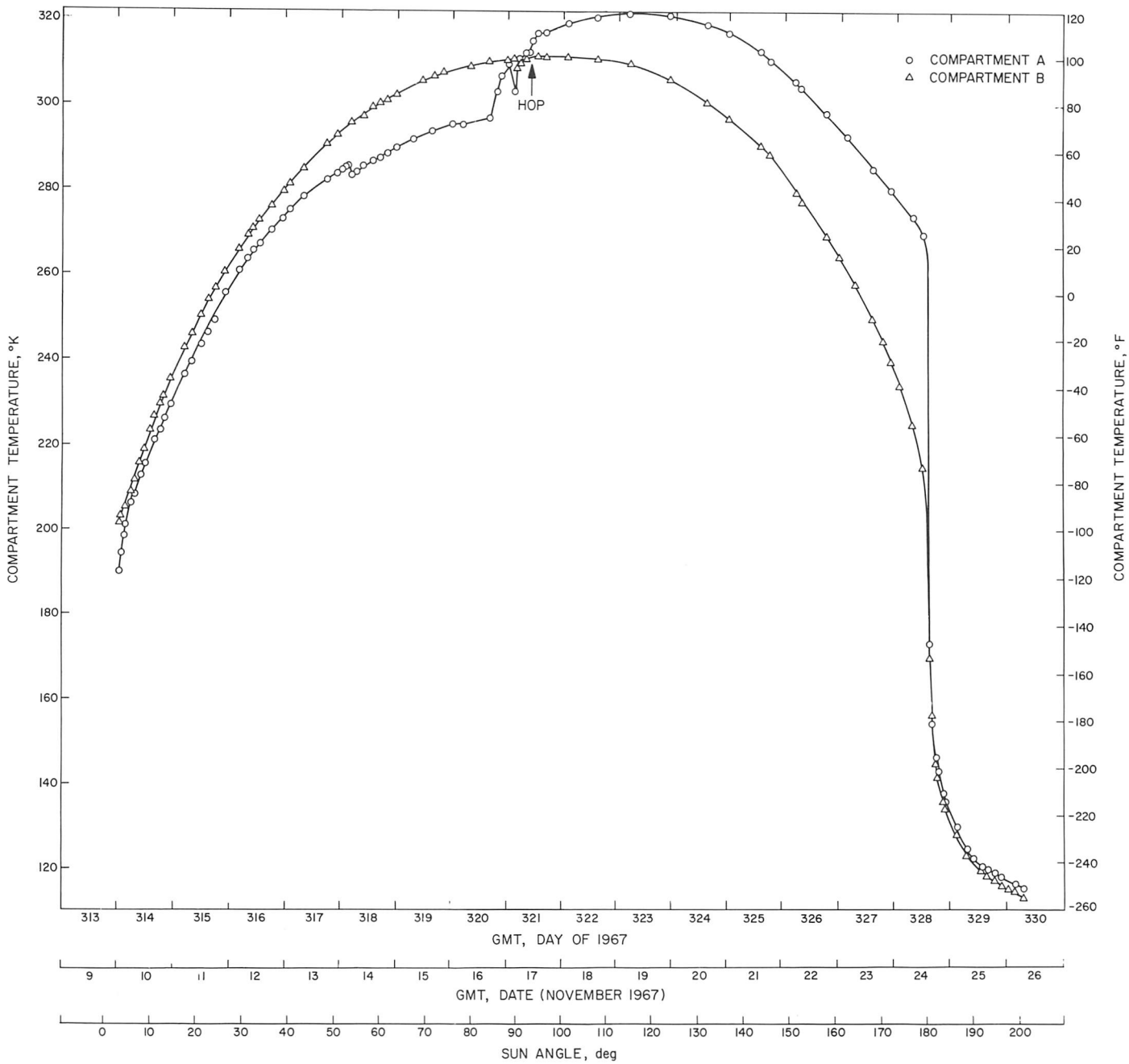

Fig. V-7. Temperatures of outboard faces of compartments A and B.

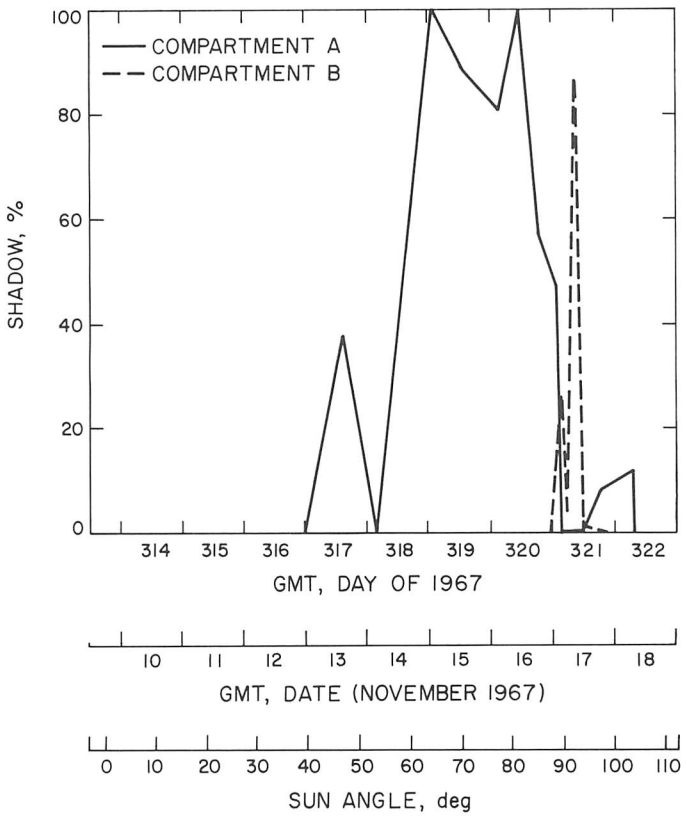

Fig. V-8. Percentage of shadow on outboard faces of compartments A and B.

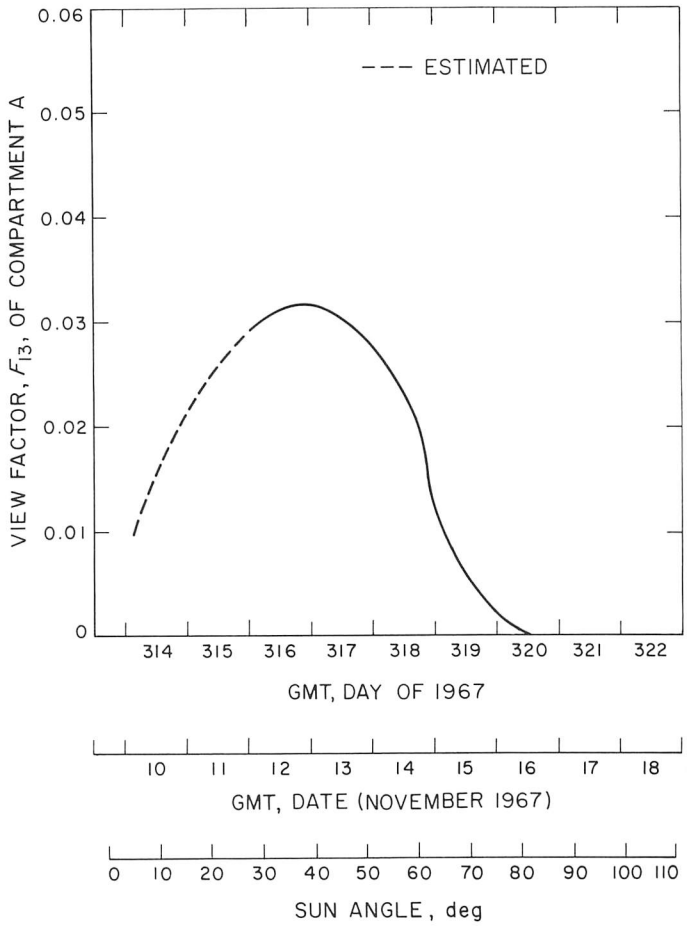

Fig. V-9. View factor, F_{13}, for compartment A and shaded part of lunar surface.

where

T_1 = compartment surface temperature

T_2 = lunar surface brightness temperature

T_3 = lunar surface brightness temperature in shadow; $T_3^4 \ll T_2^4$ is assumed

S = solar insolation = 1423 W/m²

F_{12} = geometric view factor from compartment to lunar surface

= 0.321 for compartment A after initial landing

= 0.350 for compartment A after hop

= 0.318 for compartment B after initial landing

= 0.316 for compartment B after hop

F_{13} = geometric view factor from compartment to lunar surface in shadow (from Fig. V-9)

$\dot{q}$ = conduction heat flux between inside and outside of compartment wall

= 3.5 W/m²

σ = Stefan-Boltzmann constant

= 5.675×10^{-8} W/m² °K

ϵ_1 = compartment surface emittance

= 0.87 ±0.02

ϵ_2 = lunar surface emittance

= 1.0 (assumed)

α_{1s} = compartment surface solar absorptance

= 0.20 ±0.02

β = angle between direction of sun and normal to compartment surface (from Fig. V-6)

ϕ = sun angle (between lunar surface and direction of sun)

ρ_2 = lunar reflectance to solar irradiation

= 0.084

F. Calculation Results and Comparisons

Figure V-10 represents the lunar surface brightness temperatures, as calculated from the telemetered compartment A and B temperatures. The temperature derived from compartment A is higher in the morning than that of compartment B; in the afternoon, the reverse is true. The crossover of the temperature curves occurred around lunar noon. The difference in brightness temperatures, as sensed by compartments A and B, suggests that the lunar surface exhibits directional emission. Generally, compartment A looks with or toward the sun while compartment B looks toward the north; thus, it is expected that compartment A would sense a higher lunar surface brightness temperature than compartment B in the morning and lower in the afternoon.

In Fig. V-11, lunar surface brightness temperatures, as sensed by compartments A and B, are compared with the Lambertian and observed lunar surface temperatures, as given in Fig. V-1. In Fig. V-12, lunar surface brightness temperatures are compared with theoretical homogeneous model cooling curves, as given in Fig. V-2.

Figure V-13 compares the lunar surface brightness temperatures, as derived from compartment B data, for *Surveyors I, III, V,* and *VI*. The temperature curves for *Surveyors III* and *V* were shifted 10 deg to the left and 15 deg to the right, respectively, to account for the approximate slope of the lunar surface at the landing site. Lunar surface temperatures derived from *Surveyors I, III,* and *VI* suggest directional emission of the lunar surface in the morning, but not in the afternoon. Because of the unique landing configurations of *Surveyor V*, the results are difficult to compare with those of *Surveyors I, III,* and *VI* at this time.

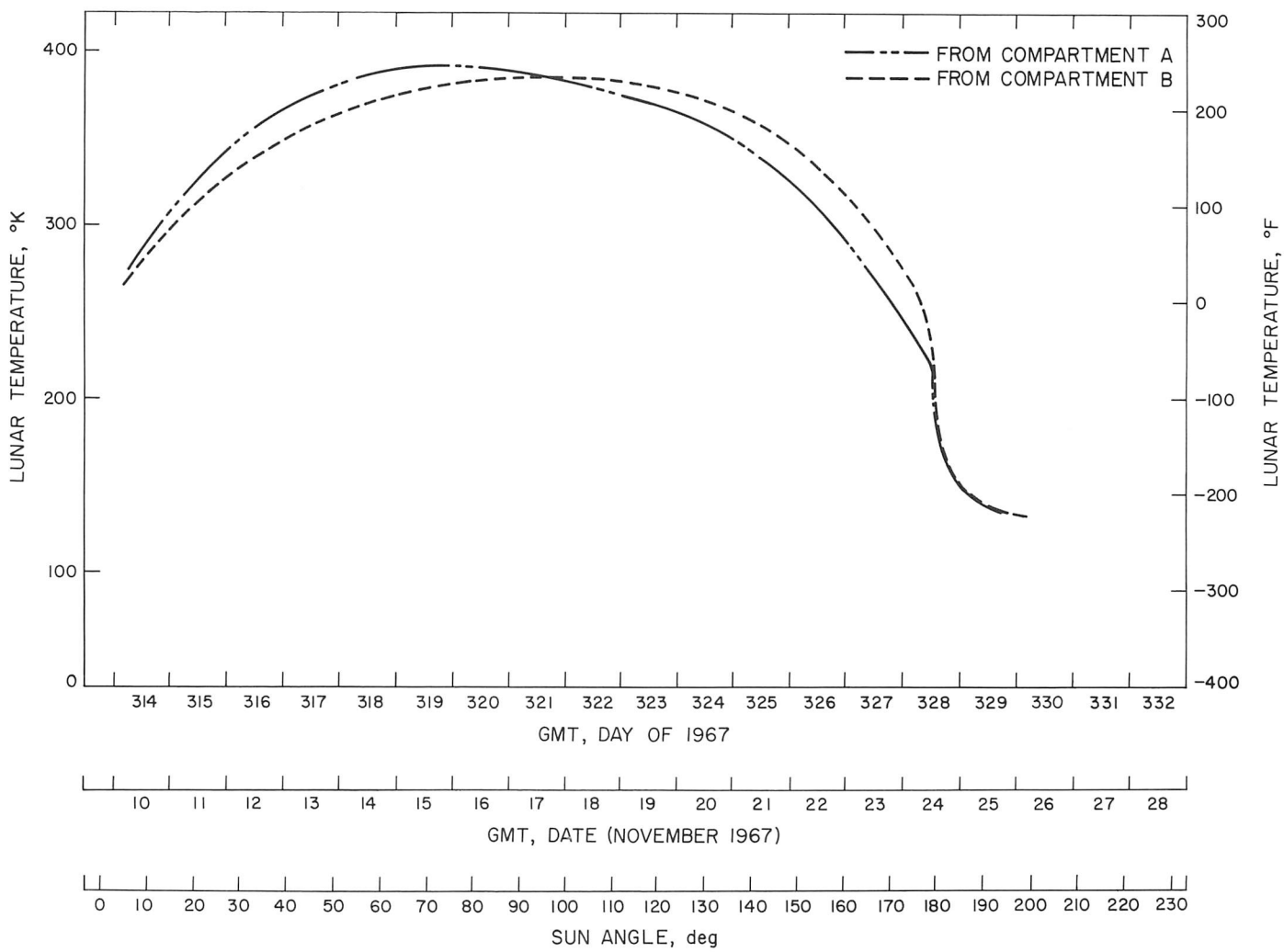

Fig. V-10. Lunar surface brightness temperatures, as calculated from compartment A and B telemetry data.

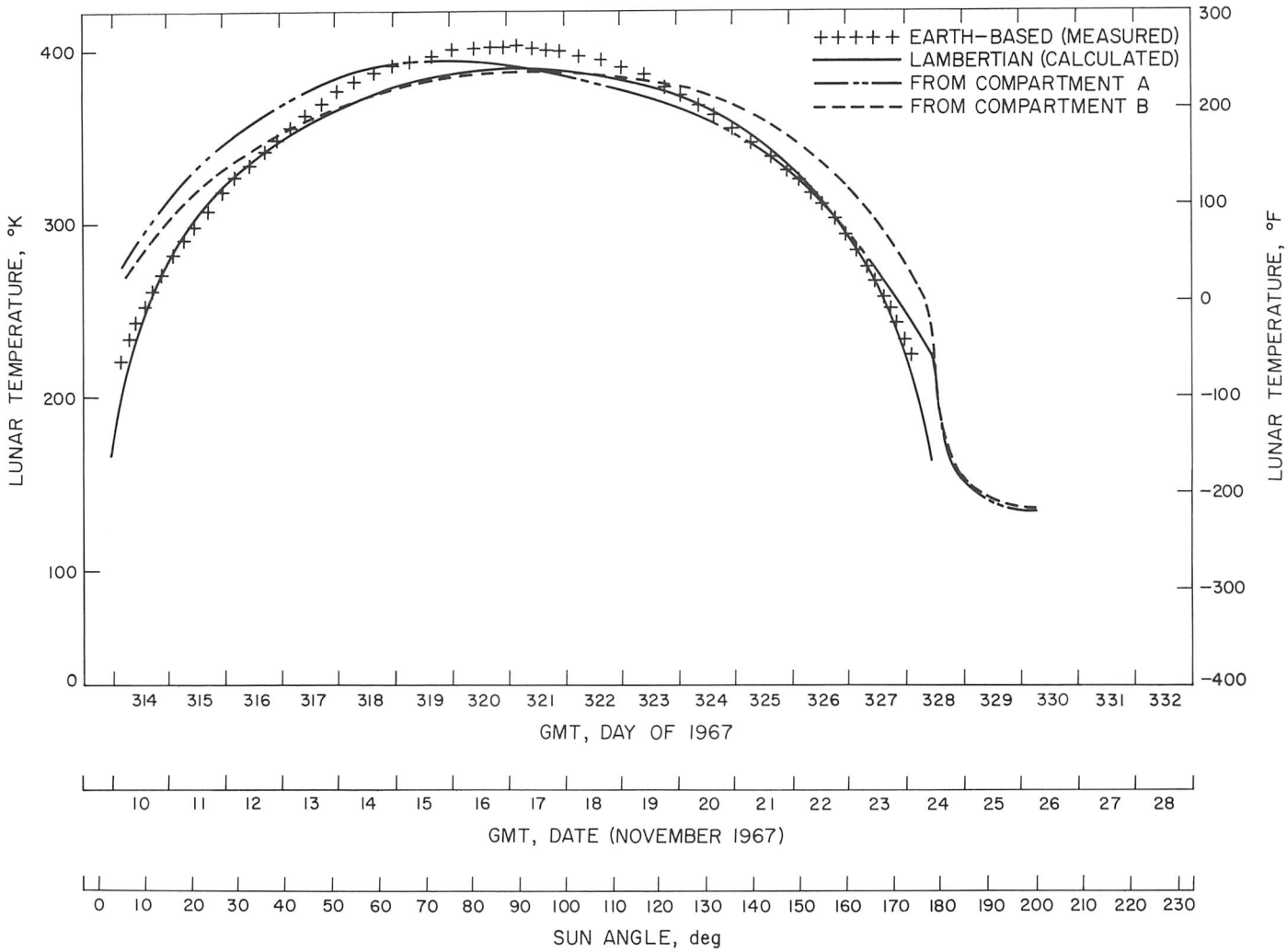

Fig. V-11. Lunar surface brightness temperatures derived from compartment A and B data compared with earth-based (measured) and Lambertian (calculated) temperatures.

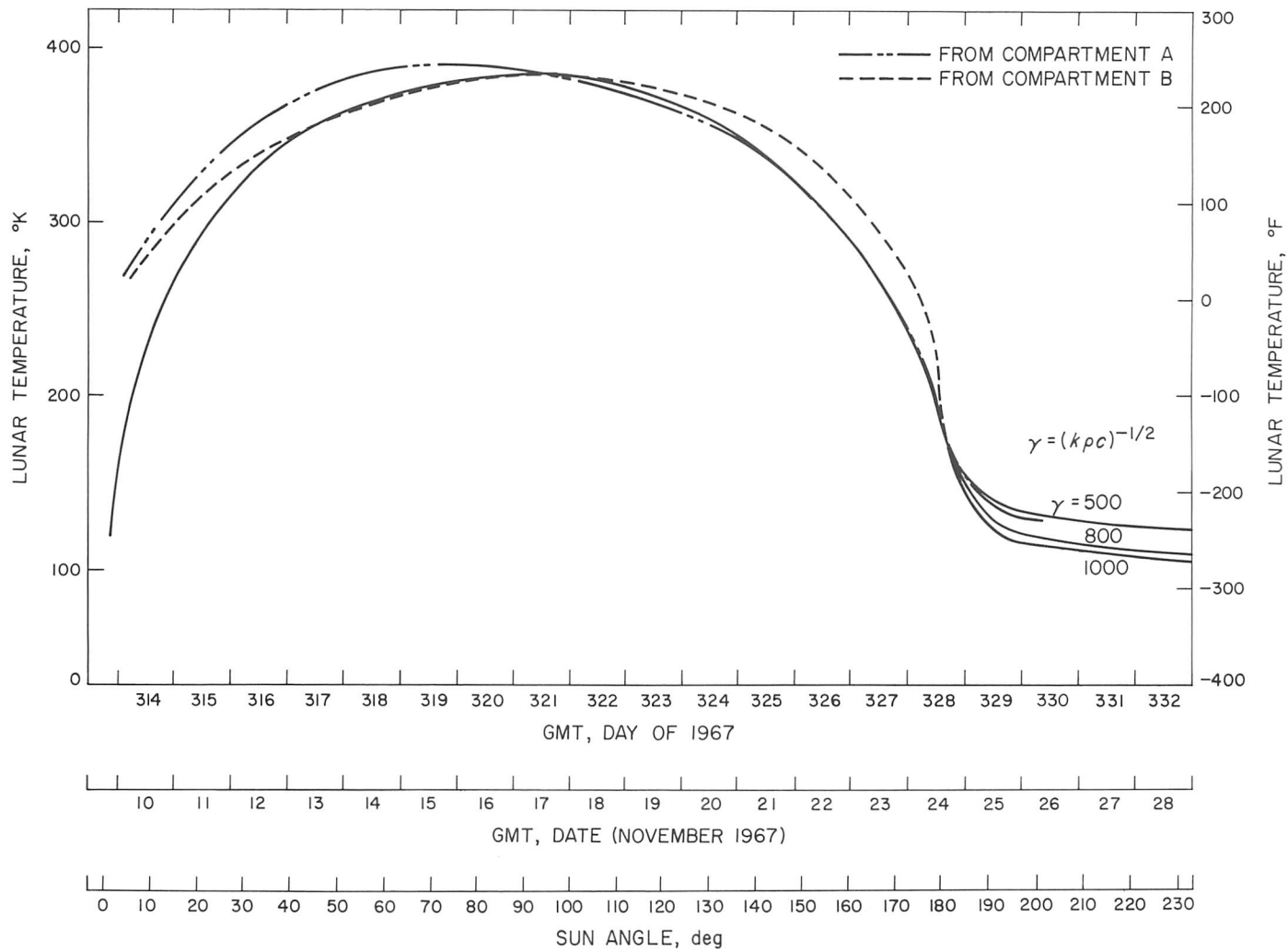

Fig. V-12. Lunar surface brightness temperatures derived from compartment A and B data compared with theoretical homogeneous model temperatures.

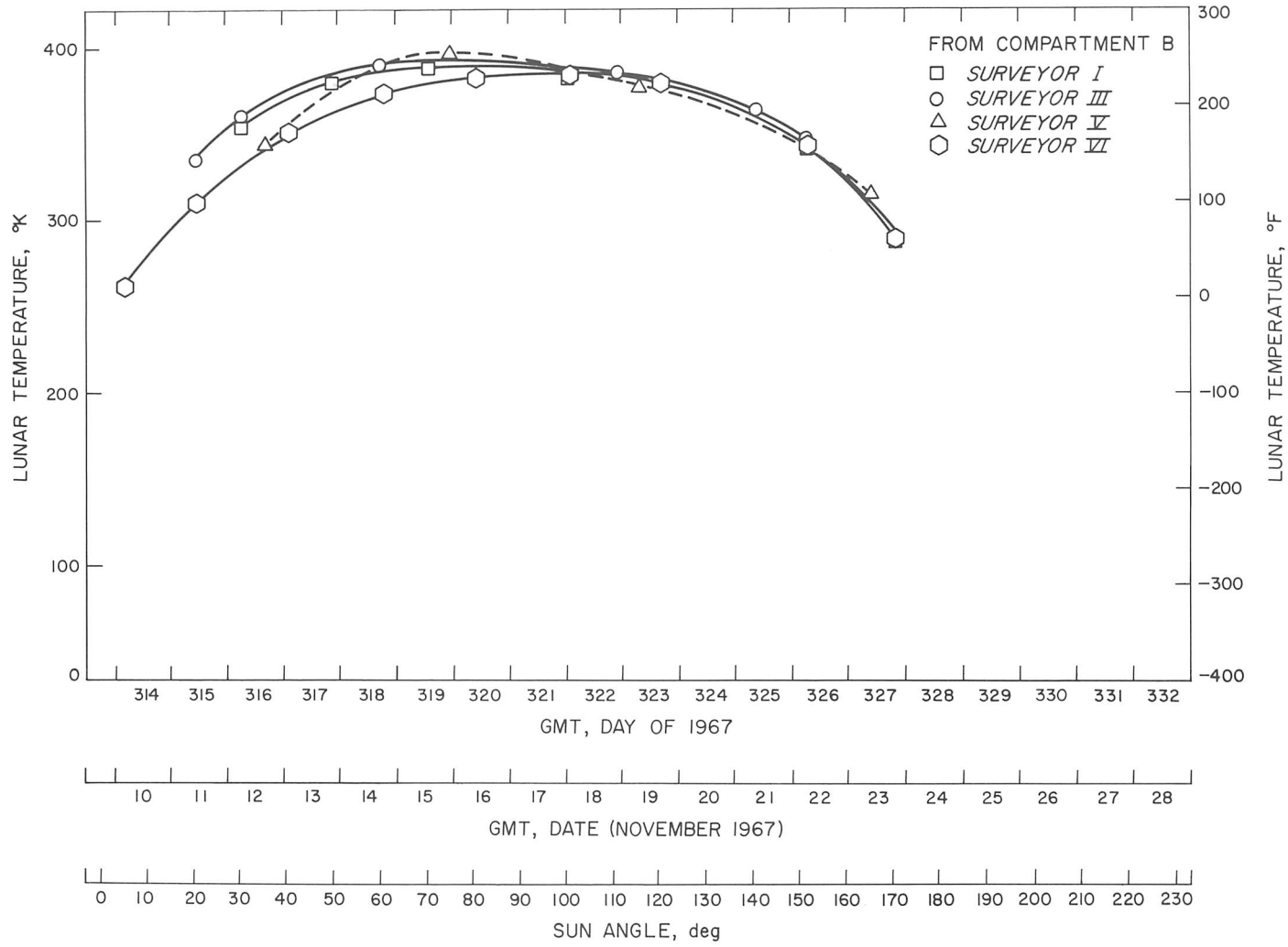

Fig. V-13. Lunar surface brightness temperatures from compartment B data compared with data from *Surveyors I, III, V,* and *VI* (adjusted in time for *Surveyor VI*).

Figure V-14 shows the lunar surface brightness temperatures, as derived from compartment temperature data, after sunset for *Surveyors I, V,* and *VI*; also included are theoretical cooling curves for several values of γ taken from Fig. V-2. Note that, during the lunar night, all of the spacecraft sensed lunar surface temperatures consistent with an effective γ of about 500.

G. Discussion

The lunar surface brightness temperatures sensed by *Surveyor VI* during the day generally can be explained in terms of the directional effects of infrared emission from the surface. However, the data obtained after sunset indicate that the surface viewed by *Surveyor VI* has an effective γ of around 500 in contrast to a value of 1100 predicted from earth-based eclipse data. This contradiction between lunar surface and earth-based data has several possible explanations:

(1) There are rocks that cool slower than the surface. Because the compartments view the scene obliquely, the apparent fraction of rocks viewed may be considerably higher than when viewed from above.

(2) An incorrect value of heat flow from the interior of the compartments may have been used.

(3) Radiation from the spacecraft may be heating the lunar surface in the immediate vicinity.

(4) The telescope is unable to resolve thermal inhomogeneity to a scale comparable to the *Surveyor VI* landing site.

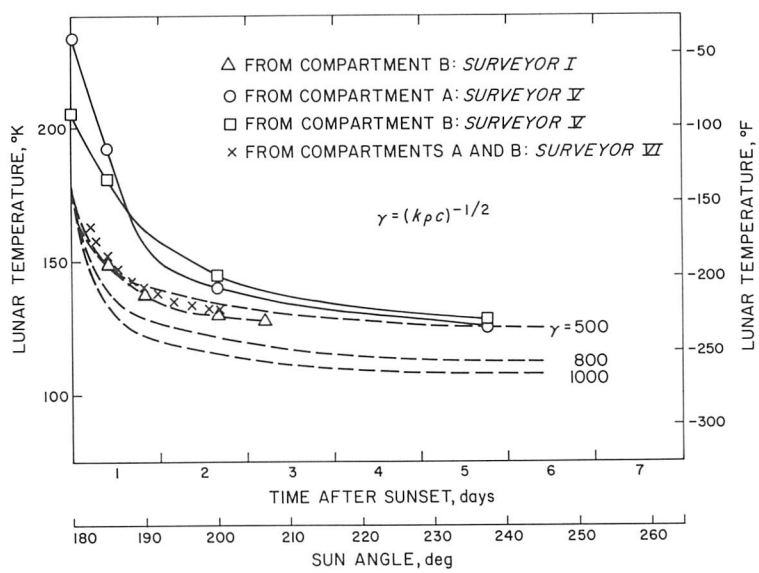

Fig. V-14. Lunar surface brightness temperatures after sunset compared with *Surveyors I, V,* and *VI* (adjusted in time for *Surveyor VI*).

References

V-1. Lucas, J. W., Conel, J. E., Garipay, R. R., Hagemeyer, W. A., and Saari, J. M., "Lunar Surface Thermal Characteristics," *Surveyor I Mission Report. Part II: Scientific Data and Results,* Technical Report 32-1023, pp. 45–59, Jet Propulsion Laboratory, Pasadena, Calif., September 10, 1966.

V-2. Lucas, J. W., Conel, J. E., Garipay, R. R., Hagemeyer, W. A., Jones, C. B., Saari, J. M., Vitkus, G., and Wang, J. T., "Lunar Surface Temperatures and Thermal Characteristics," *Surveyor III Mission Report. Part II: Scientific Results,* Technical Report 32-1177, pp. 155–188, Jet Propulsion Laboratory, Pasadena, Calif., June 1, 1967.

V-3. Lucas, J. W., Garipay, R. R., Hagemeyer, W. A., Saari, J. M., and Vitkus, G., "Lunar Surface Temperatures and Thermal Characteristics," *Surveyor V Mission Report. Part II: Science Results,* Technical Report 32-1246, pp. 89–113, Jet Propulsion Laboratory, Pasadena, Calif., November 1, 1967.

V-4. Saari, J. M., and Shorthill, R. W., *Isothermal and Isophotic Atlas of the Moon,* NASA Report CR-855, September 1967.

V-5. Jones, B. P., *Diurnal Lunar Temperatures,* Paper 67-289, presented at AIAA Thermophysics Specialist Conference, New Orleans, Louisiana, April 17-20, 1967.

V-6. Saari, J. M., and Shorthill, R. W., *Isotherms in the Equatorial Region of the Totally Eclipsed Moon,* Boeing Scientific Research Laboratories Document D1-82-0530, April 1966.

(Blank Page)

VI. Astronomy

R. H. Norton (Chairman), J. E. Gunn, W. C. Livingston, G. A. Newkirk, and H. Zirin

There were 44 pictures of the K- and F-coronas obtained during a 6-hr period following sunset on the spacecraft at 13:53 GMT on Day 328. For the first time, polaroid filters were used to make polarization measurements of the corona.

As the corona set, progressively larger exposure times were used to photograph the fainter F-corona. A complete sequence of pictures was taken at each stage, through the clear filter and through the three polaroid filters. Later, when the integration time reached 10 min, calibration frames of blank sky were taken to obtain a measurement of the vidicon background level.

In these observations, it was noticed that a previous image was sometimes incompletely erased. Although data reduction techniques will be used to correct this situation, it is uncertain that full correction can be achieved; therefore, the interpretation of polarization measurements may be difficult.

An inspection of the pictures indicates that, at 19:03 GMT, the time of the last 10-min frame, the upper limb of the sun was approximately 10 solar radii below the horizon. The F-corona can be traced above the horizon at distances ranging from 10 to 30 solar radii from the sun. Figure VI-1 shows a 10-min, wide-angle picture of the solar corona, taken at 18:37 GMT, nearly 5 hr after the upper limb of the sun had set.

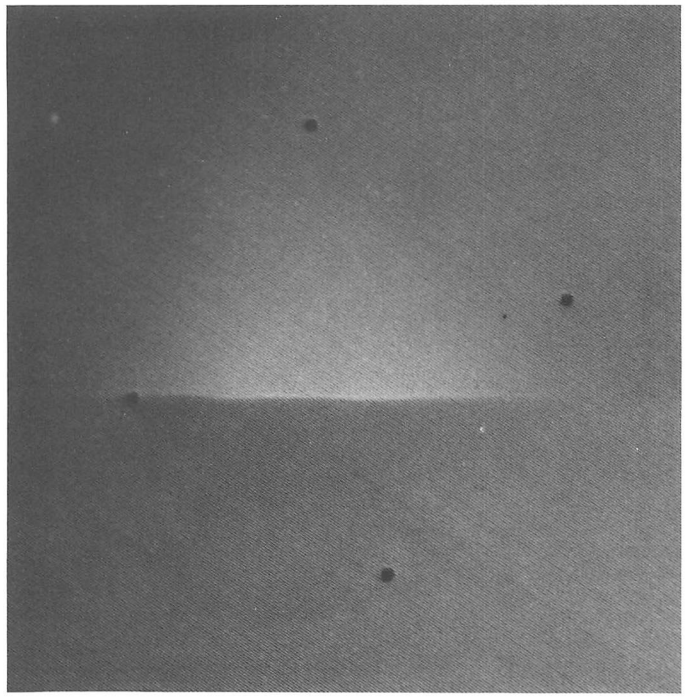

Fig. VI-1. A 10-min, wide-angle picture of the solar corona. In this view, the corona may be seen extending 20 solar radii above the lunar horizon; the center of the sun is 11 solar radii below the horizon. Note that the lunar foreground to the western horizon is illuminated by earthshine (Day 328, 18:37:02 GMT).

(Blank Page)

VII. Chemical Analysis of the Moon at *Surveyor VI* Landing Site: Preliminary Results

Anthony L. Turkevich (Principal Investigator), Ernest J. Franzgrote, and James H. Patterson[1]

Surveyor V provided the first direct chemical analysis of lunar surface material by means of the Alpha-Scattering Experiment at Mare Tranquillitatis (Refs. VII-1 and VII-2). The Alpha-Scattering Experiment on *Surveyor VI* is essentially a duplicate of that on *Surveyor V;* however, the analysis was performed at a different landing site (Sinus Medii). In this report, the discussion of the alpha-scattering instrument and the experimental operations is brief; emphasis is placed on the areas in which the recent experiment differs. (See Refs. VII-1 through VII-5 for a more detailed description of the experiment and the instruments.) The Alpha-Scattering Experiment provides quantitative information on elements heavier than lithium by analysis of the energy spectra of alpha particles and protons obtained from the interaction of a collimated beam of alpha particles with material on the lunar surface. The technique has better qualitative resolution for the lighter elements; in most cases, however, there is less sensitivity for these than for the heavier ones.

Only part of the data has been analyzed thus far, and that only in a preliminary manner. However, enough information is available for comparison with the *Surveyor V* results and with the chemical composition of materials available on earth.

[1]See Appendix for the authors' affiliations.

A. Instrument Description

1. General

The alpha-scattering instrument used on *Surveyor* consists of a sensor head, which is deployed to the lunar surface for the analysis, and an electronics package located on the spacecraft in thermal compartment C (see Fig. VII-1 for location).

In the sensor head are six source capsules containing alpha-emitting curium-242, collimated so that the alpha-particle stream is restricted to the sample opening. Near the sources are two small solid-state detectors arranged to collect only those alpha particles that are scattered at an angle of 174 ± 3 deg by the sample. Also in the sensor head are four larger detectors, each with a guard detector in anticoincidence, to analyze protons from (α, p) nuclear reactions in some of the lighter elements. The electronic amplification of the detector signals and most of the analog electronic circuitry are also in the sensor head.

Time-analog signals from the sensor head (which are proportional to particle energies) are converted in the electronics package to digital form and encoded for transmission to earth. Compartment C contains the power supplies for the instrument and the command logic for its operation.

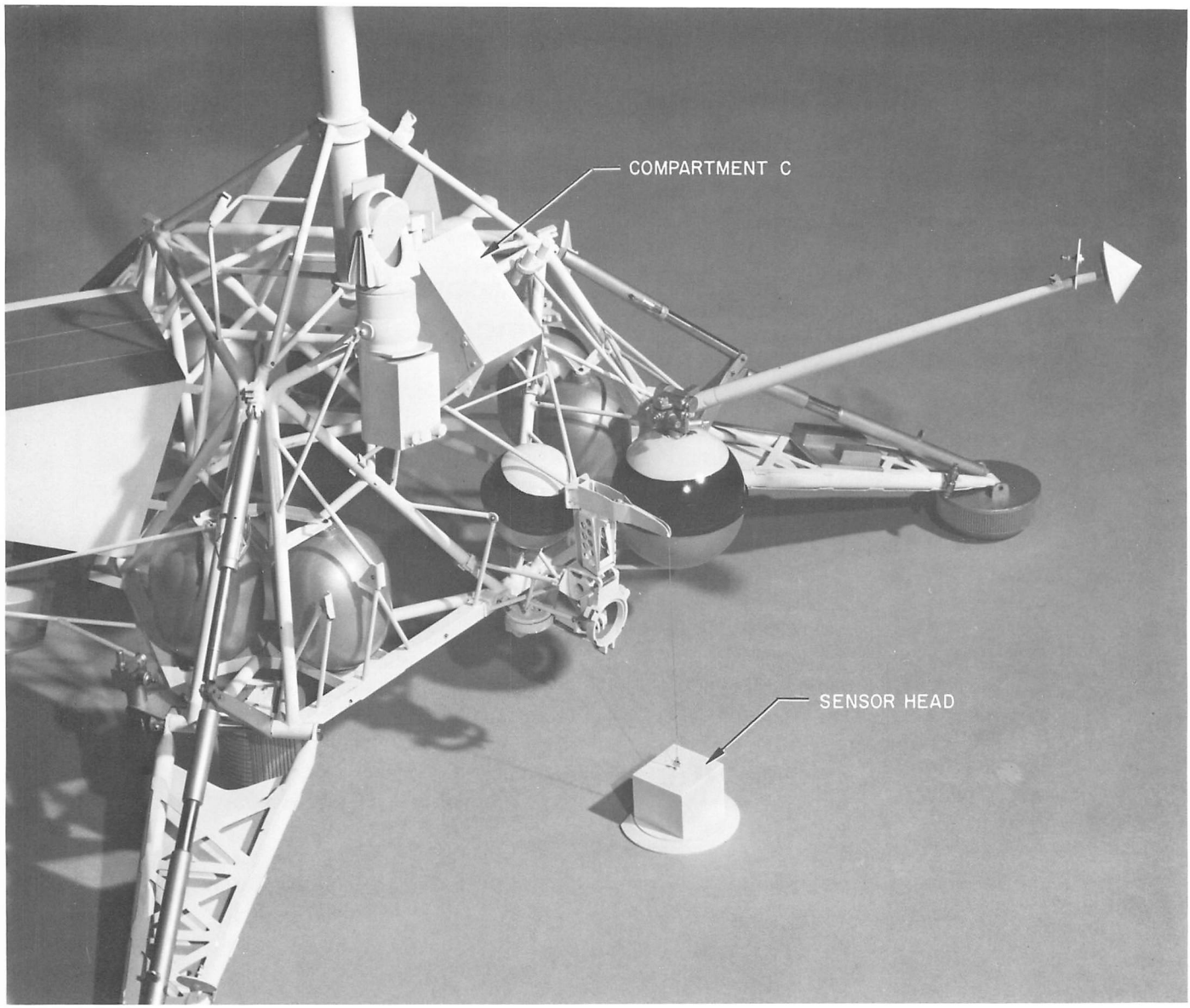

Fig. VII-1. Photograph of a 1/5-scale model of a *Surveyor* spacecraft showing the location of the alpha-scattering instrument. The sensor head is shown in its nominal lunar surface position. Electronic cables are not simulated on this model.

After the landing, the alpha-scattering instrument is first operated with the sensor head in the stowed position, with a material of known chemical composition (the standard sample) at the sample opening of the instrument. On command, a supporting platform and the standard sample fall away, leaving the sensor head suspended by a nylon cord about 56 cm above the surface to determine the lunar background. Finally, on command, the sensor head is lowered to the surface for the lunar sample measurement.

2. Characteristics of *Surveyor VI* Alpha-Scattering Instrument

The construction and assembly of this instrument (F-1 in pre-flight logs) were completed on December 19, 1966. The science calibration was finished on February 16, 1967, and the instrument delivered to Hughes Aircraft Company on March 7. The radioactive sources were installed in the instrument on October 20 at Cape Kennedy, Florida. By the launch date (November 7, 1967), the instrument had been operated for 1309 hr. Calibration data, which show the long-term stability of the *Surveyor VI* instrument, are given in Fig. VII-2.

Table VII-1 lists some characteristics of the sources and detectors in the *Surveyor VI* instrument. It will be noticed that the alpha detector films were not well matched. This reduces the sharpness of the fine structure of the alpha spectra at low energy. Unfortunately, there was no opportunity for operation of the instrument on the moon's surface with individual alpha detectors.

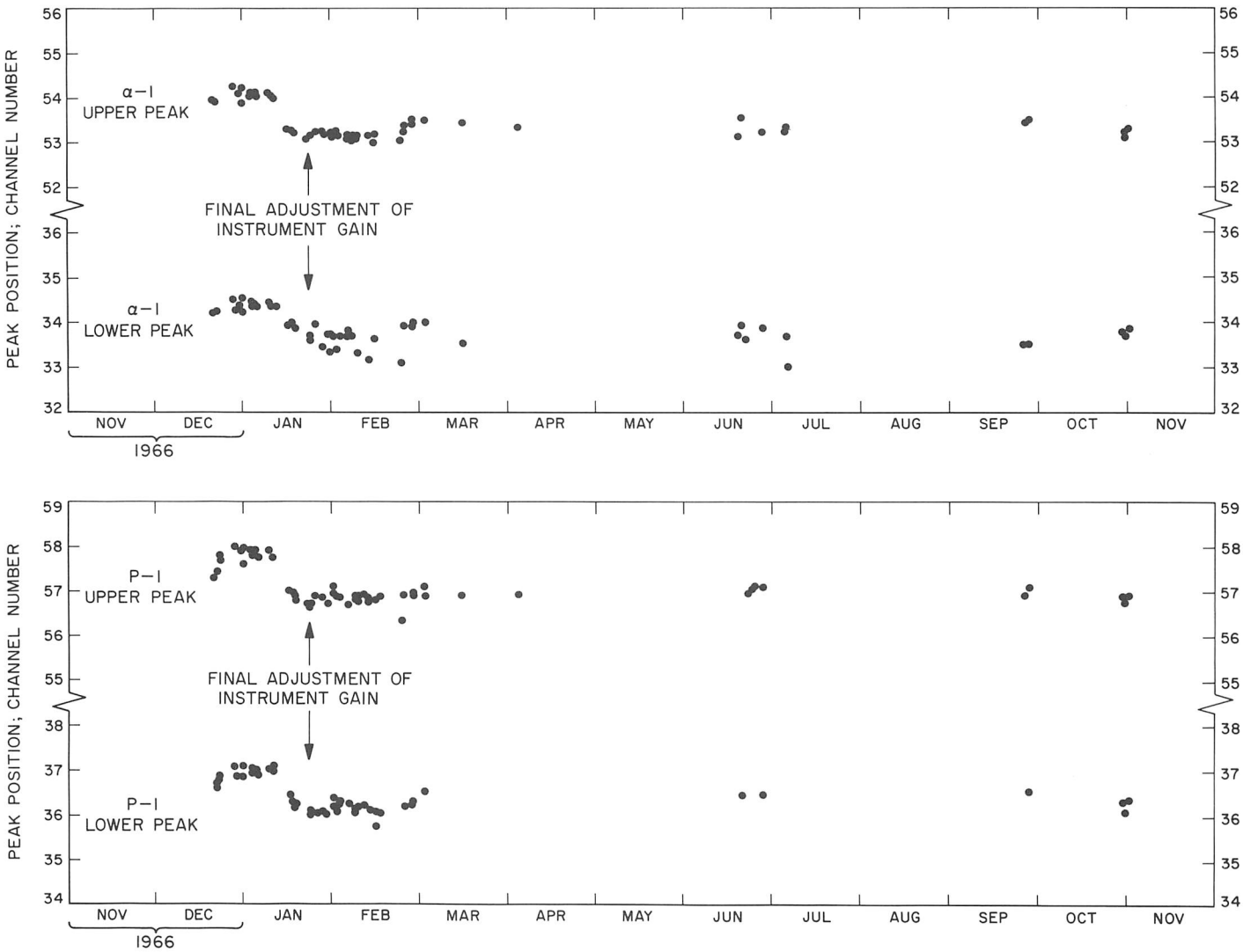

Fig. VII-2. Calibration-pulser peak positions vs time, showing the long-term stability of the *Surveyor VI* instrument. The data are shown for one alpha and one proton detector; the remaining detector systems behaved similarly.

Table VII-1. Characteristics of *Surveyor VI* alpha-scattering instrument

Alpha Source Characteristics	
Intensity as of November 9, 1967 (total for six sources)	2.76×10^{11} disintegrations/min
Mean energy, as measured through source capsule protective films	6.03 ± 0.01 MeV
Energy-spread range for six sources (full width at half maximum)	1.2 to 1.8%
Thickness of secondary protective film (energy loss for 6.1-MeV alpha particles)	0.027 MeV
Alpha Detectors	
Thickness of evaporated-gold surface (energy loss for 6.1-MeV alpha particles)	0.039 MeV
Thickness of alpha-mask films (energy loss for 6.1-MeV alpha particles)	
Detector 1	0.040 MeV
Detector 2	0.029 MeV
Proton Detectors	
Gold-foil thickness (11.3 to 11.4 μ, equivalent to 21.9 to 22.1 mg/cm^2)	
(Energy loss for 6.1-MeV alpha particles)	6.1 MeV
(Energy loss for 2.0-MeV protons)	1.24 MeV
Guard Detector System	
Approximate electronic threshold	0.30 MeV
Guard ratemeter response	
10 events/sec	0.080 V
30 events/sec	0.300 V
100 events/sec	0.900 V
300 events/sec	1.800 V
1000 events/sec	2.500 V
Electronics energy scale	
(Temperature of sensor head and of digital electronics = 25°C)	
Alpha	$N = 18.94E - 10.9$
Proton	$N = 18.86E - 10.7$

N = channel number; E = energy deposited by particle in detector, MeV.

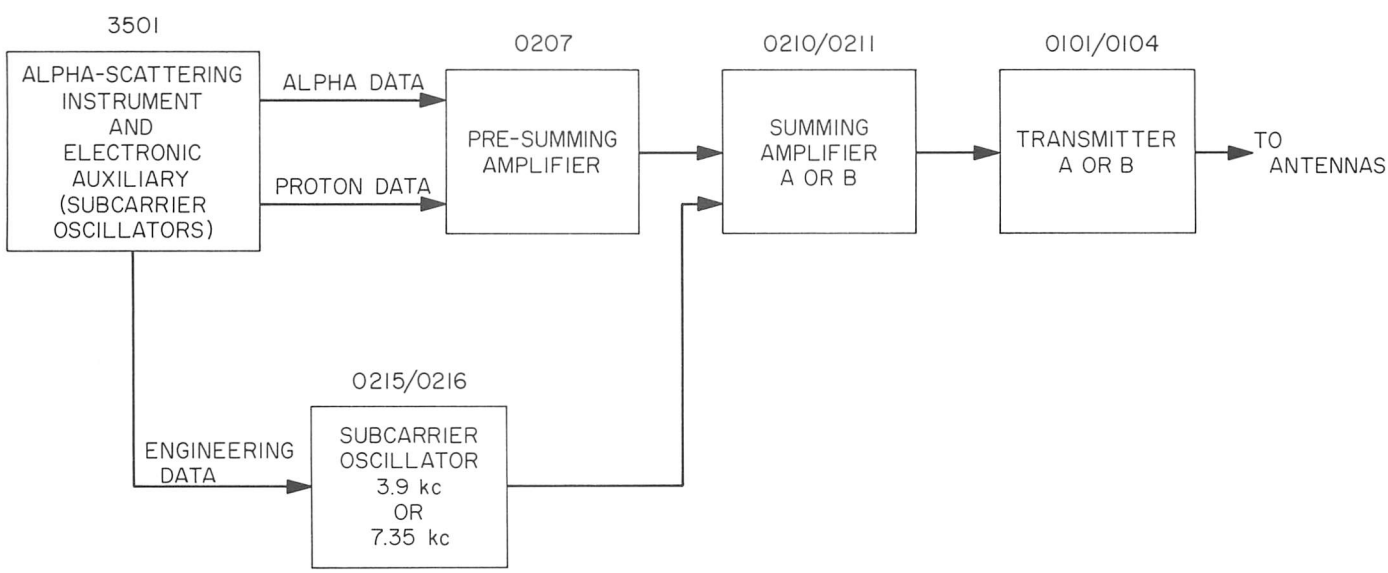

Fig. VII-3. Electronic configuration of the spacecraft, showing how data are received from alpha-scattering instrument. Redundancy is provided both in the engineering-data subcarrier oscillators and in the summing amplifier/transmitter combination. The various units can be activated individually, as indicated by the command designations above the blocks.

B. Experiment Control

Methods for control of the Alpha-Scattering Experiment during the mission are described in detail in Ref. VII-1. In general, data transmitted from the spacecraft are received at the Tracking Stations of the Deep Space Network. Here the prime data are recorded on magnetic tape for post-mission science processing. Batches of these data are relayed in near-real time via teletype to the Space Flight Operations Facility (SFOF) at the Jet Propulsion Laboratory. Decisions to apply power to the instrument, change detector configuration, calibrate the instrument, activate heaters, and deploy the sensor head are made at the SFOF on the basis of analysis of these data. Commands are then transmitted from the Tracking Stations to the spacecraft to implement these decisions.

Figure VII-3 shows how the spacecraft must be configured in order that data may be transmitted. In this figure, the numbers above the blocks indicate the designations of commands necessary to activate each unit. Temperature information on the alpha-scattering instrument may be transmitted without applying power to the unit, but command 3501 is required if any other data are to be obtained.

C. Mission Description

1. Pre-Launch Operations at Cape Kennedy

Final calibration of the flight instrument and preparations for launch proceeded essentially in the same manner as for *Surveyor V* (p. 126 of Ref. VII-1).

Based on experience gained during preparations for *Surveyor V*, improvements had been made in the special test facility at Cape Kennedy and in the overall efficiency of operation. For example, clean-room techniques were used to maintain cleanliness of the sensor head during source-installation procedures. Figure VII-4 shows part of this calibration facility.

The alpha-detector masks were changed at Cape Kennedy, resulting in sharper einsteinium-254 calibration peaks. The F-1 digital electronics had been removed from the spacecraft for modification of the power supply, and thus was available for temperature calibration together with the F-1 sensor head. The thin aluminum-oxide films, which are mounted on the source collimators, were not changed during preparation for the *Surveyor VI* mission.

Fig. VII-4. Source loading and calibration facilities at Cape Kennedy, Florida. Shown are the source loading room (a) and the instrument calibration room (b) as they were during pre-launch operations of the Alpha-Scattering Experiment for the *Surveyor VI* mission. On the left side of the source loading room (a) is a laminar-flow clean-bench. When the sensor head was removed from the spacecraft for the final operation at Cape Kennedy, it was kept in a "handling container." The frame in which this container was maneuvered during source loading is shown on the clean-bench. On the right side of this room is an enclosed hood of the type used for handling alpha radioactivity. In the instrument calibration room (b) two large vacuum chambers are visible. These were used for testing and storage of the sensor head and its spare. Also shown is the electronic equipment for instrument control and data analysis.

2. Launch and Landing

Surveyor VI launch, transit, and landing operations proceeded normally. Alpha-scattering instrument temperatures were obtained during transit; the sensor head temperature was slightly higher than measured during the *Surveyor V* mission. There was no operation of the instrument during transit to the moon.

Touchdown of *Surveyor VI* occurred at 01:01:05 GMT on Day 314 after a normal terminal sequence in which the main retro motor finished burning at an altitude of 13.5 km. The end-of-burning altitude was only 1.6 km for *Surveyor V*. (The effect of retro contamination of the *Surveyor V* landing site was analyzed in Appendix A of Ref. VII-1 and was found to be negligible. Using the same type of analysis for the *Surveyor VI* landing conditions, the retro contamination is estimated to be an order of magnitude less than that at the *Surveyor V* site.)

The spacecraft came to rest on a fairly flat surface (slope less than 1 deg) with the outboard side of the sensor head facing 31 deg south of east. In contrast with *Surveyor V*, there was no evidence that subsurface material was scattered into the area where the sensor head was later deployed.

3. Post-Landing Operations

a. Stowed Position (Day 314). About 4.5 hr after landing, the alpha-scattering instrument was activated. The command to apply spacecraft power to the instrument was transmitted from the Tracking Station near Goldstone, California, at 05:39:04 GMT. At that time, the temperature of the sensor head was 12°C; the digital-electronics temperature was 3°C. The guard-detector event rate was found to be about the same as that measured during the *Surveyor V* mission, and instrument voltages were normal. Between 05:41:40 GMT and 06:20:30 GMT, two 10-min accumulations of standard-sample data and five 2-min pulser calibration runs were received, and the instrument was found to be performing properly. Accumulation of data was then suspended for about 3.5 hr for television surveys.

After transfer of tracking operations from California to Australia, accumulation of alpha-scattering data was resumed. By 20:55:30 GMT, a total of 5.3 hr of standard-sample data had been received.

The data were found to agree well with pre-launch results, and a decision was made to deploy the sensor head to the background position.

b. Background position (Days 314 and 315). When the sensor head is released from the stowed position, it continues moving for some time like a pendulum. A series of television pictures of this operation was planned for *Surveyor VI* primarily to provide a direct view of the eventual sample area on the lunar surface otherwise obscured by the sensor head. Although the television pictures could not be synchronized with the motion, there was a good chance that at least one of a series of pictures would show a substantial portion of the sample area.

The sensor head was released from the stowed position by commands transmitted from the Tracking Station near Robledo, Spain, at 21:17:55 GMT on Day 314. Personnel at the Tracking Station reported that successive pictures on their television monitor showed that the instrument had been released and was moving. There were 45 television pictures obtained of the deployment operation; these pictures were commanded at 4.5-sec intervals. Figure VII-5 is a mosaic of four wide-angle television pictures showing the area of the lunar surface later analyzed by means of the Alpha-Scattering Experiment. The sensor head can be seen near the extreme end of its motion. Particles as small as 3 mm are visible in the picture; no particle larger than about 15 mm is located in the 10.8-cm-diameter sample area.

When the sensor head was deployed to the background position, its temperature (which had been rising at a rate of 1°C/hr) decreased from 22 to 17°C over a period of several hours. The electronics temperature at this time was 26°C.

The first accumulation of background data began at 21:37:45 GMT. After obtaining 33 min of background information and five 2-min calibration runs, tracking of the spacecraft was transferred from Spain to California for television operations.

Accumulation of background information was resumed at 05:05:40 GMT on Day 315. By 12:07:00 GMT, a total of 6 hr and 15 min of background spectra had been received via teletype. The amount and quality of data were considered sufficient for this stage of operation.

c. Lunar surface position (Days 315 and 316). The deployment of the sensor head to the lunar surface was monitored by observing the signal received from the alpha detectors. The deployment command was transmitted from the Tracking Station near Canberra, Australia, at 12:07:52 GMT. Moments later, station personnel reported that the rate of analyzed events had increased; the

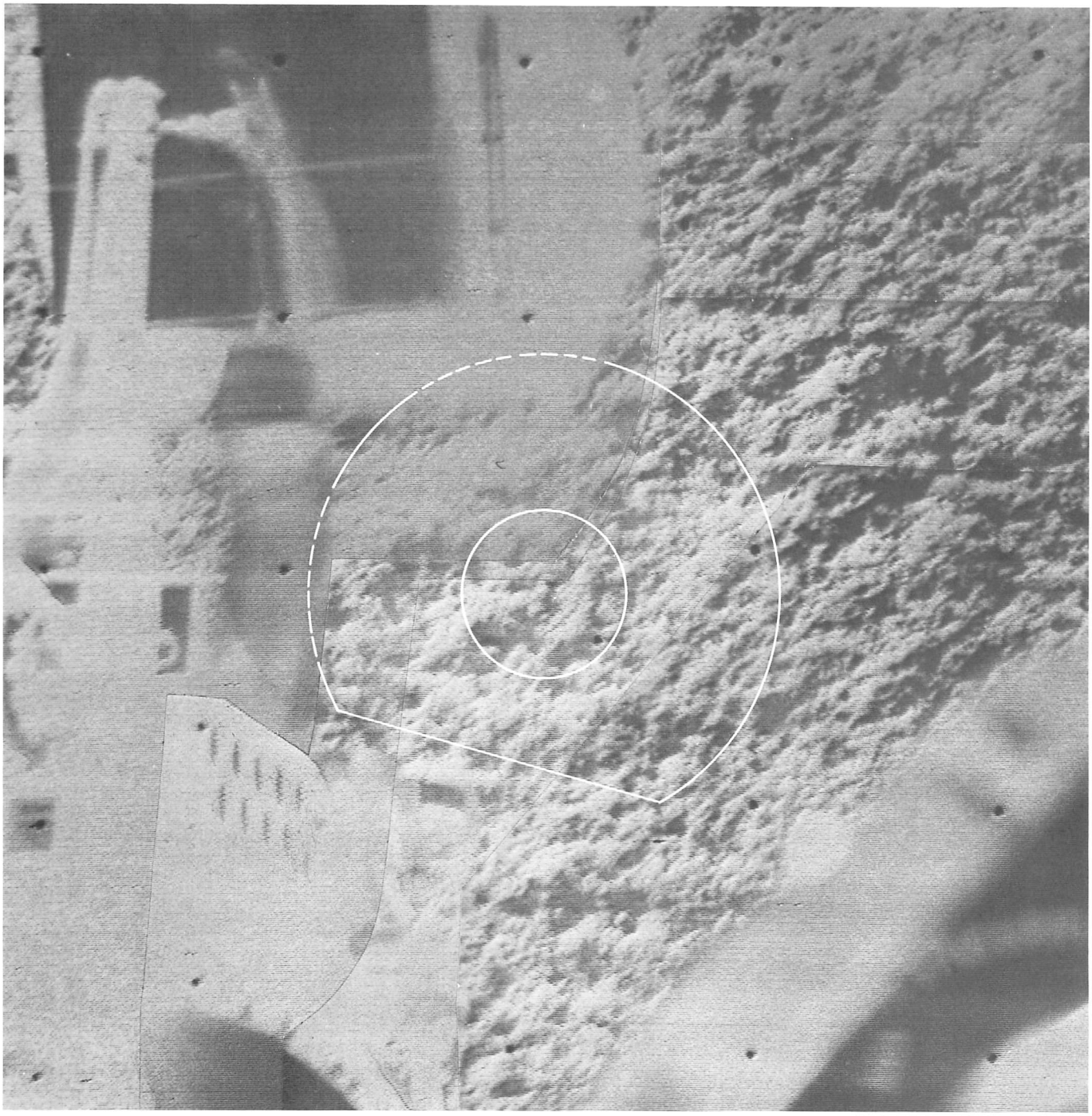

Fig. VII-5. Wide-angle mosaic of television pictures taken just after the sensor head was released from the stowed position. The circle shows the area of the lunar surface later analyzed by means of the Alpha-Scattering Experiment. (Day 314, 21:17:57 to 21:23:11 GMT).

instrument was apparently resting properly on the lunar surface.

Spectra transmitted via teletype to the Space Flight Operations Facility confirmed that data were being received from the lunar surface. Between 12:08:30 GMT and 23:00:10 GMT, 7.2 hr of data accumulation were received.

At 23:00:45 GMT on Day 315, power to the alpha-scattering instrument was turned off in preparation for television operations. Instrument temperatures at that time were 40°C for the sensor head and 43°C for the digital electronics.

During the television surveys, pictures were obtained of the sensor head on the lunar surface. Views of the *Surveyor V* and *VI* instruments, in their original deployed positions, are presented in Fig. VII-6.

The surrounding lunar material at Sinus Medii contains fewer large particles than that of Mare Tranquillitatis, although the general appearance of the two sites is similar. The sensor head shown in Fig. VII-6b was deployed closer to the spacecraft (and television camera) than the *Surveyor V* instrument (Fig. VII-6a) because the latter was on a 20-deg slope. This can be seen by comparing the position and size of the two instruments with their respective deployment mechanisms. In both missions, the sensor head appears to have been deployed onto a relatively smooth area so that the distance of the examined sample from the alpha detectors should not have been far from nominal.

At the conclusion of the television surveys, power to the instrument was again commanded at 07:48:14 GMT on Day 316. By this time, the sensor head temperature had risen to 43°C and the digital electronics temperature to 45°C.

The first 20-min data accumulation received after resuming operations showed a large number of events in the low-energy region of the proton system. The next accumulation also showed this noise, but at a lower rate. A series of 2-min calibration runs was begun at 08:25:50 GMT to see if the noise could be isolated to a single proton detector. The noise was intermittent, and the search was complicated by some low-energy noise from the calibration pulser, but eventually spectra were received by teletype that indicated proton detector 3 was noisy. The command to turn off this detector was transmitted at 10:33:15 GMT; accumulations were resumed at 10:33:45 GMT using the remaining five detectors.

By 19:55:00 GMT, a total of 15.7 hr of noise-free lunar surface data had been received; 8.5 hr of these data were accumulated using only three of the four proton detectors. Soon thereafter, the sensor head temperature had risen to its upper operating limit of 50°C and the instrument was turned off. The temperature was not expected to return below the upper operating limit until Day 320 when the sensor head would be shaded by part of the spacecraft.

d. Lunar surface operations (Days 320 and 321). The maximum temperatures reached between Days 316 and 320 were 61°C for the sensor head and 62°C for the digital electronics. At about 06:00 GMT on Day 320, the temperature of the sensor head began to drop at a rate of 4°C/hr because of spacecraft shadowing. (The digital electronics were already shadowed.) At 12:57 GMT, the instrument was commanded on with the sensor head temperature at 36°C and the digital electronics temperature at 31°C. Calibration runs showed that proton detector 3 was behaving normally at the lower temperature. At 16:49:16 GMT on Day 320, the detector was turned back on, and normal operation was resumed using all detectors.

By 03:30:30 GMT on Day 321, a total of 30 hr of accumulations, of which 27 hr, 44 min, were known to be noise-free, had been received. The command to turn the instrument off was transmitted at 03:32:20 GMT for television operations in preparation for the spacecraft hopping maneuver (see Section IV).

e. Post-hop operations (Days 321 to 328). At 10:32 GMT on Day 321, the vernier engines were fired; subsequent television pictures showed that the spacecraft had moved 2.4 m and that the sensor head was now upside down. Figure VII-7 shows pictures of the sensor head taken with the wide and narrow-angle lenses of the television camera. In the wide-angle picture (Fig. VII-7a), the instrument can be seen beneath part of the deployment mechanism; note the bent portion of the circular plate. Figure VII-7b, the narrow-angle picture, shows some of the detectors visible through the sample port.

At 12:48:20 GMT, a short operation showed that the instrument was functioning electronically, but that many events were being registered at around channel 103 in the alpha system. This indicated that curium-242 contamination was present in the sensor head and, therefore,

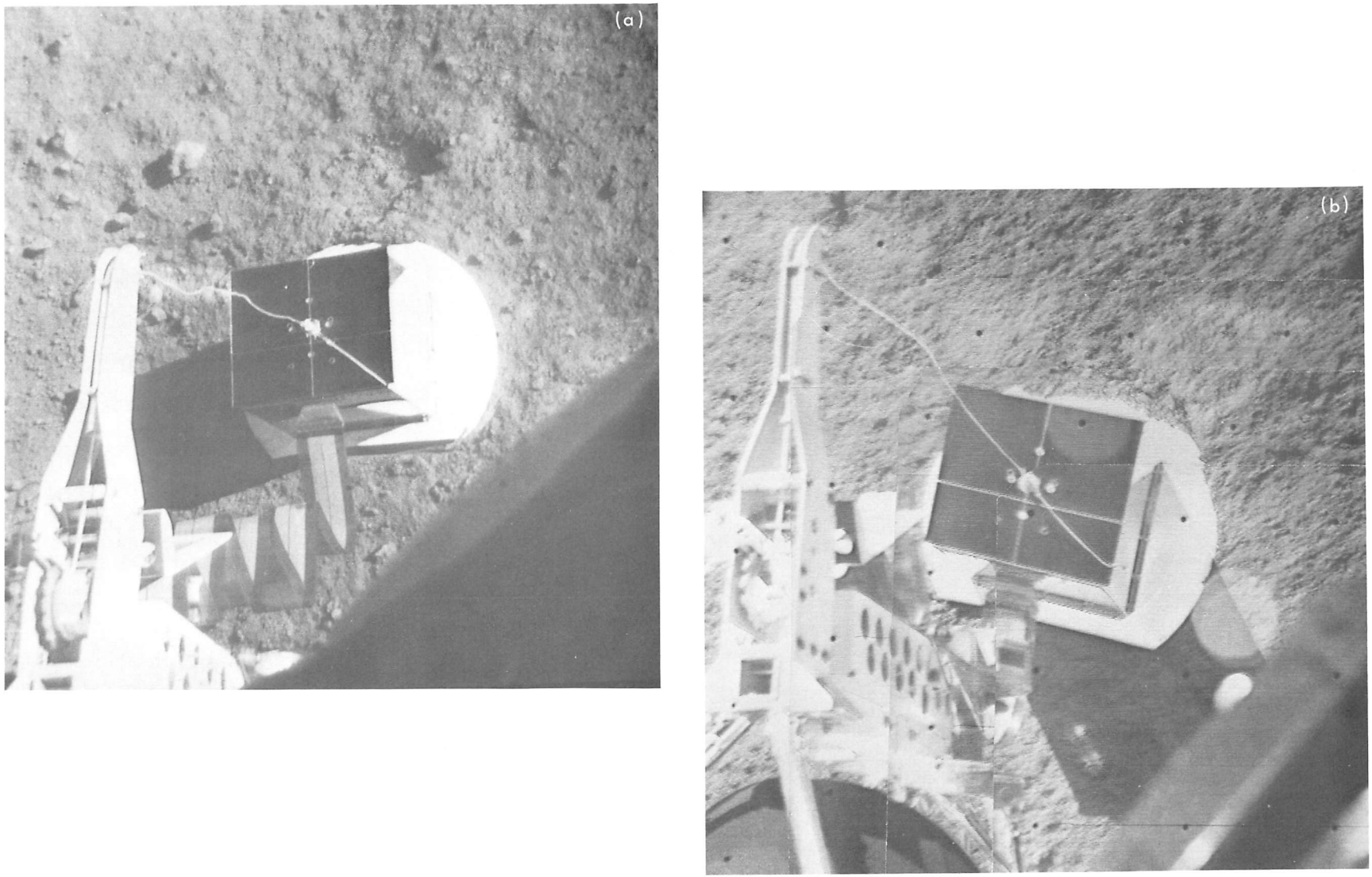

Fig. VII-6. Alpha-scattering instruments on lunar surface: (a) *Surveyor V* at Mare Tranquillitatis (Day 255, 00:39:54 GMT); (b) *Surveyor VI* at Sinus Medii (Day 316, 04:58:04 to 05:00:52 GMT, wide-angle mosaic).

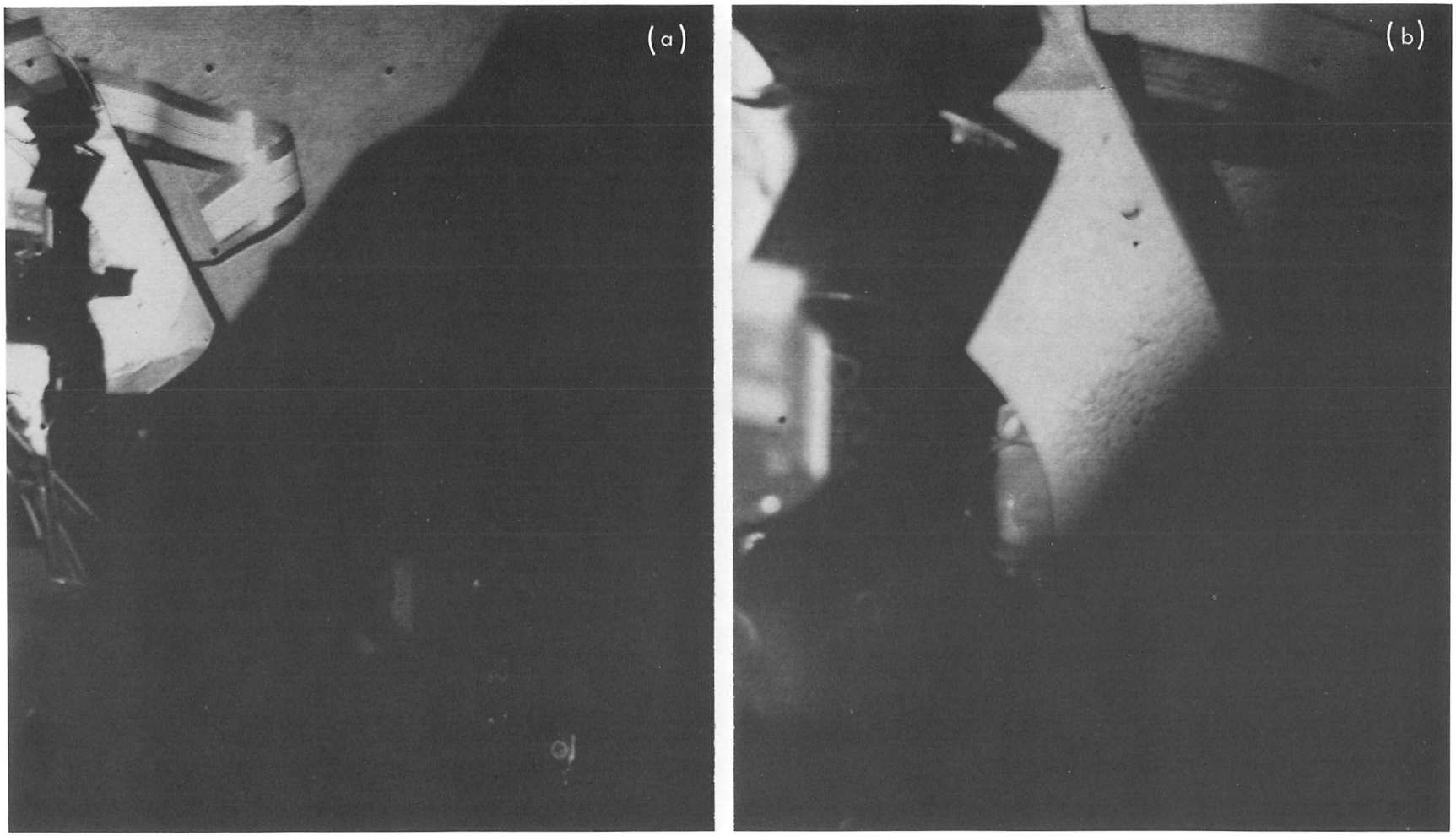

Fig. VII-7. Alpha-scattering sensor head after spacecraft hopping maneuver. (a) Wide-angle picture. The sensor head is partially visible in an upside-down position on the lunar surface below part of the deployment mechanism (Day 321, 11:41:53 GMT). (b) Narrow-angle picture. Through the circular sample port can be seen several of the proton and alpha detectors (Day 321, 11:43:47 GMT).

that at least one of the source-protective films had been broken. It can be estimated that a maximum of about a millicurie of curium-242 (half-life 163 days) will eventually escape from the sensor head.

The spectra also showed a large increase in event rate in the proton system. Because of the possibility of obtaining useful information on solar protons and cosmic rays, measurements were continued periodically for the remainder of the lunar day.

A total of 13 hr of data was obtained on Days 322, 324, 326, 327, and 328. Much of the operation was performed with individual alpha and proton detectors. The final data were obtained on Day 328, 4 hr after local sunset.

D. Results

1. General Comments

At the date of this writing, the primary data recorded at the Tracking Stations are not yet available. All the results reported here are based on spectra relayed via teletype stations. These spectra were sent in essentially "real time" for instrument performance analysis and mission planning purposes. Moreover, even these data have, as yet, been corrected only approximately for non-nominal instrument behavior. Finally, the interpretation of the data in terms of elemental composition has been made so far for only eight chemical elements. Thus, the preliminary results reported here must be assigned larger errors than will be applicable at a later state of data analysis.

2. Background Data

Although the background-measuring phase is the second operational phase of the Alpha-Scattering Experiment, it will be discussed first, since the results from it are used to evaluate both the standard-sample and lunar-sample data.

Of the total of 6.25 hr of data collection in this background phase, 6.1 hr of teletyped data have been subjected to preliminary certification and corrected crudely for the temperature characteristics of the instrument. The results, in units of events per channel per 1000 min, are shown on a logarithmic scale as a function of channel number (energy) in Fig. VII-8 for both alpha and proton modes of the instrument. The statistical errors (1σ) associated with the data points are indicated by vertical bars.

The prominent features of Fig. VII-8 are the same as observed in the background phase of the *Surveyor V* mission. The peaks in both alpha and proton modes in the vicinity of channel 110 are due to the alpha particles from Es^{254} placed near the individual detectors as internal energy markers. The quality of these einsteinium sources was significantly better on *Surveyor VI* than on *Surveyor V*.

The background in the alpha mode of Fig. VII-8, over most of the energy range, is several times higher than that in *Surveyor V*. Moreover, it shows a drop at approximately channel 93, which is characteristic of the response of the instrument to a gold sample. This feature of the instrument had been detected in the pre-launch tests at Cape Kennedy. It was diagnosed as due to a larger-than-previously-encountered recoil behavior of the Cm^{242} flight sources prepared for this mission. Recoiling atoms from the alpha decay of Cm^{242} were transferring radioactive material from the source plate to the protective films which cover the collimating opening of the source capsule. In this position the radioactivity was not collimated, and could strike the gold-plated upper surface of the bottom plate of the instrument. Because of the high probability of scattering by gold, even a small amount of radioactivity in this position produced an easily detectable increase in background in the alpha mode of the instrument. This feature was present, but less pronounced, in the *Surveyor V* background spectrum.

This enhanced background in the alpha mode, moreover, gradually increased with time (as more radioactivity was transferred to the films). Its presence will probably make impossible a significant estimate of the amounts of elements heavier than nickel at the *Surveyor VI* landing site; it should not significantly affect the other results of the mission.

The background measured in the alpha mode in channels above the Es^{254} peak (not shown in Fig. VII-8) corresponds to events depositing at least 6.3 MeV in the alpha detector. The rate of such events is very low (54 ± 12 per 1000 min). It agrees with the corresponding rate of *Surveyor V* and is consistent with the contribution calculated for solar and cosmic ray particles.

In the proton mode, except for the energy region close to the Es^{254} peak, most of the background is due to solar and cosmic ray particles. The values observed on *Surveyor VI* and presented in Fig. VII-8 (lower spectrum) are similar, but a little higher than those observed on *Surveyor V* and predicted from literature data on low-energy particles in space. The slightly lower values of the

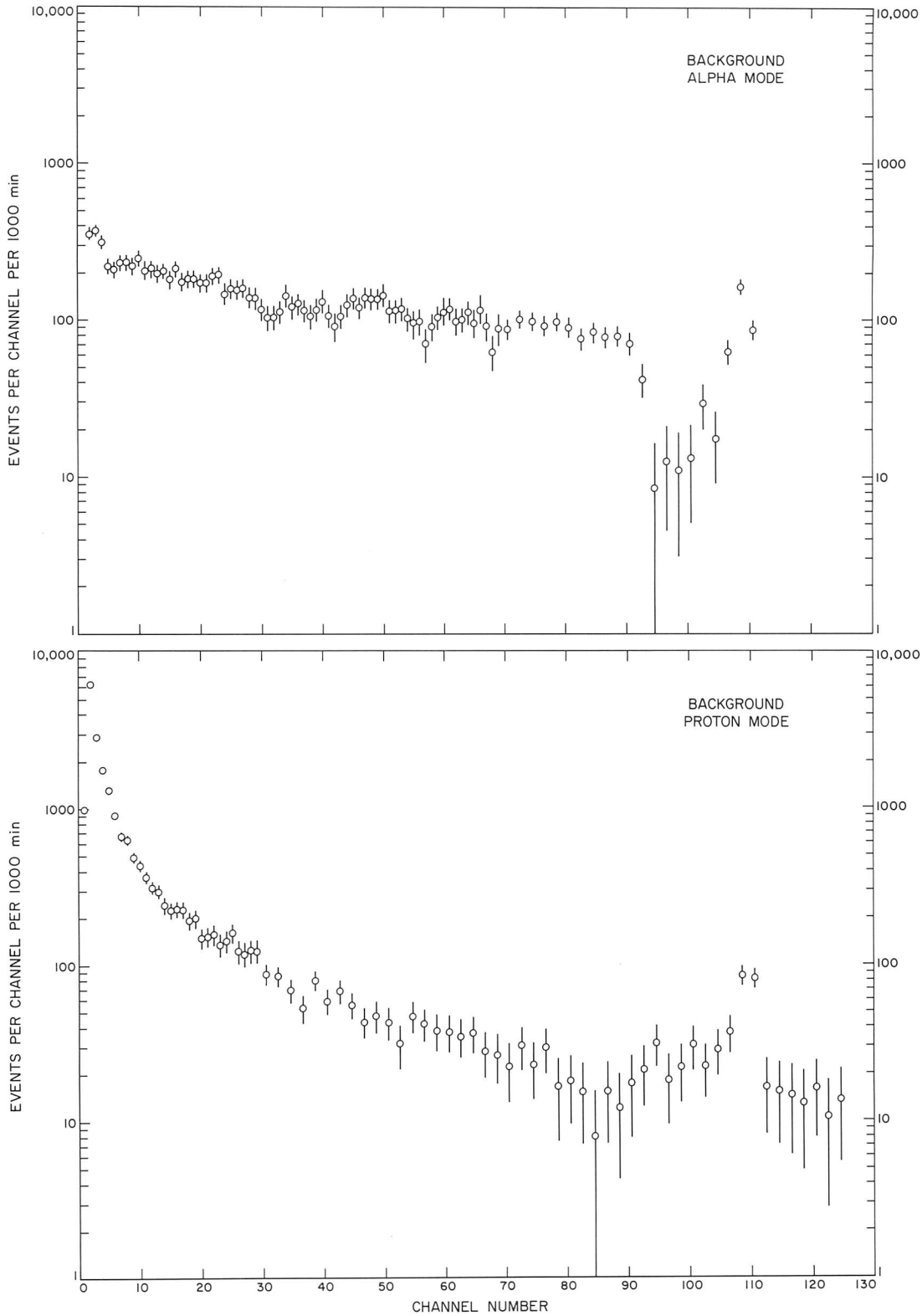

Fig. VII-8. Results of background measurements on the moon. Data taken on the *Surveyor VI* mission by the alpha-scattering instrument in the alpha and proton modes during 366 min of measurement during the background phase on the moon. The experimental points with statistical (1σ) errors are averages of two channels in the regions of low counting rates to improve their statistical significance. The experimental points have been corrected approximately using the temperature coefficient of the instrument. The peaks at approximately channel 110 in both modes are due to Es^{254} placed near the detectors before launch.

background in the proton mode observed on *Surveyor V* may be due to the greater amount of shielding provided by the local lunar terrain in the *Surveyor V* mission, since that spacecraft landed in a small crater. This general similarity of the background rates attributable to cosmic ray and solar particles during the two missions is in agreement with preliminary data obtained from the *Imp IV* satellite, in orbit around the earth. These data indicate that the flux of protons of energies greater than about 1 MeV was approximately the same during the time of the *Surveyor V* and *VI* missions.[2] The constancy of this solar and cosmic ray background was further monitored during the experiment by the rates in the proton mode at channels above the Es^{254} region (channels 113–124, and the overflow channel, 126). During the period in which the data of this report were gathered, this rate was constant to about 10% at 1.06 events per min.

In the data analysis described in this report, the actual background data of Fig. VII-8, without any smoothing and taking into account the observed statistical errors, have been subtracted from the standard- and lunar-sample data (see below).

3. Standard-Sample Data

During the *Surveyor VI* mission, 5.3 hr of data were accumulated on the standard sample in the stowed phase, soon after the spacecraft landed on the moon, and before the sensor head was released to the background-measuring position. Of these, 4.7 hr of data have been examined and corrected approximately to standard instrument response. These data are presented in Fig. VII-9 in the usual units with statistical errors indicated. A smooth-curve version of the background (through the data of Fig. VII-8) is shown to indicate the approximate magnitude of the subtraction in different energy regions.

The observed data in this phase compare favorably with predictions based on pre-launch measurements corrected for estimates of solar and cosmic ray backgrounds expected during the mission. Even the gross data show clearly, in the alpha mode, the characteristic high-energy breakpoints due to the carbon (channel 14), oxygen (channel 27), silicon (channel 50), and iron (channel 73) in the sample. Similarly, in the proton mode, the group of protons producing a peak at approximately channel 82 is indicative of the presence of sodium in the sample. The lack of an appreciable number of events above background in channels greater than 90 indicates little or no aluminum.

In addition to these general, expected, features, the data of Fig. VII-9 indicate that the thin films covering the radioactive-source capsules had survived the launch, transit, and touchdown conditions. If they had broken, some of the Cm^{242} would have been transferred from the source capsules to the sample and there would have been a buildup in the alpha spectrum at approximately channel 103, corresponding to the energy of the alpha particles of Cm^{242}.

The data of Fig. VII-9, after subtraction of the background, have been treated, so far, only by preliminary computational techniques. These have included a library of only eight elements (C, O, Na, Mg, Al, Si, "Ca" and "Fe"), and only partial correction for instrument characteristics. The resulting representation of the standard-sample data in terms of this library is shown in Fig. VII-10. The main features of both alpha and proton spectra are well reproduced. Only in fine details are there significant systematic deviations, arising, probably, from inadequate corrections for instrument characteristics.

Table VII-2 presents the resulting chemical analysis of the standard sample obtained under lunar conditions. Also shown (column 3) are the results of treating the data obtained at Cape Kennedy, before launch, by similar calculational techniques. The last column (column 4) shows that the results obtained under lunar conditions agree adequately with those obtained before launch. Both sets of data deviate more from the conventional analytical results than would be expected at a later stage of data analysis. For the present, the data of Figs. VII-9 and VII-10 give assurance that the alpha-scattering instrument had arrived on the moon in a satisfactory condition to perform chemical analyses of the lunar surface material.

4. Lunar-Sample Data

Of the approximately 27 hr of data on lunar-sample measurements obtained by means of the Alpha-Scattering Experiment, a large part was collected using only three of the four proton detectors (see above). Of the total data, those obtained during a little more than 13 hr (790 min) have been examined in a preliminary way and analyzed by first-cut calculational techniques.

[2]We are indebted to Dr. John Simpson of the University of Chicago and to his collaborators at the Goddard Space Flight Center for these data. Their availability in near-real time gave confidence that adequate warning of solar-flare-induced increases in background would be given.

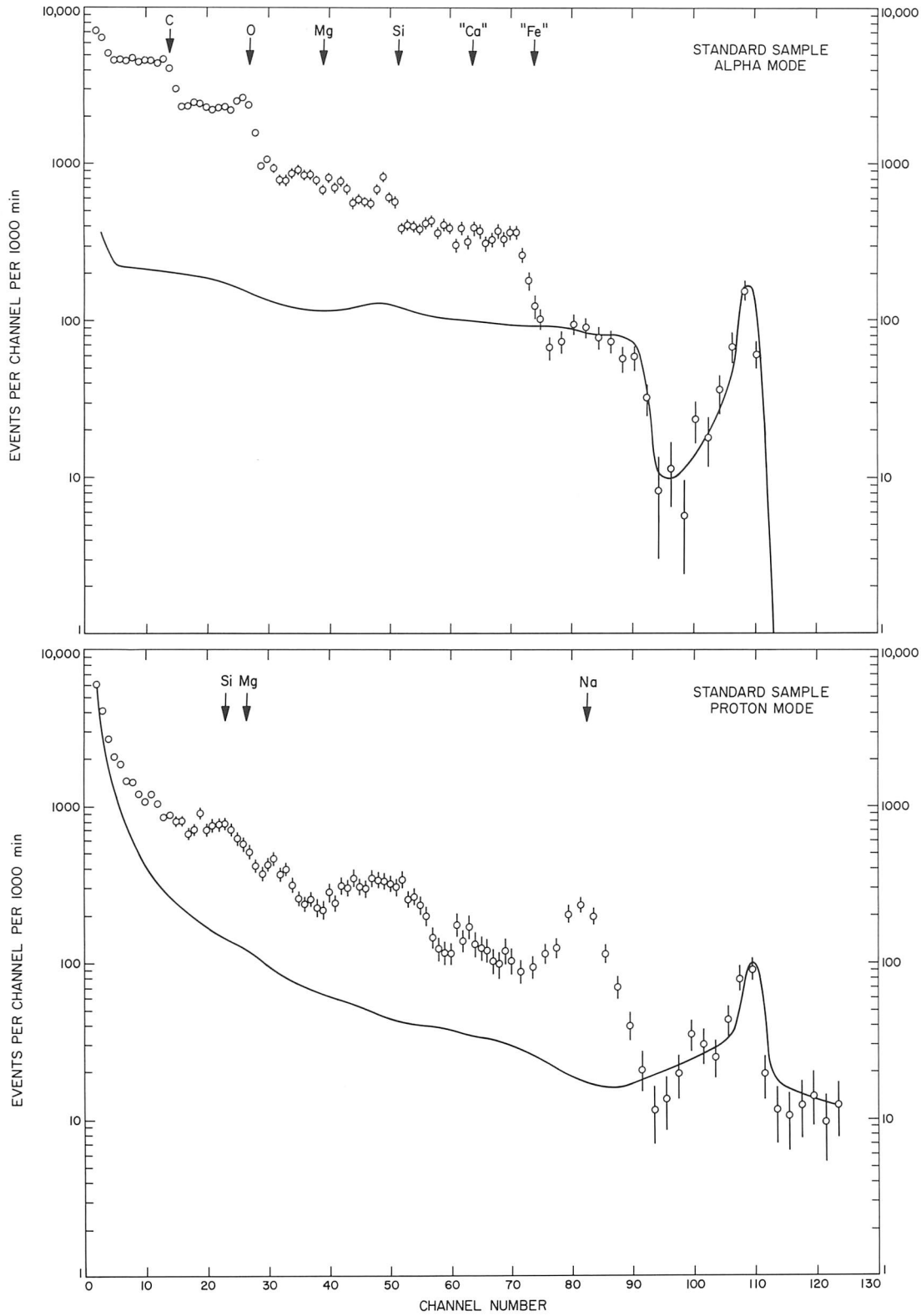

Fig. VII-9. Results of standard-sample measurements on the moon. Data taken on the *Surveyor VI* mission by the alpha-scattering instrument in the alpha and proton modes during 280 min of measurement of the standard sample after lunar landing. The experimental points are indicated with statistical (1σ) error bars. They have been corrected approximately using the temperature coefficient of the instrument. For comparison, the smooth curve shows the approximate magnitude of the background (Fig. VII-8).

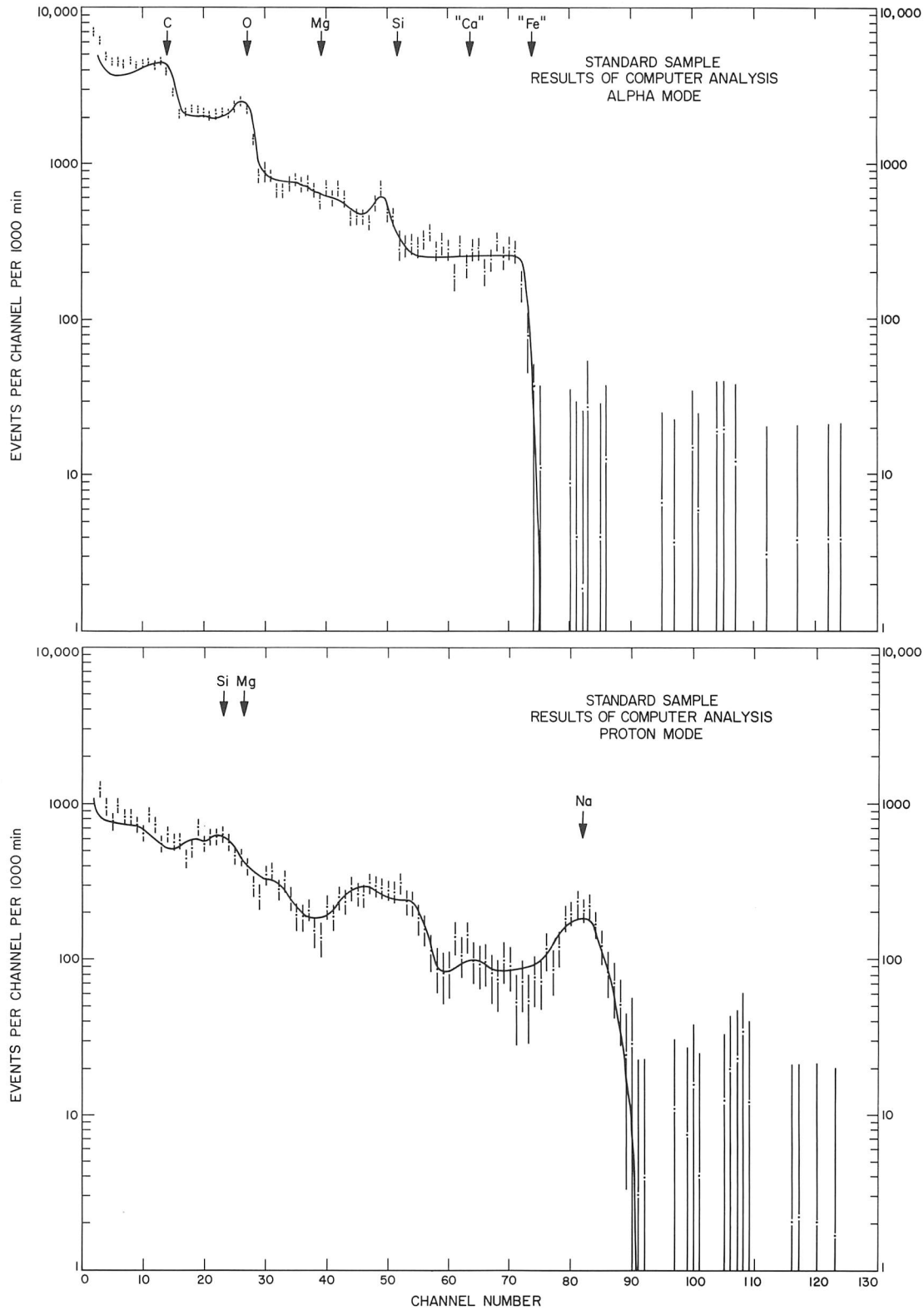

Fig. VII-10. Computer analysis of standard-sample data. The calculated spectra (smooth curves), using an eight-element library, are compared with the data (points with 1σ error bars) taken during 280 min of analysis of the standard sample on the *Surveyor VI* mission on the moon. The background (Fig. VII-8) has been subtracted before the comparison is made. The computer analysis has been made over channels 8–85 in the alpha mode and over channels 8–110 in the proton mode.

Table VII-2. Analysis of standard sample on *Surveyor VI*

Element	Percent of atoms[a]		
	Surveyor VI mission	Pre-launch data	Conventional analysis
C	23	22	23[b]
O	39	40	45
Na	10	9	6
Mg	7	9	7
Al	−1	0	0
Si	16	14	13
"Ca"	0	2	0
"Fe"	6	5	5

[a]Excluding elements lighter than beryllium.

[b]The standard glass sample is covered by a polypropylene grid.

The raw data from this period, corrected approximately to standard instrument response, are shown in Fig. VII-11. The ordinates are in the units of events per channel per 1000 min, with statistical errors indicated. Shown also is the smooth-curve version of the background observed during the *Surveyor VI* mission.

The gross features indicated by Fig. VII-11 are those shown by the spectra of many terrestrial rocks examined by this technique and by the data found during the *Surveyor V* mission at the Mare Tranquillitatis site. In the alpha mode (Fig. VII-11, upper spectrum), there is a sharp drop in intensity at channel 27 that is characteristic of the presence of oxygen in the sample; the slight peak and subsequent decrease in response at approximately channel 50 indicates the presence of silicon; the final drop to background levels at about channel 73 shows that elements in the region of iron, cobalt, and nickel are the heaviest present in appreciable amounts in the sample. One feature more clearly visible here than in the *Surveyor V* data at this stage of analysis is the "break" in intensity a little above channel 60. This is the region where elements with approximately the mass of calcium would have their high-energy limits of alpha scattering.

The gross proton spectrum (Fig. VII-11, lower spectrum) has fewer features standing out above the background. Very important ones, however, are the sharp drop in intensity at approximately channel 62 and the significant levels, above background, in the energy regions between channels 70 to above 100. This behavior is characteristic of protons produced by alpha particles impinging on aluminum.

Computational analysis of the data of Fig. VII-11 (after background subtraction), in terms of the standard library of eight elements, leads to the comparison with the observed data shown in Fig. VII-12. The synthesis from the library spectra represents the gross features of the observed spectra very well. However, there are systematic discrepancies outside the experimental errors. Some of these, such as the behavior in the alpha mode in the region of channels 28 and 73, appear to be caused by a slight mismatch in energy scales between the lunar data and the library used in the synthesis. This, of course, will be remedied at a later stage of analysis.

The results obtained in this way for the chemical composition of the sample of the lunar surface examined in the *Surveyor VI* mission are presented in Table VII-3. It must be remembered that the alpha-scattering technique is not sensitive to elements lighter than beryllium, and that, in the present stage of analysis into only eight components, the "calcium" is to be taken as representing elements having masses in the approximate range of 30 to 47, and "iron" as representing elements with masses between approximately 47 and 65.

The preliminary nature of these results is reflected in the magnitude of the errors assigned at the present stage of analysis. These errors are subjective estimates and will be reduced by a more refined analysis of these and more complete data.

Table VII-3. Chemical composition of lunar surface at landing sites

Element	Atomic percent[a]	
	Surveyor V[b]	*Surveyor VI*
C	< 3	< 2
O	58 ±5	57 ±5
Na	< 2	< 2
Mg	3 ±3	3 ±3
Al	6.5 ±2	6.5 ±2
Si	18.5 ±3	22 ±4
"Ca"[d]	13 ±3[c]	6 ±2
"Fe"[e]		5 ±2

[a]Excluding elements lighter than beryllium.

[b]*Surveyor V* results are from Refs. VII-1 and VII-2.

[c]*Surveyor V* results were for the total of atoms heavier than silicon. A lower limit of 3% was set for "Fe."

[d]"Ca" here denotes elements with mass numbers between approximately 30 and 47, and includes, for example P, S, K, and Ca.

[e]"Fe" here denotes elements with mass numbers between approximately 47 and 65, and includes, for example, Fe, Co, and Ni.

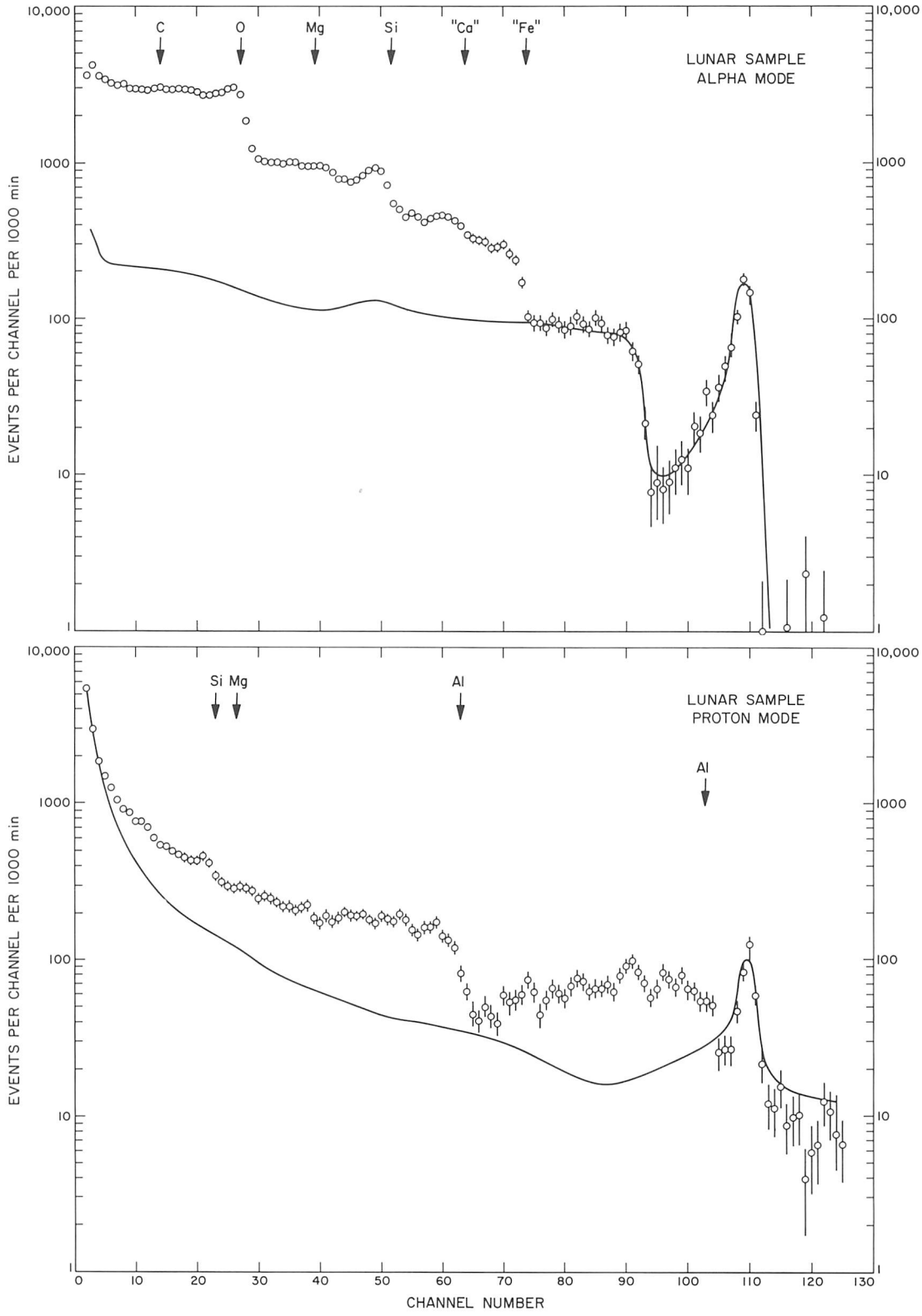

Fig. VII-11. ***Surveyor VI*** **lunar sample. Data obtained by means of the Alpha-Scattering Experiment in the alpha and proton modes during 790 min of measurement on the lunar surface. The experimental points are indicated with statistical (1σ) errors. The data have been corrected to standard instrument response. The solid curve in each case is a smoothed version of the background observed in the previous stage of lunar operations.**

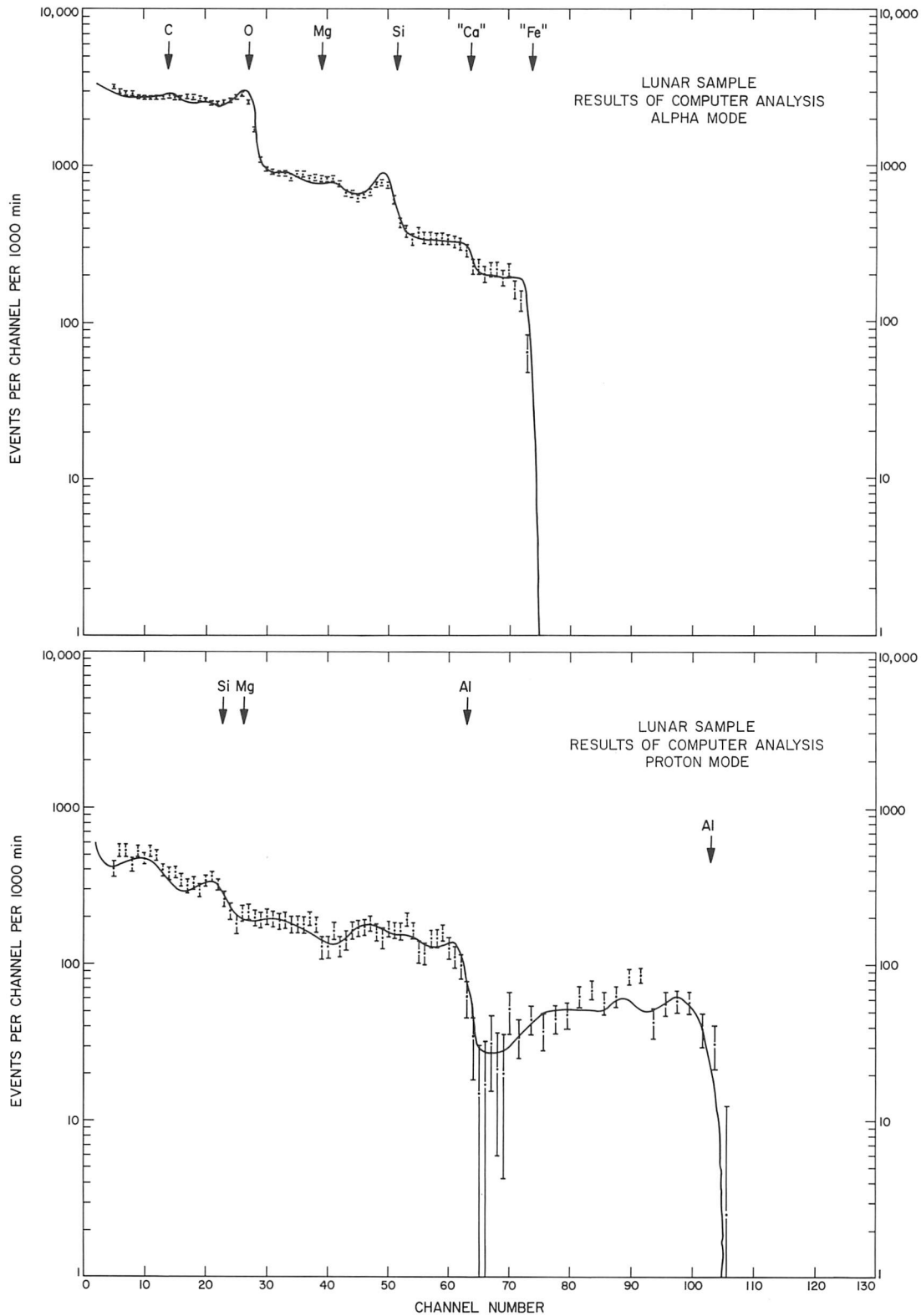

Fig. VII-12. Computer analysis of *Surveyor VI* lunar-sample data. The calculated spectra (smooth curves), using an eight-element library, are compared with the data (points with 1σ error bars) taken during 790 min of analysis. The background (Fig. VII-8) has been subtracted before the comparison is made. The computer fit has been made over channels 8–85 for the alpha mode, and over channels 8–110 for the proton mode.

Table VII-3 also shows the results found by the same technique at the *Surveyor V* landing site. At both sites, the most abundant chemical element is oxygen and next in numbers of atoms is silicon. Aluminum is very prominent in both samples. At present, only upper limits can be assigned to the amounts of carbon and sodium present. Well within the assigned errors, the results of the two analyses are the same.

5. Post-Hop Data

After the hopping maneuver (see Section IV of this report), the alpha-scattering instrument was found to be upside down on the lunar surface (see Fig. VII-7), thus ending the possibility of obtaining any more lunar data. The electronics and detector systems, however, had survived the hopping maneuver. The data obtained after the hop contained a large number of events, particularly around channel 103 in the alpha spectrum. This indicated that at least one of the protective films over the radioactive sources had broken.

The rates in the proton mode of the instrument were also significantly higher than before the hop. Qualitatively, this was understandable in that the proton detectors in the new position of the sensor head were exposed to radiation from space (through the 10.8-cm sample opening in the instrument) with essentially no shielding other than the gold foil over the detectors.

These event rates in the proton mode did not remain constant, however. During the course of the lunar afternoon they fell significantly, with a larger decrease in the low-energy portion of the spectrum. At the time of this report, there are several possible explanations for this behavior. Because of the nonstandard mode of operation, it may be, for example, an instrumental effect. It may, on the other hand, represent a significant decrease in the number of low-energy solar protons reaching the surface of the moon during the late lunar afternoon. This could arise, for example, either as a result of a decrease in the number of low-energy particles following a solar flare, or as a result of shadowing by the moon of the source of such particles.

E. Discussion

1. Comparison With *Surveyor V* Results

Perhaps the single most important result of the Alpha-Scattering Experiment on the *Surveyor VI* mission is the finding that the chemical composition at the *Surveyor VI* landing site is essentially the same as at the *Surveyor V* site. This agreement provides a basis for assuming that considerable portions of the mare areas of the moon have a similar chemical composition.

This similarity of results from the two missions is indicated by the detailed results of the computer analysis of the data presented in Table VII-3. The large errors assigned to these results at the present stage of analysis, of course, could accommodate a considerable range of chemical compositions for the sample. However, these large assigned errors are estimates primarily of systematic effects not possible to evaluate accurately at present. It is, therefore, worth examining the results on the two missions at an earlier stage of data reduction to try to detect smaller differences in chemical composition at the two sites.

In Fig. VII-13, the raw data from the two missions are compared directly. They have been corrected only for the background and approximately for the temperature coefficients of the respective instruments. All of the data from the *Surveyor VI* mission (both proton and alpha) have been normalized by a factor that brings the oxygen region of the alpha mode (channels 8 to 25) into coincidence with that region of the *Surveyor V* data. This is done in order to take into account differences in source strength, measurement duration, and possible differences in sample distances between the two missions. The *Surveyor V* data are shown via the smooth curves; *Surveyor VI* data are shown as points with associated statistical (1σ) error bars.

Figure VII-13 indicates very good correlation, both qualitative and quantitative, between the *Surveyor V* and *Surveyor VI* data in both alpha and proton modes in all energy regions. Most of the small systematic deviations (such as near the regions of rapidly changing intensity) are attributable to the slightly different energy scales of the instrument. Except at such regions, the response is usually the same, within statistics, in comparable energy regions of both spectra. One region of possibly significant deviation is in the alpha mode above channel 52. In this case, there is the previously mentioned resolution into "calcium" and "iron" contributions in *Surveyor VI* which was not evident in the first sample examined by *Surveyor V*. In addition, the total contributions of elements heavier than silicon appear to be somewhat less (relative to oxygen and silicon) at the *Surveyor VI* site.

These differences are small, however, compared to those that might be expected from significantly different rock types. For example, Fig. VII-14 shows spectra taken

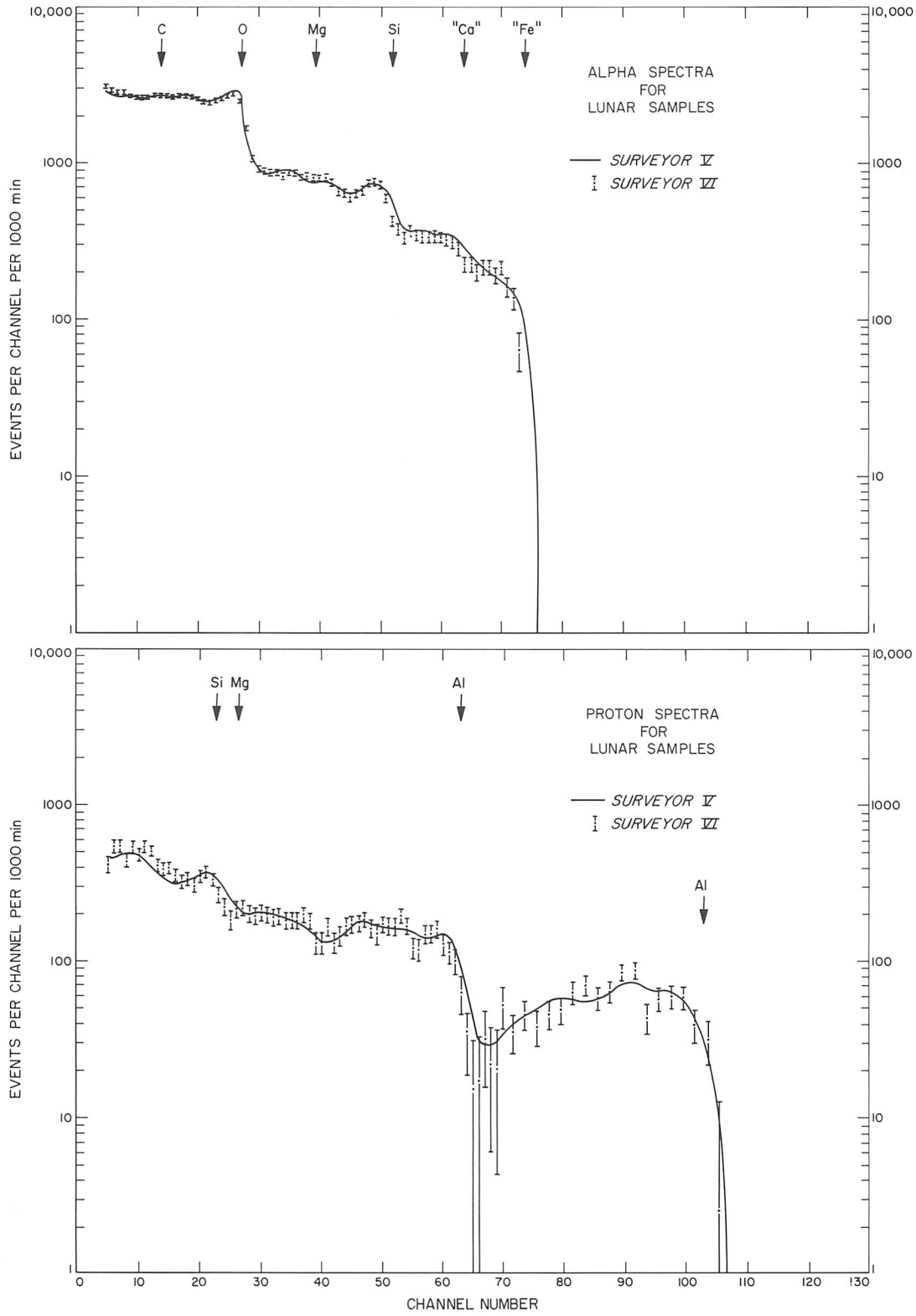

Fig. VII-13. Comparison of *Surveyor V* and *Surveyor VI* lunar-sample data. The data from the first sample of *Surveyor V* (background subtracted) are shown by smooth curves. The *Surveyor VI* data (also background subtracted) are indicated by points with error bars. The latter have been multiplied in both alpha and proton modes by a common factor to make them match in the oxygen region of the alpha mode.

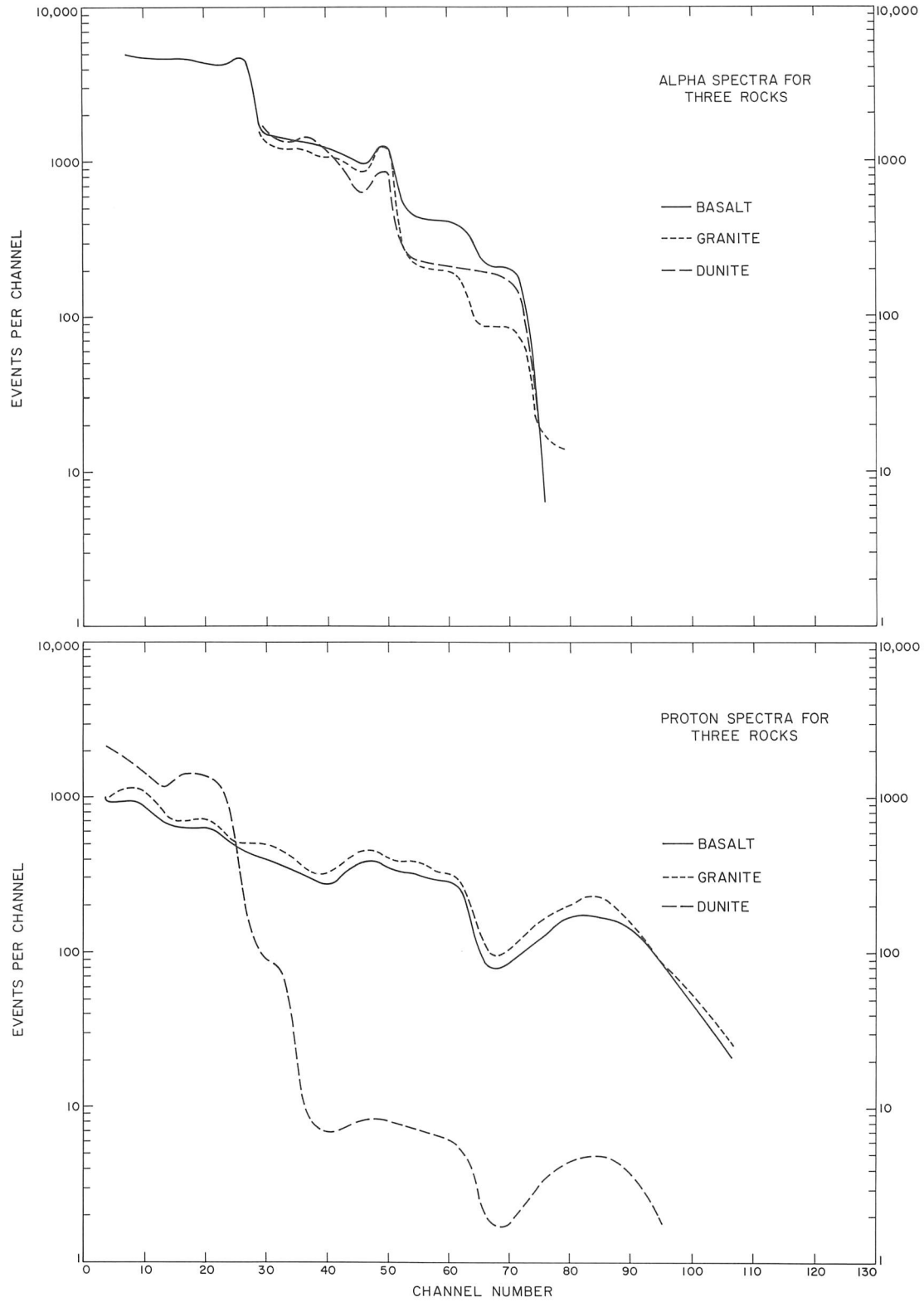

Fig. VII-14. Alpha-scattering instrument response from three rocks. Data taken with a *Surveyor* prototype instrument (P-2) on samples of basalt (USGS-W-1), granite (USGS-G-2), and dunite (USGS-DTS-1). All data from each rock have been multiplied by a factor to make the responses equal in the oxygen region of the alpha mode.

with a *Surveyor* prototype instrument (P-2) from samples of basalt, dunite, and granite.[3] (The construction of this instrument was similar to that of the flight instruments except that the sensitive depth of the proton detectors of P-2 was shallower than in the *Surveyor* instruments. This resulted in a change of shape of the spectra of highest-energy protons from aluminum.) The data have been normalized in the same way as for Fig. VII-13, so that the alpha spectra in the region characteristic of scattering by oxygen are matched. In the proton mode it is seen that, although there are only small differences between the spectra from basalt and granite, the spectrum from dunite (and therefore chondritic meteorites) is distinctive. In the alpha mode, particularly in the energy regions above channel 40, there are marked differences among the three types of rocks. No such differences, in either proton or alpha mode, are indicated in the data from *Surveyors V* and *VI*. It must be concluded that, although some differences between the two landing sites may become established upon more detailed analysis of the data, the basic chemical composition of the surface material is the same.

Two further remarks can be made pertinent to the generality of these analytical results: *Surveyor V* landed inside a small crater in Mare Tranquillitatis, and the sample examined was partly material ejected by the footpads during the landing. *Surveyor VI* landed in Sinus Medii on relatively flat terrain, and the sample examined was, as far as can be determined, undisturbed surface material. Second, the two missions differed in the height at which the retro rocket burned out. In the *Surveyor V* mission, the end of burning was at 1.6 km; in the *Surveyor VI* mission, it was at 13.5 km. The retro rocket produces Al_2O_3 and conceivably could affect the analytical results. Estimates made at the time of *Surveyor V* indicated that, even there, the effect on the retro-rocket exhaust should have been negligible (see Ref. VII-1, Appendix A). The amount of Al_2O_3 contamination estimated for the *Surveyor VI* site is an order of magnitude less. The findings on *Surveyor VI* of the same atomic percent of aluminum as in *Surveyor V* confirms the validity of these estimates.

The similarity of the results at the two sites make it unlikely that this chemical composition is applicable only to unique places on the moon. It appears much more probable now that this composition is representative of large portions of the surface material of lunar maria.

[3]U. S. Geological Survey Standards W-1, DTS-1, and G-2, respectively.

2. Chemical State of Lunar Surface Material

The Alpha-Scattering Experiment provides no direct information about the chemical state of the elements measured. However, chemical experience allows us to extrapolate from data such as in Table VII-3 to what may be the most probable chemical state of the bulk of *Surveyor*-type lunar surface material. Specifically, the large atomic fraction of oxygen, more than 50% by atom, indicates that the metals present are in oxide states. The mean values, particularly in the case of the *Surveyor VI* results, indicate apparent oxygen deficiency. However, well within the present limits of errors, there is enough oxygen to combine with all the elements considered. For example, Table VII-4 presents the weight percentages of oxides that would be consistent with the analytical results from the two missions.

Table VII-4. An oxide composition consistent with *Surveyor V* and *VI* analytical results

Oxide	Weight percent
Na_2O	—[a]
MgO	5
Al_2O_3	13
SiO_2	50
CaO	15
FeO	16

[a]The presence of sodium has not been established with certainty. Sodium oxide could be present in amounts up to 3% by weight.

It must be emphasized that the assigned percentages in Table VII-4 are not unique. The limits of variation are hard to estimate at present. However, the table is an example, consistent with the results of the Alpha-Scattering Experiment, of the chemical state of the major elements in the lunar mare surface material.

It should be noted that Table VII-4 is meant to illustrate the oxide composition of the *bulk* of the lunar material examined. Minor constituents adding up to maybe as much as 10% by weight may be present. In addition, the analytical errors do not exclude some unoxidized metal, or radiation-decomposed oxides. A volumetric limit to metallic iron, the most likely non-oxidized metal, is however, placed by the magnet test (see Section VIII of this report).

One can speculate even further about the chemical state of this material. It is improbable that it exists as a mere mixture of oxides. Rather, the oxides are likely to be combined into more complex minerals. This is the state

of material of similar chemical composition in most other natural samples available to us, such as terrestrial rocks and meteorites.[4] Even with the present large analytical errors, the types of likely minerals are strongly restricted, although not defined uniquely. For example, the chemical composition given in Tables VII-3 and VII-4 is consistent with the bulk of the material being a mixture of minerals of the feldspar and pyroxene classes. As the analytical errors are reduced and as the amounts of the minor constituents are established, it will become possible to further define the mineral composition of this material.

Although this interpretation of the analytical results represents an extrapolation from the actual results of the Alpha-Scattering Experiment, it should provide a more secure base from which to predict various other properties of the lunar mare surface material than has been available until now. For example, lunar material in the state postulated should be chemically inert. It should not react with the usual materials of instruments or of structures brought in contact with it. This is consistent with the lack of obvious chemical action of lunar surface materials with the aluminum-clad spacecraft footpads. Similarly, since the present analytical results provide information, not only of the principal chemical elements present, but also of the probable chemical state, it should be possible now to evaluate more confidently the practicality of utilizing the raw materials on the moon.

Finally, even these preliminary results should make it possible to improve predictions of detailed physical and chemical properties (such as melting point, density, hardness, compressibility, etc.) of the particles making up lunar surface material by comparison with terrestrially available materials of similar chemical composition.

3. Comparison With Samples Available on Earth

From the results of the *Surveyor V* mission, it was concluded that the chemical analysis of the lunar surface material at Mare Tranquillitatis resembled that of some terrestrial basalts and that of a somewhat rare type of meteorite—basaltic achondrites. The results from the present mission, since they agree essentially with those of the *Surveyor V* mission, support this conclusion. In addition, the new results make possible a slightly more detailed comparison, because they provide a partial breakdown of the elements of mass numbers 30–65. This comparison of the *Surveyor VI* results with the chemical composition of some terrestrial dunites, basalts and granites, and three samples of meteoritic material, is shown in Fig. VII-15. The present data are again nearest to the chemical composition of terrestrial basalts and to that of the meteoritic basaltic achondrites. This chemical evidence speaks strongly against the two largest classes of meteorites (metallic and chondritic) coming from the mare regions of the moon. As in the case of the *Surveyor V* results, the abundances of "calcium" and "iron" in the lunar sample examined here are too large to be compatible with a granitic chemical composition, or with one similar to that of tektites.

4. Implications About the Origin of the Moon

One of the most important applications of these chemical analytical results is in providing clues as to the history and origin of the moon. This topic is examined from a geological standpoint in Section IX. If it is assumed that the moon originally came from material with the same chemical composition as the solar atmosphere, the relative abundances of elements that are nonvolatile (and do not form stable volatile compounds) should be the same on the moon as in the solar atmosphere. The comparison between solar abundances and the *Surveyor VI* results for sodium, magnesium, silicon, "calcium" and "iron" is shown in Fig. VII-16. Both solar and *Surveyor VI* results have been normalized to unit value for silicon. In addition, it has been assumed that the solar abundance of sulfur would not be available in the formation of a body such as the moon because of the volatility of hydrogen sulfide.

Figure VII-16 shows that there is significant disagreement between the solar abundances of nonvolatile elements and those observed at the *Surveyor VI* landing site. The relative abundances of sodium and iron are within experimental error; on the other hand, the values for magnesium, aluminum, and "calcium" are in strong disagreement. Aluminum and "calcium" have been enriched relative to silicon; magnesium has been depleted in the sample examined by *Surveyor VI* relative to the solar abundances.

This comparison indicates that the original solar-system material, if it were to form the lunar maria, would have to undergo large-scale cosmochemical processes that concentrated some elements and removed others before the lunar mare surface was formed. Presumably, it was a process similar to that which produced differentiation

[4]In making this additional extrapolation from the basic analytical results, it must be kept in mind that, on the lunar surface, the material may be in a noncrystalline form, either a glass, or too radiation damaged to be identified crystallographically.

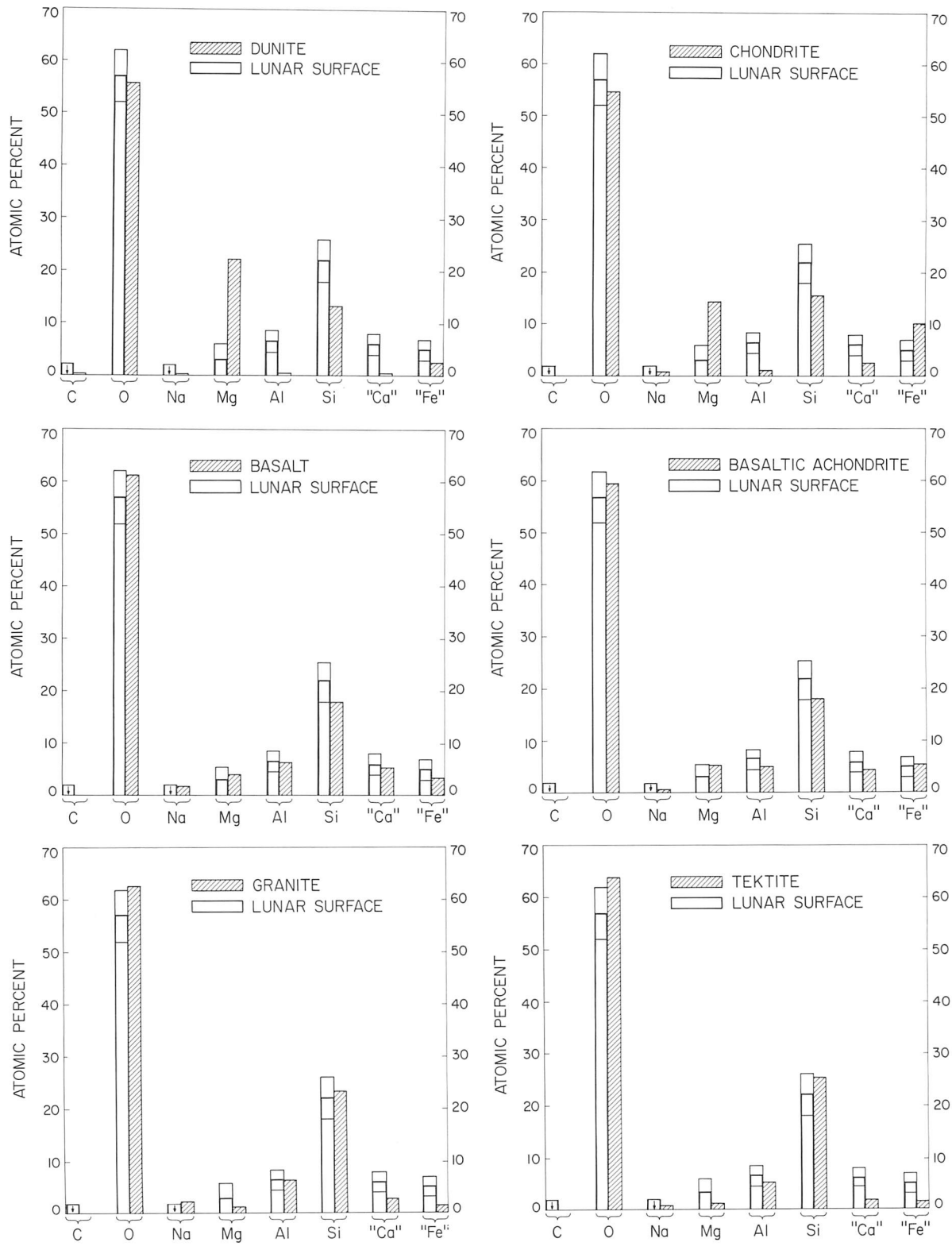

Fig. VII-15. Comparison of the observed chemical composition of the *Surveyor VI* lunar sample (open bars) with the average composition of selected materials (cross-hatched bars). The dunite and basaltic achondrite values are from Ref. VII-6; the basalt values are for Continental Basalts from Ref. VII-7; the granite values are for the North American Crust from Ref. VII-8; the chondrite values are the averages of the low-iron group from Ref. VII-9; the tektite values are those for the Indo Malayan body quoted in Ref. VII-6.

of the material making up the earth. This process could have occurred on the moon itself or in some parent body.

F. Summary

Surveyor VI has established that the chemical composition of the sample of lunar surface material in Sinus Medii is very similar to that found by *Surveyor V* at Mare Tranquillitatis. This chemical composition suggests that much of the lunar mare surface material is made up of chemical compounds and minerals that are well known on earth. If this material originally came from the sun, it must have undergone extensive cosmochemical processing to change the relative abundances of the chemical elements from those present on the sun.

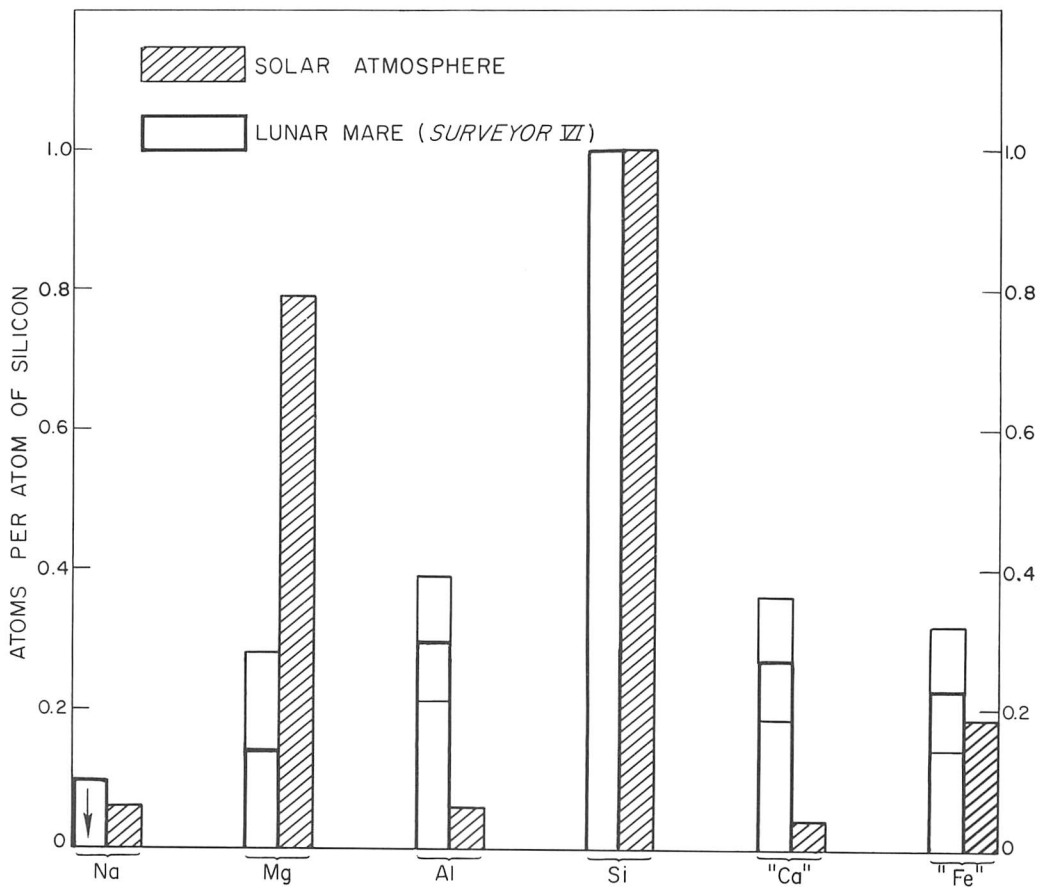

Fig. VII-16. Comparison of the observed chemical composition of the *Surveyor VI* lunar sample with that of the nonvolatile elements in the solar atmosphere. The two compositions have been normalized to unity of silicon. The solar values are from Ref. VII-10.

References

VII.1. Turkevich, A. L., Franzgrote, E. J., and Patterson, J. H., "Chemical Analysis of the Moon at *Surveyor V* Landing Site: Preliminary Results," *Surveyor V Mission Report. Part II: Science Results,* Technical Report 32-1246, Jet Propulsion Laboratory, Pasadena, Calif., November 1, 1967.

VII-2. Turkevich, A. L., Franzgrote, E. J., and Patterson, J. H., "Chemical Analysis of the Moon at the *Surveyor V* Landing Site," *Science,* Vol. 158, pp. 635–637, 1967.

VII-3. Patterson, J. H., Turkevich, A. L., and Franzgrote, E. J., "Chemical Analysis of Surfaces Using Alpha Particles," *J. Geophys. Res.,* Vol. 70, No. 6, pp. 1311–1327, 1965.

VII-4. Turkevich, A., Knolle, K., Emmert, R. A., Anderson, W. A., Patterson, J. H., and Franzgrote, E. J., "Instrument for Lunar Surface Chemical Analysis," *Rev. Sci. Inst.,* Vol. 37, No. 12, pp. 1681–1686, 1966.

VII-5. Turkevich, A. L., Knolle, K., Franzgrote, E. J., and Patterson, J. H., "Chemical Analysis Experiment for the *Surveyor* Lunar Mission," *J. Geophys. Res.,* Vol. 72, No. 2, pp. 831–839, 1967.

VII-6. Palm, A., and Strom, R. G., *Space Sciences Laboratory Research Report,* Series 3, Issue 5, University of California, Berkeley, Calif., 1962.

VII-7. Turekian, K. K., and Wedepohl, K. H., "Distribution of the Elements in Some Major Units of the Earth's Crust," *Geol. Soc. Amer. Bull.,* Vol. 72, pp. 175–192, 1961.

VII-8. Condie, K. C., "Composition of the Ancient North American Crust," *Science,* Vol. 155, pp. 1013–1015, 1967.

VII-9. Urey, H. C., and Craig, H., "The Composition of the Stone Meteorites and the Origin of Meteorites," *Geochem. et Cosmochim. Acta.,* Vol. 4, pp. 36–82, 1953.

VII-10. Urey, H. C., "The Abundance of the Elements With Special Reference to the Problem of the Iron Abundance," *Quart. J. Roy Astron. Soc.,* Vol. 8, pp. 23–47, 1967.

Acknowledgment

The Alpha-Scattering Experiment on the *Surveyor VI* mission has been the product of the work of many organizations and people. In addition to the authors, at the Enrico Fermi Institute of the University of Chicago, Mr. Ed Blume, Mr. Tom Economou, Mr. Ken Sowinski, and Mr. Bernd Wendring participated in the final tests and calibration of the instrument and in mission operations supporting the experiment.

The Laboratory of Astrophysics and Space Research, also at the University of Chicago, in addition to constructing the instrument, provided extensive support for the final testing and calibration of the instrument at Cape Kennedy and mission support especially via Mr. Wayne Anderson and Mr. Gene Drag. The detector status was continually monitored by Dr. Anthony Tuzzolino.

At the Argonne National Laboratory, Mr. Harry E. Griffin and Mr. Dale Henderson prepared and tested the curium and einsteinium alpha radioactive sources used. Mr. Dale Suddeth provided electronic support during the final calibration and during mission operations.

At the Jet Propulsion Laboratory, Mr. Robert Holman, Mr. Henry Giunta, Mr. Charles Fondacaro, and Mr. William Seeger participated in the final tests and calibration of the instrument at Cape Kennedy. Mr. Richard E. Parker, Mr. George O. Ladner, Jr., Mr. Maurice Clary, Mr. Carl Heinzen, and Mr. Floyd Roberson provided support in controlling the instrument during mission operations, under the direction of Mr. Jack Lindsley and Mr. Donald D. Gordon. Dr. Stanley L. Grotch supervised the real-time calculational monitoring, and computational support was provided by Miss Christine Nelson and Mrs. Sally Rubsamen.

(Blank Page)

VIII. Electromagnetic Properties: Magnet Test

J. Negus de Wys

After the *Surveyor V* mission, it was concluded that Mare Tranquillitatis appeared to be composed of basaltic material; however, speculation persisted concerning the similarity of the composition of the *Surveyor V* landing site to that of other maria on the lunar surface.

Surveyor VI landed in a mare-type area in Sinus Medii just north of a so-called "wrinkle" ridge. Data derived from the magnet test at the *Surveyor VI* landing site afforded a comparison with the data from the magnet test at the *Surveyor V* landing site, as well as with results from various laboratory studies using powdered rock and powdered iron. (See Fig. VIII-1 for the *Surveyor* landing locations and maria distributions.)

The ~500-gauss magnet attracts magnetite (Fe_3O_4, a common mineral in igneous rocks), pure iron (Fe), and nickel-iron (Ni-Fe) from meteorites.

Surveyor V results showed closest agreement with laboratory studies in 37–50μ basalt without any other addition of iron material. Scoriaceous basalt also showed close agreement. The compositional homogeneity of the mare unit had not been established prior to *Surveyor VI,* but merely suggested from *Lunar Orbiter* photographs, television pictures from the previous *Surveyor* missions, and reflectance properties. Other maria could show meteoritic addition or different composition from that found in Mare Tranquillitatis.

A. Magnet Assembly Description

The magnet assembly, as on *Surveyor V,* consisted of a magnetized Alnico V bar $5 \times 1.27 \times 0.32$ cm and a similar-size, unmagnetized bar of Inconel X-750; both bars were bonded with RTV-60 (bonding agent) and attached to a bracket on footpad 2 to permit viewing by the television camera. (The magnet assembly on *Surveyor VI,* before encapsulation at Cape Kennedy, Fla., is shown in Fig. VIII-2.) With the exception of the bracket top, which is painted with the gray and white stripe pattern of the footpad top, the magnet assembly is painted blue. Magnetic flux readings along the pole faces range from 260 to 680 gauss. The north magnetic pole extends down the left side of the magnet; the south pole extends down the right side.

The control bar shows readings of <0.1-gauss over the entire surface. (See Fig. VIII-3 for magnetic-strength readings and final plot of the *Surveyor VI* magnet.)

Fig. VIII-1. Photograph of the moon showing the location of landed *Surveyor* spacecraft. Note *Surveyor V* in Mare Tranquillitatis and *Surveyor VI* in Sinus Medii; *Surveyors V* and *VI* have had the magnet assembly attached to footpad 2 (Table Mountain Observatory photograph taken on February 28, 1964, at 07:55:23 UT).

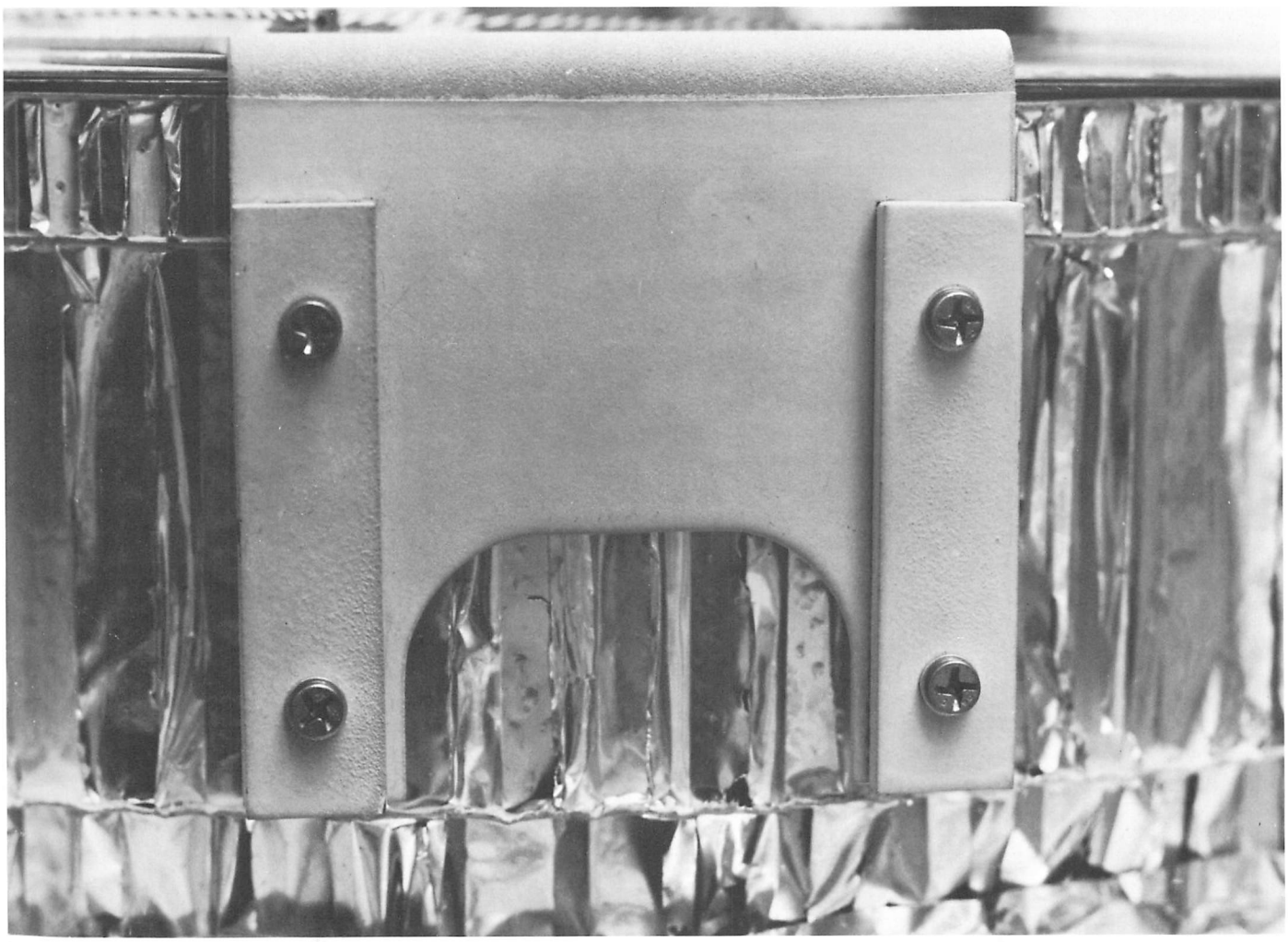

Fig. VIII-2. Magnet assembly at Cape Kennedy before encapsulation. Magnet is on the left; nonmagnetic control bar is on the right. Magnetic north pole is on the left side of the magnet.

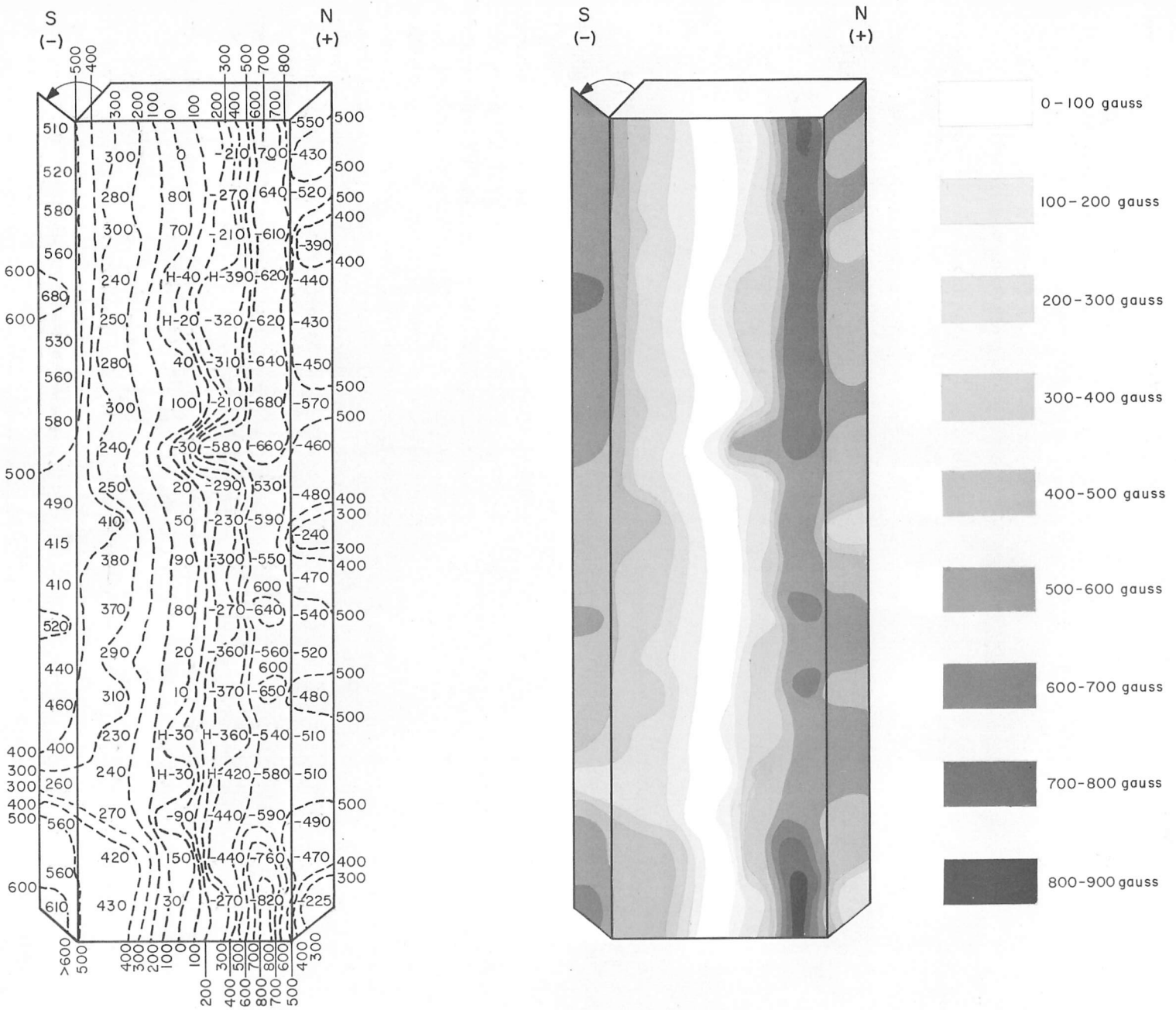

Fig. VIII-3. Gauss readings and tonal plot of readings for magnet on *Surveyor VI*. Note that areas of higher gauss readings are the darkest.

B. Landing

Surveyor VI landed north of a wrinkle ridge on Sinus Medii, a mare area. Footpad 2 bounced about 25 cm leaving a spur between imprints (Fig. VIII-4), and then slid about 8 cm. From laboratory studies, it was determined that the footpad at no time penetrated the lunar surface deeper than 6 cm. Thus, the magnet made no contact with the lunar surface material during the initial landing.

C. Attitude Control Jet Firing

The attitude control jets were fired with a nominal pressure of 4.7×10^3 dynes cm^{-2} on Day 315 at 03:22:45 GMT (for ~4 sec), and at 03:47:16 GMT (for ~60 sec). No change was observed in the magnet assembly. A comparison of a post attitude control jet firing with laboratory tests of an attitude control jet is shown in Fig. VIII-5. The exhaust force vectors of the jet, relative to the magnet assembly, are shown in Fig. VIII-4.

D. Hop and Second Landing

After the 2.5-sec firing of the vernier rocket engines, *Surveyor VI* performed a hop from the original landing position to a position about 2.4 m to the southwest at 10:32 GMT on Day 321. In the movement, the spacecraft rose about 3.5 m above the lunar surface. During this second landing, footpad 2 penetrated the lunar surface material about 10 cm and bounced, causing a horizontal displacement of approximately 12 cm. This landing mode caused contact with the lunar surface material over the lower seven-eighths of the magnet. (See Fig. VIII-6 for movement during the hop and related strain-gage curve; mosaics of footpad 2, before and after the hop, are shown in Fig. VIII-7a and b.) The peaks in the strain-gage data for footpad 2 indicate that the movement from b to c was a bounce, not a slide. Therefore, an instantaneous impact with the surface material may be assumed. Figure VIII-8 shows a closeup of the magnet following the surface impact. (This represents an impact very similar to those achieved in the laboratory.) *Surveyor V* had slid through about 1 m of material during landing.

E. Laboratory Studies

For comparison with the picture of the magnet after contacting the lunar surface material in Sinus Medii, the following laboratory studies were performed:

(1) Impact (in atmosphere) in rock powders using 37–50μ and 50–150μ sizes: rhyolite, dacite, basalt, periodotite, and serpentine.

(2) Impact (in 10^{-6}-torr vacuum) in the same rock powder sequence as (1).

(3) Impact (in atmosphere) in powdered Little Lake basalt with 0 to 20% by volume additions of pure powdered iron, and in powdered Pisgah scoriaceous basalt.

(4) Impact (in 10^{-6}-torr vacuum) in the same rock powder and iron addition sequence as (3).

(5) Impact (in atmosphere) in hydrated lime with 0 to 20% powdered iron by volume additions.

(6) Impact (in atmosphere) in three powder sizes of Little Lake basalt: $<37\mu$, 37–50μ, 50–150μ.

(7) Attitude-control jet exhaust studies using powdered Little Lake basalt and 0 to 4% by volume powdered iron additions. These were conducted in a 10^{-6}-torr vacuum.

A more detailed description of these studies may be found in Refs. VIII-1 and VIII-2. A comparison of the laboratory studies most closely resembling the lunar results is given in Fig. VIII-9.

F. Comparison With Magnetic-Strength Plot

By careful comparison of the magnetic-strength plot with the pictured lunar results (Fig. VIII-10), it may be noted that most of the magnetic particles are adhering in areas showing magnetic strengths of 400 gauss. Peaks in strength (400 to 900 gauss) correlate with accumulations of dark magnetic material. Some bridging across the zero-gauss area may be noted. The top one-eighth of the magnet appears not to have contacted the lunar surface. Although the footpad and the magnet slid through about 1 m of material during the *Surveyor V* landing, *Surveyor VI* appears to have had only one instantaneous lateral impact. This probably accounts for the fact that less material appears on the *Surveyor VI* magnet assembly than on that of *Surveyor V*.

G. Size of Magnetic Particles

Most particles again appear to be below camera resolution (1 mm). In Fig. VIII-11, an enlarged view of the magnet may be seen with a grid overlay of 1-mm squares. A few particles appear to be individual grains ~1 mm, and one elongate particle appears to be about 1.6 mm; this may however, be an elongate chain of particles. The appearance is similar to the results found with impact in scoriaceous basalt with an uneven particle-size distribution.

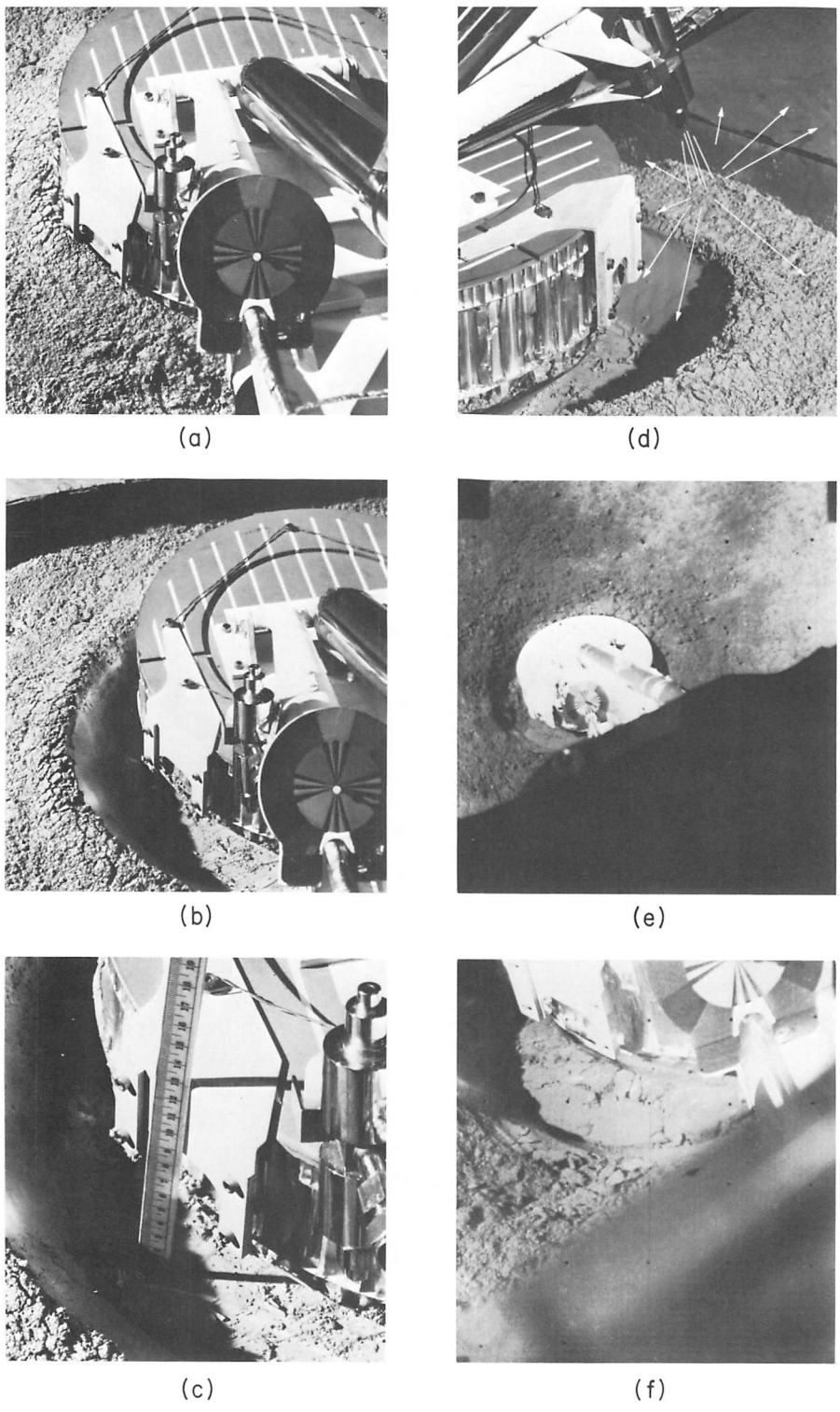

Fig. VIII-4. Laboratory simulation and actual initial lunar landing. The spur is not reproduced in the simulation; however, the depth of penetration may be concluded to be approximately 6 cm (c), which is in agreement with a clean magnet in the lunar pictures (e, f). In (d) the relationship to the attitude control jet vectors may be seen.

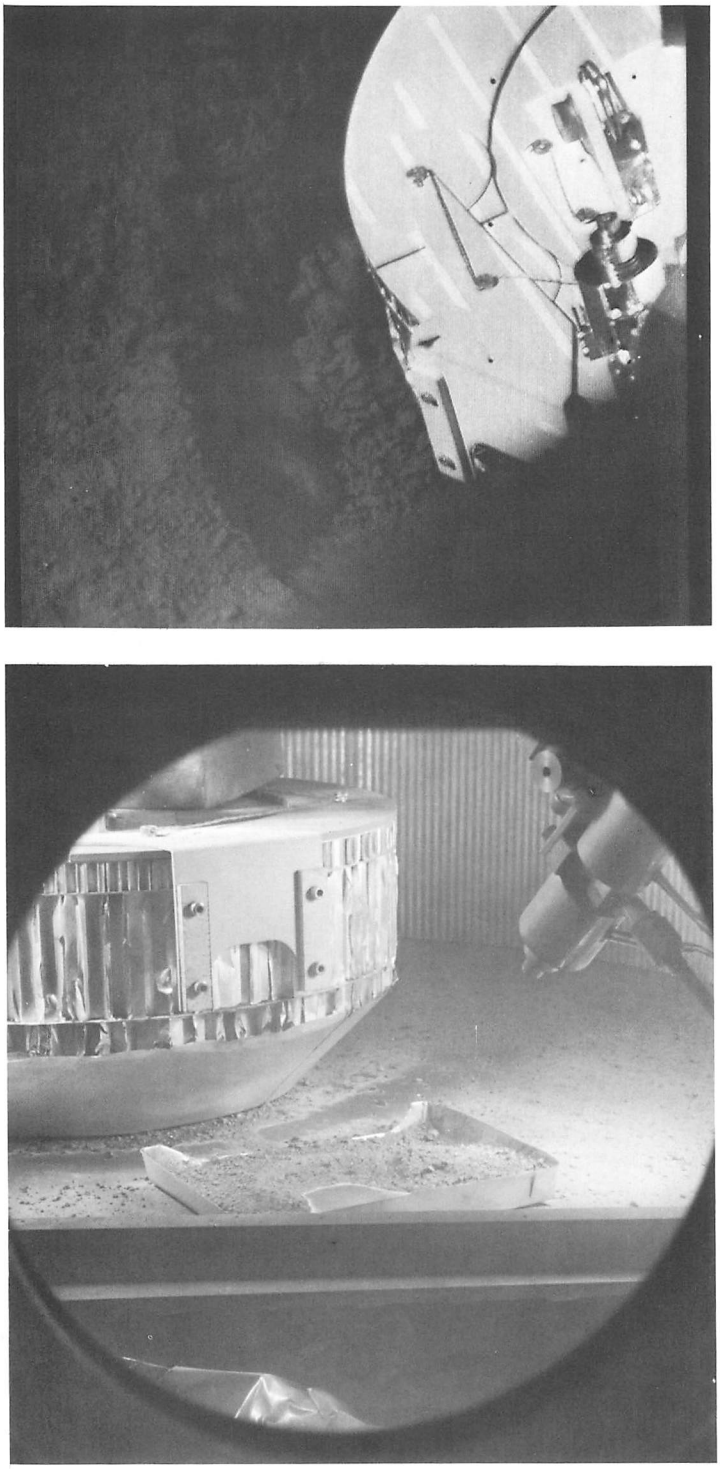

Fig. VIII-5. Comparison of lunar results of attitude control jet firing on magnet assembly (top) with laboratory jet study results (bottom). A sequence of basalt samples (37–50μ size particles) with varying additions of powdered iron were fired into with 2- to 3-sec firing times. The result after firing into basalt with a 4% by volume addition of powdered iron in 10^{-6}-torr vacuum is shown at the bottom. Very little material is seen to adhere to the magnet even with this most advantageous configuration of the attitude control to the magnet, and with a relatively high iron content. It could be concluded from the laboratory sequence that with $<4\%$ iron, no change in the magnet appearance would be expected on the moon.

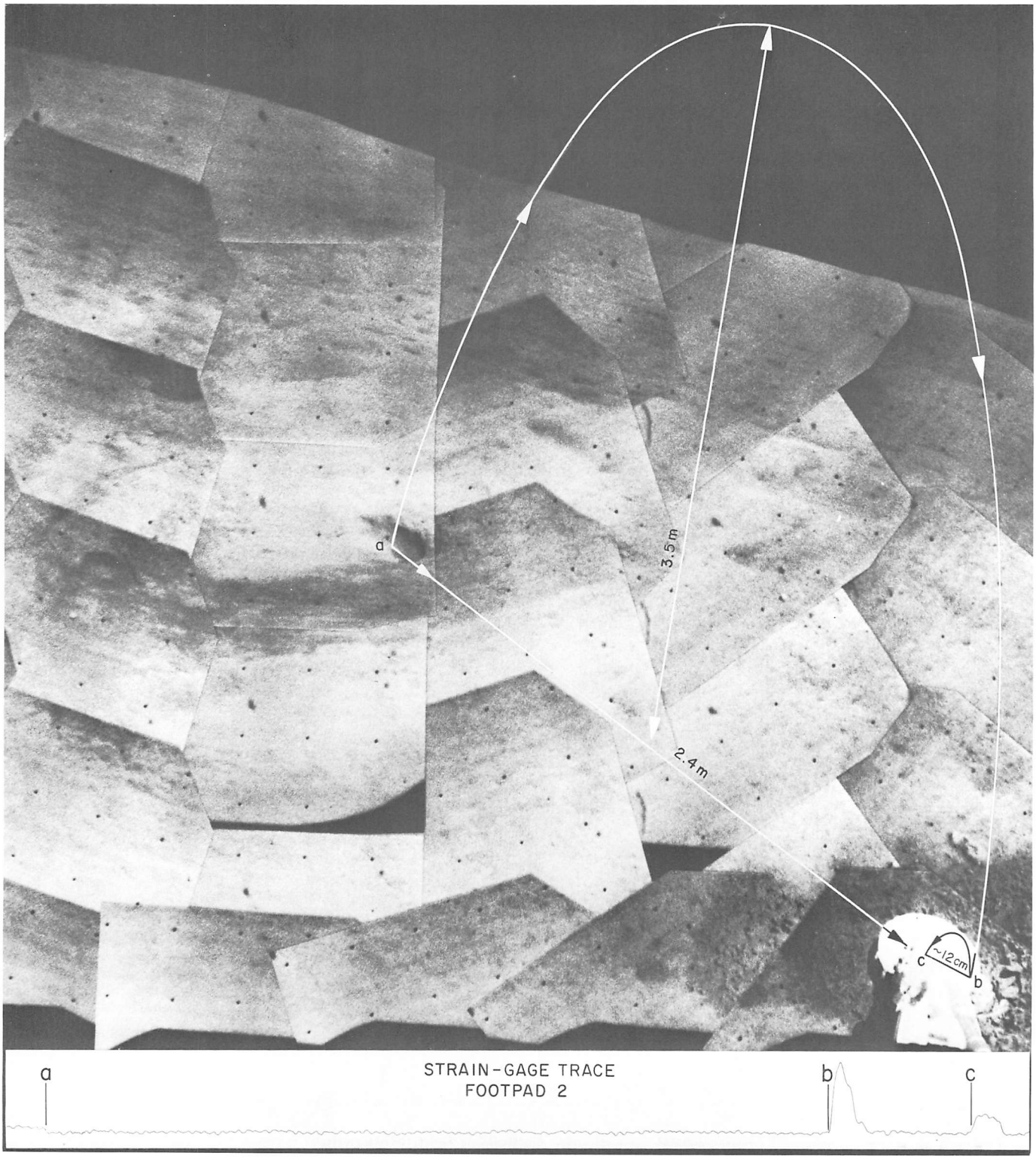

Fig. VIII-6. Hopping movement followed by footpad 2. The original landing point of footpad 2 is seen at position (a). The spacecraft rose about 3.5 m and landed (b) at a position about 2.4 m to the southwest. In landing, a small bounce occurred at footpad 2, to the left (c). Penetration appears to have been up to 10 cm, causing the lower seven-eighths of the magnet to contact lunar surface material. The strain-gage data for footpad 2 seen at the bottom indicates that the movement from b to c was a bounce rather than a slide.

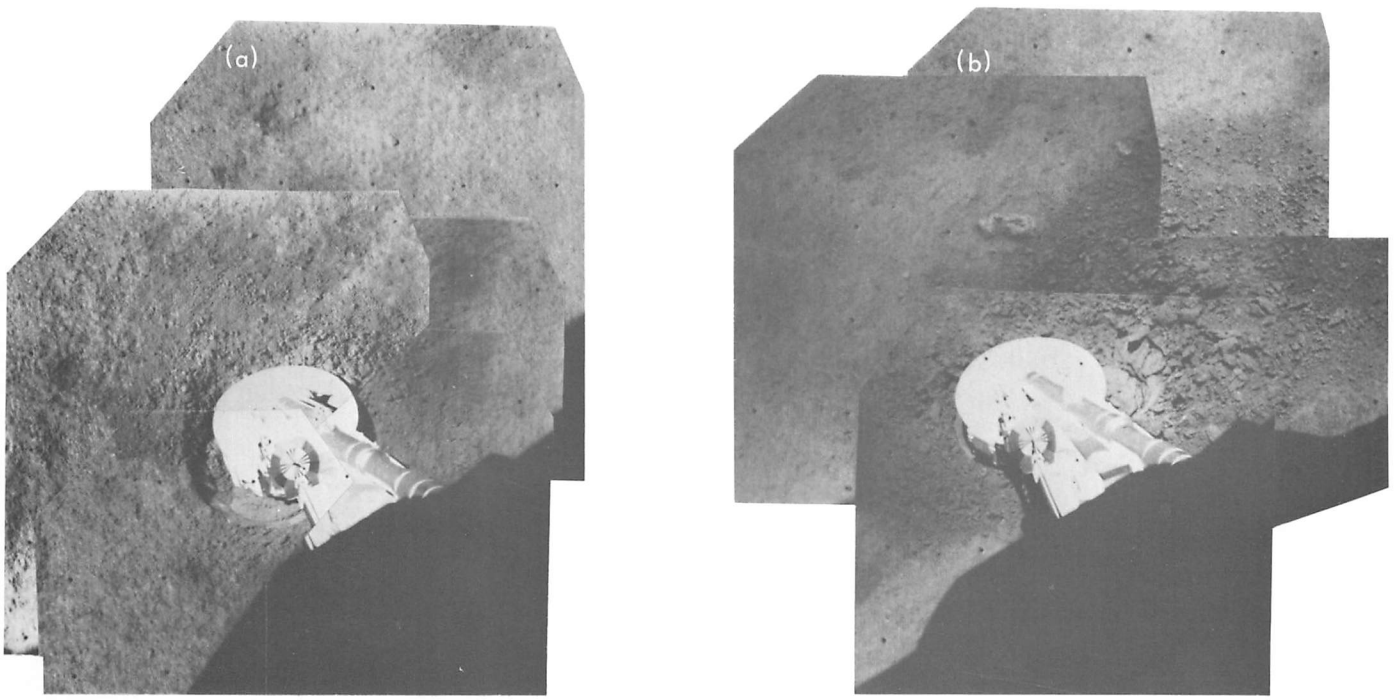

Fig. VIII-7. Footpad 2: (a) before and (b) after the 2.4-m hopping maneuver. Note difference in imprint relationship in (a) and (b). In (a) the penetration on the side of the magnet assembly is about 6 cm. In (b) the penetration into the lunar material was approximately 10 cm, causing a contact with about seven-eighths of the length of the magnet. Only the top one-eighth of the magnet is clean.

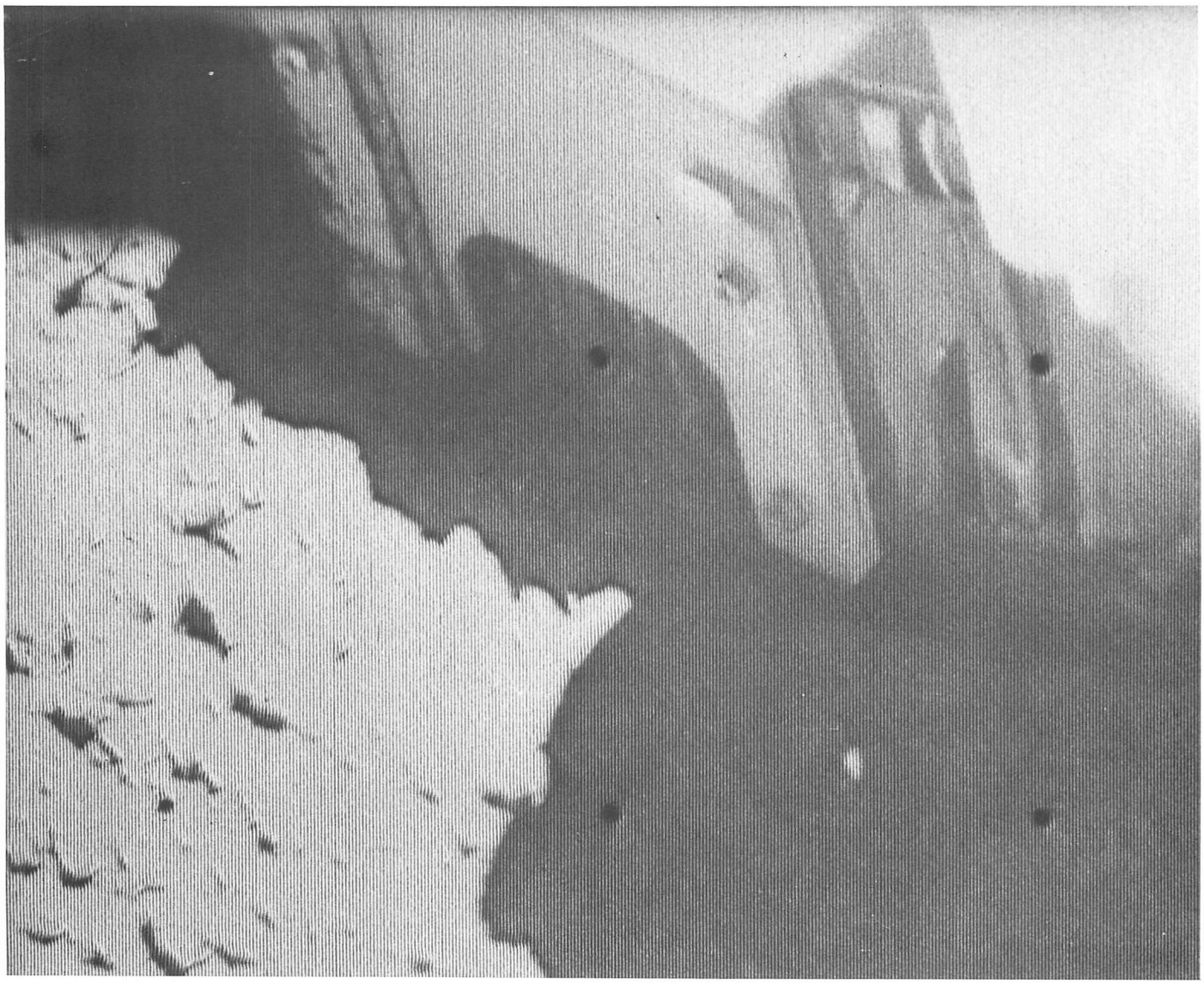

Fig. VIII-8. Closeup of magnet assembly after the hop. Note material on magnetic-pole edges. A small amount of material bridges the low-magnetic-field area.

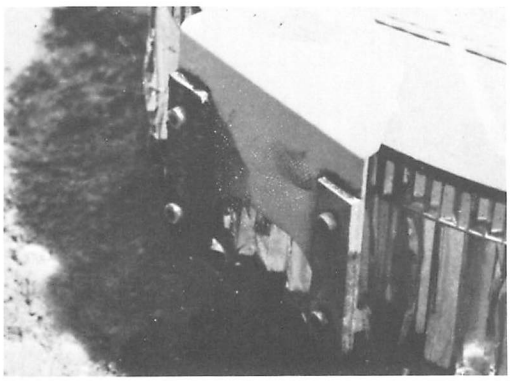

SCORIACEOUS BASALT

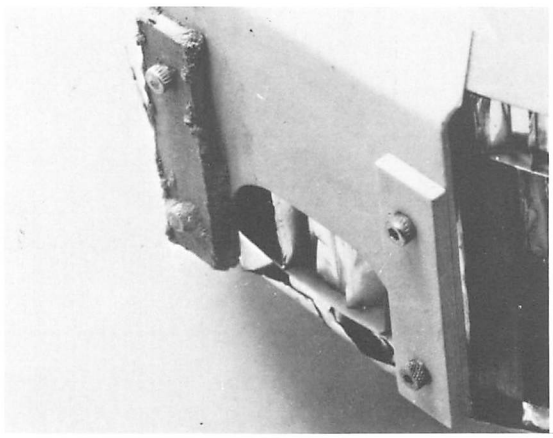

50 – 150 μ

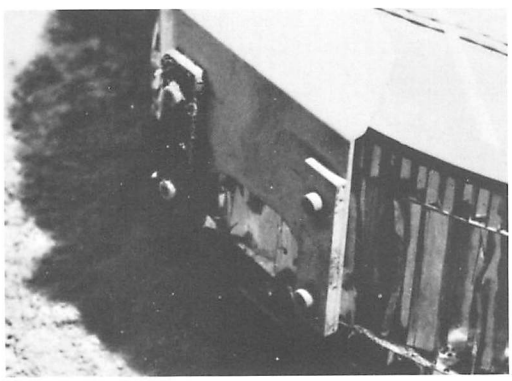

BASALT + 1% Fe

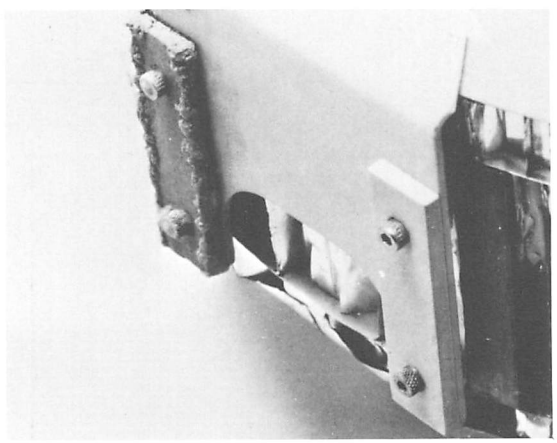

37 – 50 μ

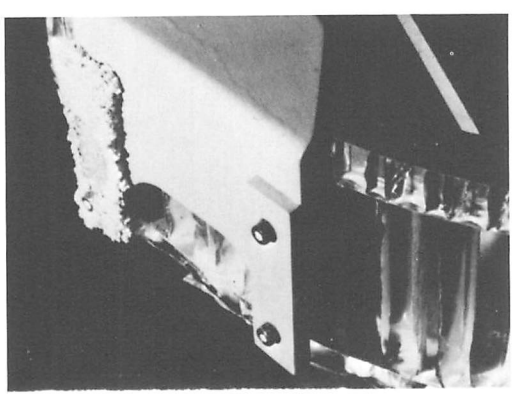

0.25% Fe

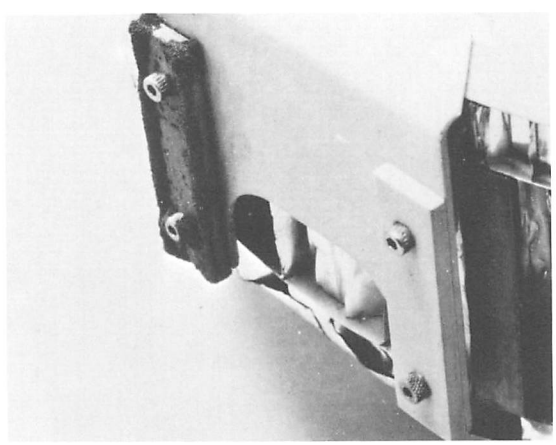

< 37 μ

Fig. VIII-9. A comparison of the laboratory test results most closely resembling the lunar results. The sequence on the right is in Little Lake basalt with no added iron. Lower left is impact in CaOH with 0.25% Fe. This amount of added iron represents a limit for the amount of magnetic material seen in lunar pictures.

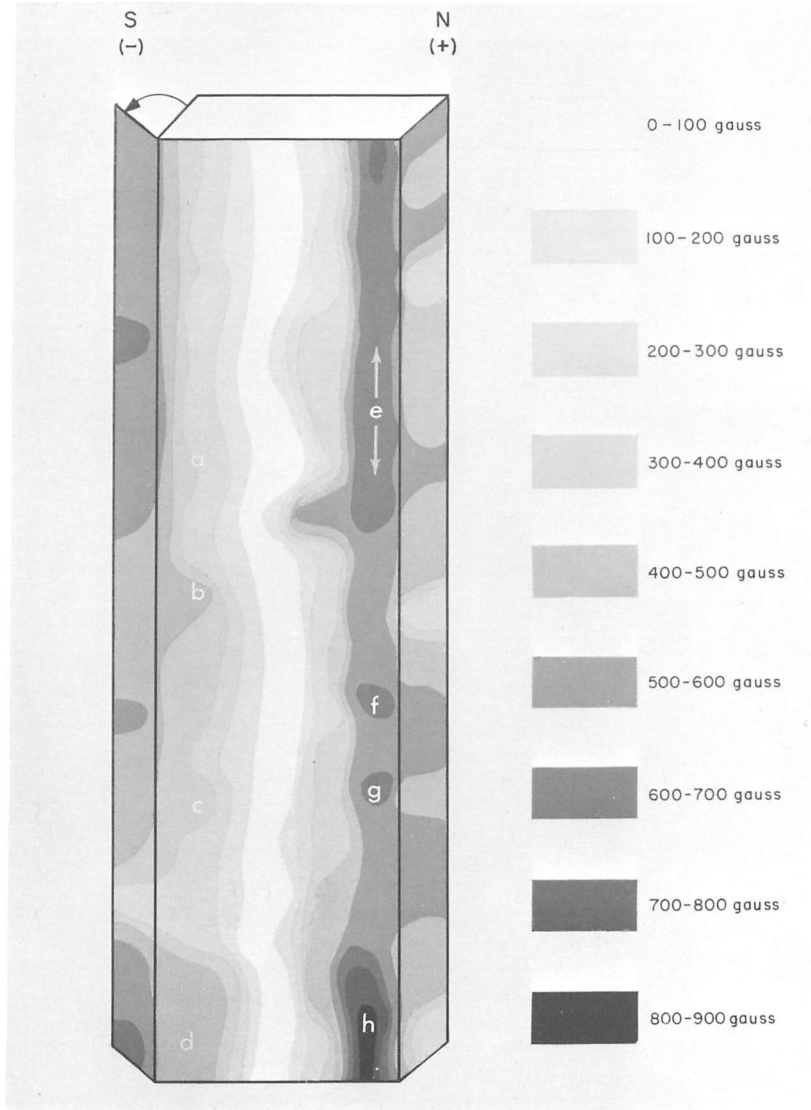

Fig. VIII-10. Comparison of enlarged view of *Surveyor VI* magnet with tonal plot of gauss strength. (Compare with Fig. VIII-3.) Letters indicate the same relative areas on the lunar magnet and on the magnetic-strength plot.

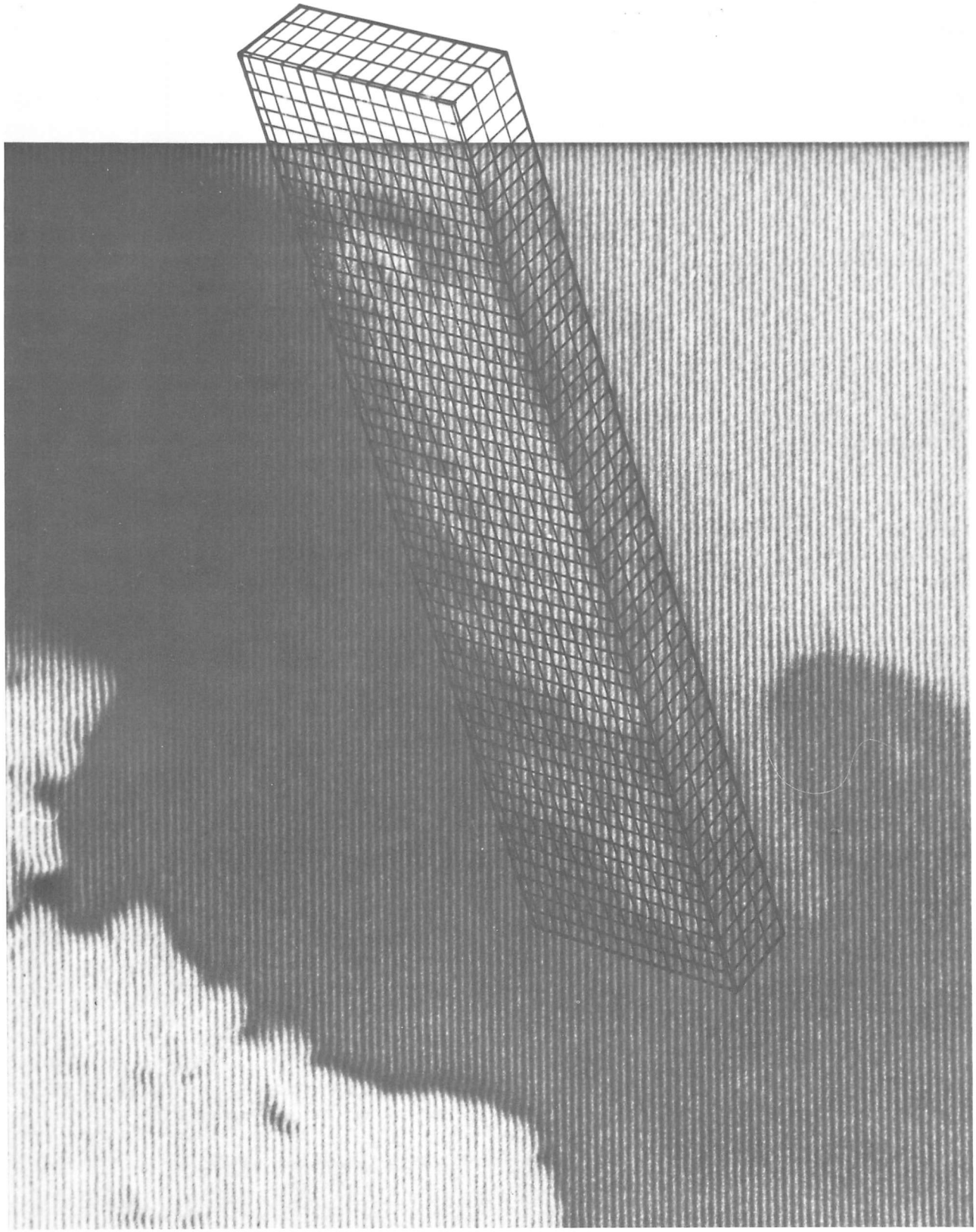

Fig. VIII-11. Enlarged view of *Surveyor VI* magnet with grid overlay. Grid line spaces are equivalent to 1 mm, which is approximate resolution of the *Surveyor VI* camera. Most particles appear to be <1 mm; some may be $\simeq 1$ mm. All appear to occur in clumps or groups of particles.

H. Discussion

No magnet contact was made with the lunar surface during the initial landing of *Surveyor VI* in Sinus Medii. The primary requirement of contact with the lunar surface to obtain a test with the magnet was achieved in the landing following the hopping operation. This must have been instantaneous contact and withdrawal.

From comparison with various laboratory studies, the *Surveyor VI* magnet appeared to have considerably less material than collected in tests in the basalt with 1% by volume addition of powdered iron. Tests conducted in hydrated lime with additions of powdered iron suggest, by comparison, that 0.25% of added iron is a possible upper limit for free magnetic particles added to a rock powder with no iron.

The discrepancy in the amount of material collected by the magnets on *Surveyors V* and *VI* could have resulted either from the difference in landing mode or a difference in surface constituents in the two maria. Laboratory impact studies generally consist of single simple impacts, similar to the second landing of *Surveyor VI*. Therefore, the *Surveyor VI* magnet results probably give a truer indication of the magnetic material percentage than the *Surveyor V* magnet results. Tests of different simulated landing modes suggest that the difference in amount is probably attributable to landing mode effects.

The limit of 0.25% by volume of iron is certainly not indicative of extensive meteoritic impact. Cratering and pulverization, if by impact, could be expected to add considerably more iron.

Some particle sizes do appear to be about 1 mm (camera resolution) and possibly larger. Larger (1.6 mm), apparent single particles may in fact be clumping or chain effects by smaller particles.

In laboratory studies, the closest similarity in detailed appearance is shown by the Pisgah scoriaceous basalt with a wide range of size distributions. It is interesting to note that scoria from Pisgah Crater was found[1] to have an albedo most similar to the lunar maria.

If the material adhering to the magnets on *Surveyors V* and *VI* is from inherent basalt components only, the particles are most probably magnetite.

I. Conclusions

(1) A small amount of magnetic material is present in Sinus Medii. The amount of attracted magnetic material appears to be $<0.25\%$ by volume, from comparison with laboratory studies. The uncertainty may be reduced when further laboratory simulation studies have better indicated the differences in accumulation produced by different landing modes and pulverization effects on inherent magnetite in basalts.

(2) A wider size distribution than previously indicated is suggested by smaller and larger particles, some pieces about camera resolution or slightly larger.

(3) Results from the magnet test appear again to verify a basaltic composition. The overall appearance most closely resembles tests in Pisgah scoriaceous basalt. This also agrees with laboratory reflectance studies.

(4) Panoramic appearances of the maria in the *Surveyor I, III, V,* and *VI* landing sites have been similar. Magnet, alpha-scattering, and thermal data are similar in *Surveyors V* and *VI*. Reflectance data are also alike. Therefore, it may be concluded that basaltic composition may dominate all of the maria units, and the basalt may be scoriaceous.

(5) Extensive meteoritic addition appears to be precluded by the low amount of magnetic material present in the two mare areas from which data have been obtained.

The magnet tests on *Surveyors V* and *VI*, therefore, lend support to a volcanic origin of the mare material, and would further suggest fine particles at the time of origin, rather than subsequent pulverization by impact.

[1] J. B. Adams, private communication.

References

VIII-1. de Wys, J. Negus, "Lunar Surface Electromagnetic Properties: Magnet Experiment," *Surveyor V Mission Report*, Part II: *Science Results*, Technical Report 32-1246, pp. 151–175, Jet Propulsion Laboratory, Pasadena, Calif., November 1, 1967.

VIII-2. de Wys, J. Negus, "*Surveyor V* Magnet Experiment," *Science*, Vol. 158, No. 3801, pp. 632–635, November 3, 1967.

(Blank Page)

IX. Theory and Processes Relating to the Lunar Maria From the *Surveyor* Experiments

J. A. O'Keefe, J. B. Adams, D. E. Gault (Chairman), J. Green, G. P. Kuiper, H. Masursky, R. A. Phinney, and E. M. Shoemaker[1]

Prior to the *Surveyor* missions, there were three principal theories about the chemical constitution of the lunar maria: that they were (1) chrondritic, (2) basaltic, or (3) silicic. Three types of materials recovered on earth were suspected of coming from the maria: (1) chrondritic meteorites, (2) basaltic achondrites, and (3) tektites.

The *Surveyor* chemists have now spoken: Turkevich, Franzgrote, and Patterson find that, in Mare Tranquillitatis (Ref. IX-1) and Sinus Medii (see Section VII of this report), the composition is basaltic. It is unmistakably too poor in magnesium to be like either kind of chrondritic meteorite. It is too rich in the heavier elements, iron and calcium, to resemble terrestrial silicic rocks (the granitic kindred) or tektites.

How far are we justified in extrapolating these remarkable results? Let us first see what can be deduced from the other two *Surveyor* missions, both of which were in Oceanus Procellarum.

From a study of the on-board radar[2] used to guide the *Surveyors* to their landings on the lunar surface, the radar cross section is found to be approximately the same at all four *Surveyor* sites, within approximately 2 db. The data are not conclusive, since the difference between silicic rocks and basalts is only approximately 3 db, but they suggest a similarity. Brown's estimates are especially valuable as compared with ground-based radars because he is able to separate and exclude the effects of rocky craters, which show quite different values of the radar cross section.

The bearing strength and other dynamical properties of the upper surface layer have been found by *Surveyor* so far to vary somewhat from station to station. A range in bearing strength from 0.2 to 0.55 bar is indicated. On the other hand, it should be kept in mind that this bearing strength is a sensitive function of porosity. The above-mentioned range in bearing strength implies a range of not more than 5 to 10% in the porosity, whatever the

[1]R. Collins was not present for this mission.

[2]W. E. Brown, private communication.

actual value of the porosity itself. Hence, it is not likely that changes in the dielectric constant of individual grains could be masked by changes in the porosity so as to yield the same bulk dielectric constant. It follows that constancy of the radar cross section, so far as it can be established, probably implies similarity of the material.

In the *Surveyor* images, the mare material appears, at all four sites, to consist principally of a particulate material whose average grain size falls below the resolution of the camera (about 0.5 mm). Pieces larger than 1 mm cover less than 10% of the lunar surface in the *Surveyor I* images and 10 to 15% in the others. The depth of the fine-grained, weakly cohesive layer varies from less than 2 m to more than 10 m.

At all four *Surveyor* sites, circular craters are seen of all sizes down to about 2 cm. There are numerous surface irregularities below this size, but they are no longer round, either because they are not craters or because craters below a certain size have a different shape. From *Lunar Orbiter* and telescopic data, it is known that the maria are always poorer in telescopic craters than typical highland terrain; while in subtelescopic craters, it is found that the maria are considerably richer.

From all these similarities, it is reasonable to think that the maria form a reasonably homogeneous class of objects, and hence that they are all basaltic in composition.

Shoemaker had already pointed out (Ref. IX-2) that a basaltic composition would give a logical explanation for the low domes seen on the maria. At the scale of the *Lunar Orbiter* photographs, these domes appear to consist of flows like those of a small terrestrial shield volcano. J. Green (Ref. IX-3) also diagnosed some lunar craters as indicative of basaltic volcanism.

Kuiper and Whitaker (Refs. IX-4 and IX-5) had also drawn attention to broad flow-like structures up to 200 km in length, sometimes having a different color from their surroundings, often superposed on one another, and possessing lobate termini. These, they suggested, were analogous to large terrestrial flows of basaltic lava. A silicic lava, by contrast, would be expected to be several orders of magnitude more viscous, and hence to have surface irregularities 10 or more times as high. The existence of the flows described by Kuiper and Whitaker has been confirmed by *Lunar Orbiter* studies (see Fig. IX-1).

It does not appear possible at this time to refine the classification of the basalt represented by the alpha-scattering analyses. (For the present purposes, the word basalt is taken to mean "rock of basaltic composition;" data are not available to make the textural distinctions between diabase and basalt, etc.) The possibilities have been considered that it is:

(1) An alkali basalt.

(2) A basalt of the tholeiitic series.

(3) A basaltic andesite of the tholeiitic series.

(4) A ferrobasalt of the Icelandic or Skaergaard type.

(5) A basaltic achondrite.

These five classes of basalts are not on an equal footing: the first four correspond to compositional differences, while the fifth is principally a matter of place of origin.

Turkevich's upper limit of 2 atomic percent sodium (corresponding roughly to 3% NA_2O by weight; see Section VII of this report) is inconsistent with a basalt which has evolved very far along the line of the oceanic alkali basalts.

The rock could perhaps have evolved a certain distance toward a ferrobasalt; if allowance is made for possible contributions from Ti and K to the quantity listed as "Ca," then it will be seen that FeO may noticeably exceed CaO by weight. This possibility is again within observational errors.

The most intriguing possibility[3] is that the mare rocks are identical in chemical composition with the basaltic achondrites. This possibility is suggested by the slight indication of iron enrichment since, from the compositional standpoint, the basaltic achondrites resemble the ferrobasalts. It will be further tested when actual values for the sodium content (rather than upper limits) become available, since basaltic achondrites are unique among basalts in having very low sodium content.

If this last hypothesis is correct, then it will greatly strengthen the arguments offered by Duke and Silver (Ref. IX-6) to the effect that the basaltic achondrites come from the moon. If this proposition should become accepted, then it would mean that mankind already possesses several dozen lunar samples, from which very important deductions can be made about the moon's past history.

[3]J. Green dissents.

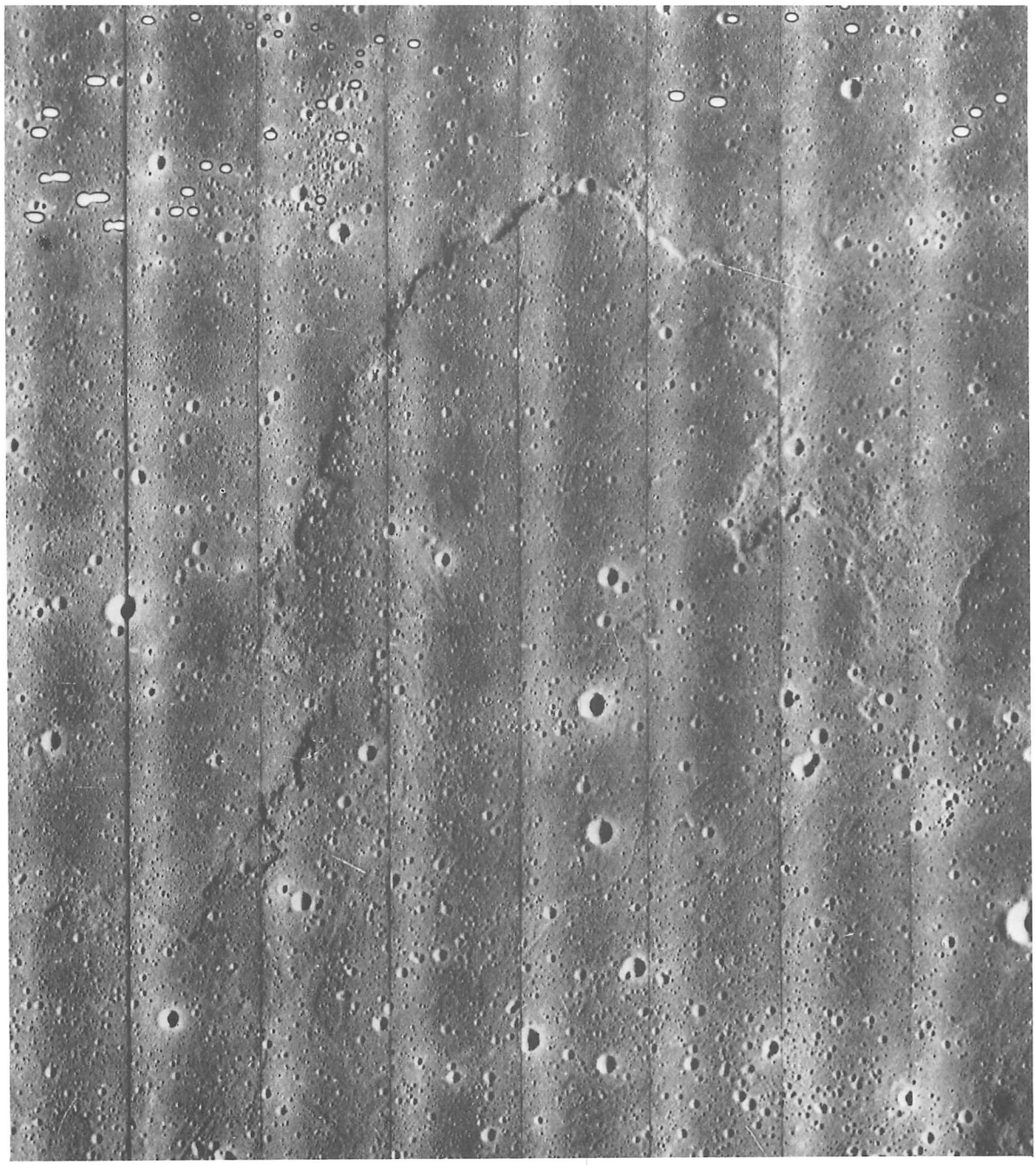

Fig. IX-1. Medium-resolution *Lunar Orbiter* photograph showing flow structure in Mare Imbrium.

The basaltic achondrites appear to have differentiated from a more mafic material at about the same time as the formation of the solar system, some 4.5 billion years ago. If they are lunar in origin, this means that the moon was at least partially molten at that time. The basaltic achondrites are conspicuously low in sodium and potassium; this has caused speculation (Ref. IX-6) that the parent body from which they came passed through an episode of intense differential volatilization.

The basaltic achondrites are low in nickel compared with either the solar composition or the composition of the chondritic meteorites; this poses an important question, namely where the moon's nickel has gone, if the basaltic achondrites are really lunar samples. This is another aspect of the problem of the iron content of the moon.

On the other hand, there are important objections to the idea that basaltic achondrites come from the moon. They have some significant resemblances to chondritic meteorites. In particular, the ages-in-space of meteorites are often used as a clue to their origin; these ages are approximately the same for basaltic achondrites as for chondritic meteorites. It is also true that both basaltic achondrites and chondritic meteorites have trapped noble gases (Refs. IX-7 through IX-9) whose abundances relative to one another are very different from those of the solar atmosphere and are suspected of representing the result of absorption on fine particles in the early history of the solar system. For these reasons, it may be argued that basaltic achondrites and chondritic meteorites (including carbonaceous chondrites) must come from the same place.

Difficulties of a different kind arise from the calculations of shock metamorphism. Gault (Ref. IX-10) calculates that any shock sufficiently strong to accelerate a rock to lunar escape velocity ought to produce phase transformations of the rock. One of two basaltic achondrites does indeed show evidence of shock-induced phase transformations, but the majority does not.

The working group notes this range of opinion and notes that more precise information about the chemical constitution of the lunar basalts is likely to be of high interest. At the present, the most that can be said is that the mare material analyzed is approximately like the most common type of basalt; but it may be somewhat more rich in the heavy elements.

At each *Surveyor* site, the material underlying the lunar surface has appeared darker than the top. Wherever the footpads, the crushable blocks, or the vernier engines have overturned the surface layers, the freshly exposed material is found to be darker (by about 30% in the case of *Surveyors I, III,* and *VI,* and considerably less in the case of *Surveyor V*). The underlying material at these sites is darker than all but the darkest parts of the surface material anywhere on the moon. The lighter surface layer is believed to be a millimeter or less in thickness.

There is no agreement about the cause of the difference in brightness. Among the possibilities are:

(1) Mechanical or electric concentration of very fine particulate material toward the surface.

(2) Breaking up of the topmost particles by micrometeorite impact.

(3) An originally dark material erupted volcanically, then altered by bleaching of the uppermost layer.

(4) A coating of dark material on the subsurface particles, perhaps analogous to the material called by geologists "desert varnish" (Ref. IX-11), or perhaps identical with the layer of metal-enriched material suggested by students of sputtering processes (Refs. IX-12 and IX-13).

It is important to keep in mind that although there is wide agreement that the chemical nature of the mare surface material at the *Surveyor V* and *VI* sites is basaltic, yet there remain alternative hypotheses of the manner of formation of the weakly cohesive, fine, granular material which we see. One explanation for the powdery state of the lunar material is comminution by meteorite and micrometeorite impact on initially porous basalt; but some observers, noting the rarity of coarse fragments or even large sand-size particles are inclined to believe that the mare material was laid down as volcanic ash.

The first pictures of the western horizon after sunset were taken when the center of the solar disk was about ⅔ of a degree below the horizon. At that time, a bright line was visible extending a total distance of about 5 deg along the horizon (see Fig. IX-2). The line gradually died out; it was no longer visible when the sun's center was 1.2 deg below the horizon, even though the exposures were much longer. Two causes have been suggested for this line. In the first place, it may be due to individual particles of dust ejected by micrometeorite impact and suspended electrostatically or in ballistic trajectory above the surface (Ref. IX-14). In this reference, it is suggested that these grains are of micron size and that they are suspended for a few seconds only. These particles might

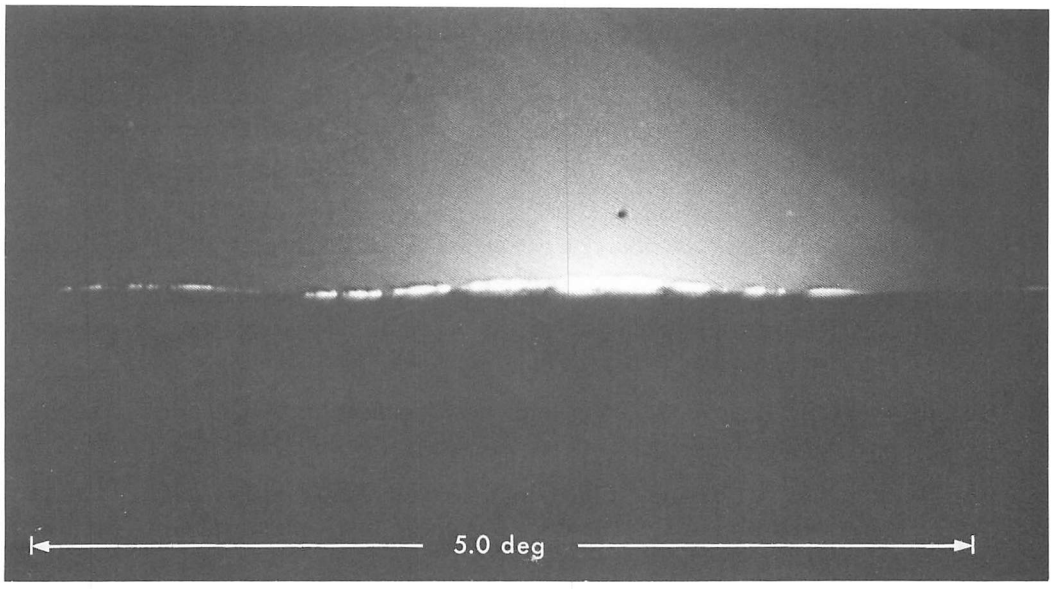

Fig. IX-2. Lunar horizon west of the spacecraft. This picture shows the sunlight diffracted at the limb of the moon (Day 328, 14:18:30 GMT).

form a layer a few tens of centimeters thick above the moon's surface; they might catch the sunlight and scatter it into the shadow just as the terrestrial sky scatters light at twilight. On the other hand, it is possible that the line is produced by diffraction at the horizon. The character of the diffraction in this case would presumably be affected by the size of the irregularities of the horizon.

Rough measurements show an intensity for the bright line of about 4×10^{-7} lumens/(cm^2 radian) along the horizon at a point 40 min of arc vertically above the sun, and about 55 min away from the sun in a horizontal direction.

The fact that the light can be seen at a distance of 2.5 deg from the sun in a horizontal direction, yet becomes invisible at a distance of only 1 deg in the vertical direction, is probably not due to lack of uniformity in the scattering power of the particles, but to shadowing of the horizon by terrain further west.

References

IX-1. Turkevich, A. L., Franzgrote, E. J., and Patterson, J. H., "Chemical Analysis of the Moon at *Surveyor V* Landing Site: Preliminary Results," *Surveyor V Mission Report. Part II: Science Results*, Technical Report 32-1246, pp. 119–149, Jet Propulsion Laboratory, Pasadena, Calif., November 1, 1967.

IX-2. Shoemaker, E. M., "Interpretation of Lunar Craters," *Physics and Astronomy of the Moon*, Chapter 8, p. 303, edited by Z. Kopal, Academic Press, New York and London, 1962.

IX-3. Green, J., "Tidal and Gravity Effects Intensifying Lunar Defluidization and Volcanism," *Annals N. Y. Acad. Sci.*, Vol. 123, pp. 403–469, 1965.

IX-4. Kuiper, G. P., "The Surface Structure of the Moon," *The Nature of the Lunar Surface*, Chapter 4, pp. 99–105, edited by W. N. Hess, D. H. Menzel, and J. A. O'Keefe, Johns Hopkins Press, Baltimore, Md., 1965.

References (contd)

IX-5. Whitaker, E. A., "The Surface of the Moon," *The Nature of the Lunar Surface,* Chapter 3, pp. 79–98, edited by W. N. Hess, D. H. Menzel, and J. A. O'Keefe, Johns Hopkins Press, Baltimore, Md., 1966.

IX-6. Duke, M. B., and Silver, L. T., "Petrology of Eucrites, Howardites and Mesosiderites," *Geochim. et Cosmochim. Acta,* Vol. 31, pp. 1637–1665, 1967.

IX-7. Eberhardt, P., Geiss, J., and Grögler, N., "Distribution of Rare Gases in the Pyroxene and Feldspar of the Khor Temiki Meteorite," *Earth and Planetary Sciences Letters,* Vol. 1, pp. 7–12, 1966.

IX-8. Marti, K., "Trapped Xenon and the Classification of Chondrites," *Earth and Planetary Sciences Letters,* Vol. 2, pp. 193–196, 1967.

IX-9. Zähruger, J., "Isotopie-Effekt und Häufigkeiten der Edelgase, in Steinmeteoriten und auf der Erde," *Zeitschrift für Naturforschung,* Vol. 17a, pp. 460–471, 1962.

IX-10. Gault, D. E., and Heitowit, E. D., "The Partition of Energy for Hypervelocity Impact Craters Formed in Rock," *Proceedings of the Sixth Hypervelocity Impact Symposium,* Vol. II, Part 2, p. 419, 1963.

IX-11. Shoemaker, E. M., Batson, R. M., Holt, H. E., Morris, E. C., Rennilson, J. J., and Whitaker, E. A., "Television Observations From *Surveyor III*," *Surveyor III Mission Report. Part II: Scientific Results,* Technical Report 32-1177, p. 9–67, Jet Propulsion Laboratory, Pasadena, Calif., June 1, 1967.

IX-12. Hapke, B. W., "Optical Properties of the Moon's Surface," *Nature of the Lunar Surface,* Chapter 7, pp. 141–154, edited by W. N. Hess, D. H. Menzel, and J. A. O'Keefe, Johns Hopkins Press, Baltimore, Md., 1966.

IX-13. Rosenberg, D. L., and Wehner, G. K., "Darkening of Powdered Basalt by Simulated Solar-Wind Bombardment," *J. Geophys. Res.,* Vol. 69, No. 13. pp. 3307–3308, 1964.

IX-14. Gold, T., "The Moon's Surface," *Nature of the Surface of the Moon,* Chapter 5, pp. 107–121, edited by W. N. Hess, D. H. Menzel, and J. A. O'Keefe, Johns Hopkins Press, Baltimore, Md., 1966.

X. Selenographic Location of *Surveyor VI*

F. B. Winn

This section of this report describes the post-landing tracking data acquired by the Deep Space Instrumentation Facility (DSIF) and the utilization of that data to determine the selenographic location of the probe and the geographical locations of the three Deep Space Stations (DSS) used in the tracking operations. The discussion relating to data utilization encompasses the application of data rejection techniques and relative weighting of observables and parameters. The lunar ephemerides employed in the data reduction are discussed. The solutions for the probe positions are presented in tabular form along with determinations from other sources for comparison.

A. Weighting the Data

The data acquisition procedures and the associated influences on the solutions are reflected in the weighting techniques. The coherent two-way doppler, as acquired (Fig. X-1), contained some blunder points,[1] systematic bias, and trends. The detection of these characteristics was accomplished by using the raw data in the Single-Precision Orbit Determination Program (SPODP, Ref. X-1) recursive least-squares fit, and inspecting the "observed minus computed" (O − C) residuals. This initial residual set adequately demonstrates any pronounced irregularities in the data sample (see Figs. X-2 to X-4).

Once the erroneous information had been detected and removed from the data sample, the remaining acquired tracking data (one data point/min) were compressed into 5-min data points to facilitate processing. The compressed data were used in the final reductions. The compression procedure resulted in a DSS 11 (Goldstone, California) tracking data loss of 14.5% (Table X-1). Much of these data can be regained if the compression intervals are shorter, or if the data are not compressed. This will be done in future analyses.

The most outstanding feature revealed by the raw tracking data residuals was a consistent bias of DSS 61 (Madrid, Spain) two-way doppler data on 4 consecutive days. Tracking data from DSS 61 on Days 322 to 325 exhibited a bias of approximately 0.03 Hz (2 mm/sec). As a consequence, the 1291 data points collected during this period by DSS 61 were removed from the solution.

[1]Blunder points refer to data points outside the mean 3σ limit of the data sample. Such points can be related to sporadic noise from various sources, i.e., atmosphere, teletype communication lines, the present state of hardware technology, etc.

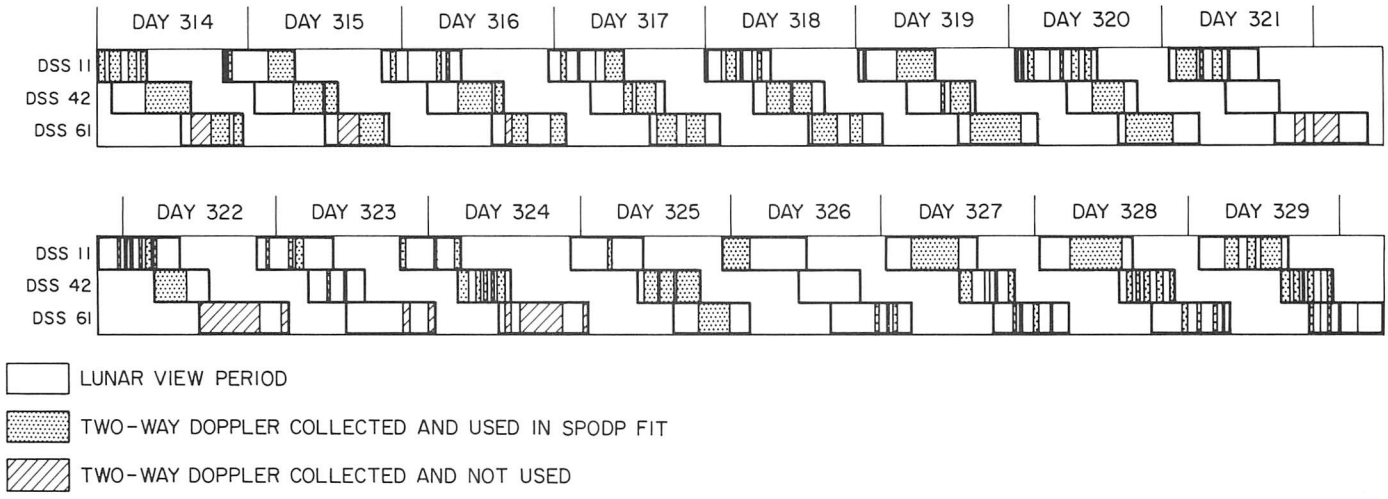

Fig. X-1. Portions of lunations used to acquire coherent two-way doppler tracking data.

The tracking data received at DSS 11 and DSS 42 (Canberra, Australia) were free of this symptom. This data condition is unique to DSS 61. At this time, the cause is unknown.

Another data feature associated with DSS 61 was the occurrence of a series of blunder points resulting from improper incrementing of the least-significant digits of the doppler cycle counter. Examination of Fig. X-4 shows such an occurrence on Days 315, 316, 323, and 325.

The a priori standard deviation attributed to each of the surviving data points was 0.05 Hz. The assignment of this weight reflects model limitations in addition to the known data noise.

Table X-1. *Surveyor VI* post-landing summary of coherent two-way doppler data (1-min data points)

DSS	Points received, %	Points used, %	Biased data, %	Blunder points, %	Points lost in compression, %
11	1863 100%	1585 85.1%	0 0%	8 0.4%	270 14.5%
42	2962 100%	2675 90.3%	0 0%	26 0.9%	261 8.8%
61	4413 100%	2835 64.2%	1291 29.3%	84 1.9%	203 4.6%
Total	9238 100%	7095 76.8%	1291 14%	118 1.3%	734 7.9%

B. A Priori Parameter Constraints

It is possible to constrain the terrestrial Tracking Station parameters in the SPODP tracking reduction to those of some previous determination. However, such a constrained solution can lead to difficulties. There are many time-dependent variables incorporated in the theoretical model (e.g., E. W. Brown's Lunar Theory, Eckert's corrections to Brown's theory, lunar librations, terrestrial diurnal rotation, refraction, ionosphere, space plasma effects, etc.). There is a series of models used to provide these time-dependent parameters, each imperfect in its own way. Thus, there is always the danger of introducing systematic errors into tracking-data fit by constraining to the previously determined terrestrial Tracking Station positions in accordance to the associated variance/covariance matrix. It was with this perspective that the parameter list remained unconstrained.

The a priori standard deviations associated with the parameters were:

(1) *Surveyor VI* lunar radius: 10 km.

(2) *Surveyor VI* selenographic latitude: 5.0 deg (150 km).

(3) *Surveyor VI* selenographic longitude: 5.0 deg (150 km).

(4) DSS 11 terrestrial spin axis distance: 300 m.

(5) DSS 11 geographic longitude: 0.5 deg (30 km).

(6) DSS 42 terrestrial spin axis distance: 300 m.

(7) DSS 42 geographic longitude: 0.5 deg (30 km).

(8) DSS 61 terrestrial spin axis distance: 300 m.

(9) DSS 61 geographic longitude: 0.5 deg (30 km).

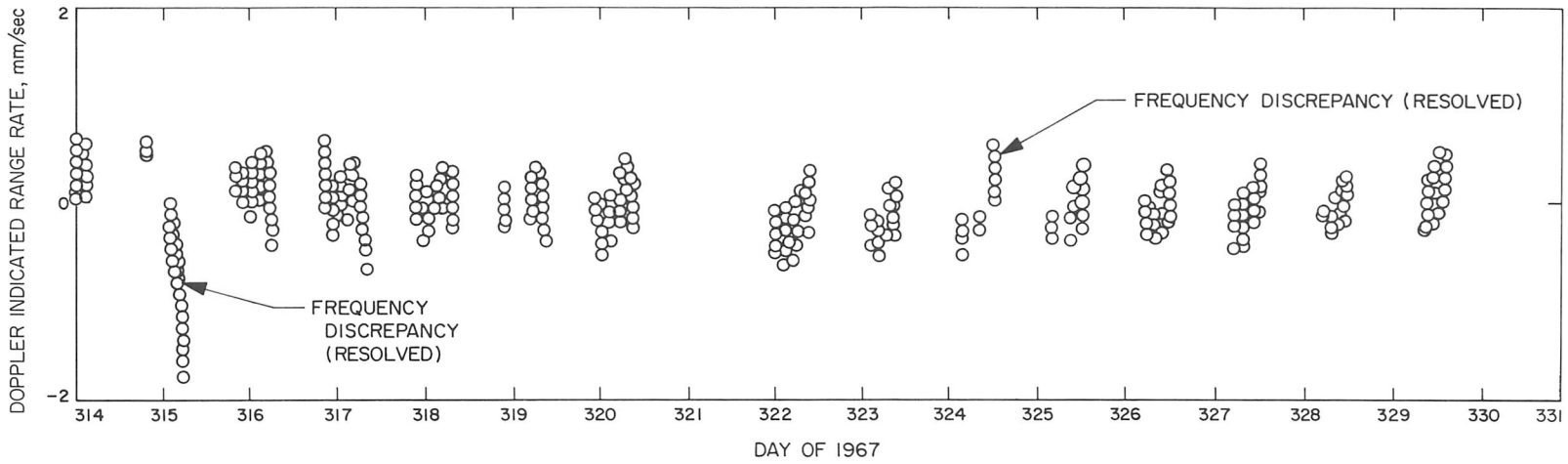

Fig. X-2. *Surveyor VI*, DSS 11 (Goldstone, California). First lunar day, O — C residual set (one data point/min). DE 29/LE 5 was used.

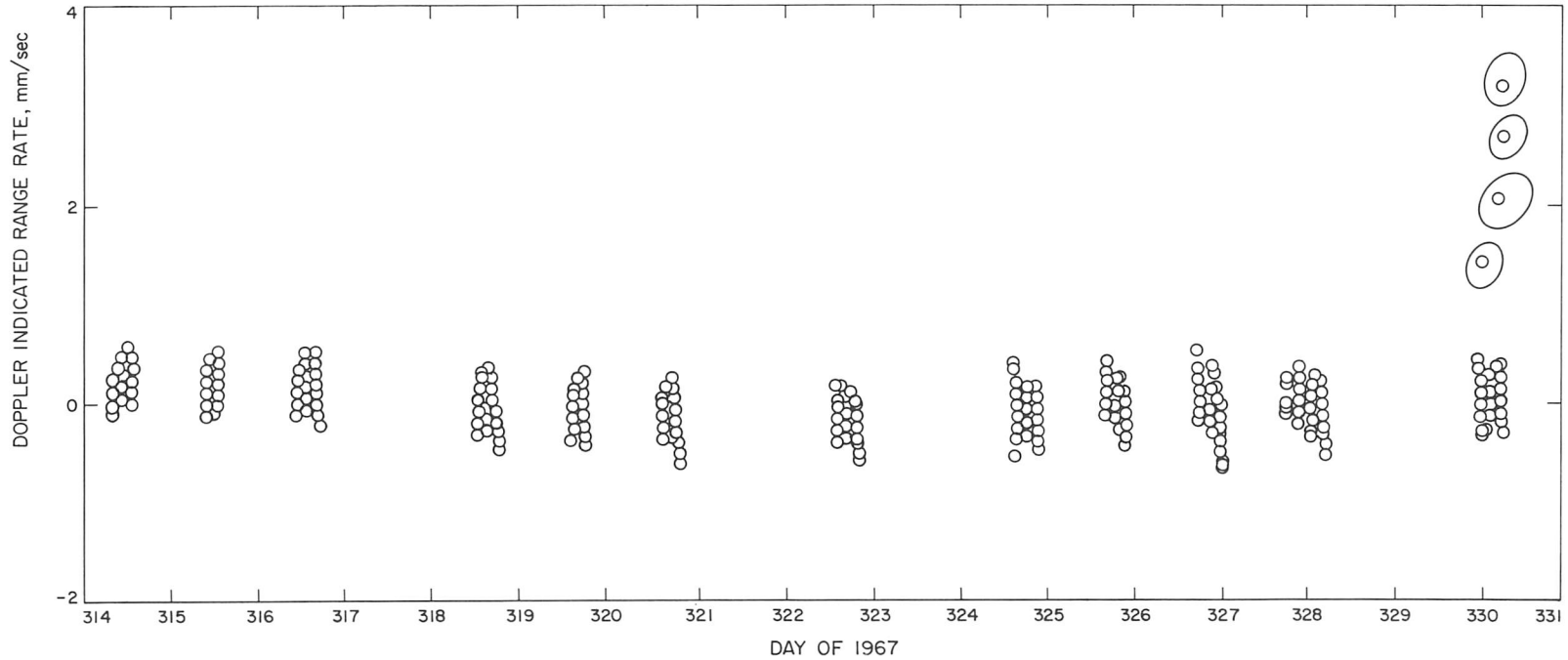

Fig. X-3. *Surveyor VI*, DSS 42 (Canberra, Australia). First lunar day, O — C residual set (one data point/min). DE 29/LE 5 was used.

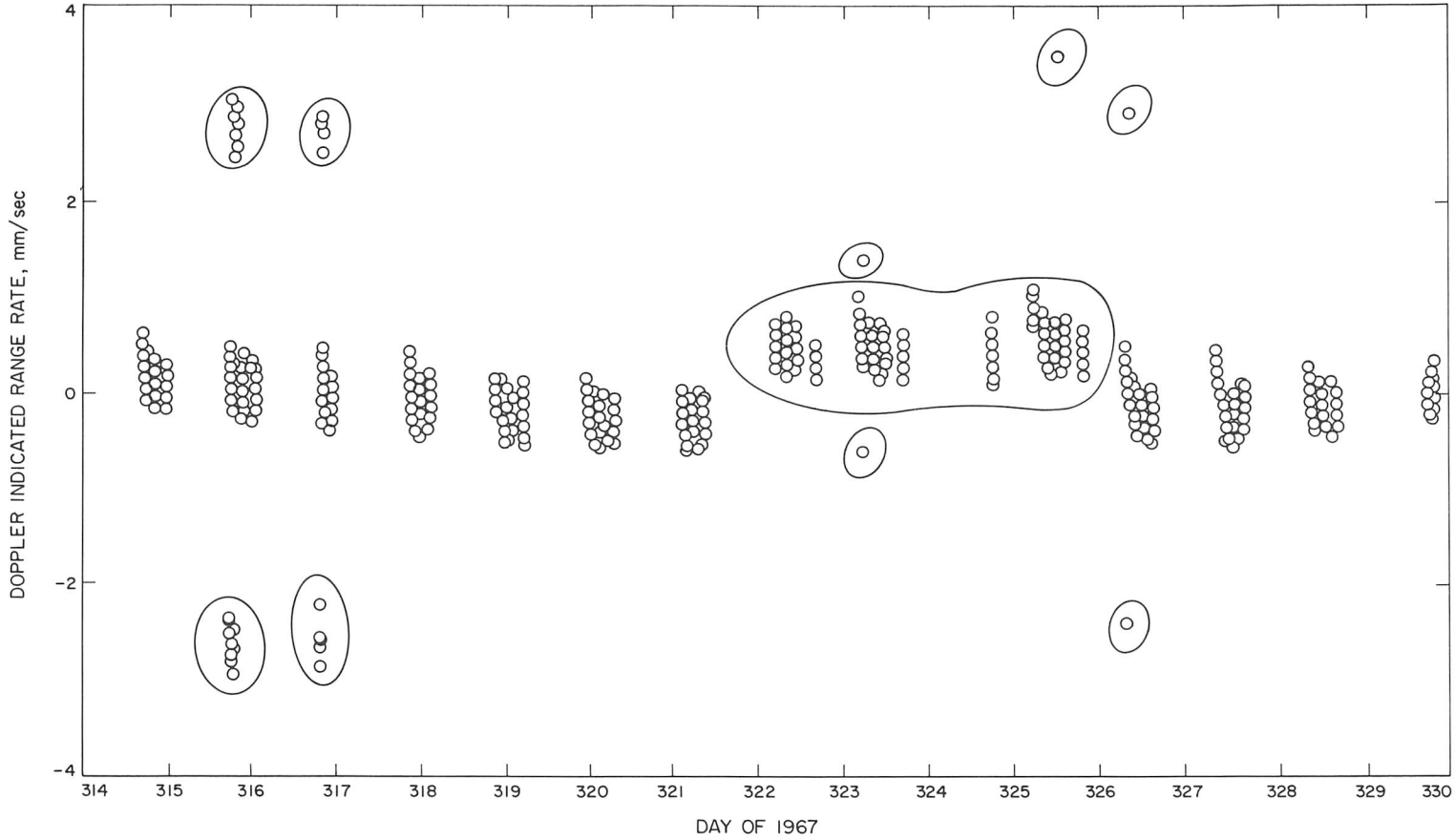

Fig. X-4. *Surveyor VI*, DSS 61 (Madrid, Spain). First lunar day, O — C residual set (one data point/min). DE 29/LE 5 was used.

C. Lunar Ephemerides

Two parallel solutions were executed: one used Lunar Ephemeris 4 (LE 4); a second solution employed Lunar Ephemeris 5 (LE 5).

LE 4 was coupled with the JPL planetary ephemeris to produce Developmental Ephemeris 19 (DE 19/LE 4, Ref. X-2). LE 4 can be regarded as E. W. Brown's Lunar Theory with Eckert's corrections (Ref. X-3). LE 4 has recently been discovered to have radial components of position and velocity which deviate from observation (Figs. X-5 to X-10).

LE 5 is the lunar ephemeris component of Developmental Ephemeris 29 (DE 29/LE 5, Ref. X-4). LE 5 is a numerical integration of the equations of motion which used LE 4 positions as input observables. Essentially, this amounts to a smoothed LE 4, which is gravitationally consistent.

D. The Analysis

The new integrated ephemeris (DE 29/LE 5) was superior to DE 19/LE 4 (see Figs. X-5 to X-10). As with *Surveyors I, III,* and *V, Surveyor VI* has residual traits that are diurnal. Although the diurnal trait remains in the two-way doppler residuals, the DE 29/LE 5 solution is markedly improved compared with the DE 19/LE 4 solution. The remaining imperfections in the lunar ephemeris are the suspected cause of these diurnal anomalies. Investigation of this phenomenon is currently underway (see Ref. X-5); attention has been primarily devoted to the J_{2_0} defect (coefficient of the second harmonic term of the harmonic expansion series used to describe the gravitation potential), and the possible faulty fitting of observations to Brown's Lunar Theory (Fig. X-11).

The longer-termed residual trends demonstrated by the DE 19/LE 4 data reduction were as anticipated (see Figs. X-5 to X-7). The residuals' sinusoidal pattern was descriptive of the range-rate differences between LE 5 and LE 4 after least-squares minimization had been attempted. LE 5 is a better model of the lunar motion than LE 4. The LE 5 − LE 4 range-rate difference plot was compared with the O − C residual plot, and a high correlation was evident (see Fig. X-12).

The residuals of the data reduction using DE 29/LE 5 have no long-term trend, and thus indicate the ability of DE 29/LE 5 to model the lunar motion (see Figs. X-8 to X-10). The parameters, as determined by the two solutions, are presented in Table X-2 with the formal standard deviations specified.

Table X-2. Parameter solutions using DE 19/LE 4 and DE 29/LE 5

Parameters	Initial parameter estimates	A priori standard deviation	DE 19/LE 4 parameter solution	Standard deviation	DE 29/LE 5 parameter solution	Standard deviation
RADS, m	.17360000 04	.10000000 02	.17440351 04	.89418043 00	.17364401 04	.89430626 00
LATS, deg	.43700000 00	.50000000 01	.47414386 00	.69354688−02	.45857298 00	.69722913−02
LONS, deg	.35862999 03	.50000000 01	.35865131 03	.19282753−01	.35863256 03	.19360616−01
STA DSS 11						
RI, m	.63719989 04	.30000000 00	.63719974 04	.26452748−02	.63719972 04	.26452726−02
LO, deg	.24315070 03	.49999999−02	.24315079 03	.98969545−04	.24315081 03	.98969667−04
STA DSS 42						
RI, m	.63716881 04	.30000000 00	.63716809 04	.27011610−02	.63716774 04	.27011539−02
LO, deg	.14898140 03	.49999999−02	.14898152 03	.99103591−04	.14898156 03	.99103715−04
STA DSS 61						
RI, m	.63700005 04	.30000000 00	.63700031 04	.22066633−02	.63700049 04	.22066612−02
LO, deg	.35575114 03	.49999999−02	.35575126 03	.99571756−04	.35575126 03	.99571881−04

The parameters are defined as:

RADS	selenocentric radial distance of *Surveyor*
LATS	selenographic latitude of *Surveyor*
LONS	selenographic longitude of *Surveyor*
RI	geocentric radial distance
LO	geographic longitude

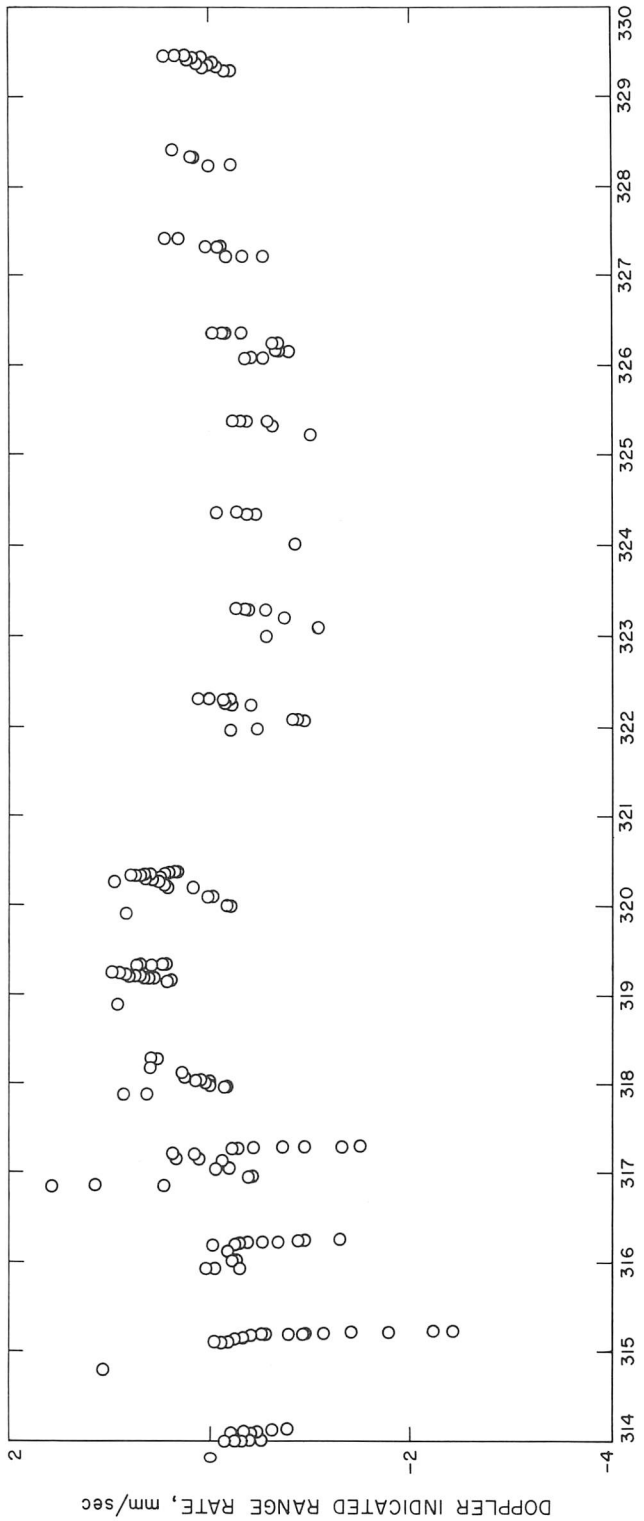

Fig. X-5. *Surveyor VI*, DSS 11 (Goldstone, California). First lunar day, O — C residual set (compressed five data points/min). DE 19/LE 4 was used.

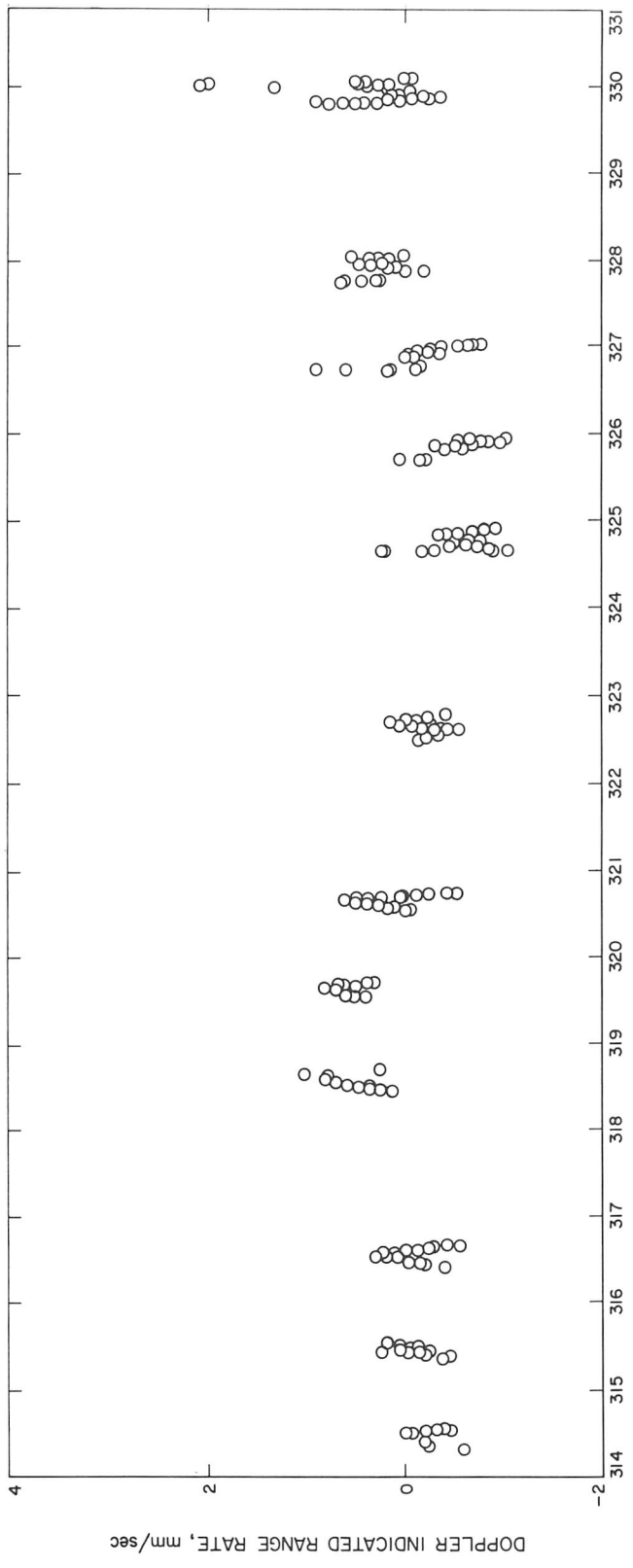

Fig. X-6. *Surveyor VI*, DSS 42 (Canberra, Australia). First lunar day, O — C residual set (compressed five data points/min). DE 19/LE 4 was used.

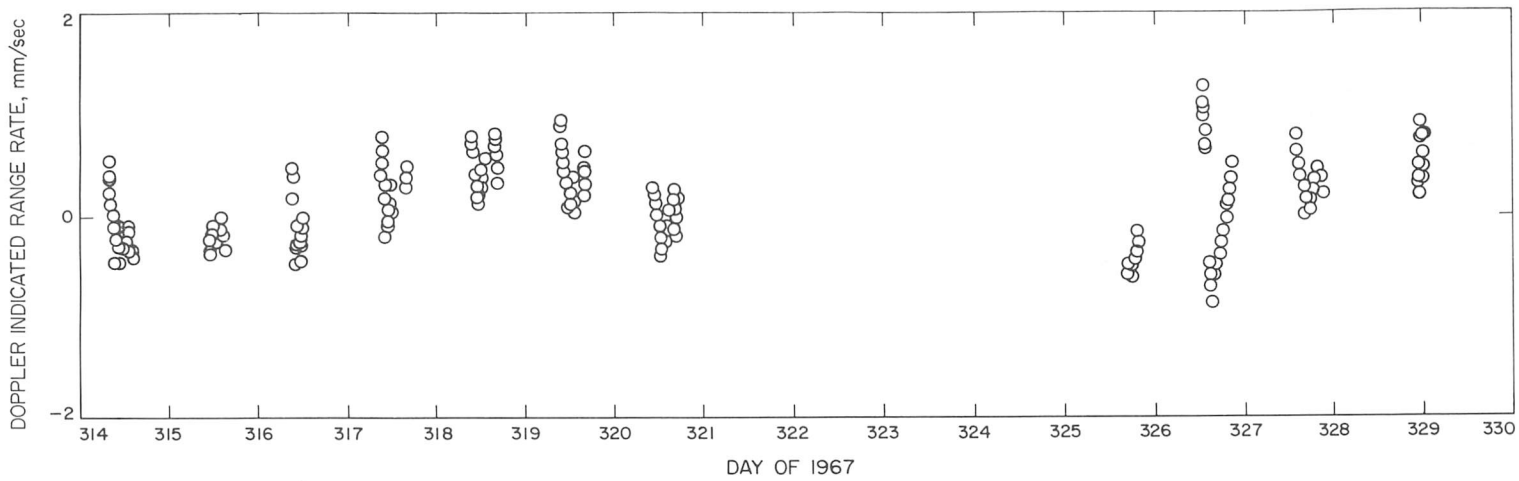

Fig. X-7. *Surveyor VI*, DSS 61 (Madrid, Spain). First lunar day, O — C residual set (compressed five data points/min). DE 19/LE 4 was used.

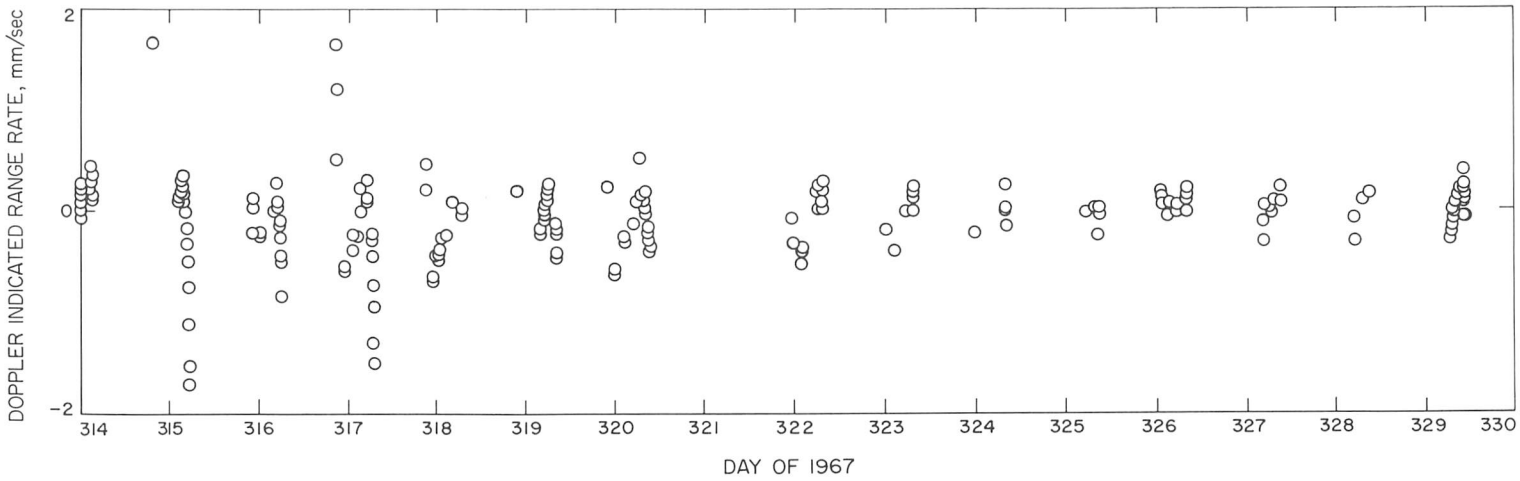

Fig. X-8. *Surveyor VI*, DSS 11 (Goldstone, California). First lunar day, O — C residual set (compressed five data points/min). DE 29/LE 5 was used.

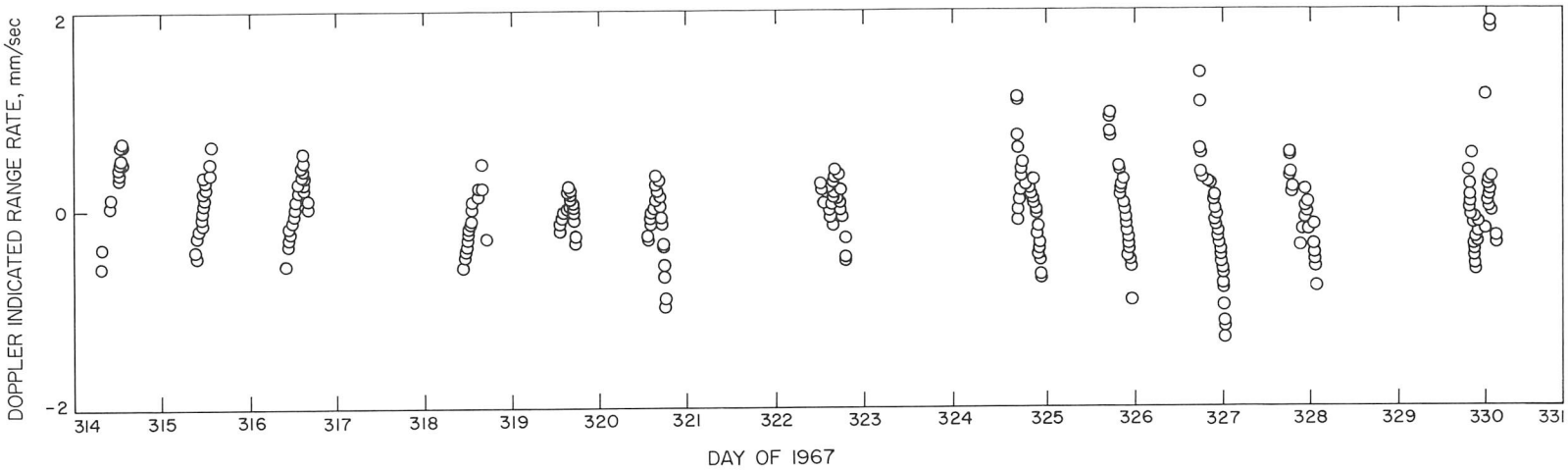

Fig. X-9. *Surveyor VI*, DSS 42 (Canberra, Australia). First lunar day, O — C residual set (compressed five data points/min). DE 29/LE 5 was used.

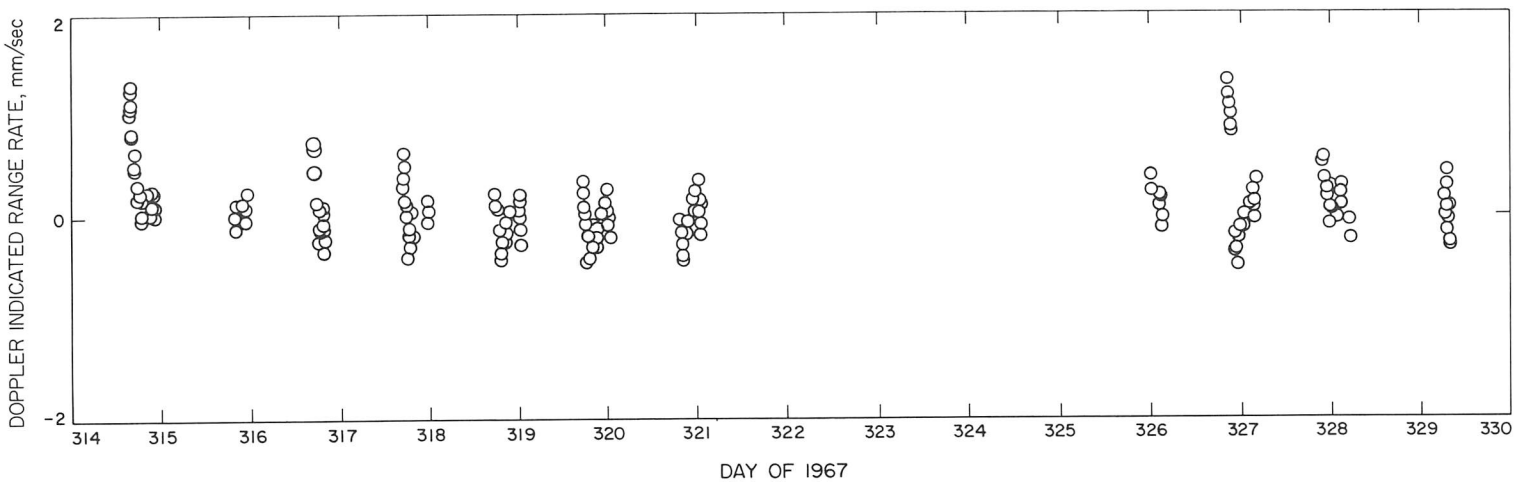

Fig. X-10. *Surveyor VI*, DSS 61 (Madrid, Spain). First lunar day, O — C residual set (compressed five data points/min). DE 29/LE 5 was used.

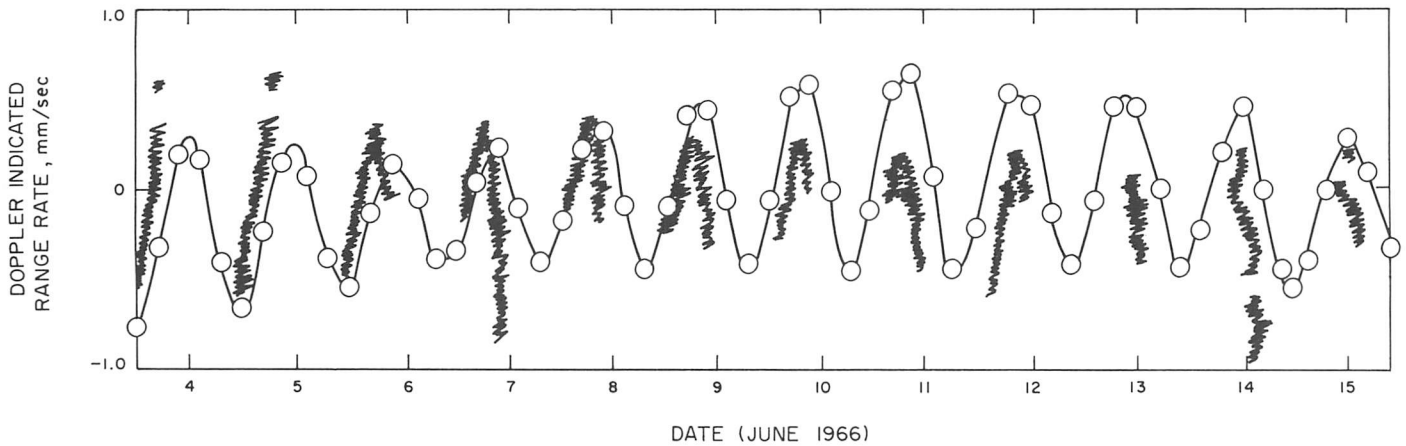

Fig. X-11. Combined amplitude and period of the J_{2_0} defect and the faulty fit of observations to Brown's Lunar Theory are plotted to the same scale as the *Surveyor VI* O − C residual set.

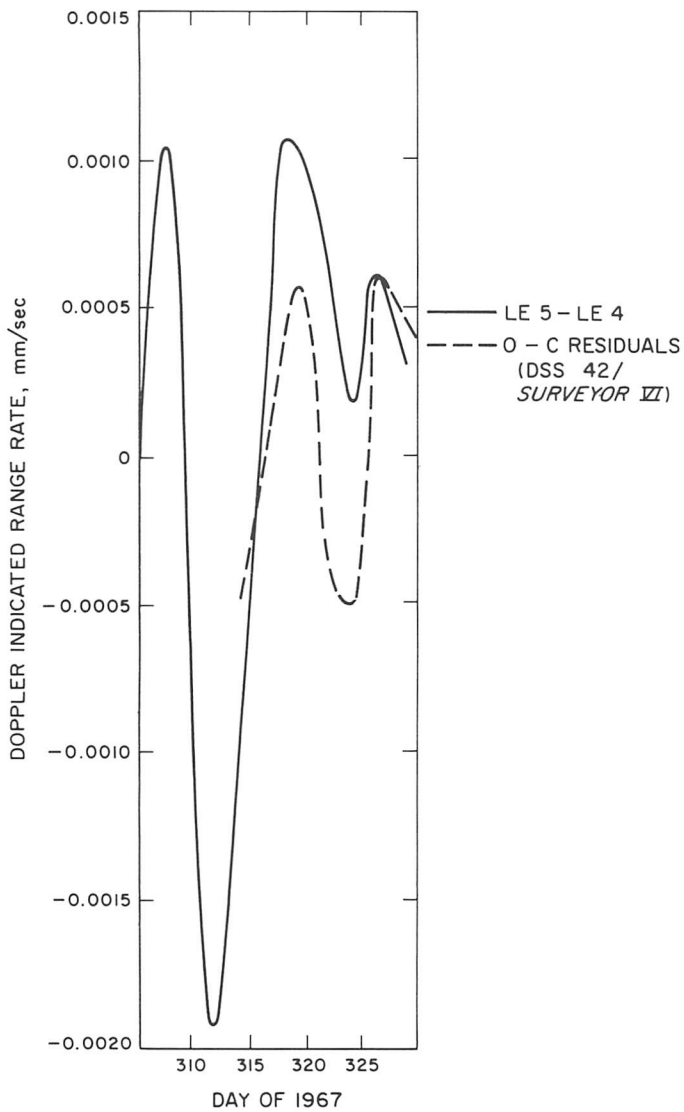

Fig. X-12. LE 5 lunar radial component minus LE 4 lunar radial component function and the *Surveyor VI* O − C residual set of DSS 42 (Canberra, Australia) graphed to same scale.

Table X-3. Covariances of estimated parameters using two solutions

DE 19/LE 4									
	RADS	LATS	LONS	RI (11)	LO (11)	RI (42)	LO (42)	RI (61)	LO (61)
RADS	.79955865 00	.49297340−02	−.12042165−01	.76281168−03	.61770981−04	.94726538−03	.61195725−04	.92869864−04	.62782887−04
LATS	.49297340−02	.48100729−04	−.10926643−03	.49583951−05	.54416304−06	.65101314−05	.54706721−06	.15456238−05	.54764868−06
LONS	−.12042165−01	−.10926643−03	.37182456−03	−.18247060−04	−.18729096−05	−.20642610−04	−.18932005−05	.55872871−05	−.18972037−05
RI (11)	.76281168−03	.49583951−05	−.18247060−04	.69974792−05	.80745608−07	.11740255−05	.93635681−07	−.35714657−06	.94929678−07
LO (11)	.61770981−04	.54416304−06	−.18729096−05	.80745608−07	.97949710−08	.10518258−06	.95437568−08	−.29403279−07	.95728073−08
RI (42)	.94726538−03	.65101314−05	−.20642610−04	.11740255−05	.10518258−06	.72962710−05	.94350615−07	−.22455155−06	.10688160−06
LO (42)	.61195725−04	.54706721−06	−.18932005−05	.93635681−07	.95437568−08	.94350615−07	.98215218−08	−.30306350−07	.96708690−08
RI (61)	.92869864−04	.15456238−05	.55872871−05	−.35714657−06	−.29403279−07	−.22455155−06	−.30306350−07	.48693629−05	−.20311192−07
LO (61)	.62782887−04	.54764868−06	−.18972037−05	.94929678−07	.95728073−08	.10688160−06	.96708690−08	−.20311192−07	.99145348−08

DE 29/LE 5									
	RADS	LATS	LONS	RI (11)	LO (11)	RI (42)	LO (42)	RI (61)	LO (61)
RADS	.79978370 00	.49594124−02	−.12089498−01	.76298045−03	.61787890−04	.94745035−03	.61212787−04	.92800336−04	.62800060−04
LATS	.49594124−02	.48612847−04	−.11028174−03	.49869273−05	.54710564−06	.65471029−05	.55001754−06	.15532146−05	.55061559−06
LONS	−.12089498−01	−.11028174−03	.37483346−03	−.18318709−04	−.18804620−05	−.20722672−04	−.19008489−05	.56129893−05	−.19048517−05
RI (11)	.76298045−03	.49869273−05	−.18318709−04	.69974670−05	.80745348−07	.11740135−05	.93635369−07	−.35715094−06	.94929373−07
LO (11)	.61787890−04	.54710564−06	−.18804620−05	.80745348−07	.97949949−08	.10518201−06	.95437814−08	−.29403575−07	.95728317−08
RI (42)	.94745035−03	.65471029−05	−.20722672−04	.11740135−05	.10518201−06	.72962325−05	.94350102−07	−.22455826−06	.10688104−06
LO (42)	.61212787−04	.55001754−06	−.19008489−05	.93635369−07	.95437814−08	.94350102−07	.98215467−08	−.30306643−07	.96708939−08
RI (61)	.92800336−04	.15532146−05	.56129893−05	−.35715094−06	−.29403575−07	−.22455826−06	−.30306643−07	.48693538−05	−.20311487−07
LO (61)	.62800060−04	.55061559−06	−.19048517−05	.94929373−07	.95728317−08	.10688104−06	.96708939−08	−.20311487−07	.99145596−08

The parameters are defined as:

RADS	selenocentric radial distance of *Surveyor*	RI (42)	geocentric radial distance of DSS 42
LATS	selenographic latitude of *Surveyor*	LO (42)	geographic longitude of DSS 42
LONS	selenographic longitude of *Surveyor*	RI (61)	geocentric radial distance of DSS 61
RI (11)	geocentric radial distance of DSS 11	LO (61)	geocentric longitude of DSS 61
LO (11)	geographic longitude of DSS 11		

The relative displacement of the two error ellipsoids arising from the two SPODP solutions using DE 19/LE 4 and DE 29/LE 5 ephemerides demonstrates the influence of different lunar motion models. The ellipsoidal centers were displaced:

8000 m radially.
550 m lunar latitude.
885 m lunar longitude.

The solutions for the terrestrial Tracking Station positions are less sensitive to the ephemerides differences. The relative displacements of the Tracking Station error ellipses are:

DSS 11: 0 m radially; 2 m terrestrial longitude.
DSS 42: ~4 m radially; ~6 m terrestrial longitude.
DSS 61: ~2 m radially; 0 m terrestrial longitude.

The statistical dependence or independence of one parameter in relation to other parameters within a recursive least-squares solution can be inferred from the correlations of the parameter in question and the remaining parameter list. The magnitudes of the parameter correlations in the correlation matrices presented in Table X-3 are indicative of the relative statistical independence of the parameters in the SPODP solutions using DE 19/LE 4 and DE 29/LE 5.

Table X-4. Summary of *Surveyor VI* location determinations

Source	Selenographic latitude (ϕ), °N	σ_ϕ	Selenographic longitude (λ), °W	σ_λ	Lunar radius (R)	σ_R
1[a]	0.49	—	1.40	—	—	—
2[b]	0.437	0.065	358.630	0.006	—	—
3[c]	0.474	0.007	358.651	0.019	1744.^{m}04	0.89
4[d]	0.458	0.007	358.632	0.019	1736.44	0.89

[a]E. A. Whitaker, Lunar and Planetary Laboratory, University of Arizona, derived from comparison of *Lunar Orbiter IV* photograph of *Surveyor VI* lunar sight and the Orthographic Atlas.

[b]Terminal cruise SPODP position (cruise data; see Ref. X-6).

[c]SPODP data reduction using DE 19/LE 4 (post-landed *Surveyor* data).

[d]SPODP data reduction using DE 29/LE 5 (post-landed *Surveyor* data).

It is of interest to note the values of the *Surveyor VI* selenographic position determinations from available sources. Table X-4 shows the various determinations. The various terrestrial Tracking Station determinations from all available sources and their solutions are presented in Table X-5.

Table X-5. Summary of Deep Space Station locations[a]

Station	Source	Spin axis distance (R_s), m	Longitude (λ), deg
DSS 11 (Goldstone)	*Surveyor I*	5206.3276	243.15085
	Surveyor III	—	—
	Surveyor V	.2670	.15114
	Surveyor VI (DE 19/LE 4)	.3317	.15081
	Surveyor VI (DE 29/LE 5)	.3315	.15083
	Combined *Ranger* position of DSS 12 corrected to DSS 11 by land survey	.3266	.15089
	Goddard survey	.3718	.15094
DSS 42 (Canberra)	*Surveyor I*	5205.3474	148.98130
	Surveyor III	.3581	.98127
	Surveyor V	.3553	.98175
	Surveyor VI (DE 19/LE 4)	.3423	.98147
	Surveyor VI (DE 29/LE 5)	.3395	.98151
	Goddard Survey	.2940	.98006
DSS 61 (Madrid)	*Surveyor I*	—	—
	Surveyor III	4862.5993	355.75101
	Surveyor V	.5992	.75149
	Surveyor VI (DE 19/LE 4)	.6031	.75120
	Surveyor VI (DE 29/LE 5)	.6045	.75120
	Mariner V post-encounter tracking data solution for DSS 12 corrected to DSS 61 by land survey	.6077	.75122
	JPL land survey	.6482	.75182

[a]These coordinates are referenced to one pole, 1903.0.

References

X-1. Warner, M. R., and Nead, M. W., *SPODP — Single Precision Orbit Determination Program,* Technical Memorandum 33-204, Jet Propulsion Laboratory, Pasadena, Calif., February 15, 1965.

X-2. Lawson, C. L., *Announcement of JPL Developmental Ephemeris No. 19,* Technical Memorandum 33-162, Jet Propulsion Laboratory, Pasadena, Calif., April 13, 1967.

X-3. Mulholland, J. D., and Block, N., *JPL Lunar Ephemeris Number 4,* Technical Memorandum 33-346, Jet Propulsion Laboratory, Pasadena, Calif., August 1, 1967.

X-4. Mulholland, J. D., "Preparations for Numerical Integration of the Lunar Motion," *Supporting Research and Advanced Development,* Space Programs Summary 37-47, Vol. III, pp. 6–7, Jet Propulsion Laboratory, Pasadena, Calif., October 31, 1967.

X-5. Mulholland, J. D., "A Possible Explanation of Landed *Surveyor* Residuals," *The Deep Space Network,* Space Programs Summary 37-49, Vol. II, Jet Propulsion Laboratory, Pasadena, Calif., January 31, 1968.

X-6. *Surveyor VI Mission Report. Part I: Mission Description and Performance,* Technical Report 32-1262, Jet Propulsion Laboratory, Pasadena, Calif. (to be published).

(Blank Page)

Appendix

Surveyor Science Teams and Cognizant Personnel

Analysis of the scientific data, for the *Surveyor VI* mission, was conducted by the *Surveyor* Scientific Evaluation Advisory Team, Investigator Teams, and Working Groups. Membership for *Surveyor VI* was:

A. *Surveyor* Scientific Evaluation Advisory Team

L. D. Jaffe, Chairman	Jet Propulsion Laboratory
S. A. Batterson	Langley Research Center
W. E. Brown, Jr.	Jet Propulsion Laboratory
E. M. Christensen	Jet Propulsion Laboratory
S. E. Dwornik	NASA Headquarters
D. E. Gault	Ames Research Center
J. W. Lucas	Jet Propulsion Laboratory
R. H. Norton	Jet Propulsion Laboratory
R. F. Scott	California Institute of Technology
E. M. Shoemaker	U. S. Geological Survey
R. H. Steinbacher	Jet Propulsion Laboratory
G. H. Sutton	University of Hawaii
A. L. Turkevich	University of Chicago

B. Investigator Teams

1. Television

E. M. Shoemaker, Principal Investigator	U. S. Geological Survey
R. A. Altenhofen	U. S. Geological Survey
R. M. Batson	U. S. Geological Survey
H. E. Holt	U. S. Geological Survey
G. P. Kuiper	University of Arizona
E. C. Morris	U. S. Geological Survey
J. J. Rennilson	Jet Propulsion Laboratory
E. A. Whitaker	University of Arizona

2. Alpha-Scattering

A. L. Turkevich, Principal Investigator	University of Chicago
E. J. Franzgrote	Jet Propulsion Laboratory
J. H. Patterson	Argonne National Laobratory

C. Working Groups

1. Lunar Surface Thermal Properties

J. W. Lucas, Chairman	Jet Propulsion Laboratory
J. E. Conel	Jet Propulsion Laboratory
D. Greenshield	Manned Spacecraft Center

R. R. Garipay	Hughes Aircraft Company
W. A. Hagemeyer	Jet Propulsion Laboratory
H. C. Ingrao	Harvard College Observatory
B. P. Jones	Marshall Space Flight Center
J. M. Saari	The Boeing Company
G. Vitkus	Northrop Corporation

2. Lunar Surface Electromagnetic Properties

W. E. Brown, Jr., Chairman	Jet Propulsion Laboratory
J. Negus de Wys	Jet Propulsion Laboratory
R. A. Dibos	Hughes Aircraft Company
G. B. Gibson	Manned Spacecraft Center
D. O. Muhleman	California Institute of Technology
W. H. Peake	Ohio State University
V. J. Peohls	Ryan Aeronautical Company

3. Lunar Surface Mechanical Properties

E. M. Christensen, Chairman	Jet Propulsion Laboratory
S. A. Batterson	Langley Research Center
H. E. Benson	Manned Spacecraft Center
R. Choate	Jet Propulsion Laboratory
R. E. Hutton	TRW Systems
L. D. Jaffe	Jet Propulsion Laboratory
R. H. Jones	Hughes Aircraft Company
H. Y. Ko	University of Colorado
R. F. Scott	California Institute of Technology
F. N. Schmidt	Bellcomm, Inc.
R. L. Spencer	Jet Propulsion Laboratory
F. B. Sperling	Jet Propulsion Laboratory
G. H. Sutton	University of Hawaii

4. Astronomy

R. H. Norton, Chairman	Jet Propulsion Laboratory
J. E. Gunn	Jet Propulsion Laboratory
W. C. Livingston	Kitt Peak National Observatory
G. A. Newkirk	High Altitude Observatory
H. Zirin	Mt. Wilson and Palomar Observatories

5. Lunar Theory and Processes

D. E. Gault, Chairman	Ames Research Center
J. B. Adams	Jet Propulsion Laboratory
R. J. Collins	University of Minnesota
T. Gold	Cornell University
J. Green	McDonnell-Douglas Corp.
G. P. Kuiper	University of Arizona
H. Masursky	U. S. Geological Survey
J. A. O'Keefe	Goddard Space Flight Center
R. A. Phinney	Princeton University
E. M. Shoemaker	U. S. Geological Survey
H. E. Urey	University of California, San Diego

The cognizant personnel of the various science and instrument aspects of the *Surveyor VI* mission were:

A. Program and Project Scientists

S. E. Dwornik	Program Scientist
L. D. Jaffe	Project Scientist
R. H. Steinbacher	Associate Project Scientist
E. M. Christensen	Assistant Project Scientist

B. Cognizant Scientists and Science Staff

E. J. Franzgrote	Cognizant Scientist, Alpha-Scattering Experiment
R. E. Parker	Alpha-Scattering Experiment
T. H. Bird	Cognizant Scientist, Television Experiment
J. J. Rennilson	Television Experiment
D. L. Smythe	Television Experiment
M. Benes	Television Experiment
J. N. Strand	Television Science Data Handling
E. T. Johnson	Cognizant Engineer, Image Processing Laboratory
S. L. Grotch	Non-Television Science Data Handling
C. H. Goldsmith	*Surveyor* Experiment Test Laboratory
A. L. Filice	Landing Sites

C. Instrument Development

D. H. Le Croissette	Manager, *Surveyor* Instrument Development
C. E. Chandler	Project Engineer, Instruments
R. J. Holman	Cognizant Engineer, Alpha-Scattering Instrument
M. I. Smokler	Supervisor and Cognizant Engineer, Television Instrument

D. Space Science Analysis and Command

J. N. Lindsley	Director
D. D. Gordon	Assistant Director
R. C. Heyser	Director, Television Performance Analysis and Command
D. L. Smythe	Director, Television Analysis and Command
E. J. Franzgrote	Director, Alpha-Scattering Instrument Analysis and Command
C. R. Heinzen	Command Controller

(Blank Page)